The galaxy cluster Fornax, Unveiled in CO: how dense environments drive galaxy evolution

by

Nikki Zabel

A Thesis submitted to Cardiff University
for the degree of Doctor of Philosophy

26 November 2020

I see beyond the plight of humans. I see a universe ever-expanding, with its galaxies embedded within the ever-stretching four-dimensional fabric of space and time. However big our world is, our hearts, our minds, our outsize atlases, the universe is even bigger. There are more stars in the universe than grains of sand on the world's beaches, more stars in the universe than seconds of time that have passed since Earth formed, more stars than words & sounds ever uttered by all humans who have ever lived. The day we cease the exploration of the cosmos is the day we threaten the continuing of our species. In that bleak world, arms-bearing, resource-hungry people & nations would be prone to act on their low-contracted prejudices, and would have seen the last gasp of human enlightenment. Until the rise of a visionary new culture that once again embraces the cosmic perspective; a perspective in which we are one, fitting neither above nor below, but within.

Neil deGrasse Tyson/
Avenged Sevenfold, *"Exist"*

Acknowledgements

Well, this is probably a cliché by now, but this was not how I'd imagined the final year of my PhD. From one day to the next I found myself working from my apartment, never to return to our familiar "galaxies" office at 53 The Parade again. What a year it's been. But here we are: I did it! I managed to finish my PhD during a global pandemic, and I'm so glad I am finally allowed to call myself a Doctor.

First of all I would like to thank my viva panel for taking the time to read this thesis, and for being there at the very end of the ride. Dr. Mattia Negrello and Prof. Alastair Edge, who led the conversation and made it such a pleasant experience. Thanks also to Prof. Steve Eales and his furry friend for chairing the session.

I'd also like to thank the many collaborators I've had the pleasure to work with over the years, who have contributed to this thesis in a variety of ways, reviewed my work, and provided me with many helpful suggestions and constructive feedback. I hope to collaborate with many of you again in the future.

On a more technical note, I would like to acknowledge the many facilities, databases, and software, many of which open-source, that have made this thesis possible or have made my life significantly easier during the process. More detailed acknowledgements are given in the publications of the individual chapters.

Of course, this has been a journey I have by no means completed alone. To begin with, the PHYSX department in Cardiff has got to be one of the friendliest places you could possibly work in. Cardiff had stuck with me after I received many enthusiastic replies to my careful enquiries about PhD positions at the School, all within a few hours (for the mainlanders: Donald Duck magazine probably couldn't match the number of exclamation points in Tim's email). This was among the main reasons I ended up accepting this position. As it turns out, my impression of the place was pretty accurate. The amicable atmosphere in the office, the many coffee (and

cake) breaks, and pub trips made me feel at home very quickly. Not to mention the "special tea" sessions, office puzzles, Bandaoke nights, barbecues, rugby watching, and epic (>12 hour lasting) Christmas parties. I could not have asked for a more fun environment to do my PhD in. So thanks to all of you in the department contributing to making this such a lively one! And of course, a special thanks to the "galaxy lads", who I've had the pleasure to share an office with, and who have time and again proven to be the hard core of the bunch. I can't wait to come back and ~~get smashed~~ celebrate with you all properly!

A big thank you also to "Team Grand", who have been both a very fun and supportive (professionally and personally) research group. I have fond memories of silly things like group meetings with party hats and cake and port and Christmas-decorating Tim's office on his birthday, but also of productive group meetings, and people always being ready to help each other out with science problems big and small. A special thanks of course to my academic twin James, who made going to the office feel like a holiday every day and later carried me through the lockdown.

Dr. Timothy Davis, I could not have wished for a better supervisor. The projects you let me carry out were fun and diverse, they allowed me to really dive into the wonderful world of galaxy evolution and contribute some meaningful results to the community. Thank you for trusting me with your ALMA data, but also for presenting me with so many opportunities, be it conferences, observing experiences, being part of telescope proposals, or new collaborations. Know I haven't been taking these for granted! Though most of all thank you for always being ready to help, most of the time instantly (!), and for being a reassuring voice on the odd days frustration gained the upper hand.

Last but not least, thanks to my loyal friends across the pond, who have been by my side throughout this experience despite the distance. Both to those of you whom I talk to on a daily basis, and to those who I see a few times per year, but always manage to make it feel like the old days. You know who you are! I am very grateful for all the daily jokes, ranting sessions, heavier conversations, video calls, and visits. The same, of course, goes for my parents and siblings, who I'm grateful to know always have my back.

Oh, and thanks to my cheeky fluff-ball Puff for vaguely accepting my eternal presence during this lockdown.

Abstract

This thesis investigates the effects of dense environments on galaxy evolution by studying the cold molecular gas in Fornax cluster galaxies. Cold molecular gas is the direct fuel for star formation. Therefore, understanding the way it is affected by the cluster is key to understanding galaxy evolution in such dense environments, and, with a large fraction of galaxies residing in groups and clusters, galaxy evolution as a whole. I will show that dense environments can directly affect the cold molecular gas reservoirs of galaxies, which in turn impacts related properties such as their star formation relations and gas-to-dust ratios.

This thesis starts by presenting data from the ALMA Fornax Cluster Survey (AlFoCS). This includes moment maps, position-velocity diagrams, and spectra, as well as several integrated properties. All low-mass galaxies in Fornax, comprising roughly half the sample, have disturbed molecular gas reservoirs. With the exception of the massive spiral NGC1365, galaxies in the Fornax cluster have systematically lower molecular gas fractions than field galaxies at fixed stellar mass. Therefore, the Fornax cluster is (still) an active environment, that directly impacts even the tightly bound molecular gas in its galaxies.

Using Hα observations from MUSE, the star formation relation in the Fornax cluster is calculated, and compared to those found by Kennicutt (1998) and Bigiel et al. (2008). The star formation relation in Fornax is close to these "classic" relations, albeit closer to their low-depletion time sides. There is, however, large scatter both between different galaxies and within them. The slightly decreased depletion times could be due to the compression of the molecular gas as a result of environmental effects as galaxies enter the cluster for the first time (e.g. ram pressure stripping).

Finally, I study gas-to-dust (H_2-to-dust, HI-to-dust, and total gas-to-dust) ratios in the Fornax cluster, using additional observations from *Herschel* and ATCA.

These ratios are studied both as a function of stellar mass, and of metallicity, estimated from the MUSE data. Gas-to-dust ratios in the Fornax cluster are systematically suppressed. This is both driven by decreased HI-to-dust ratios as well as decreased H_2-to-dust ratios. H_2-to-dust ratios in the Virgo cluster, on the other hand, are found to be increased. The low H_2-to-dust ratios in Fornax could be due to the accumulated production of dust during the star formation process, while H_2 is slowly depleted and not replenished as efficiently. Alternatively, H_2 could be stripped from these galaxies more efficiently than dust, or the ISM in Fornax galaxies could be different in such a way that we are not probing the gas and/or dust reservoirs accurately. The surprising difference with the more massive and dynamically active Virgo cluster suggests that different kinds of dense environments affect galaxies differently.

In summary, in this thesis I will show some of the ways in which molecular gas is affected by environment, as well as the implications for related properties. I will conclude with some remaining puzzles, and how these can be solved with next-generation instruments.

Publications

First Author:

Nikki Zabel, Timothy A. Davis, Matthew W. L. Smith, Natasha Maddox, George J. Bendo, Reynier Peletier, Enrichetta Iodice, Aku Venhola, Maarten Baes, Jonathan I. Davies, Ilse de Looze, Haley Gomez, Marco Grossi, Jeffrey D. P. Kenney, Paolo Serra, Freeke van de Voort, Catherine Vlahakis, and Lisa M. Young, 2019, MNRAS, 483, 2251: *"The ALMA Fornax Cluster Survey I: stirring and stripping of the molecular gas in cluster galaxies"* - Chapter II

Nikki Zabel, Timothy A. Davis, Marc Sarzi, Boris Nedelchev, Mélanie Chevance, J. M. Diederik Kruijssen, Enrichetta Iodice, Maarten Baes, George J. Bendo, Enrico Maria Corsini, Ilse de Looze, P. Tim de Zeeuw, Dimitri A. Gadotti, Marco Grossi, Reynier Peletier, Francesca Pinna, Paolo Serra, Freeke van de Voort, Aku Venhola, Sébastien Viaene, and Catherine Vlahakis, 2020, MNRAS, 496, 2155: *"AlFoCS + Fornax3D: resolved star formation in the Fornax cluster with ALMA and MUSE"* - Chapter III

Nikki Zabel, Timothy A. Davis, Matthew W. L. Smith, Marc Sarzi, Alessandro Loni, Paolo Serra, Maritza A. Lara-López, Phil Cigan, Maarten Baes, George J. Bendo, Ilse De Looze, Enrichetta Iodice, Dane Kleiner, Bärbel S. Koribalski, Reynier Peletier, Francesca Pinna, P. Tim de Zeeuw, accepted for publication in MNRAS, "*AlFoCS + F3D II: unexpectedly low gas-to-dust ratios in the Fornax galaxy cluster*" - Chapter IV

Co-Author:

Timothy A. Davis, Jenny E. Greene, Chung-Pei Ma, John P. Blakeslee, James M. Dawson, Viraj Pandya, Melanie Veale, and **Nikki Zabel**, 2019, MNRAS, 486, 1404: *"The MASSIVE survey - XI. What drives the molecular gas properties of early-type galaxies?"*

James M. Dawson, Timothy A. Davis, Edward L. Gomez, Justus Schock, **Nikki Zabel**, and Thomas G. Williams, 2019, MNRAS, 491, 2506: *"Using machine learning to study the kinematics of cold gas in galaxies"*

Maria A. Raj, Enrichetta Iodice, Nicola R. Napolitano, Marilena Spavone, Hung-Shuo Su, Reynier Peletier, Timothy A. Davis, **Nikki Zabel**, Michael Hilker, Steffen Mieske, Jesus Falcón-Barroso, Michele Cantiello, Glenn van de Ven, Aaron E. Watkins, Heikki Salo, Pietro Schipani, Massimo Capaccioli, and Aku Venhola, 2019, A&A, 628, A4: *"The Fornax Deep Survey with the VST - VII. Evolution and structure of late-type galaxies inside the virial radius of the Fornax cluster"*

Sébastien Viaene, Marc Sarzi, **Nikki Zabel**, Lodovico Coccato, Enrico M. Corsini, Timothy A. Davis, Pieter de Vis, P. Tim de Zeeuw, Jesus Falcón-Barroso, Dimitri A. Gadotti, Enrichetta Iodice, Mariya Lyubenova, Richard McDermid, Lorenzo Morelli, Boris Nedelchev, Francesca Pinna, Thomas W. Spriggs, and Glenn van de Ven, 2019, A&A, 622, A89: *"The Fornax 3D project: dust mix and gas properties in the centre of early-type galaxy FCC 167"*

Timothy A. Davis, **Nikki Zabel**, James M. Dawson, 2020, ASCL, *"KinMS: Three-dimensional kinematic modelling of arbitrary gas distributions"*

A. Loni, P. Serra, D. Kleiner, L. Cortese, B. Catinella, B. Koribalski, T. H. Jarrett, D. Cs. Molnar, T. A. Davis, E. Iodice, K. Lee-Waddell, F. Loi, F. M. Maccagni, R. Peletier, A. Popping, M. Ramatsoku, M. W. L. Smith, and **N. Zabel**, accepted for publication in A&A, *"A blind ATCA HI survey of the Fornax galaxy cluster: Properties of the HI detections"*

Contents

List of Tables

List of Figures

Chapter 1
Introduction

> Words are flowing out
> Like endless rain into a paper cup
> They slither while they pass
> They slip away across the universe
>
> The Beatles, *"Across the Universe"*

In this thesis I will present new results on the impact of environment on the evolution of galaxies. In this chapter I outline the background and physics underlying these results.

1.1 Extragalactic Astronomy

On the very first day of 1925 the heated discussion that had been dividing the astronomical community throughout the early 1920s[1] was finally settled. With his 100-inch reflector, the "highest resolving power available", Edwin Hubble showed that there is no difference between the stars in the "nebula" Messier 33 (shown in Figure 1.1) and "ordinary galactic stars" (Hubble, 1926). Conclusion: Messier 33

[1] Astronomers disagreed on what the fuzzy blobs in the sky were: some argued that they were huge systems of stars, very far away, while others were convinced they were just small clouds of gas. This eventually lead to the "Great Debate" between Harlow Shapley (in favour of the latter, though he was right about the Milky Way being much bigger than people thought at the time) and Heber D. Curtis (who was actually right), which did not come to a satisfying conclusion until 1925 (Shapley & Curtis, 1921).

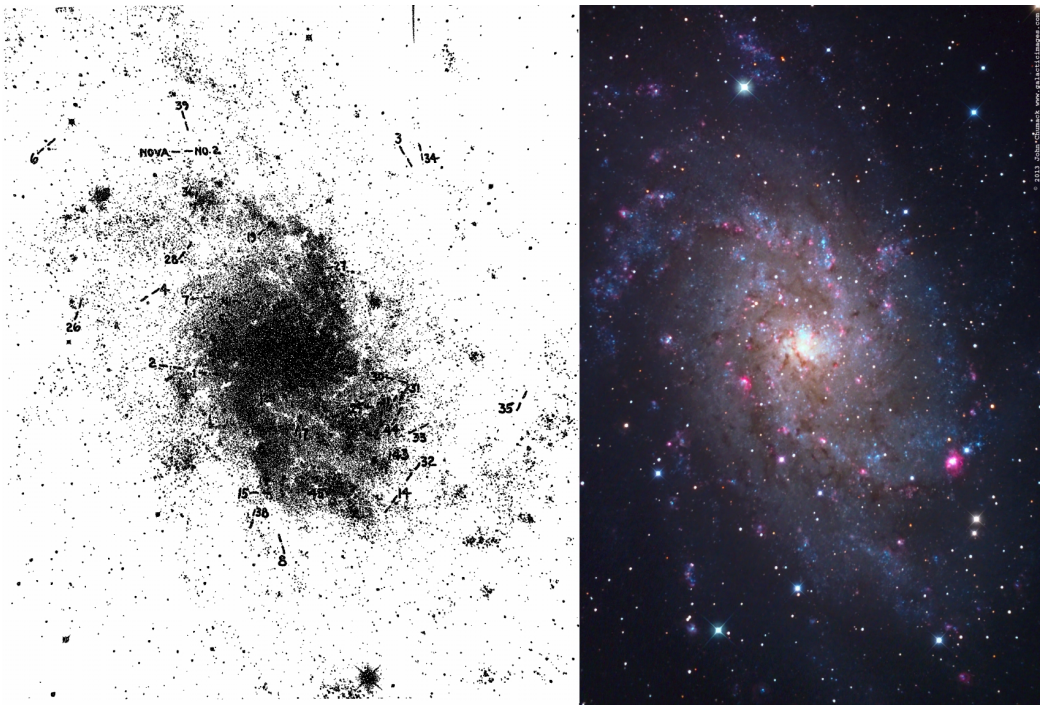

Figure 1.1: Messier 33 (also known as the Triangulum Galaxy) as seen through Hubble's 100-inch reflector with an exposure time of 8.5 hours (left, Hubble 1926), and as a modern-day false-colour image (right, credit: John Chumack, 2013, `www.galacticimages.com`).

was a second Milky Way[2]. And if there was a second Milky Way, there was probably a third Milky Way. Quite possibly, all those fuzzy nebulae were other Milky Ways.

Extragalactic astronomy was born.

Interestingly, the word "galaxy" was suggested by - the good sport - Shapley, who was of the opinion that a new word should be adopted to reflect this new reality. Hubble himself stubbornly clung on to the term "extra-galactic nebulae" until the day he died.

1.1.1 GALAXY MORPHOLOGY

Even before realising what exactly they were looking at, astronomers had been aware that "nebulae" came in various shapes and sizes (e.g. Reynolds 1916. Reynolds later criticised Hubble's classification, see below). However, it was again Hubble

[2] "Here is the letter that destroyed my universe" poor Shapley uttered to Cecilia Payne-Gaposchkin (known for her pioneering work on stellar spectra, which was also completed on January 1, 1925) when Hubble's news arrived.

(proving unstoppable after his major discovery) who came up with a classification scheme that stuck and is still in use today. Hubble first used his classification in the same 1926 paper that proved that nebulae were, in fact, galaxies. His famous "tuning fork" diagram was first published in his book "Realm of the Nebulae" in 1936 (Hubble, 1936), and is shown in Figure 1.2. On the base of the tuning fork there are the ellipticals, also referred to as "early-types", which then split off into (un-barred) spirals and barred spirals, collectively referred to as "late-types".

Both groups of galaxies (as well as all other galaxies that do not fit in either of those categories) are comprised of stars (and their remnants), dark matter, and an "interstellar medium" (ISM). The interstellar medium essentially comprises everything in galaxies that is not stars or dark matter. This includes different gas phases, dust, (and, according to some, the various types of radiation). More details on the ISM and components that are important for this work can be found in §1.1.6. Besides the ISM, there also is gas inside galaxies' haloes, called the "circumgalactic medium" (CGM). In galaxy clusters, which we will discuss in more detail in §1.1.2 and §1.1.5, the space between galaxies is filled with an extremely hot plasma: the "intracluster medium" (ICM), which I will discuss further in §1.1.5.

Elliptical galaxies consist of older stars, characterised by red colours. As the name suggests, they are shaped like ellipsoids (how "stretched" they look varies, and is indicated with a number, as shown in Figure 1.2). They maintain their shape thanks to the random motions of the stars ("velocity dispersion").

Spiral galaxies contain what is essentially a mini-elliptical in their centres, called the "bulge". Around that, they have discs that harbour young stars (in addition to older ones), characterised by their blue colours, supported by rotational motions. Of course, they also have spiral arms: density waves in the disc that result in beautiful looking patterns. The number and density (how wound-up they are) of these arms varies between galaxies, and is described with a letter in Hubble's classification (see Figure 1.2). In addition to spiral arms, late-type galaxies can have bars: non-axisymmetric central structures composed of stars (our own Milky Way has one of those). These galaxies make up the lower prong of Hubble's tuning fork. At least half of all spiral galaxies contain a bar. Bars are thought to channel gas inwards from the spiral arms, thus fuelling star formation in galactic centres. They are thought to be temporary structures, that come and go as the galaxy evolves. They appear to be significantly more common in the Local Universe than in the Early Universe (Sheth et al., 2008), which suggests that they are formed in the later evolutionary stages of galaxies.

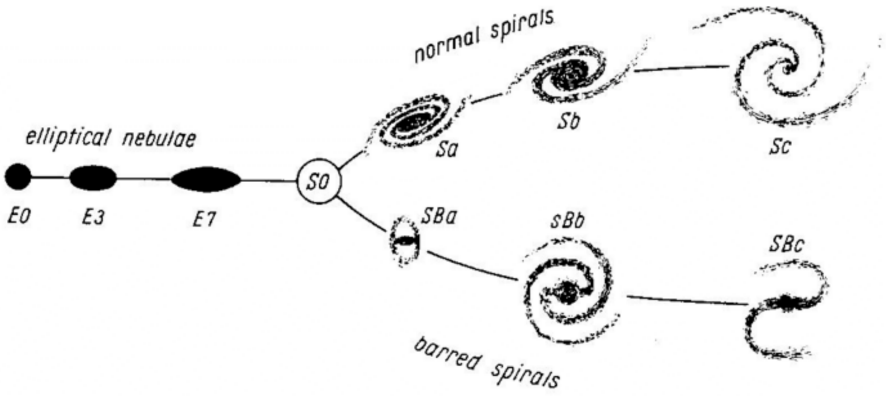

Figure 1.2: Hubble's "tuning fork" diagram of galaxy classification. Galaxies are subdivided into ellipticals ("early-types"), spirals, and barred spirals (both "late-types"). As this terminology suggests, astronomers were under the (wrong) impression that galaxies evolved according to this diagram from left to right.

In between the elliptical and the spiral galaxies, we have the "lenticular" galaxies, right at the split of the tuning fork (Figure 1.2). Lenticular galaxies do have discs, but lack spiral arms. Therefore, they are considered a separate class, between spirals and ellipticals. In terms of other properties than morphology (i.e. spectral features or scaling relations, see below), lenticulars have more in common with ellipticals than spirals, and are therefore considered early-type galaxies. The "early-type" vs. "late-type" nomenclature reflects the (incorrect) interpretation at the time that the tuning fork should be interpreted as an evolutionary sequence from left to right. Of course, we now know that this interpretation of Hubble's diagram was not exactly right. However, it is true that these galaxy types do reflect different evolutionary stages. It is, actually, more accurate to read the tuning fork diagram from right to left. Nonetheless, the "late-type" vs. "early-type" terminology stuck, which means that we are - as does not appear to be uncommon in the field of astronomy - left with some rather confusing vocabulary that describes the opposite of what is scientifically accurate.

1.1.2 Galaxy Evolution

Despite the wrong initial interpretation of Hubble's tuning fork diagram, this was, very soon after the very discovery of galaxies, astronomers' first attempt at studying their evolution. Since 1936, the Hubble's tuning fork diagram has been expanded, fine-tuned, and revised more than once (e.g. de Vaucouleurs 1959, van den Bergh 1976, Elmegreen & Elmegreen 1987). Besides morphological classification, there are several other properties based on which galaxies can be classified, which

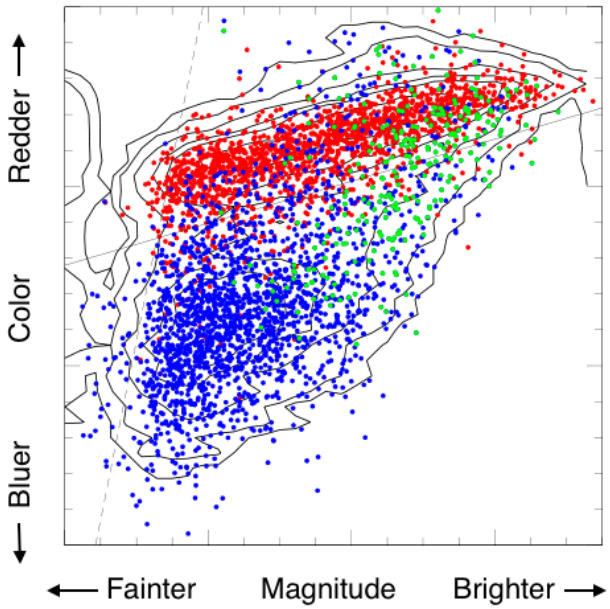

Figure 1.3: Colour-magnitude diagram using galaxies in the Sloan Great Wall, a collection of five superclusters spanning a redshift range of z = 0.04 - 0.12. The magnitudes in this Figure are i-band magnitudes, ranging from -16 to -23.5, and the colours on the y-axis are g-i colours, ranging from 0 to 1.5. We can clearly see the red sequence, consisting of early-type, passive galaxies, and the blue cloud, consisting of late-type, star forming galaxies. In between, we can see the green valley, a class of galaxies transitioning from active to passive. This figure is from Gavazzi et al. (2010), and was adapted by Ben Cook for Astrobites.

are often related. These include colour, how many stars they form at any given time ("star formation rate", SFR), and the way their light is distributed (their "de Vaucouleurs profiles" (or "profils", if your French is good enough to read the original work), de Vaucouleurs 1948, later famously expanded upon by José Luis Sérsic, Sérsic 1963). De Vaucouleurs published this work shortly after the advent of photometry (later improved further by the development of charged coupled devices, CCDs), which allowed him to *éliminer ou réduire les erreurs systématiques et accidentelles* present in previous work, and was, moreover, a major leap forward for the field of galaxy evolution, and astronomy as a whole. Further developments in the field of galaxy evolution over the years include the decomposition of galaxies into bulges and discs (e.g. Kormendy 1977), the discovery of additional structures such as rings (e.g. Kormendy 1979), and more detailed (three-dimensional) studies of discs, bulges, and elliptical galaxies (e.g. van der Kruit & Searle 1982, de Jong 1996, Peletier & Balcells 1996, Caon et al. 1993).

Almost 100 years after Hubble's tuning fork diagram sparked the first studies of galaxy evolution, we are still very much trying to figure it out. As hinted at above,

we now know that early-type galaxies represent a later evolutionary state than late-type galaxies. Elliptical galaxies tend to be more massive and brighter than their spiral-shaped friends. Furthermore, as can be derived from their red colours, they form few to no new stars, and are therefore sometimes referred to as "red and dead" or "retired" galaxies.

The way a star evolves depends pretty much exclusively on its mass. High-mass stars are much bluer and brighter than their low-mass counterparts, and evolve more rapidly. Moreover, galaxies form many more low-mass stars than high-mass stars, with the probability distribution function of a star of a certain mass being formed declining rapidly with stellar mass according to the "initial mass function" (IMF), typically following a (broken) power law (e.g. Salpeter 1955, Miller & Scalo 1979, Kroupa 2001, Chabrier 2003). Thus, the longer a galaxy forms stars, the more old, red stars it will harbour relative to bright, blue stars. As the higher-mass stars evolve off the main sequence and become red giants, the overall colour of the galaxy becomes redder over time.

This allows the two morphological classes of galaxies to be readily be identified in the "colour-magnitude diagram", an example of which is shown in Figure 1.3. In this Figure elliptical galaxies are shown as red markers, while spiral galaxies are shown as blue markers. Together, the elliptical galaxies form the "red-sequence", spanning a range of brightnesses. Similarly, the spiral galaxies form the "blue cloud", which occupies a more blob-shaped region in the fainter and bluer space of this diagram. In green, we have the "green valley", which comprises galaxies in the process of transitioning from spiral to elliptical. This transition is thought to take place relatively rapidly, although timescales differ between different galaxies and galaxy types (e.g. Schawinski et al. 2014 and references therein). How exactly galaxies "quench" their star formation, and transition from late-type galaxies into early-type galaxies, is the key question in the field of galaxy evolution. Various mechanisms have been identified that contribute to this evolutionary process. The most important ones are highlighted below.

Mergers

One way in which spiral galaxies are known to evolve into elliptical galaxies is through merging. Mergers take place throughout cosmic time, and are an important aspect of every theory of galaxy evolution. They are expected to play a key role in the ΛCDM cosmological model, due to its hierarchical nature. There are several types of galaxy mergers. They can happen between gas-rich and gas-poor galaxies (wet vs. dry

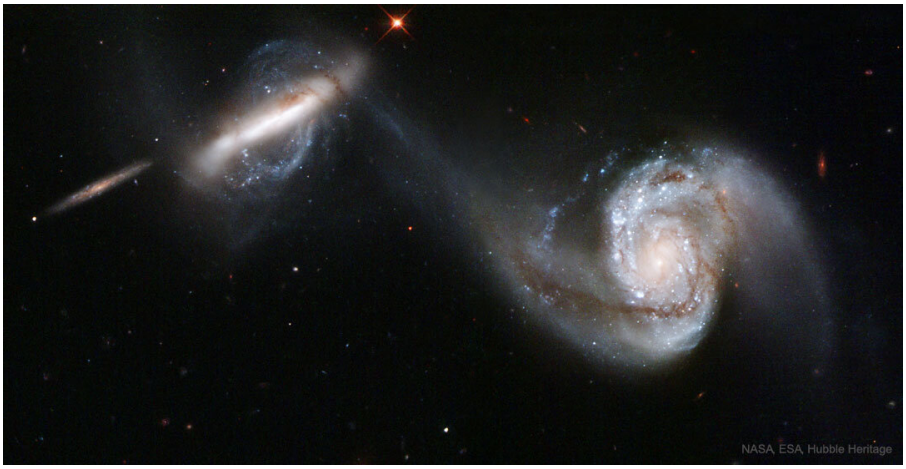

Figure 1.4: The merging galaxy pair Arp 87, consisting of NGC3808A and NGC3808B. Both are large, spiral galaxies, which makes this merger a wet, major merger. Credit: NASA/ESA/Hubble

mergers), galaxies of similar mass (major mergers) or galaxies of significantly different mass (minor mergers), and any permutation thereof. Figure 1.4 shows the ongoing major merger between the spiral galaxies NGC3808A and NGC3808B (together the pair is referred to as Arp 87).

If the mass difference between merging galaxies is small, and at least one of them is gas-rich, a merger usually results in an initial "star burst", where the SFR is significantly increased for a relatively short amount of time as a result of the forces and motions of the merger. At the same time, the newly formed system undergoes "violent relaxation" (Lynden-Bell, 1967), in which it settles into a new equilibrium on very short timescales. During this process, an entirely new morphology and light distribution is created. If one or both galaxies had discs before, these are often destroyed, and the end product is a spheroid-shaped system, supported by velocity dispersion. Thus, on relatively short cosmic timescales, an elliptical galaxy is born (e.g. Fu et al., 2013; Oteo et al., 2016; Fraternali et al., 2020).

Passive evolution

When a galaxy finds itself isolated for an long amount of time, it can undergo "passive" or "secular" evolution. Eventually, it will use up all its fuel, and be left with a population of old stars. This sort of evolution is relatively calm and steady, and does not result in significant changes in morphology apart from through disc fading processes. It is mostly observed in higher-mass galaxies ($\log(M_\star/M_\odot > 10$), and in particular galaxies with a massive bulge (e.g. Fang et al. 2013; Bluck et al. 2014; Bremer et al. 2018) and/or high central velocity dispersion (e.g. Wake et al. 2012;

Teimoorinia et al. 2016).

Feedback

For much of their lives, galaxies can be seen as closed systems, in which their internal physical processes regulate their star formation and evolution, thus creating a feedback loop. The feedback counteracting star formation mainly comes from stellar winds and radiation, supernovae, and/or active nuclei (AGN, supermassive black holes that are actively accreting material). In recent years, feedback mechanisms have become essential in simulations of galaxy formation and evolution, which consistently fail to reproduce observed parameters such as star formation histories unless feedback is included. An example of this is shown in Figure 1.5. An in-depth discussion of various feedback mechanisms can be found in Krumholz (2014).

While radiative feedback and stellar winds happen on small scales (<1 pc), they affect the evolution of the entire galaxy. Without stellar feedback, gas would be converted into stars on free-fall time scales. In reality, only a small percentage of gas is converted into stars in a free-fall time (Bigiel et al., 2008; Krumholz et al., 2012; Leroy et al., 2013). Moreover, without stellar feedback, most of the gas inside galaxies should have been converted to stars by the present day (White & Frenk, 1991; Blanchard et al., 1992; Balogh et al., 2001). This is clearly not the case. Therefore, including stellar feedback into models of galaxy formation is crucial to match observations (see Somerville & Davé 2015 for an overview). Stellar winds disperse the self-gravitating dense cloud of gas, thus slowing down star formation. Furthermore, they can supply up to half the gas mass returned to the ISM (e.g. Leitherer et al., 1992). The FUV radiation emitted by stellar populations has large cross sections with dust grains and hydrogen atoms. Therefore, this radiation is very efficiently absorbed by the ISM. The momentum carried by these photons is important on molecular cloud-scales, which have escape velocities much smaller than the momentum flux caused by this radiation (Krumholz, 2014).

The mechanism first suggested to regulate star formation is supernovae. Supernovae create significant amounts of kinetic energy. They shock the surrounding ISM, significantly increasing its temperature. Thus, supernovae are also capable of significantly slowing down star formation. There exists a minority of strong stellar winds that, like supernovae, are capable of causing significant shocks and increased temperatures. However, the impact of such winds is metallicity (see §1.1.6), dependent, and shown to be inefficient in low-metallicity galaxies (Dib et al., 2011). Some supernovae are capable of creating galactic-scale winds that contain a variety

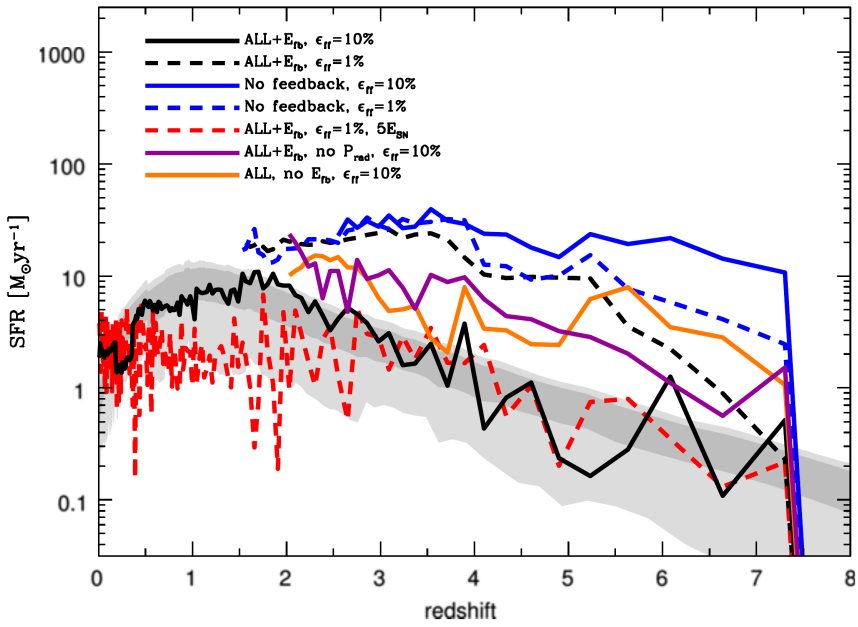

Figure 1.5: Figure 4 from Agertz & Kravtsov (2015), illustrating the importance of feedback in the theory of galaxy formation & evolution. It shows the simulated star formation history of a galaxy over cosmic time, using a variety of prescriptions within the framework of the Adaptive Mesh Refinement code `RAMSES` (Teyssier, 2002). The data shown in gray is from Behroozi et al. (2013) for a galaxy forming in a dark matter halo of mass $M_{\rm vir} = 10^{12} M_\odot$ at $z = 0$. The dark-gray shaded area represents the 1σ confidence interval, and the light-gray shaded area the 2σ confidence interval. The blue lines represent simulations in which no feedback is used. Such simulations overestimate the SFR significantly, especially at higher redshifts. The implementation of stellar feedback only (dashed black line) does not solve this problem. In order to reproduce the data, either very efficient stellar feedback (solid black line) or a considerable amount of supernova feedback (red dashed line) is needed, though the latter results in an underestimation of the SFR at lower redshifts. The two remaining lines represent simulations where either radiation pressure (purple) or thermal feedback (yellow) is neglected. Both these prescriptions fail to reproduce the data, highlighting the importance of both stellar feedback mechanisms.

of ISM phases. In low-mass galaxies these winds can be strong enough to remove material from the galaxy. Thus, supernova feedback can have significant impact on galaxy evolution, even on larger scales. Last but not least, there is feedback from AGN. Energy and radiation is generated when material is accreted onto the black hole. This can remove gas from the galactic bulge and quench star formation. There are two major modes of AGN feedback: radiative (quasar/wind) and kinetic (radio jet/maintenance) mode. The former typically occurs in disc galaxies, and results in the displacement of cold gas. The second mode typically occurs in more massive, bulge-dominated galaxies with hot haloes, and results in powerful jets. The energy produced by accretion easily exceeds the binding energy of a typical galaxy by a large factor, and therefore has a significant impact on its evolution. A detailed review of AGN feedback can be found in Fabian (2012).

Environment

As first shown by Oemler (1974) and Dressler (1980), a correlation exists between galaxy type and environment. More specifically, in dense environments the fraction of passive galaxies is significantly larger than in sparser environments. This can be seen in Figure 1.6, which shows the famous morphology-density relation from Dressler (1980). This relation suggests that a galaxy's local environment influences how it evolves, and dense environments can cause early quenching of star formation. This has been confirmed by numerous observational studies (e.g. Coziol et al., 1998; Peng et al., 2012; Bassett et al., 2013; Woo et al., 2013; Penny et al., 2016; Sun et al., 2018) as well as simulations (e.g. Pranger et al., 2017; Wang et al., 2018; Sun et al., 2018). Galaxy clusters at high ($z \gtrsim 0.4$) redshift have been shown to contain a larger fraction of blue galaxies compared to low-redshift galaxies. This observation is known as the "Butcher-Oemler effect" (Butcher & Oemler, 1978). This effect essentially provides a different view of the same phenomenon suggested by the morphology-density relation (see §1.1.2). It implies that more star formation occurs in clusters at higher redshifts, and that the quenching of this star formation is relatively recent. This has provided a new challenge for simpler galaxy evolution models, which do not automatically predict this rapid evolution.

In the local universe, at least 40% of galaxies live in groups or clusters (e.g. Zabludoff & Mulchaey 1998; Robotham et al. 2011). Therefore, environmental quenching is an important factor in galaxy evolution. Galaxy evolution in dense environments will be the central topic of this thesis. I will discuss galaxy evolution in dense environments and environmental quenching mechanisms in more detail in §1.1.5.

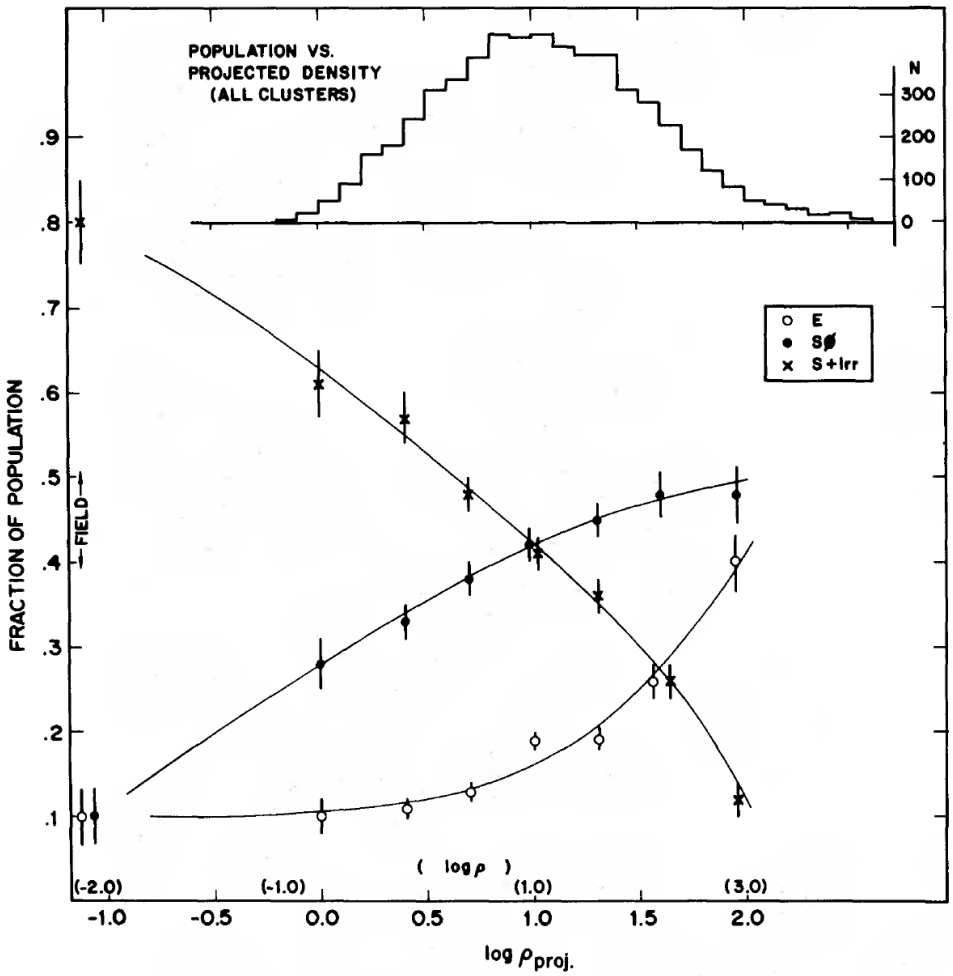

Figure 1.6: Figure 4 from Dressler (1980): the morphology-density relation. This figure shows the fraction of certain galaxy types as a function of projected galaxy density in galaxies per Mpc^2. As the projected density increases, the relative number of spiral and irregular galaxies, represented by the cross-signs, decreases, while the fraction of elliptical galaxies, represented by the open round markers, increases significantly. The fraction of lenticulars, represented by the closed round markers, also increases. The distribution of the total galaxy population used to create this plot is shown as a histogram in the upper part of the figure. This work by Alan Dressler is one of the first papers providing clear evidence that there is a correlation between galaxy density and morphology.

1.1.3 THE BIGGER PICTURE

So far we have discussed what types of galaxies there are and in what ways individual galaxies can evolve during their lifetime. In this section we will zoom out and have a look at what the galaxy population looks like on larger scales, and how it changes over cosmic time.

Galaxy evolution through cosmic time

The universe has not always looked the way it does today. We could even talk about a time so long ago that galaxies did not even exist, but the Universe consisted of a big "soup" of familiar and strange particles. However, because we are mainly interested in galaxies here, let us not go back quite that far, but rather a modest ∼12 Gyr or so. As we saw in the previous section, in the current, local Universe, galaxies evolve and merge until their star formation eventually comes to a halt. This implies that if things continue this way, we will eventually end up with a mostly empty Universe, sparsely occupied by retired galaxies - a rather unexciting thought indeed. However, it has not always been this way. Galaxies were not formed ultra star forming, slowly getting more passive as time progressed. Instead, the star formation rate in the Universe increased for a few Gyr, until it reached its peak at $z \approx 2$. After this, galaxies' collective star formation rate started declining, eventually following the downward slope we are still on today. This is shown in Figure 1.7, taken from the famous review by Madau & Dickinson (2014). It shows the history of cosmic star formation, compiled from a wide range of sources (listed in table 1 of their work). This trend is reflected in the evolution of the galaxy population through cosmic time. Figure 1.8 shows the fraction of quiescent and star forming galaxies as a function of redshift, between $z = 1$ and $z = 0$. Each panel shows a different galaxy mass range. In each panel, we can see an increase in the number of quiescent galaxies with redshift, and a decline in star forming galaxies. The increase in the number of quiescent galaxies is most pronounced in the lowest mass bin (upper-left panel) between $z = 0.5$ and $z = 0$. It looks like soon early-type galaxies will outnumber late-type galaxies in every stellar mass bin. Indeed, Kelvin et al. (2014) found that ∼70% of the stellar mass in the local Universe is found within elliptical and lenticular galaxies.

The hierarchical Universe

It is clear that, as time progresses, spiral galaxies are transformed in to elliptical galaxies. However, it is not just the relative number of morphological types and universal star formation rate that change with time. The distribution of galaxies

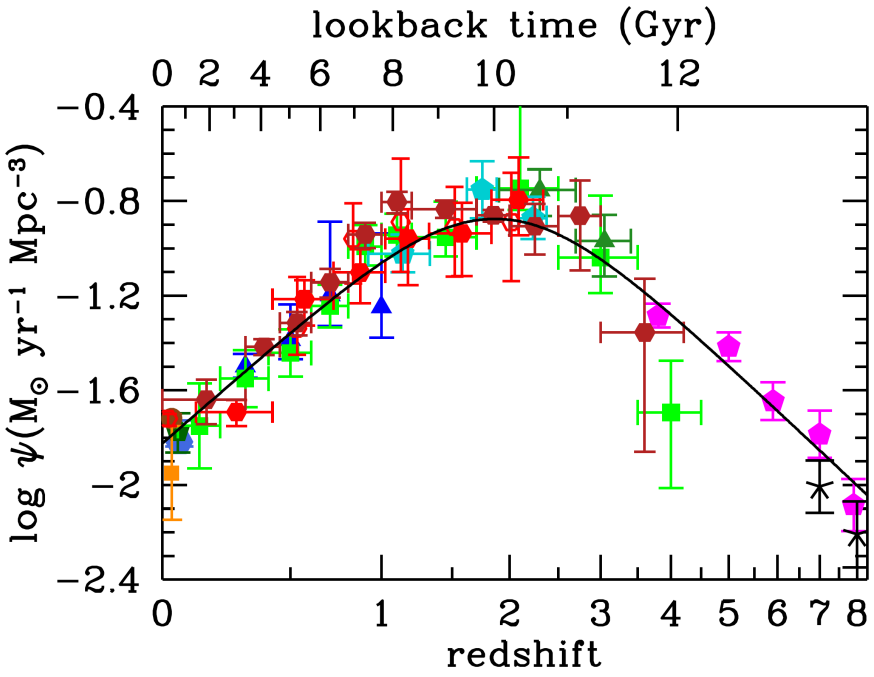

Figure 1.7: The history of cosmic star formation from far-UV (green, blue, magenta) and infrared (red, orange) measurements, compiled by Madau & Dickinson (2014). The star formation in the Universe peaks at redshift ∼2 (∼10 Gyr ago), after which has been declining until the present day.

within the Universe evolves too. As we have seen in §1.1.2, two galaxies can collide and merge to become a more massive galaxy. Similarly, it is thought that structures of all sizes merge to form larger structures. Galaxies tend to stick together and form galaxy groups. When enough such groups merge together, they can eventually form a galaxy cluster. Such clusters, too, group together to form *super*clusters. This is called "hierarchical clustering". Even superclusters are connected: in the large-scale structure of the Universe they form filaments, connecting galaxies throughout the entire Universe with each other. Between these filaments there are "voids", parts of the Universe where the galaxy density is relatively low. Together these filaments and voids form what is known as the "cosmic web". This large-scale structure is shown in Figure 1.9, which shows the distribution of light in the nearby Universe, derived from the distribution of dark matter according to the Millennium Simulation (Springel et al., 2005).

1.1.4 Galaxy clusters

As described above, galaxy clusters form the largest structures in the Universe. They host hundreds to thousands of galaxies, bound together by a dark matter halo.

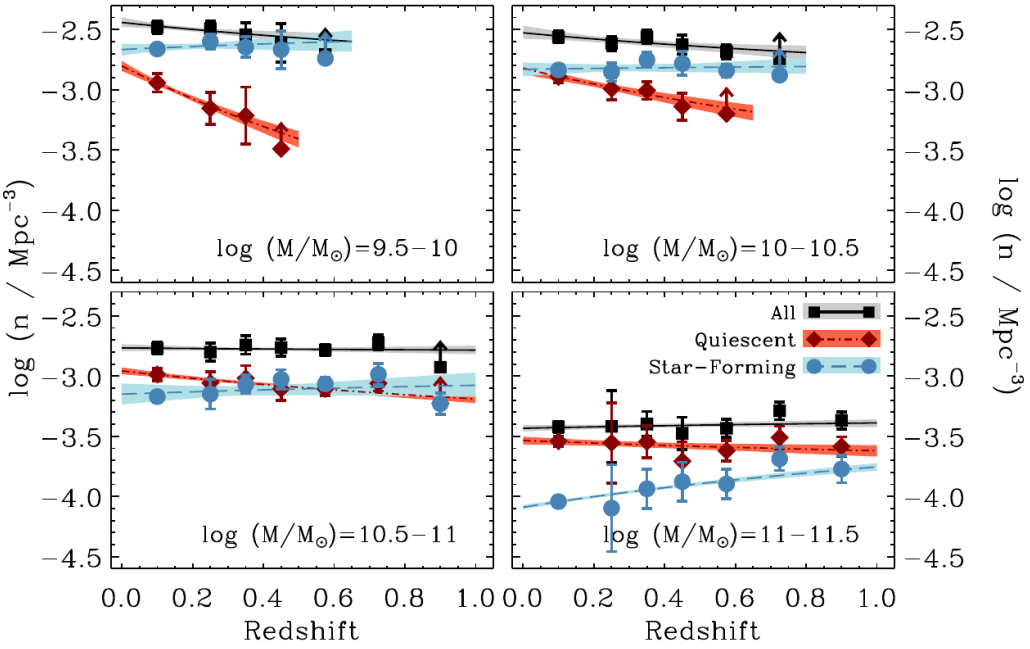

Figure 1.8: Figure 12 from (Moustakas et al., 2013): the evolution of the galaxy population in number density between redshift 1 and 0. Quiescent galaxies are shown in red, star forming galaxies in blue, and the total population in black. Each panel represents a different stellar mass range, with galaxy mass increasing from left to right and from top to bottom. The straight lines represent least-squares power-law fits to the data, with the shaded areas representing 1σ confidence intervals. The fraction of quiescent galaxies has increased since $z = 1$, with the most notable increase being a factor 2-3 in low-mass galaxies since $z = 0.5$. This figure is based on a sample totalling ∼210,000 galaxies, selected from the PRism MUlti-object Survey (PRIMUS) and the Sloan Digital Sky Survey (SDSS).

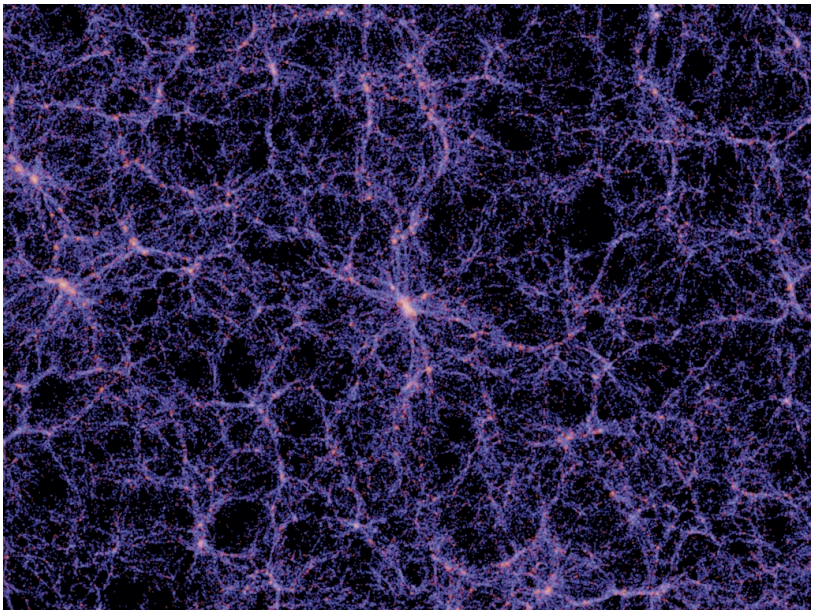

Figure 1.9: The large-scale distribution of light in the Universe at $z = 0$, as predicted by the Millennium Simulation. The total width of the image represents ∼400 Mpc. The Millennium Simulation used over 10 billion dark-matter particles in a cubic volume of over 600 Mpc on a side to trace the evolution of matter distribution over cosmic time (Springel et al., 2005).

Since clusters are the places in the Universe with the highest galaxy number densities, they are important laboratories for studying galaxy evolution in dense environments. The studies presented in this thesis are, therefore, studies of galaxy evolution in the cluster environment. Galaxy clusters are typically a few Mpc in size, with masses of the order $\sim 10^{13} - 10^{15} M_{\odot}$ (most of which is dark matter). The space between galaxies in clusters is filled with hot gas, the "intracluster medium" (ICM). The ICM emits X-rays, which provides one way in which distant clusters can be found. At the heart of each galaxy cluster we typically find a massive elliptical galaxy (the "central" galaxy or "brightest cluster galaxy", BCG), around which the other galaxies ("satellite" galaxies) orbit.

One of the first catalogues of galaxy clusters in the nearby Universe was created by George O. Abell, as part of his PhD thesis (Abell, 1958). He created his catalogue by visually inspecting plates from the Palomar Observatory Sky Survey (POSS). The Abell catalog of rich clusters of galaxies initially contained 2712 clusters in the northern hemisphere, and was later expanded by Harold G. Corwin and Ronald P. Olowin to include the southern hemisphere. It currently contains 4073 galaxy clusters at $z \leq 0.2$.

Below, I discuss the three galaxy clusters closest to us: the Virgo, Fornax, and

Coma clusters. Through studies of these objects (the Virgo cluster in particular) we have gained much insight in the galaxy evolution in the Universe.

The Virgo cluster

The Virgo cluster is the galaxy cluster closest to us, at ∼16.5 Mpc (Mei et al., 2007). It is located in the constellation of Virgo, which consists of two different Babylonian constellations: the "furrow" (east) and the "Frond of Erua" (west, basically a goddess holding a palm-frond, described in the MUL.APIN, ∼1000 BC).

Thanks to its proximity, and because it is located in the northern hemisphere, the Virgo cluster has been studied extensively over the past decades, and is often treated as a textbook example of a galaxy cluster. It was first catalogued by Binggeli et al. (1985), who counted ∼2000 galaxies (at a magnitude limit of $m_B = 18$). Its mass is $\sim 1.2 \times 10^{15} M_\odot$ (Fouqué et al., 2001), and its virial radius ∼1.55 Mpc (McLaughlin, 1999). At its centre lies - the now very famous - M87, a giant elliptical with a stellar mass of $\sim 2.4 \times 10^{12} M_\odot$ (Wu & Tremaine, 2006). Other notable galaxies in the Virgo cluster include M49, M86, M84, M90, NGC4388, and many more.

While most of its galaxies are distributed around BCG M87, Virgo contains several subgroups and structures (e.g. Gavazzi et al., 1999; Boselli et al., 2014c; Lisker et al., 2018). One of these substructures is centred around M86, a giant, blueshifted elliptical, and another around the extremely luminous M49. Each structure is quite different from the others in terms of galaxy composition and velocity dispersion. In addition to these substructures, Virgo has several infalling groups. Since these substructures and groups are still in the process of merging with the main cluster, this suggests that the Virgo cluster is relatively young, and dynamically still very active.

The Virgo cluster lies at the heart of the similarly named Virgo Supercluster (also referred to as the Local Supercluster), which contains at least another 100 galaxy groups and clusters. This includes the Local Group, the small group of galaxies that includes the Milky Way and Andromeda galaxy.

Recent studies of the Virgo cluster include the Next Generation Virgo Survey (NGVS, Ferrarese et al. 2012), the Burrell Schmidt Deep Virgo Survey (Mihos et al., 2017), the *Herschel* Virgo Cluster Survey (HeViCS, Davies et al. 2010), the GALEX Ultraviolet Virgo Cluster Survey (GUVICS, Boselli et al. 2011), and the Virgo Environmental Survey Tracing Ionised Gas Emission (VESTIGE, Boselli et al. 2018a). It is also covered by the Arecibo Legacy Fast ALFA (ALFALFA) survey (Giovanelli et al., 2005). Observations for the ALMA large program "the Virgo Environment

Traced in CO (VERTICO, PI: T. Brown), in which I am involved, are ongoing. I will discuss this program in more detail in §5.2.

The Fornax cluster

The Fornax cluster (Abell S373) owes its name to its location in the Fornax constellation, which was named by Nicolas Louis de Lacaille in 1756 (de La Caille, 1763). He initially named it "Fornax Chemica", the "chemical furnace", in honour of his friend Antoine Lavoisier, who is seen as the father of modern chemistry. It was later shortened to "Fornax" by Francis Bailey. The Fornax cluster will be the main subject of the studies presented in this thesis. Only marginally further away than the Virgo cluster, Fornax is located at a distance of about 19.95 Mpc (Tonry et al., 2001). It is a relatively poor cluster, with a mass of $7 \times 10^{13} M_{\odot}$ (Drinkwater et al., 2001) (this is only $\sim$1/10 of the mass of the Virgo cluster). It was first catalogued by Ferguson (1989) (shortly after the Virgo cluster was catalogued by Binggeli et al. (1985), up to the same magnitude limit of $m_B = 18$), who counted 340 galaxies. This number has recently increased drastically with the completion of the Fornax Deep Survey Peletier et al. (2020), which imaged the area around the Fornax cluster up to magnitudes of $m_r = 21$, and catalogued over 500 dwarf galaxies alone (Venhola et al., 2018). Despite its lower mass and smaller number of galaxies, the galaxy density in Fornax is 2-3 times higher than that in Virgo. Its central gas density, on the other hand, is roughly four times lower than that in Virgo, and the temperature of this gas is lower too (Schindler et al., 1999; Paolillo et al., 2002; Scharf et al., 2005). This difference in characteristics means that we expect different environmental processes to be more important in both clusters (see §1.1.5). At the centre of the Fornax cluster we find the massive elliptical NGC1399, which has a stellar mass of $\sim 7 \times 10^{12} M_{\odot}$ if you include its stellar halo (Iodice et al., 2016). Some of the other brightest galaxies in the cluster include NGC1365 (the big spiral in the bottom-right of Figure 1.10, which is so big that people have quadruple-checked if it's not secretly a foreground galaxy - it is not), NGC1404, NGC1427A, NGC1316, and NGC1310. NGC1316 is the central galaxy of a sub-group that is currently falling into the cluster (I will discuss such groups in more detail in §1.1.5).

Located in the southern hemisphere, the Fornax cluster was initially studied much less than Virgo (visible from the north). However, in recent years, with many powerful telescopes and instruments being commissioned in the south, this has started to change. As mentioned above, the Fornax Deep Survey is a recent, deep

Figure 1.10: False-colour image of the Fornax cluster, taken with the VST Survey Telescope as part of the Fornax Deep Survey (Peletier et al., 2020). Credit: ESO (Aniello Grado, Luca Limatola).

optical survey, which has discovered a significant number of new galaxies in the cluster. Furthermore, it has been studied with the *Herschel* Space Telescope (see §1.2.3) in the *Herschel* Fornax Cluster Survey (HeFoCS, Davis et al. 2013), the Multi Unit Spectroscopic Explorer on the Very Large Telescope (VLT/MUSE, see §1.2.2) in Fornax3D (Sarzi et al., 2018), and the Australia Telescope Compact Array (ATCA) by Lee-Waddell et al. 2018 and Loni et al., submitted to A&A.

The Coma cluster

The Coma cluster (Abell 1656) is further away from us than the Virgo and Fornax clusters, at ∼100 Mpc (Thomsen et al., 1997). It is located in the constellation of Coma Berenices, which means "Berenice's Hair" in Latin. It refers to Queen Berenice II of Egypt, who sacrificed her hair as a votive offering. The Coma cluster has some historical significance: it was one of the first places dark matter (or "dunkle Materie") was first discovered (Zwicky, 1933).

In addition to being further away, Coma is also more massive than the other two nearby clusters, with a virial mass of $\sim 1.88 \times 10^{15} M_{\odot}$ (Kubo et al., 2007). Its virial radius is ∼3 Mpc (Boselli & Gavazzi, 2006), roughly twice that of the Virgo

cluster. Though at first glance it appears to be quite regular due to its spherical symmetry and central concentration, in reality it is dynamically very active. It contains several substructures (identified both in velocity space and as over densities, Fitchett & Webster 1987; Colless & Dunn 1996; Conselice & Gallagher 1998; Mendelin & Binggeli 2017). At its heart we find not one, but two massive ellipticals: NGC4874 & NGC4889. It is likely that the cluster in its current shape is the result of a merger between two sub-clusters associated with these two ellipticals (Briel et al., 1992; Gerhard et al., 2007). Other notable galaxies in the Coma cluster include NGC4921, NGC4911, NGC4839, and NGC4841. Unlike its closer siblings, the Coma cluster was not neatly catalogued in the 1980s. An attempt at an optical catalogue was made in 1977 by Godwin & Peach (1977), however many of these galaxies later turned out to not actually be members of the Coma cluster. Recently, Fuller et al. (2016) created the Coma Cluster Catalogue, based on the SDSS spectroscopic survey. This survey is sensitive to magnitudes up to $m_r \leq 17.8$, comparable to the early Fornax and Virgo Cluster Catalogues. They identify 744 galaxies within the virial radius. Given the much larger distance towards Coma, this catalogue only includes the most massive galaxies in the cluster. Correcting for this, there must be at least three times as many galaxies in the Coma cluster detectable at the distance of Fornax and Virgo. This means that the Coma cluster is at least as rich in galaxies as the Virgo cluster. Keeping in mind that it has twice the radius of the Virgo cluster (and therefore $\sim$8 times the volume), the galaxy density in Coma is likely low relative to its halo mass.

Similarly to Virgo, the Coma cluster is part of the Coma Supercluster. The other main component of this supercluster is the Leo Cluster (Abell1367). This supercluster is, in turn, part of the Coma Filament, which is again part of the Coma Wall. The Coma Wall (also referred to as the Great Wall) is at least 150 Mpc long, and one of the largest known superstructures in the observable universe (Geller & Huchra 1989, see Figure 1.11). These structures around the Coma cluster provide valuable observational evidence of the Hierarchical Universe described in §1.1.3.

Recent observations of the Coma cluster include the ones by Casoli et al. (1996), Boselli et al. (1997), Yagi et al. (2010), Churazov et al. (2012), van Dokkum et al. (2015), Fuller et al. (2016), and Lal (2020). The cluster is also covered by ALFALFA.

1.1.5 Galaxy clusters & evolution

With so many galaxies in relatively little space, galaxy evolution within clusters is more complex than galaxy evolution not in galaxy clusters (the "field"). As we

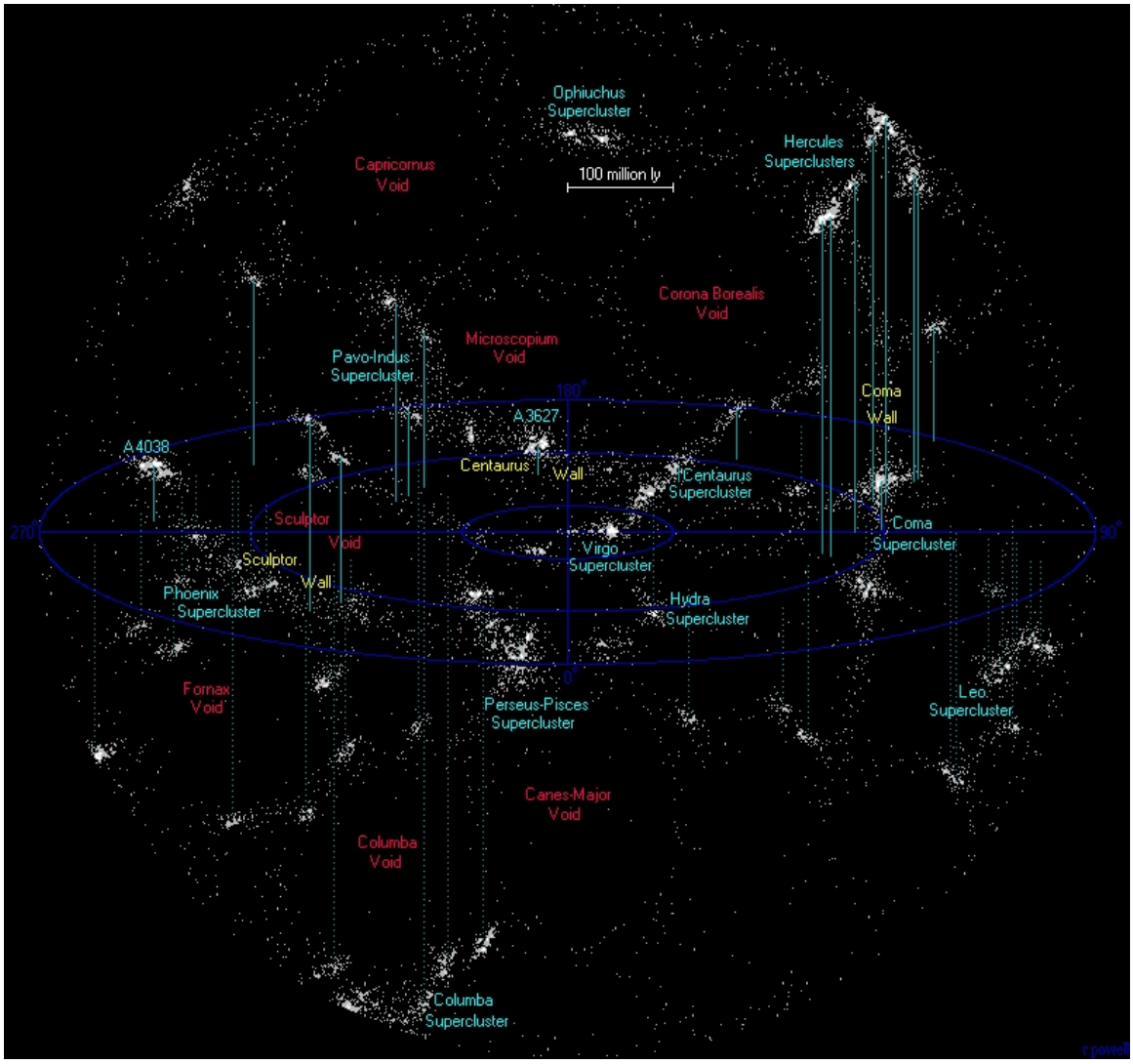

Figure 1.11: Schematic view of the Local Universe, created by Richard Powell for `www.atlasoftheuniverse.com`. We can see the Virgo Supercluster close to the centre of the image (close to the Milky Way in the very centre) and the Coma Wall on the right side of the image, stretching all the way from the top to the bottom. The blob to the lower-right of the centre, opposite the Virgo Supercluster, is likely the Fornax cluster, although individual clusters are not annotated.

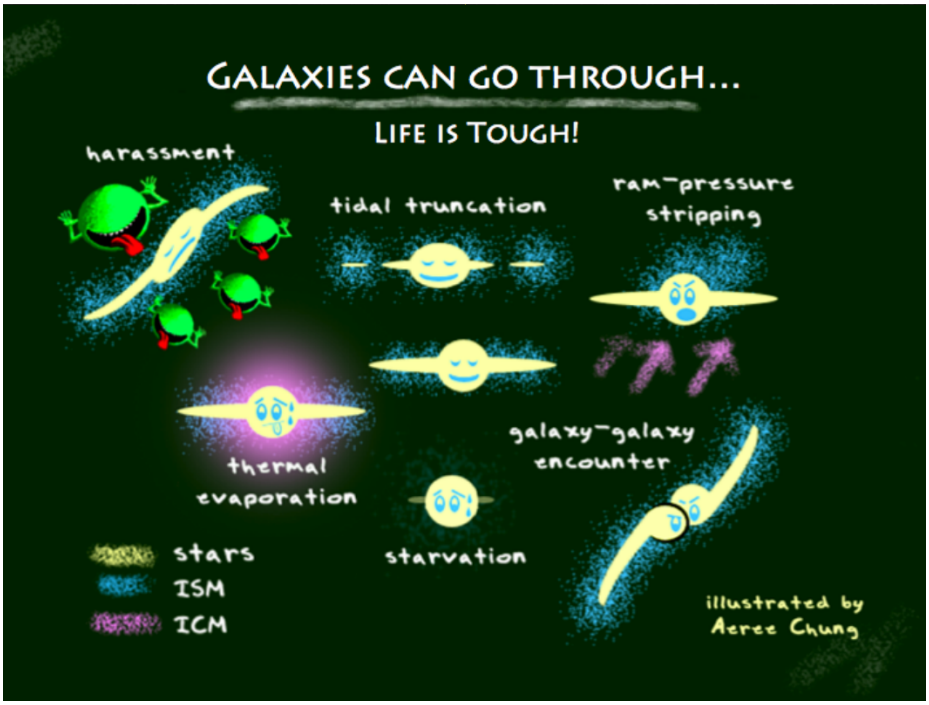

Figure 1.12: Cartoon by Aeree Chung (Yonsei University, Korea) showing some of the environmental effects that can lead to the quenching of star formation in cluster galaxies, described in §1.1.5.

have seen in §1.1.2, the relative number of passive galaxies increases with the number of galaxies per unit volume. This suggests that the star formation in galaxies residing in clusters is quenched more rapidly than in galaxies in the field (or preferentially passive galaxies cluster together). Because the relative velocities of cluster galaxies are high (typically around 1000 km s^{-1}), mergers, one of the main ways in which spiral galaxies evolve into ellipticals in the field (see §1.1.2), are rare here. While it is possible that the other evolutionary processes mentioned in §1.1.2 are more efficient in clusters, it is more likely that different evolutionary processes play a role in galaxy clusters than in the field. Indeed, several such processes have been suggested and observed. They are described below, and some of them are illustrated in Figure 1.12.

Ram pressure stripping

As described in §1.1.4, the space between cluster galaxies, the intracluster medium, is filled with hot gas. As galaxies move through this medium at high velocity, they feel a strong headwind from this hot gas, which is capable of removing material from it. This process is called "ram pressure stripping" (RPS), and was first described by Gunn & Gott (1972). They derive the ram pressure exerted on a galaxy to be as

follows:

$$P_r \approx \rho_e v^2, \tag{1.1}$$

where ρ_e is the density of the intracluster medium and v the velocity of the galaxy with respect to it. Ram pressure stripping has been confirmed to affect galaxies in clusters in numerous studies, both observationally (e.g. Vollmer et al., 2004; Kenney et al., 2004; Vollmer et al., 2006, 2008; Yoon et al., 2017; Lee et al., 2017) and in simulations (e.g. Farouki & Shapiro, 1980; Abadi et al., 1999; Kronberger et al., 2008; Steinhauser et al., 2016; Ramos-Martínez et al., 2018; Arthur et al., 2019; Wang et al., 2020). Recently, an entire MUSE (see §1.2.2) large program has been dedicated to the observation of 100 galaxies actively undergoing RPS (so-called "jellyfish" galaxies). This program is called the GAs Stripping Phenomena in galaxies with MUSE (GASP, Poggianti et al. 2017), and has resulted in many new insights into RPS[3]. One such jellyfish galaxy, the Norma jellyfish galaxy, is shown in Figure 1.13. As we can see in this image, RPS can result in spectacular tails of material extending far beyond the stellar body of the galaxy. Recently, evidence has been found that the material in these tails of stripped material can become dense and clumpy enough for star formation to be ignited in situ (Verdugo et al., 2015; Boselli et al., 2018b; Moretti et al., 2019).

Galaxy-galaxy interactions

As mentioned in §1.1.2, the relative velocities of galaxies located in clusters are often too high for two galaxies to become gravitationally bound to each other when they cross paths. Therefore, galaxy mergers are rare within clusters. Instead, when two cluster galaxies encounter each other at high velocity, they undergo a relatively brief interaction that disturbs the morphology and contents of both (or all) galaxies involved. This phenomenon was first described by Moore et al. (1996), who referred to it as "harassment". To date, signatures of past galaxy-galaxy interactions have been found in several groups and clusters (e.g. Nishiura et al., 2000; Hernández-Fernández et al., 2012; Brosch, 2015). Galaxy mergers within clusters are, however, not impossible. Often substructures exist within clusters (see, for example, §1.1.4), in which galaxies have velocities that are more similar, and close enough for mergers to happen (e.g. Benavides et al., 2020). Furthermore, in smaller groups of galaxies the velocity dispersion can be low enough for mergers to occur, which means they can play a role in the "pre-processing" of galaxies before they enter the actual cluster (see §1.1.5). Examples of mergers observed in galaxy groups and clusters from observations are

[3]see `https://web.oapd.inaf.it/gasp/publications.html` for an overview of publications

Figure 1.13: False-colour image of jellyfish galaxy ESO137-001, created with data from ALMA (§1.2.1, MUSE (§1.2.2), and the Hubble Space Telescope (`www.spacetelescope.org`). Credit: ALMA (ESO/NAOJ/NRAO), Jachym et al. (2019).

Rubin et al. (1990); Mendes de Oliveira et al. (1998); Verdes-Montenegro et al. (2002); Rafferty et al. (2013); Paudel et al. (2017, 2018); Ge et al. (2020), and Barnes (1989); Bekki (1998) from simulations.

Tidal interactions

Even when two cluster galaxies do not go through a merger or undergo a violent encounter, they can still have an effect on each others morphologies and star formation rates through tidal interactions. With many galaxies in a relatively small volume, they can easily come close enough together to experience tidal forces. Even with no other galaxies near, closer to the cluster centre, a galaxy can experience tidal forces from the cluster potential itself. Observations (both from data and simulations) of galaxies undergoing tidal interactions include Bitsakis et al. (2011); Da Rocha et al. (2011); Eigenthaler et al. (2015); Smith et al. (2016); Penny et al. (2016); Clarke et al. (2017); Mihos et al. (2017). Such forces are particularly effective in reshaping lower-mass galaxies. It can result in severe truncation of discs (e.g. Richstone, 1976; Merritt, 1983), the formation of bars and other features (e.g. Kwak et al. 2019, see also below), or even the complete transformation of late-types into early-types. In particular, the existence of a relatively recently discovered population of dwarf elliptical galaxies (dEs) with disc-like features and kinematics is seen as evidence that these might be the remnants of late-type galaxies that have been affected by tidal interactions (e.g. Jerjen et al., 2000; Barazza et al., 2002; De Rijcke et al., 2003; Lisker et al., 2006a,b; Toloba et al., 2011; Janz et al., 2014). While dwarf galaxies are intrinsically unstable to bar formation, and end up forming bars even in isolation, (e.g. Kwak et al., 2017),

several studies have shown that bar strength and pattern speed are correlated with galaxy encounters (e.g. Gerin et al., 1990; Noguchi, 1996; Oh et al., 2008; Berentzen et al., 2004; Łokas et al., 2014; Gajda et al., 2017).

Strangulation & starvation

Besides the active stripping of gas by the intracluster medium (§1.1.5), it can also prevent the formation of new stars in a more passive way. In the field, galaxies are usually able to maintain a certain level of fuel for formation by accreting new material, for example from other galaxies, tidal debris, or by cooling their own CGM, as first suggested by Oort (1970); Larson (1972); Cox & Smith (1976). If the infall rate of this diffuse outlying gas is comparable to the depletion time of the gas inside the galaxy, this can significantly prolong the amount of time the galaxy is able to form stars (Tinsley & Larson, 1978). In galaxy groups and clusters, however, while tidal debris can be present, there is little to no evidence of isolated, intergalactic gas clouds (e.g. Lo & Sargent, 1979; Haynes et al., 1979). Moreover, Larson et al. (1980) showed that in galaxy groups and clusters it only takes relatively mild stripping to remove the diffuse outlying gas from galaxies. They also showed that, if this gas is removed, the galaxy will initially carry on forming stars as usual, but will eventually run out of fuel and stop forming stars. This process has later been baptised "strangulation" or "starvation".

Thermal evaporation & viscous stripping

As described in §1.1.5, ram pressure has been proven to be effective in removing material from cluster galaxies. However, as galaxies move through the hot ICM, galaxies experience other effects in addition to RPS. Thermal evaporation was suggested by Cowie & Songaila (1977) to potentially be the dominant mechanism for gas removal in cluster galaxies. Nulsen (1982) demonstrated that there are other "transportation mechanisms" besides RPS that can play an important role in removing gas from galaxies, such as viscous stripping and thermal conduction. They showed that stripping rates increase significantly if such processes are included, and exceed those associated with RPS alone. In some cases "turbulent viscous stripping" becomes important. This process is due the convection from the hot ICM into the surface of the galaxy's ISM, and is most effective when the turbulent forces at this interface are strong compared to the inertial forces (low Reynolds numbers).

Galaxy groups & pre-processing

As discussed in §1.1.2 and §1.1.3, galaxies are often found in groups besides clusters and the field. According to the theory of the hierarchical Universe, such groups will often eventually merge with each other to form larger groups, or get absorbed by clusters. Simulations by Benavides et al. (2020) show that ∼38% of galaxies in clusters in the Local Universe were accreted as part of a group, rather than individually. This means that, when galaxies enter a cluster, many of them will have already experienced the environmental processes present in the group. This is called "pre-processing". Simulations by Joshi et al. (2019) have shown that individual galaxies that enter a cluster cease gaining mass as far as three virial radii out from the cluster centre, and start losing dark matter and gas as soon as they cross the virial radius. Joshi et al. (2017) find that galaxies lose ∼35 - 45% of their mass before entering a cluster if they are part of a group, while this is only ∼12% for individual galaxies. Similar numbers are found by Jung et al. (2018), whose simulations show that 34% of cluster galaxies are gas-poor before entering the cluster as a result of pre-processing. Galaxies that enter clusters as part of a group, on the other hand, already peak in mass when they join their group. Observations of the NGC7162 Galaxy Group show evidence of past interactions within the group (Reynolds et al., 2019). Other observational evidence of pre-processing is found by e.g. Kautsch et al. (2008), Mahajan (2013), Hess & Wilcots (2013), Roberts & Parker (2017), Lisker et al. (2018), Seth & Raychaudhury (2020). By losing material on their infall, groups can also contribute to the ICM and intracluster light (e.g. Mihos et al. 2017).

Infalling subgroups are known to exist around all three nearby clusters. Being part of a larger supercluster, the Coma cluster is surrounded by several galaxy groups. These groups show the effects of various degrees of pre-processing, and are confirmed to be consistent with accretion of gas from the filaments of the cosmic web (e.g. Seth & Raychaudhury 2020, see also §1.1.3). The Virgo cluster is a dynamically young and active cluster (see §1.1.4). Studies of the phase-space distribution of its galaxies, in combination with simulations, show evidence that it is actively accreting new groups of galaxies, that slowly get dispersed as they move through the cluster (e.g. Lisker et al., 2018). The Fornax cluster harbours a subgroup surrounding NGC1316 (Fornax A) that is at the early stage of falling into the main cluster (e.g. Raj et al., 2020).

The above processes all play a part in removing material from cluster galaxies, eventually leading to the quenching of their star formation, either shorter or longer timescales. Of some of these mechanisms - ram pressure stripping in particular - many

convincing examples have started to accumulate in recent years, with the advance of more sensitive telescopes and instruments and detailed simulations. However, their relative importance, the way they relate and cooperate, and how they affect different phases of the ISM (see below) is still poorly understood. One of the goals of this thesis is to help figure out if any of these mechanisms is dominant, and if their relative importance differs between different galaxy clusters.

Cooling flows

While most environmental processes I have discussed thus far act to quench the star formation in galaxies, this is not true for all of them. For central galaxies within clusters, cooling flows can act as important sources of gas for ongoing star formation. At least half of galaxy clusters contain a cooling flow/are cool-core clusters (Salomé 2013, see also Fabian 1994 for a review). Observations from Chandra and XMM-Newton have shown that the cooling times of hot gas can be of the order 100 Myr in the central 50 kpc of such cool core clusters (e.g. Fabian et al., 2001; Voigt & Fabian, 2004). Until recently it was thought that BCGs did not typically contain any molecular gas (see §1.1.6), with one exception that was thought to be the result of a merger (NGC1275, e.g. Lazareff et al., 1989; Reuter et al., 1993; Bridges & Irwin, 1998). At the present day significant reservoirs of molecular gas have been detected in tens of BCGs (Edge 2001; Salomé & Combes 2003; Russell et al. 2019; Olivares et al. 2019, see Pulido et al. 2018 for a compilation of single-dish CO detections). The amounts of molecular gas found correlates with mass deposition rates derived from X-rays, and with Hα luminosities, and the morphologies and velocity fields of this gas suggest gas accretion onto the AGN (e.g. Salomé et al., 2006; Lim et al., 2008; Ho et al., 2009). On larger scales the molecular gas in NGC1275 follows (both morphologically and kinematically) filaments detected in the optical (Conselice et al., 2001, and references therein) and X-ray (Fabian et al., 2006; Hatch et al., 2005), to as far as $\sim$50 kpc away from the central galaxy. Simulations suggest that the presence of this gas can be explained by compression of gas along the radio lobes of AGN, causing it to cool more efficiently in these areas (Revaz et al., 2008). When the gas is cold enough, it can detach itself from the outflows and fall back onto the BCG.

Besides molecular gas, FIR atomic lines (CII, OI, NII) have been observed in BCGs, as well as dust continuum emission, despite estimated short dust destruction timescales (Edge et al., 2010a,b). Furthermore, several other gas phases at different temperatures have been detected in BCGs (e.g. Heckman et al., 1989; Donahue et al., 2000; Bregman et al., 2001). These observations and derived quantities are consistent

with observations of star forming galaxies. However, it is unclear what triggers star formation in BCGs.

In classic cooling flow models the gas in the centres of clusters with dense cores cools hydrostatically: the cool gas is compressed by pressure of from the gas around it. This gas is then replaces with gas from the outer regions of the ICM, and so on, thus creating a flow. However, there are several discrepancies between these classical models and observations, most notably resulting in the too rapid cooling of gas. Therefore, they have been advanced in more recent years to include mechanisms such as conduction (Zakamska & Narayan, 2003), various forms of heating by the AGN (e.g. Mathews et al., 2006; Guo et al., 2008; Voit & Donahue, 2015), sound waves (Ruszkowski et al., 2004), turbulence (Dennis & Chandran, 2005), etc. to combat this discrepancy. The currently dominant theory is that chaotic cold accretion (CCA) plays an important role in the cooling of gas onto BCGs. If the ratio of the cooling time and the free-fall time of the gas falls below ∼10, cold material starts condensing out of the hot ICM, and raining down onto the central galaxy (e.g. Gaspari et al., 2013, 2015; Wang et al., 2020).

1.1.6 Phases of the ISM

As hinted at in §1.1.2, the interstellar medium in galaxies consists of various different components, or "phases". Each phase has a certain temperature and density range, varying anywhere between ∼10 - 10^7 K and ∼ 10^{-4} - > 10^6 particles cm^{-3}, respectively. This implies that different phases trace different regions and events within a galaxy. Under the right circumstances, phases can transition into each other. Below I will give an overview of the ISM phases most important to this work, what they probe, and how they are used in the study of galaxy clusters.

Atomic hydrogen (HI)

Perhaps the most useful ISM phase to study the effects of the cluster environment is the neutral, atomic hydrogen, HI. The main reason for this is that in field galaxies this gas is typically distributed in a relatively large disc, which extends further out than any of the other ISM phases. Combined with the fact that it is not very dense (up to several tens of particles per cm^3), this means that this gas phase is relatively easily affected by environmental effects such as RPS (§1.1.5, see also Giovanelli & Haynes 1985; Rasmussen et al. 2006; Odekon et al. 2016). HI is directly observable thanks to its hyperfine electron spin transition. Since the proton and the electron both have a charge, the spin motion generates a dipolar magnetic field: the "magnetic moment".

The electron of a hydrogen atom has a "spin" quantum number, which describes whether the spin of the electron is aligned with that of the proton, or in opposite direction. When both spins are aligned, the vectors of both magnetic moments add up: this is the higher-energy state. Thus, if the electron spin is in the same spin state as that of the atom, and "flips" to become antiparallel (the vectors now partly cancel each other, so that the energy is much lower), a small amount of energy ($\sim 6 \times 10^{-6}$ eV) is released in the form of a 21.1 cm photon. This is observable in the radio regime of the spectrum, at ∼1420 MHz. The probability that an electron spontaneously flips its spin is very low: it only occurs every $\sim 3.5 \times 10^{14}$ s for any given atom. However, galaxies contain enough HI for this transition to happen very frequently, making the HI-21 cm line one of the most useful probes for ISM studies in the local Universe. For reference, the Milky Way contains about $6 \times 10^9 M_\odot$ of HI, which is a typical amount (Phillipps 2005, its stellar mass is $\sim 6 \times 10^{10} M_\odot$, Licquia & Newman 2015). This is equivalent to about 10^{66} hydrogen atoms, meaning that a spin flip should occur $\sim 3 \times 10^{51}$ times each second. Moreover, when hydrogen atoms in the ISM collide with each other, they can exchange electrons. If the spin of the "new" electron is different from the "old" one, this also changes the hyperfine state of the hydrogen atom.

Since the atomic hydrogen is easily stripped by the environmental mechanisms described in §1.1.5, it has often been used as a tracer of these effects, which can eventually lead to the quenching of star formation. It has been found that galaxies residing in clusters are often HI "deficient" (they contain less HI than galaxies in the field at fixed stellar mass, e.g. Chamaraux et al. 1980, Solanes et al. 2001, Verdes-Montenegro et al. 2001, Gavazzi et al. 2006, Chung et al. 2009, Hess & Wilcots 2013). Furthermore, HI in cluster galaxies is often more morphologically and kinematically asymmetric and/or disturbed than in the field (e.g. Dickey & Gavazzi, 1991; Chung et al., 2007; Scott et al., 2018; Reynolds et al., 2020; Watts et al., 2020).

Molecular hydrogen (H_2)

The most abundant element in the Universe is also found in molecular form: H_2. While environmental effects are often probed with HI (see §1.1.6), in this thesis I will study the effects of the cluster environment on H_2. Molecular gas is much denser and more centrally located than atomic gas (I will expand on this below), and may therefore not seem a straightforward probe for environmental effects. However, since it forms the intermediate step between atomic gas and star formation, it would have significant implications for galaxy evolution if it can be directly affected by the cluster

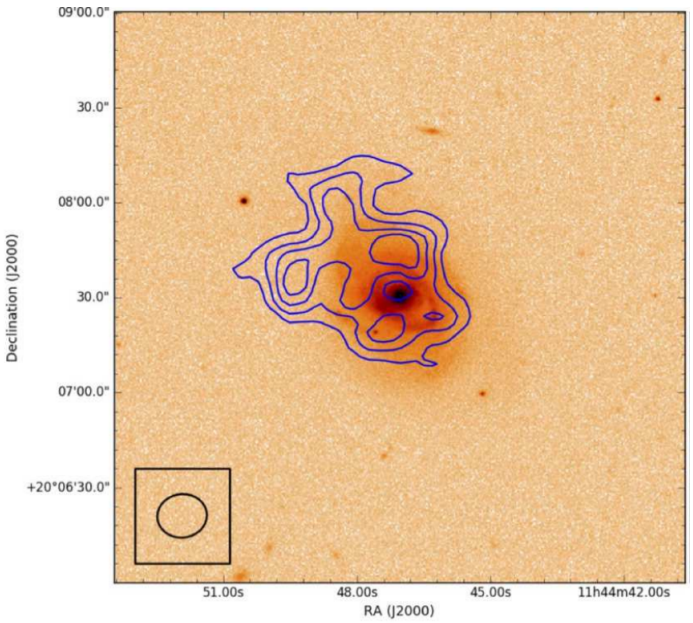

Figure 1.14: Intensity map of the asymmetric HI in the galaxy CGCG 97-121 in Abell 1367 (the Leo cluster, part of the Coma supercluster, see §1.1.4), shown as blue contours on an optical image. The HI data are from the Karl G. Jansky Very Large Array (VLA), the beam of the observations is shown in the lower-left corner. This Figure comes from the appendix of Scott et al. (2018), who studied the effects of the cluster environment on the HI in late-type galaxies in Abell 1367.

environment. Moreover, since it is more difficult to remove from a galaxy by environmental processes, it allows us to study galaxy evolution in dense environments even after HI as been stripped completely. The key aim of this thesis is therefore to find out whether and how molecular gas is directly affected by the cluster environment.

Molecular hydrogen gas is much denser than atomic hydrogen gas, with $10^2 - 10^6$ particles cm^{-3}. It often exists in the form of molecular clouds, though it can exist in more diffuse shape. The increased density and discretised nature of this gas imply that it occupies much less volume within galaxies than HI, and it is found in the more central regions of galaxies. H_2 forms the intermediate step between HI and stars. Stars typically form in "giant molecular clouds" (GMCs), huge clumps of molecular gas, at least $10^4 M_\odot$ and typically 10-100 pc in size. Besides being very dense, these clouds are some of the coldest parts of the ISM, with typical temperatures around 10 K. The Milky Way is quite rich in molecular gas, with an estimated mass of $H_2 \approx 3 \times 10^9 M_\odot$ (Phillipps, 2005). Unfortunately, unlike HI, it turns out to be quite difficult to observe H_2. Normally, we would observe molecules like this through their rotational (and/or vibrational) lines. The rotational states of molecules are quantised. If a molecule transitions from a higher to a lower rotational level, it

Figure 1.15: This is part of the Orion Molecular Cloud Complex, a star forming region consisting of two giant molecular clouds, Orion A and Orion B. It is one of the most active places star formation takes place, and parts of it can be seen with binoculars or even the naked eye. As we can see in this image, GMCs have significant substructure. Credit: Rogelio Bernal Andreo.

emits energy in the form of a photon, that can be observed. However, this only works if a molecule has an asymmetric charge distribution (a "polar" molecule), i.e. if it consists of two atoms, these would have to be two different atoms for this to apply. H_2 is symmetric, and therefore has no permanent dipole moment. This is why it is effectively impossible to observe it directly (it does have vibrational transitions, however these only occur at high temperatures (>1000K) and are therefore no good as a tracer for the bulk of the gas). This issue is generally "solved" by using the next-most abundant molecule as a proxy, and translating the amount we find of it to the amount of H_2 that should be present. This next-abundant molecule is CO, carbon monoxide, which is indeed asymmetric and therefore does have a permanent dipole moment. While this "shortcut" sounds easy enough, in reality it is not that straightforward. The conversion from the flux from the CO spectrum measured (usually the CO(1-0) and CO(2-1) lines, the ones corresponding to the first and second rotational transitions, at ∼115 GHz (2.6 mm) and ∼230 GHz (1.3 mm), respectively, are used for this) to the amount of H_2 requires a certain conversion factor, X_{CO}. It turns out that this factor varies dramatically not only between galaxies, but also between different regions within the ISM of a galaxy. This is mostly because not all H_2 can be traced by CO, but there can be H_2 where no CO is observable. This is referred to as "CO-dark gas". In the Milky Way, anywhere between 30 and 70% of the molecular

gas is estimated to be CO-dark or at least CO-poor (e.g. Grenier et al., 2005; Wolfire et al., 2010; Paradis et al., 2012; Langer et al., 2014; Smith et al., 2014).

It is not easy to measure the correct value of X_{CO}. Methods to do this include virial techniques, the use of isotopologues of CO (i.e. ^{13}CO, for example), dust and extinction measurements, and gamma-ray observations (for an extensive description of each of these methods, see Bolatto et al. 2013). Therefore, many studies simply assume the recommended value for the Milky Way: 2.0×10^{20} cm^{-2} (K km s^{-1})$^{-1}$. Not only is this value quite insecure (the uncertainty on it is 30%), it is also likely to be inaccurate for galaxies that are not like the Milky Way. For an extensive review of X_{CO} and the issues associated with it, please see Bolatto et al. (2013). One of the factors X_{CO} heavily depends on is the metallicity of the ISM (see §1.1.6), i.e. how much of the gas consists of metals in relation to H_2. Therefore, several studies have attempted to derive a relation between metallicity and X_{CO} (e.g. Narayanan et al., 2012; Accurso et al., 2017). While this should give more accurate estimates of the amount of H_2, measuring metallicities can in itself be challenging, as we will see in §1.1.6. The choice of X_{CO} can quite heavily influence the results of studies involving molecular gas, which is something that should be kept in mind.

Ionised gas

Besides in atomic and molecular form, hydrogen also exists in ionised form: HII. This gas is typically found in "HII regions", where the ionisation is due to recent star formation: the young, blue stars formed here emit large amounts of UV radiation. Besides young stars, there are other sources that can ionise hydrogen, such as AGN and old stellar population. Gas ionised by these sources is not confined to HII regions. The source of the ionisation can be determined by "BPT diagrams" (Baldwin et al., 1981). BPT diagrams are named after the authors of the paper in which they were first presented: Baldwin, Phillips, and Telervich. They use a combination of emission line ratios to determine the dominant source of ionisation. The most well-known version uses the line ratios $[NII]_{6584}/H\alpha$ vs. $[OIII]_{5007}/H\beta$ (these lines and the notation used are explained below), however there are several other commonly used BPT diagnostics. There is no clear distinction between HII regions or AGN being the dominant source of ionisation. In fact, there is a significant "composite" region in the diagram, in which both sources contribute more or less equally. Dividing lines between various regions in the diagram have been developed from models and large statistical samples. The most widely used dividing lines are the ones from Kewley et al. (2001), which sets an upper limit for star forming galaxies, and Kauffmann et al.

Figure 1.16: False-colour image of the HII region Sh 2-252 (the Monkey nebula). It contains several star clusters, and the most important source of ionising radiation is the O-star HD42088. Credit: Filipe Alves.

(2003), which distinguishes purely star forming galaxies. Furthermore, one can split the AGN up in Seyfert galaxies, and Low-Ionisation Nuclear Emission-line Region galaxies (LINERS). Seyfert galaxies have quasar-like nuclei with very high surface brightnesses and strong, high-ionisation emission lines, while LINERS have relatively strong low-ionisation emission lines. The dividing line for this was determined by Schawinski et al. (2007). An example of a BPT diagram is shown in Figure 1.18. The relative volume of HII gas is similar to that of molecular clouds, and its particle densities can also come close to those in molecular clouds ($<$ 1 % of the volume within a galaxy, and 10^2 - 10^4 particles cm^{-3}), but it is much hotter ($\sim$ 5000 K). Besides the large variety in densities, the sizes of HII regions can also range from less than a parsec to several tens of parsecs. Similarly to other gas phases, we can observe HII regions through the emission of photons as electrons move from higher to lower energy levels after being captured by protons ("recombination"). This results in emission lines, which can be observed with instruments such as MUSE (see §1.2.2). Some of the most notable emission lines include Hα at $\lambda = 6563$ Å, Hβ at $\lambda = 4861$ Å, [NII] at $\lambda = 6583$ Å, [OII] at $\lambda = 3729$ Å, and [OIII] at $\lambda = 4959$ Å and $\lambda = 5007$ Å. The square brackets indicate "forbidden" lines. Such lines correspond to highly improbable transitions, which violate one or more of the "selection rules" of quantum

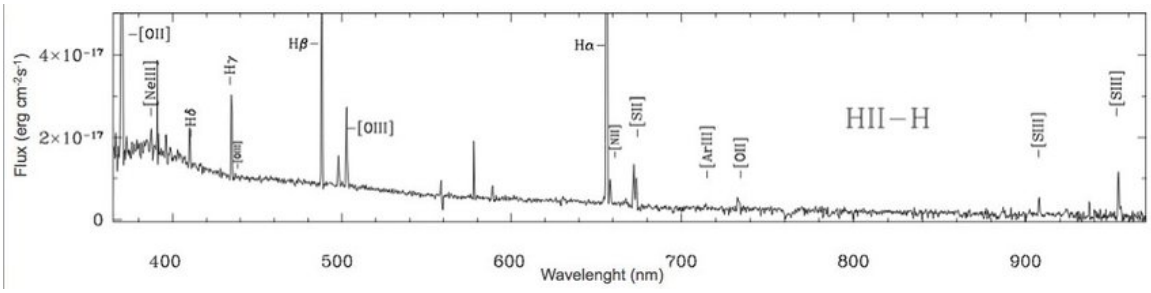

Figure 1.17: Emission line spectrum of an HII region in the irregular galaxy Sextans B. The most important lines are identified, as well as some less prominent ones (Rodrigues, 2010).

mechanics. They therefore occur at a much lower rate than "permitted" transitions. Different emission lines are sensitive to different ISM conditions. Therefore, they can be used as diagnostic tools. For example, the [OIII] line is sensitive to temperature, while the [OII] line is more sensitive to density. Thus, the relative fluxes of particular combinations of emission lines can teach us about the physical conditions of the ISM.

Emission lines can also be used to measure the "metallicity" of the ISM. Thus far, we have talked about the different forms and phases of hydrogen. This is because it is by far the most abundant element in the Universe. However, there are many other elements present in the ISM. In terms of abundance, hydrogen is followed by helium, carbon, oxygen, nitrogen, etc. Any element heavier than helium is referred to as a "metal". The metallicity of a gas or an object is a measure of how abundant such metals are compared to hydrogen. It is an important probe of the evolutionary state of a galaxy, as it increases with age as galaxies undergo chemical enrichment. In this thesis I will use the metallicities of HII regions in combination with other observations describe the evolutionary state of galaxies in the Fornax cluster.

Usually the oxygen abundance compared that of hydrogen is used as a proxy for metallicity. In theory, the addition of all oxygen lines in a spectrum should be used to measure the total amount of oxygen present. However, in reality it is difficult to measure all these lines. Instead, the ISM conditions measured with the diagnostic lines described above are often used to create models that predict the relative flux of the emission lines. The comparison of observed combinations of emission lines and these models then provide an estimate of the oxygen abundance, and thus the metallicity. The problem with this methodology is that there is a wide variety of photoionisation models, as well as empirical methods to measure the electron temperature of the gas, that predict a range of different metallicities at fixed stellar mass. These discrepancies can be huge (up to 1 dex in some cases), which makes it difficult to compare metallicity measurements between, or sometimes even within different studies. An overview and

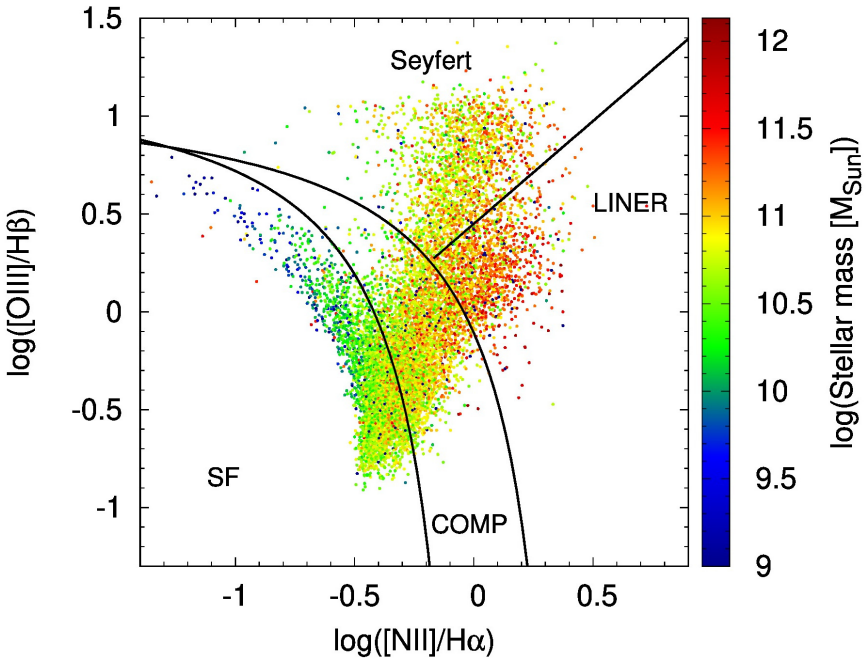

Figure 1.18: BPT diagram of SDSS-FIRST sources (Zajaček et al., 2019). The dominant source of ionisation is shown in each area of the plot. The dividing lines are those from Kewley et al. (2001, top curved line) and Kauffmann et al. (2003, bottom curved line). The straight line in the upper-right area of the plot divides Seyferts and LINERS, and is from Schawinski et al. (2007).

extensive description of some of these methods and models, and the discrepancies between them, is provided by Kewley & Ellison (2008). A similar study, including more recent models, can be found in Sánchez et al. (2019).

The hot ionised medium

Star-forming galaxies contain significant amounts of hot ionised gas. This gas has temperatures $> 10^5$ K, and very low densities (<0.003 cm^{-3}). As a result it takes up about 50% of the ISM in volume, but only a few percent in mass. From its morphology it can be concluded that it originates in supernovae and winds from massive stars, as well as star forming regions (e.g. Strickland & Stevens, 2000; Tyler et al., 2004). As this gas has relatively large vertical scale heights ($\gtrsim$3 kpc) it is sometimes referred to as the "corona" of the galaxy, in addition to the more common "hot halo" and "circumgalactic medium". The scale height is this high because the low-density hot gas is very buoyant. The hot, convecting bubbles mix with cooler gas phases, and eventually cool and rain back down onto the disc after being ejected into the galactic halo (galactic fountains). It can even leave the galaxy entirely as a galactic wind. Hot gas can emit considerable amounts of X-ray radiation from free-free emission

(bremsstrahlung, e.g. Grimes et al. 2005; Tüllmann et al. 2006; Owen & Warwick 2009; Upton Sanderbeck et al. 2018), which is the major cooling mechanism for this gas. Therefore, this hot ionised gas plays an important role in evolutionary models of galaxies and galaxy clusters. Detection of soft X-ray background emission in the Local Bubble suggests that its cavity is filled by hot gas (Snowden et al., 1998).

Dust

About 1% of interstellar matter exists in the form of dust. Not the kind of dust one finds in the corners of their rooms, but solid, macroscopic grains of matter. Typical sizes of dust grains vary between 0.01 and 1 micron. Although the exact composition of cosmic dust has not been pinned down, we know that it typically consists of a mixture of carbons and silicates. It is formed in young stellar objects (e.g. Dwek & Scalo, 1980), the atmospheres of low-mass stars in their later life-stages (Matsuura et al., 2009; Boyer et al., 2012; Höfner & Olofsson, 2018), and in supernovae (Dunne et al. 2003; De Looze et al. 2017, 2019; Cigan et al. 2019; Priestley et al. 2019, see Matsuura 2017 for a review). Once dust grains find themselves in the ISM, they can grow by accreting atoms and molecules. Similarly, they can be split up and destroyed by hot gas, high-energy photons, and collisions. If a dust grain survives long enough, it can end up in a cloud that will eventually collapse and form a star or a planet.

Compared to gas, dust is very opaque, and is capable of obscuring distant objects and objects residing in gas and dust clouds. It scatters and absorbs starlight, and re-emits it at longer wavelengths, observable in the infrared and sub-mm parts of the electromagnetic spectrum. In the process, it reddens the stellar spectrum, as it scatters bluer photons more efficiently than redder ones. Dust can also polarise starlight, if the grains are aligned by a magnetic field, or reflect it if it is located behind the stars. In the Galaxy, 30-50% of the starlight is absorbed and re-radiated by dust.

Besides changing and emitting the light we observe, dust grains are important catalysts in the formation of molecular hydrogen. Generally, in the ISM, it is unlikely for two H atoms to meet and form an H_2 molecule. This is mostly because the energy involved in such collisions prevents both atoms from becoming bound. When multiple H atoms are stuck to a dust grain, the energy involved in their collision gets absorbed by this grain, making it much easier for both atoms to stick together and form a molecule. It can also shield molecular gas from interstellar radiation, thus aiding the formation of new stars and planets (van Dishoeck et al., 1993; Ciolek & Mouschovias, 1995).

Besides metallicity (§1.1.6), the amount of dust in a galaxy relative to gas can tell us something about its evolutionary state. This is especially useful if the two are combined. The study of gas-to-dust ratios as a function of metallicity in the Fornax cluster will be the topic of Chapter 4, where this is discussed in more detail.

1.2 TELESCOPES & INSTRUMENTS

1.2.1 ALMA

The longer the wavelength of the light we aim to observe, the larger a telescope needs to be to detect it at a given spatial resolution resolution, according to

$$\theta = 1.22\frac{\lambda}{D} \approx \frac{\lambda}{D}, \tag{1.2}$$

where θ is the angular resolution, λ the wavelength, and D the diameter of the telescope. CO, the molecule we use to probe H_2, emits in the millimetre regime of the electromagnetic spectrum. Therefore, we need large telescopes to be able to detect it at good resolution. Long-wavelength single-dish telescopes, some of them hundreds of meters in diameter, have been successfully operating on all continents for many decades. Among them are Jodrell Bank (76 m), Effelsberg (100m), ARECIBO (300m), FAST (500m), IRAM (30m), and Nançay (200 × 40m). Some of these and others are shown in Figure 1.19. However, there is a practical limit to what can be achieved with telescopes consisting of of a single piece of material. This limits the detection of CO and other molecules, as well as the resolution of their observations. To demonstrate this, according to Equation 1.2, to achieve $1''$ resolution for emission at a wavelength of 1 cm, you would need a telescope with a diameter of ∼2 km, which is practically impossible to build. Enter interferometers, for instance ALMA.

The Atacama Large Millimeter/submillimeter Array (ALMA) is located in the Chilean Andes, on the Chajnantor plateau (see Figure 1.20). This thesis revolves around observations taken with ALMA, which will be presented and discussed in more detail in Chapter 2. It consists of 66 antennas which can be arranged in different configurations, and spread over distances up to 16 km. Together, these dishes act like one giant single-dish telescope. This is possible because, for telescopes like ALMA, the following equation applies:

$$\theta \approx \frac{\lambda}{B}, \tag{1.3}$$

where B is the distance between two antennas, the "baseline". From this equation we can see that the diameter of a single-dish telescope can be "simulated" by two

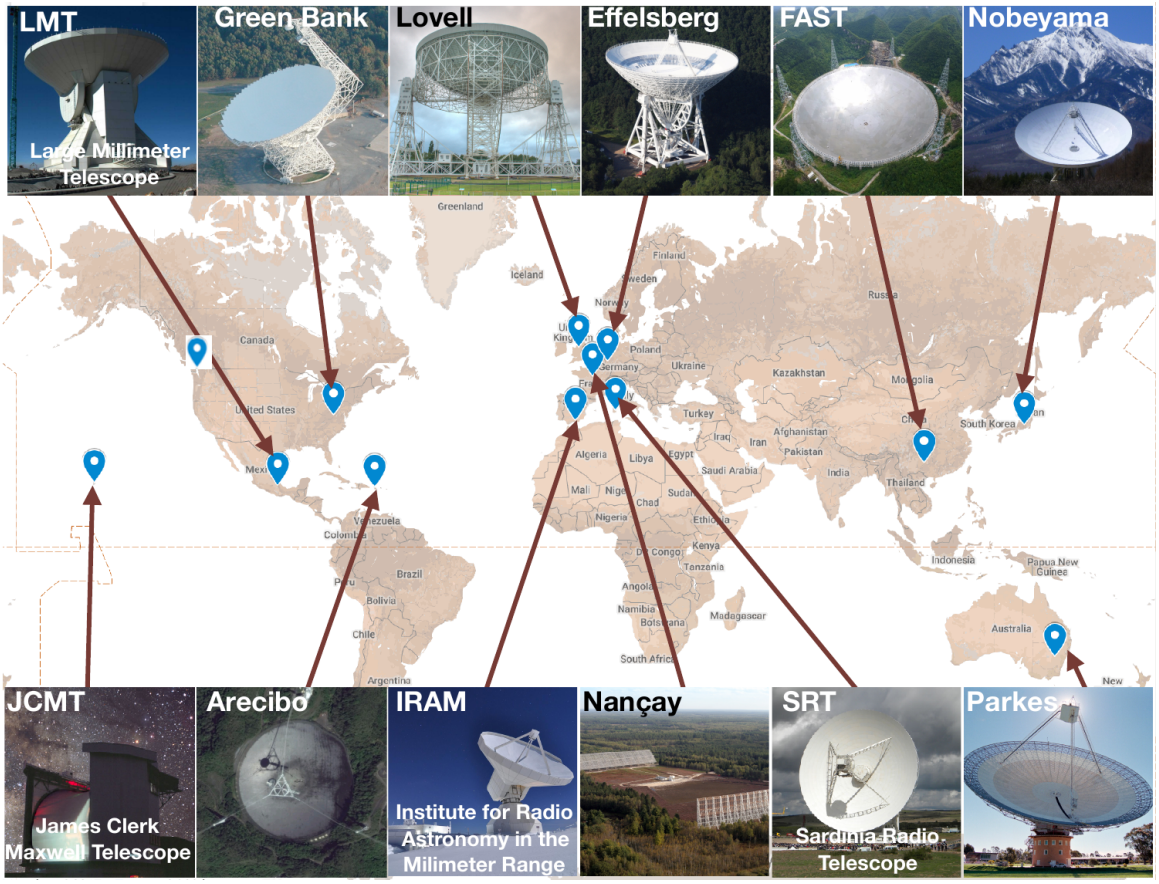

Figure 1.19: Some examples of single-dish long-wavelength telescope across the world, operating in various wavelength regimes, ranging from the mm to >1 m. Taken from a presentation from Jennifer West (University of Toronto) for the 2017 ATCA Radio Summer School.

separate telescopes. This is, very roughly, the idea behind "interferometry".

Radio interferometry was first used in astronomy in 1946, when Martin Ryle, Joseph Lade Pawsey, and Ruby Payne-Scott (who was also the first female radio astronomer) used sea-cliff interferometry (widely used in World War II) to observe the Sun. In short, they used a single antenna to simultaneously capture light directly from the Sun and light reflecting off the water, arriving at their antenna with a delay. This technique was soon after used by their group to publish scientific work (e.g. McCready et al., 1947). It took slightly longer for interferometry to take off in different wavelength regimes. In optical astronomy it was first used in the 1970s to accurately measure the diameters of stars in the optical and infrared (Johnson et al., 1974; Labeyrie, 1975). In some form, it was already around in the 19$^{\text{th}}$ century, but these early experiments made use of pinholes and slits, similar to the famous experiment by Young. The 1970s experiments were the first in which the light from separate optical telescopes was combined. The first interferometers in the millimetre regime of the electromagnetic spectrum were the Millimeter Array (MMA) in the United States, the Large Southern Array (LSA) in Europe, and the Large Millimeter Array (LMA) in Japan. After a series of smaller steps initiated by the National Radio Astronomy Observatory (NRAO) and the European Southern Observatory (ESO), the decision was made to combine these project into a larger interferometer with superior resolution: ALMA was born. Later, Japanese, Taiwanese, and Chilean partners joined the project. Thus far, ALMA is the largest and most expensive ground-based astronomy project. It offers unprecedented resolution in the millimetre regime. As it is sensitive to the coldest parts of the universe (molecular gas and dust), its main science goals include the study of protoplanetary discs, star formation (see Figure 1.23), organic molecules, and spectral line emission in higher-redshift galaxies. Other millimetre interferometers currently operating are the Submillimeter Array (SMA) and the Northern Extended Millimeter Array (NOEMA, the successor of the Plateau de Bure Interferometer (PdBI). The SMA is located on Maunakea in Hawaii, and consists of eight six-metre dishes, which can be configured to form baselines of up to 509m. It is a joint project of the Smithsonian Astrophysical Observatory and the Academia Sinica Institute of Astronomy and Astrophysics. NOEMA is located on the Plateau de Bure in the French Alps. It consists of twelve 15m antennas, twice the number of its predecessor. They can be separated by up to 760m, following two (one north-south and one east-west) tracks. It is a project of the Institut de Radioastronomie Millimétrique (IRAM).

Figure 1.20: The Chajnantor plateau with ALMA, photographed from the nearby Cerro Toco by me in 2019. Bottom-right: me posing rather stupidly with an ALMA dish moved down from the plateau for maintenance.

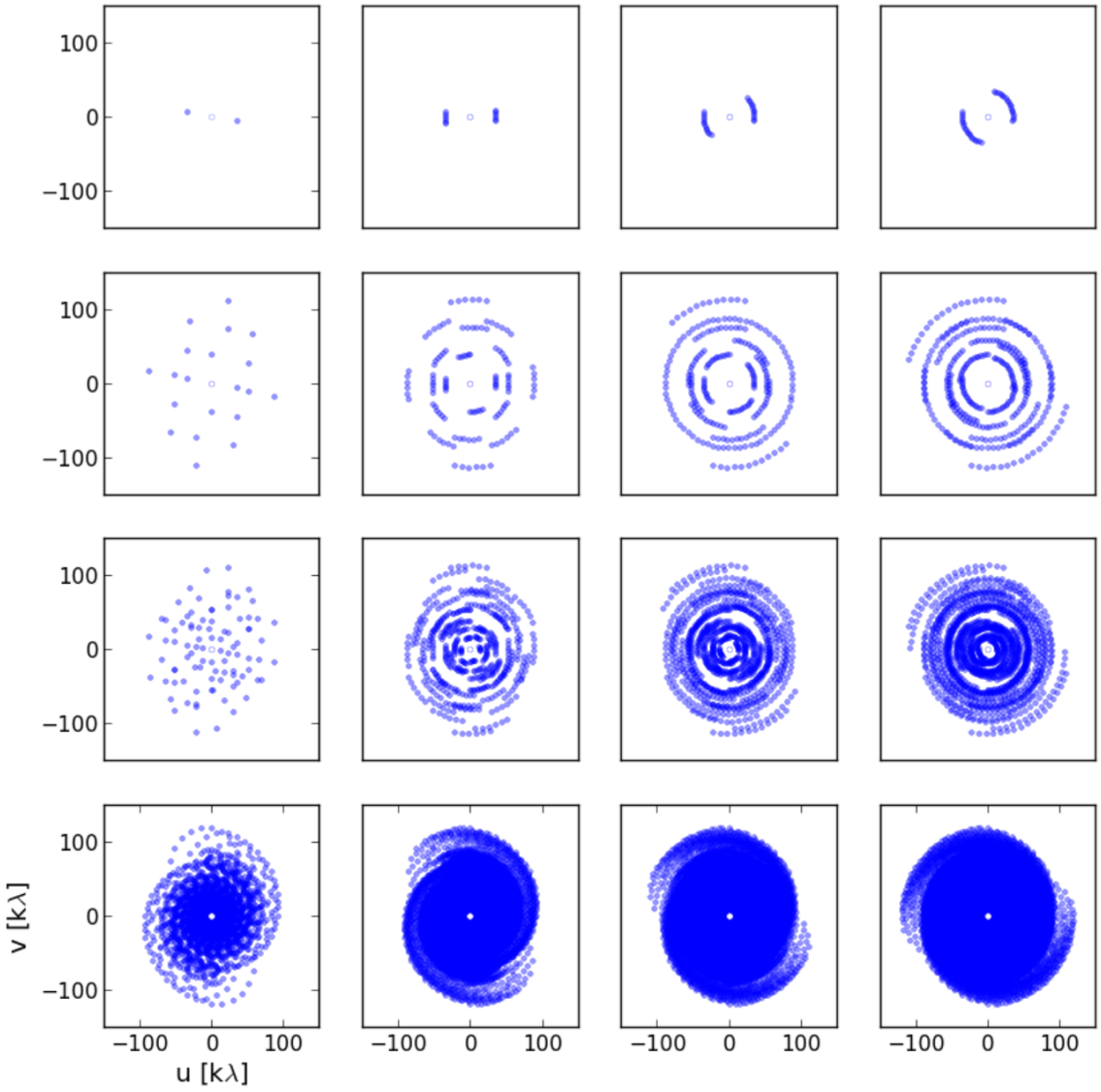

Figure 1.21: Figure 3 from Avison & George (2013): *uv* coverage of a simulated interferometer comprised of 2, 5, 10, and 15 antennas (top to bottom) and observing for 10 seconds and 2, 4, and 6 hours (left to right). In reality, the resulting coverage also depends on the declination of the source.

Interferometry

The key principle of interferometry is based on the Van Cittert-Zernike theorem:

$$T(x,y) = \int\int V(u,v)\, e^{-2\pi i(ux+vy)} du dv. \tag{1.4}$$

In words, this theorem states that the Fourier transform of the intensity distribution of a distant, incoherent source is equal to its complex visibility. Thus, an interferometer measures the Fourier transform of the light distribution of a source in the sky. $V(u,v)$, the "visibility function", can be measured in discrete points. Each baseline of an interferometer provides such a point. It creates an interference pattern similar to that in Young's famous double slit experiment, providing the information for one Fourier component. Thus, many baselines are required to build the desired Fourier transform. This is done by filling in the "uv plane" as much as possible. The uv plane is sampled by measurements from each baseline in the array, and its coverage depends on the arrangement of the dishes. The greater its coverage, the more information we have to build our Fourier transform, and the better the quality of the resulting image will be. Because the coverage of the uv plane depends on the distribution of the dishes (from the point of view of the source), the rotation of the Earth can be used to fill it: a point on the surface of the Earth will move over time from the point of view of the source, in the same way we see star trails in long-exposure images of the sky from the Earth, thus covering more of the plane. This is demonstrated in Figure 1.21. If we consider a single baseline, what we measure from each dish can be described by

$$V_1 = E\cos\left[\omega\left(t-\tau_g\right)\right] \tag{1.5}$$

$$V_2 = E\cos\left(\omega t\right), \tag{1.6}$$

where V_1 and V_2 are the signals (voltages) measured by each antenna, E the electromagnetic field from the source, $\omega = 2\pi\nu$ where ν the observing frequency, t the time, and τ_g the geometric time delay. The latter depends on the length of the baseline and position of the source, and can thus be described by $\tau_g = \frac{\boldsymbol{b}\cdot\boldsymbol{s}}{c}$, where $\mathbf{b}$ is the baseline length, $\mathbf{s}$ a unit vector in the direction of the source, and c the speed of light. The signals from both antennas are then sent to a "correlator" which, as the name suggests, cross-correlates the signals to obtain

$$R = V_1 \otimes V_2 = \frac{1}{2}E^2\left[\cos\left(\omega\tau_g\right) + \cos\left(2\omega t - \omega\tau_g\right)\right], \tag{1.7}$$

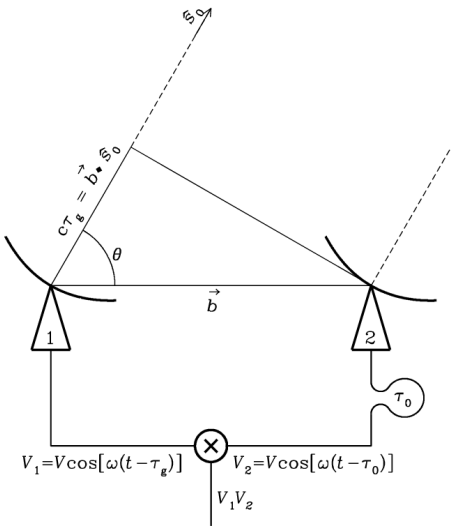

Figure 1.22: Geometry of a simple interferometer consisting of two dishes. The geometric time delay τ_g depends on the distance between the dishes $\boldsymbol{b}$ and the direction towards the source $\boldsymbol{s}$. The signals from both dishes are combined with a correlator. Image taken from the NRAO course Interferometers I (`https://www.cv.nrao.edu/course/astr534/Interferometers1.html`).

assuming the dishes measure the same E field. The second term in this equation varies rapidly, and its average is constant if the antennas are in phase. Thus, when the signal is averaged, we are left with

$$R = \frac{1}{2}E^2 \cos\left(\omega\tau_g\right) = \frac{1}{2}E^2 \cos\left(\omega\frac{\boldsymbol{b}\cdot\boldsymbol{s}}{c}\right). \tag{1.8}$$

Thus far we have implicitly assumed point sources. However, with interferometry we typically aim to resolve astronomical sources. Equation 1.8 then becomes

$$R = \int\int I_\nu\left(s\right) \cos\left(\omega\frac{\boldsymbol{b}\cdot\boldsymbol{s}}{c}\right) d\Omega, \tag{1.9}$$

where I_ν the brightness of the source at the observed frequency, and $d\Omega$ the solid angle observed by the telescope, which means that it is I_ν we are interested in. Another assumption (or rather choice, maybe) we have made this far, is that the fringe pattern is described by a cosine function. This is an even function, which means that the response R goes to zero for odd brightness distributions. This means we need a second correlator using a sine function in order to capture all of the emission from a source. We can then, finally, define the "complex visibility" as follows:

$$V = R_c - iR_s = Ae^{-i\phi} = \int\int I_\nu\left(s\right) e^{-2\pi i\nu\frac{\boldsymbol{b}\cdot\boldsymbol{s}}{c}} d\Omega, \tag{1.10}$$

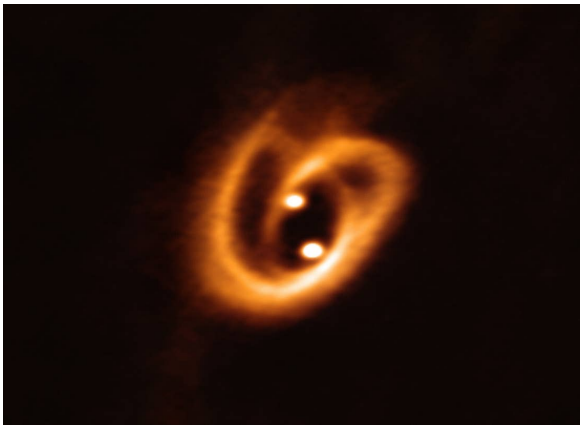

Figure 1.23: ALMA observations of the binary system [BHB2007], the "cosmic pretzel", published in Alves et al. (2019). The binary system is located in the nebula B59 (which is part of the larger Pipe Nebula), and is in the process of forming from the material in a huge disc. The resolution of this image is less than 10 AU, and demonstrates the powerful capabilities of ALMA. Credit: ALMA (ESO/NAOJ/NRAO), Alves et al. (2019).

where $A = \sqrt{R_c^2 + R_s^2}$, $\phi = \arctan\left(\frac{R_s}{R_c}\right)$, and R_c and R_s the responses of the cosine and sine correlators, respectively. The resulting equation can be recognised as a two-dimensional Fourier transform.

The resolution described by Equation 1.3 does not only provide a measure of the maximum resolution of an interferometer (given by the distance between the two antennas furthest apart, $B_{\max}$), but also a *minimum* resolution, given by the two antennas in the array that are closest together ($B_{\min}$). Putting $B_{\min}$ in Equation 1.3 thus returns the maximum angular size the interferometer is sensitive to. Since two dishes cannot be infinitely close together (they cannot overlap), an interferometer is always "blind" to structures on the sky that extend further than this maximum size: the emission is "resolved out". Sometimes single-dish observations are required in addition to interferometric ones to fill in this missing flux. To overcome part of this limitation, ALMA includes the "Atacama Compact Array" (ACA, or Morita Array), consisting of twelve 7-m and four 12-m antennas at the heart of the larger array. The latter set of antennas is called the "Total Power (TP) Array". Observations with the ACA and TP arrays are often conducted in addition to observations with a configuration using all antennas, and are scheduled separately.

1.2.2 MUSE

The Multi Unit Spectroscopic Explorer (MUSE, Bacon et al. 2010, see Figure 1.24) is a panoramic (its field of view is $1' \times 1'$ in the Wide Field Mode) integral-field

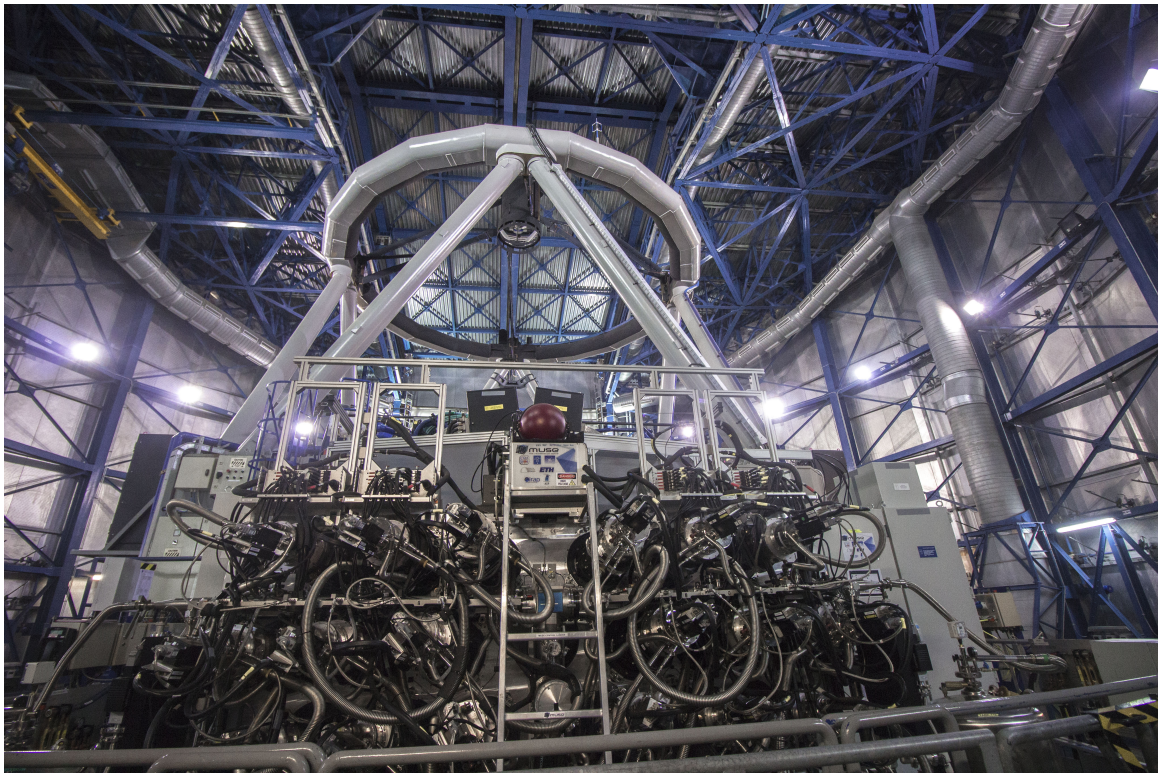

Figure 1.24: MUSE, mounted to Unit Telescope 4 (Yepun) of the Very Large Telescope, which was being prepared for observations when the photo was taken. Photographed by me in 2019.

spectrograph, operating in the visible wavelength range (0.465-0.93 μm). An integral field spectrograph is an optical instrument that combines spectrographic and imaging techniques. It can obtain spatially resolved spectra: each pixel in the resulting image has its own spectrum. In this thesis it is primarily used to observe emission lines from which the gas-phase metallicity and star formation rate can be estimated (see §1.1.6). MUSE can achieve high spatial resolution thanks to the use of adaptive optics (AO). The instrument consists of 24 separate sub-fields, which, in turn, are split up into 48 mini-slits, each linked to a spectrograph. Thanks to this setup, the data coming from MUSE, similarly to ALMA, consist of a 3D RA $\times$ Dec $\times$ velocity data cube. MUSE is mounted to Unit Telescope 4 (UT 4, "Yepun") of the Very Large Telescope, located on Cerro Paranal in the Atacama desert. Its main science goals include the study of galaxy formation, nearby galaxies, stars and stellar populations, and the solar system. To-date, MUSE has made important contributions in many fields, including the studies of black holes (e.g. McElroy et al., 2016; Poggianti et al., 2017; Giesers et al., 2018) and the distant Universe (e.g. Bacon et al., 2015; Massey et al., 2015; Borisova et al., 2016), among others.

Figure 1.25: The *Herschel* Space Observatory.

1.2.3 The *Herschel* Space Observatory

Because the atmosphere is opaque to radiation at the infrared wavelengths in which dust emits (see §1.1.6), we need space-based telescopes to detect emission from dust. The *Herschel* Space Observatory (Pilbratt et al. 2010, see Figure 1.25 is such a space-based telescope. It was launched (together with the Planck satellite) to the second Lagrangian point (L2) on 14 May 2009 and operational until 17 June 2013, when it ran out of liquid helium. *Herschel* observed in the very far-infrared into sub-mm wavelengths (∼55 - 671 μm), parts of the electromagnetic-spectrum still relatively unexplored at the time of its launch. Its main goals were to study star formation and galaxy evolution, but also the chemical composition of asteroids and comets in the Solar System. It carried a 3.5m mirror, the largest one on a space telescope to-date. It had three scientific instruments on board: the Photoconductor Array Camera and Spectrometer (PACS, Poglitsch et al. 2010), the Spectral and Photometric Imaging REceiver (SPIRE, Griffin et al. 2010), and the Heterodyne Instrument for the Far Infrared (HIFI, de Graauw et al. 2010). PACS and SPIRE were cameras and imaging spectrometers, whereas HIFI was a high-resolution spectrometer. All instruments were kept at very low temperatures (close to absolute zero) to provide the sensitivity needed to observe the cold Universe. Besides galaxy formation and evolution, *Herschel* has contributed important discoveries in the fields of star formation (e.g. Stanke et al., 2010) and astrochemistry (e.g. Goldsmith et al., 2011), and on the origin of

water present on solar system objects (e.g. Hartogh et al., 2011; Küppers et al., 2014). In Chapter 3 of this thesis I will use *Herschel* observations in conjunction with observations from ALMA to study gas-to-dust ratios in cluster environments.

1.3 THESIS OUTLINE

This thesis presents an in-depth study of the Fornax cluster, one of two galaxy clusters closest to us (see §1.1.4). It is divided over three chapters, each a self-contained, (almost) published and peer-reviewed piece of work. Central to each chapter is the molecular gas, (H_2, see §1.1.6), in the interstellar media of Fornax galaxies, observed with ALMA (see §1.2.1). The key question of this thesis is: *"Can the molecular gas in the ISM of galaxies be directly affected by the cluster environment?",* which is is then further built upon by the related questions *"Is star formation in the Fornax cluster more or less efficient than in the field?"* and *"Are gas-to-dust ratios in the Fornax cluster any different than in the field?"*. These questions are addressed by the following chapters:

Chapter 2: "The ALMA Fornax Cluster Survey I: stirring and stripping of the molecular gas in cluster galaxies" (an adaption of Zabel et al. 2019)

Chapter 3: "AlFoCS + Fornax3D: resolved star formation in the Fornax cluster with ALMA and MUSE" (an adaption of Zabel et al. 2020)

Chapter 4: "AlFoCS + F3D II: unexpectedly low gas-to-dust ratios in the Fornax galaxy cluster" (an adaption of Zabel et al. 2021)

Chapter 5: A summary of the main findings of this thesis, how it fits into the bigger picture of today's knowledge of and open questions in the field of galaxy evolution, as well as related ongoing and future work.

Chapter 2
The ALMA Fornax Cluster Survey I: stirring and stripping of the molecular gas in cluster galaxies

> Imagining other words we try
>
> Realizing somehow we're all part of this
> Wondrous cosmical tapestry
>
> Yes, *"Universal Garden"*

I present the first results of the ALMA Fornax Cluster Survey (AlFoCS): a complete ALMA survey of all members of the Fornax galaxy cluster that were detected in HIor in the far infrared with *Herschel*. The sample consists of a wide variety of galaxy types, ranging from giant ellipticals to spiral galaxies and dwarfs, located in all (projected) areas of the cluster. It spans a mass range of $10^{\sim 8.5-11} M_{\odot}$. The CO(1-0) line was targeted as a tracer for the cold molecular gas, along with the associated 3 mm continuum. CO was detected in 15 of the 30 galaxies observed. All 8 detected galaxies with stellar masses below $3 \times 10^9 M_{\odot}$ have disturbed molecular gas reservoirs, only 7 galaxies are regular/undisturbed. This implies that Fornax is still a very active environment, having a significant impact on its members. Both detections and non-detections occur at all projected locations in the cluster. Based on visual inspection, and the detection of molecular gas tails in alignment with the direction of the cluster centre, in some cases ram pressure stripping is a possible candidate for disturbing the molecular gas morphologies and kinematics. Derived gas fractions in almost all galaxies are lower than expected for field objects with the same mass, especially for

the galaxies with disturbed molecular gas, with differences of sometimes more than an order of magnitude. The detection of these disturbed molecular gas reservoirs reveals the importance of the cluster environment for even the tightly bound molecular gas phase.

2.1 INTRODUCTION

As outlined in Chapter 1, it is well known that the atomic gas in galaxies is affected by environmental processes. The situation is more complicated for the molecular gas, because it is more tightly bound to the galaxy and distributed more centrally. The debate about this has therefore been more lively. Early research often concluded that the molecular gas in cluster galaxies is the same as that in field galaxies, and is unaffected by the cluster environment (e.g. Stark et al., 1986; Kenney & Young, 1989; Casoli et al., 1991; Boselli et al., 1995; Boselli & Gavazzi, 2006). It was not until more recently that indications of deficiency, i.e. a lower mass than expected based on statistics of similar galaxies in the field, were observed for the molecular gas as well (e.g. Vollmer et al., 2008; Fumagalli et al., 2009; Boselli et al., 2014b) and also for dust (e.g. Cortese et al., 2010, 2012). Although, these deficiencies are smaller than for HI. On average galaxies which are HI deficient by a factor of $\sim$10 are CO deficient by a factor of $\sim$2. Lee et al. (2017) report examples of three galaxies in the Virgo cluster that are ram pressure stripped of their molecular gas as well as their atomic gas. At higher redshifts, evidence of molecular gas stripping and deficiencies in clusters has also recently been observed (e.g. Noble et al., 2018; Wang et al., 2018; Stach et al., 2017), although cluster galaxies with molecular gas contents similar to (e.g. Rudnick et al., 2017) or even higher than (e.g. Hayashi et al., 2018) field galaxies are found as well.

Because molecular gas is the direct fuel for star formation, the effects of the cluster environment on this phase of the interstellar medium (ISM) have immediate consequences for the star formation rate of the host galaxy. If it is directly affected by environmental processes, this could have important implications for the quenching of cluster members and therefore for galaxy evolution as a whole. The goal of this Chapter is to investigate whether the cluster environment indeed affects the molecular gas in galaxies, and if so, attempt to identify which processes are mainly responsible for this. In order to do this, I focus my attention on the Fornax cluster, introduced in Chapter 1.

Horellou et al. (1995) carried out an HI and ^{12}CO(1-0) survey of 21 spirals and lenticulars in the Fornax cluster, using the Nançay radio telescope (France) and

the Swedish-ESO Submillimeter Telescope (SEST, Booth et al. 1989), respectively. They detected 16 galaxies in HI, and 11 were detected in CO. They found that on average the CO emission of Fornax galaxies is weak: about five times lower than that of spirals in the Virgo cluster. From this it follows that the corresponding molecular gas masses are low as well: they found H_2 masses that are about ten times lower than the atomic gas masses. They attribute the decreased molecular gas masses to reduced star-formation activity, and argue that it is in agreement with low far-infrared, radio continuum and Hα luminosities. They comment, however, that although the CO emission found for the Fornax galaxies is low compared to that in infrared-selected samples, that may be typical for spirals in optically-selected samples. In this work I revisit the CO(J=1-0) in the Fornax cluster and investigate whether these observations can be confirmed.

The ALMA Fornax Cluster Survey is a complete survey of the 30 Fornax cluster members that were detected in 3 or more *Herschel* Space Observatory (Pilbratt et al., 2010) bands with the *Herschel* Fornax Cluster Survey (Fuller et al., 2014) or in HI (Waugh et al. 2002, Loni et al. in prep. based on ATCA data). The CO(1-0) rotational line (rest frequency: 115.271 GHz) was observed to create spatially resolved maps of the cold molecular gas and its kinematics in these galaxies. The survey covers a range of different galaxy stellar masses and morphologies.

A full description of the sample can be found in §2.2. The observations, data reduction, and ancillary data are described in §4.2. In §4.5 I present moment maps of the CO emission of the detected galaxies, as well as their position-velocity diagrams (PVDs) and spectra, and a comparison with optical observations. H_2 masses are estimated and compared with the expected H_2 masses for field galaxies. In §4.7 I discuss the results, and the morphologies and kinematics of the galaxies in the sample. Various environmental processes are considered as possible candidates for the irregularities observed, and the surprising detection of several dwarf galaxies is discussed. In §5.1 I summarise the work, and distil conclusions. Although accurate distance measurements are available for some of the AlFoCS galaxies, here I adopt the distance to the Fornax cluster (19.95 Mpc, Tonry et al. 2001) as a common distance to all galaxies.

2.2 Sample selection

Our sample is based on the Fornax Cluster Catalogue (FCC, Ferguson, 1989). From this catalogue, galaxies with stellar masses $> 3\times10^8$ $M_\odot$ were selected to ensure high enough metallicity to detect CO. Furthermore, galaxies were selected to contain

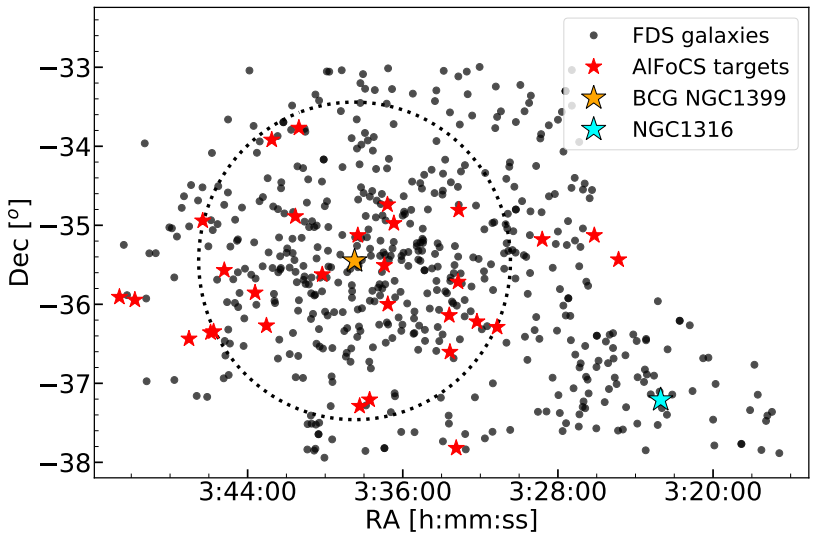

Figure 2.1: Map of the Fornax cluster. The black dots represent Fornax Deep Survey galaxies from Venhola et al. (2018, see §2.3.3), the red stars represent the AlFoCS sample. The central galaxy, NGC1399, is indicated with a larger yellow star, and the virial radius (located at 0.7 Mpc, Drinkwater et al. 2001) is shown as a dotted line. AlFoCS targets are distributed evenly over the cluster (except for the infalling subgroup, which was not covered by *Herschel*). NGC1316, the central galaxy of the infalling subgroup, is indicated with a cyan star.

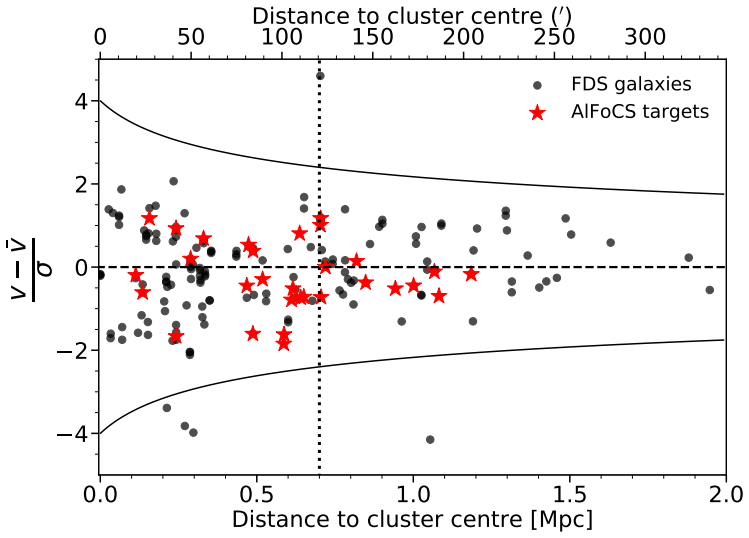

Figure 2.2: Caustic diagram of the Fornax cluster. The black data points represent the FDS galaxies for which velocity information is available, and the red stars represent the AlFoCS targets. The solid lines represent the escape velocities in the cluster as a function of distance from the cluster centre. The vertical dotted line indicates the virial radius at 0.7 Mpc (Drinkwater et al., 2001). $\bar{v} = 1493$ km s^{-1}and $\sigma = 374$ km s^{-1}(Drinkwater et al., 2001). The AlFoCS targets are distributed evenly in the caustic space.

dust (Fuller et al., 2014) or HI down to $\sim 3 \times 10^7 M_\odot$ (Waugh et al. 2002, Loni et al. in prep. based on ATCA data). This suggests ongoing star formation activity, and therefore the presence of a molecular gas reservoir. Whether a galaxy was selected based on its FIR emission or HIcontent is listed in Table 3.1. The application of these criteria on the FCC leads to a sample of 30 galaxies, spanning a wide range of morphological types, varying from giant ellipticals to irregular dwarfs. A wide range of locations within the cluster is covered by the survey. This is shown in Figure 2.1, where I compare the locations of the AlFoCS galaxies with the locations of the galaxies in the Fornax Deep Survey (FDS, Peletier et al. 2020). The FDS is a recent optical survey of the Fornax cluster, containing 573 galaxies, and is described in more detail in §2.3.3. The FDS galaxies are shown as black dots, and the galaxies targeted here are shown as red stars. The brightest cluster galaxy (BCG) NGC1399 is shown as a bigger yellow star, and the dotted line represents the virial radius of the cluster according to Drinkwater et al. (2001). The central galaxy of the currently infalling subgroup in the south-east of the figure, NGC1316, is indicated with a cyan star. Aside from a slight (<10%) deficiency of galaxies in the innermost (∼350 kpc or 1 degree) radius of the cluster centre (defined as the location of NGC1399), the AlFoCS targets are spread evenly among the cluster galaxies: they are located at all directions from the cluster centre, and both close to the central galaxy, and outside the virial radius. There are no observations in the infalling subgroup around NGC1316, as this area was not covered by *Herschel*.

To confirm that all targets are indeed cluster members, I create a caustic diagram of all galaxies with known velocities: the (projected) velocities of the galaxies (corrected for the velocity of the cluster and galaxy-to-galaxy velocity dispersion within the cluster) of the cluster as a function of their distance from the cluster centre. This is shown in Figure 2.2. The mean velocity and velocity dispersion of the Fornax cluster were taken from Drinkwater et al. (2001), and equal 1493 km $s^{-1}$and 374 km s^{-1}, respectively. The velocities of the individual galaxies are a combination of velocities from the FCC, the 2dF Galaxy Redshift Survey (Colless et al., 2001; Drinkwater et al., 1999), and the 2MASS Redshift Survey (Huchra et al., 2012). Note that velocity information is unavailable for 470 of the 573 FDS galaxies, and these were omitted from the figure. The solid lines represent the escape velocities at each projected distance from the cluster centre, assuming a Navarro-Frenk-White (NFW) density profile for the cluster dark matter distribution (Navarro et al., 1997). They were derived using equation 7 and 16 from Shull (2014), featuring a dark matter concentration parameter, which was estimated using equation 3 from Coe (2010). The dotted line again represents the virial radius, and the colours are the same as in Figure

Table 2.1 Key properties of the galaxies in the sample.

Common name	FCC #	RA	Dec	cz	$M_\star$	Selection
-	-	(J2000)	(J2000)	(km s^{-1})	($\log(M_\odot)$)	-
(1)	(2)	(3)	(4)	(5)	(6)	(7)
FCC32	32	03h24m52.4s	-35d26m08s	1319 $^\diamond$	$9.23^{+0.04}_{-0.07}$*	FIR
FCC44	44	03h26m07.4s	-35d07m39s	1233 $^\diamond$	$8.50^{+0.07}_{-0.17}$*	FIR
NGC1351A	67	03h28m48.7s	-35d10m41s	1354	9.45†	FIR, HI
MGC-06-08-024	90	03h31m08.2s	-36d17m25s	1814 $^\diamond$	8.98†	FIR, HI
FCC102	102	03h32m10.7s	-36d13m15s	1722 ‡	$8.36^{+0.08}_{-0.10}$*	HI
ESO358-G015	113	03h33m06.8s	-34d48m29s	1389	8.88†	FIR, HI
ESO358-16	115	03h33m09.2s	-35d43m07s	1701 $^\diamond$	$8.32^{+0.07}_{-0.09}$*	HI
FCC117	117	03h33m14.6s	-37d49m11s	-	$7.77^{+0.18}_{-0.20}$*	FIR
FCC120	120	03h33m34.2s	-36d36m21s	849 ‡	$8.50^{+0.07}_{-0.09}$*	HI
NGC1365	121	03h33m36.4s	-36d08m25s	1638 $^\diamond$	11.16†	FIR, HI
NGC1380	167	03h36m27.6s	-34d58m34s	1878 $^\diamond$	10.98†	FIR
FCC177	177	03h36m47.5s	-34d44m23s	1562 $^\diamond$	$10.4^{+0.01}_{-0.02}$*	FIR
NGC1386	179	03h36m46.2s	-35d59m58s	869 $^\diamond$	10.5†	FIR
NGC1387	184	03h36m57.0s	-35d30m24s	1303 $^\diamond$	10.77†	FIR
FCC198	198	03h37m42.7s	-37d12m30s	-	$8.09^{+0.05}_{-0.07}$*	FIR
FCC206	206	03h38m13.5s	-37d17m25s	1403 $^\diamond$	$9.01^{+0.07}_{-0.10}$*	FIR
FCC207	207	03h38m19.3s	-35d07m45s	1421 $^\diamond$	$8.78^{+0.04}_{-0.05}$*	FIR
NGC1427A	235	03h40m09.3s	-35d37m28s	2029 $^\diamond$	9.78†	FIR, HI
FCC261	261	03h41m21.5s	-33d46m09s	1710 ‡	8.58†	FIR
PGC013571	263	03h41m32.6s	-34d53m18s	1725 $^\diamond$	9.2†	FIR, HI
FCC282	282	03h42m45.3s	-33d55m14s	1266 ‡	9.0†	FIR
NGC1437A	285	03h43m02.2s	-36d16m24s	891 ‡	9.38†	FIR, HI
NGC1436	290	03h43m37.1s	-35d51m11s	1388 $^\diamond$	10.1†	FIR, HI
FCC302	302	03h45m12.1s	-35d34m15s	816 ‡	$8.48^{+0.09}_{-0.07}$*	HI
FCC306	306	03h45m45.4s	-36d20m48s	891 ‡	8.68†	FIR, HI
NGC1437B	308	03h45m54.8s	-36d21m25s	1515 ‡	9.39†	FIR, HI
ESO358-G063	312	03h46m19.0s	-34d56m37s	1920 ‡	10.04†	FIR, HI
FCC316	316	03h47m01.5s	-36d26m15s	1547 $^\diamond$	$8.64^{+0.07}_{-0.12}$*	FIR
FCC332	332	03h49m49.0s	-35d56m44s	1327 $^\diamond$	8.63†	FIR
ESO359-G002	335	03h50m36.7s	-35d54m34s	1431 $^\diamond$	9.21†	FIR

Notes: 1: Common name of the galaxy; 2: Fornax Cluster Catalogue number of the galaxy; 3: Right ascension; 4: Declination; 5: Velocity (defined as the object's redshift times the speed of light); 6: Stellar mass. ‡See §2.3.4; $^\diamond$Redshifts from NASA/IPAC Extragalactic Database; †Stellar masses from Fuller et al. (2014); *Stellar masses derived from 3.6 μm images, (see §4.3.1); 7: Whether the galaxy was selected based on an HI(Waugh et al. 2002, Loni et al. in prep. based on ATCA data) or a FIR (Fuller et al., 2014) detection (or both).

2.1. All AlFoCS galaxies shown here have velocities well below the escape velocity at their location, and are distributed evenly in the caustic space.

The locations, velocities, and stellar masses of the galaxies observed are listed in Table 3.1.

2.3 Observations and data reduction

2.3.1 ALMA data

Atacama Large Millimeter/submillimeter Array (ALMA) observations of the ^{12}CO(1-0) line in 29 AlFoCS targets were carried out under project 2015.1.00497.S (PI: Timothy Davis). ALMA's 12 m configuration was used, which has a primary beam size of ∼55" at ∼115 GHz. In cases where the FIR emission of the galaxy extends beyond this scale, multiple pointings are combined into a mosaic to ensure that CO is observed all the way to the outskirts of the galaxy. The largest recoverable scale is 25". Band 3 observations were performed between the 7th and 12th of January 2016, subdivided in three Scheduling Blocks (SBs) in order to meet the sensitivity requirements of the different targets whilst keeping maximum efficiency: single fields, small mosaics, and dwarfs. The sensitivities achieved are listed in Table 2.5. The first Scheduling Block consists of one Execution Block (EB): uid___A002_Xaeaf96_X515. The small mosaics are divided over two Execution Blocks: uid___A002_Xaec9ef_X5c0 and uid___A002_Xaec9ef_X88a. The same is true for the dwarfs, which are divided over Execution Blocks uid___A002_Xaecf7b_X32d4 and uid___A002_Xaecf7b_X3943. For each SB one spectral window was centred at 114.756, 114.547, and 114.716 GHz, respectively, to target the ^{12}CO(1-0) rotational line. The bandwidths are 1.875 GHz, covering 3840 channels. The other spectral windows, covering 128 channels each with total bandwidths of 2 GHz, were used to target the band 3 continuum of the individual galaxies. Their central frequencies, along with other details of the observations, are listed in Table 2.2. The expected calibration uncertainty of the data is 10%. Synthesized beam sizes and the sensitivities achieved are listed in Table 2.5.

Data reduction

The data were calibrated manually using the Common Astronomy Software Applications package (CASA, version 5.1.1, McMullin et al. 2007), using standard ALMA calibration scripts[1]. Several antennas were flagged manually, mostly because of high

[1]The scripts used can be found on `https://github.com/NikkiZabel/AlFoCS_data_reduction_scripts`

Table 2.2 Observational parameters.

SB	Date	# ants	TOT	Bandpass cal.	Flux cal.	CF spw 3	CV spw 3	BW spw 3	CF spws 0, 1, 2
-	-	-	(mins.)	-	-	(GHz)	(km s^{-1})	(km s^{-1})	(GHz, resp.)
(1)	(2)	(3)	(4)	(5)	(6)	(7)	(8)	(9)	(10)
Single fields	07-01-2016	42	52	J0336-3616	J0336-3616	114.547	1885	4898	113.001, 100.939, 102.544
Small mosaics	11-01-2016	46	125	Uranus	J0336-3616	114.756	1340	4907	112.818, 100.824, 102.713
Dwarfs	12-01-2016	43	251	Uranus	J0336-3616	114.716	1445	4900	113.161, 101.089, 102.703

Notes: 1: Scheduling Block; 2: Date of the observations; 3: Number of antennas used; 4: Total observation time in minutes; 5: Bandpass calibrator; 6: Flux calibrator; 7: Central frequency of spectral window 3 (centred on the ^{12}CO(1-0) line); 8: Central velocity of spectral window 3 (centred on the ^{12}CO(1-0) line); 9: Bandwidth of spectral window 3 (centred on the ^{12}CO(1-0) line) 10: Central frequencies of the remaining spectral windows.

system temperatures or outliers in the data of the flux calibrator. The resulting "dirty" images were then "cleaned" using the `tCLEAN` algorithm (Högbom, 1974) in CASA. In cases where both CO and continuum are detected, a continuum estimate is created using the full line-free bandwidth, and subtracted from the channels containing the CO line using the `uvcontsub` command. Cleaning of the channels containing the CO line was done interactively, using a natural weighting scheme (equivalent to a Briggs weighting scheme (Briggs, 1995) with a robust parameter of 2). Many of the sources have extended emission, and using natural weighting will help ensure that this is recovered in the data. This choice also maximises the signal-to-noise at the cost of decreased spatial resolution. The channel widths of most final data cubes are 10 km s^{-1}, as is usually chosen for this type of data (e.g. Alatalo et al., 2013), and the pixel sizes 0.5 arcseconds. Exceptions are the dwarf galaxies FCC207 and FCC261, for which channel widths of 2 km s^{-1}were used, because of their narrow line widths (see Table 2.5). The result is a three-dimensional RA-Dec-velocity data cube for each galaxy. Primary beam (PB) corrections are then carried out as a separate step using the `impbcor` command, allowing us to store both PB corrected and non PB corrected data cubes. Beam sizes and sensitivities are listed in Table 2.5. Typical rms noise levels are around ∼3 mJy/beam.

NGC1365

In order to expand our sample, an already reduced image of NGC1365 was taken from the ALMA archive (project ID: 2015.1.01135.S, PI: Egusa, Fumi). It was observed on 20 March 2016. ALMA's 12m configuration was used, with a primary beam size of ∼55" at ∼115 GHz. The mosaic covers an area of $\sim 6.6' \times \sim 4.4'$. The central frequency of spectral window 3 (the window centred on the ^{12}CO(1-0) line) is 114.848 GHz or 1100 km s^{-1}. The bandwidths are 1.875 GHz, covering 3840 channels. The spectral resolution is 2.55 km s^{-1}. To obtain the final data cube, the `CLEAN` algorithm in CASA version 4.7.0 was used. A continuum estimated and subtracted from the channels containing the CO line as described in §2.3.1. A briggs weighting scheme was adopted (Briggs, 1995) with a robust parameter of 0.5. The pixel sizes of the final data cube are 0.3 arcseconds, and the channel width 5 km s^{-1}. The synthesized beam size and the sensitivity achieved are listed in Table 2.5.

Aside from the data reduction, this observation is treated the same as the galaxies observed as part of this survey.

2.3.2 MOPRA DATA

Additional single-dish observations of Fornax cluster galaxies from the Mopra Fornax Cluster CO-Line Legacy Survey (PI: M.W.L. Smith) are included, a survey of ^{12}CO(1-0) in 28 galaxies in the Fornax cluster, carried out between the nights of 08-08-2012 and 17-09-2012. The Mopra Spectrometer (MOPS) was used in Wideband Mode, centred at a rest frequency of 115.500 GHz for all targets. Its coverage is 8.3 GHz (or 30,378 km s^{-1}), and its spectral resolution 0.915 km s^{-1}. The FWHM of the beam is 33 $\pm$ 2" at 115 GHz (Ladd et al., 2005). The calibration uncertainty is less than 10% (Ladd et al., 2005), I adopt a conservative value of 10% here. The data were reduced using the ATNF `LIVEDATA` (Barnes et al., 2001) and `GRIDZILLA` (Sault et al., 1995) packages. `LIVEDATA` is used to fit baselines and transform the raw datafiles to SDFITS files. I fit linear baselines to all spectra and mask the top and bottom 300 channels. `GRIDZILLA` is then used to combine these files into data cubes. The spatial resolution of these cubes is 0.25' per pixel. I use our own scripts to combine the data from the various pointings into a mosaic. For a few objects only single pointings were required. For these objects the data reduction is done using our own scripts to obtain the quotient spectrum by subtracting and dividing by the obtained reference spectra, perform baseline subtraction, and velocity-bin the data. A ripple in the baseline is present in some of the data. This is a known issue with the Mopra telescope, and attempts to mitigate it here, for example by flagging in Fourier space, were not successful. The noise levels in these data are higher, but the data are still usable for the aims of this work.

2.3.3 OPTICAL DATA

To allow for a comparison of the distribution of the cold molecular gas with the stellar bodies of the galaxies, and to create three-colour images, r-, g-, and u-band images were obtained from the Fornax Deep Survey (FDS, Peletier et al. 2020) for all galaxies in which CO(1-0) was detected in AlFoCS. The FDS is a new, deep multi-band optical survey of the Fornax cluster, which covers 26 square degrees around the virial radius, including the SW sub-group centred on NGC1316 (Iodice et al., 2017). It has been obtained with the ESO VLT Survey Telescope (VST), which is a 2.6-meter diameter optical survey telescope located at Cerro Paranal, Chile (Schipani et al., 2012). The imaging is done in the u', g', r' and i'-bands using the $1^o \times 1^o$ field of view OmegaCAM instrument (Kuijken et al., 2002) attached to VST. The deep images provide data with excellent resolution with mean seeing of 1 arcsec and pixel size of 0.2 arcsec. The quality of the data and the photometry of the galaxies

are described in detail in Venhola et al. (2018). The survey area is covered with homogeneous depth with the 1σ limiting surface brightness over 1 pixel area of 26.6, 26.7, 26.1 and 25.5 mag arcsec^{-2} in u', g', r' and i', respectively. When averaged over a 1 arcsec^2 area, these numbers correspond to 28.3, 28.4, 27.8, 27.2 mag arcsec^{-2} in u', g', r' and i', respectively. The photometric calibration errors of the FDS are 0.04, 0.03, 0.03, and 0.04 mag in u', g', r' and i', respectively. Venhola et al. (2018) produced Sérsic model fits for all the dwarf galaxies within the survey area using GALFIT (Peng et al., 2002, 2010). In addition, Iodice et al. (2018) have studied all bright ($m_B < 15$ mag) ETGs inside the virial radius of the cluster (some of them are presented in this work). They released the total magnitudes, effective radii and stellar masses and discussed the structure and colors of the galaxy outskirts.

2.3.4 Redshift determinations

A subset of the AlFoCS objects were observed with the 3.9m Anglo-Australian Telescope at the Siding Spring Observatory as part of a larger programme. The AAOmega spectrograph (Sharp et al. 2006; Saunders et al. 2004) and the Two-degree Field (2dF; Lewis et al. 2002) fibre positioner were used, along with the 580V and 385R gratings, providing spectral coverage over 3740–8850Å. The spectra were reduced using the 2dFDR software package (Croom et al. 2004), and spectral classifications and redshifts were determined using MARZ (Hinton et al. 2016). Velocities derived from these redshifts are listed in Table 3.1, indicated with a ‡.

2.3.5 Moment maps

Cleaned data cubes were used to produce moment maps of the CO(1-0) line emission, using the masked moment method (Dame, 2011). While PB corrected images are used in the remainder of this work, for the purpose of clarity uncorrected maps are presented in Figure 2.3, Figure 2.4, and Appendix A.1. In order to create the mask, a Gaussian smoothing was applied to a copy of the data cube, in both spatial axes as well as the velocity axis, with a full width at half the maximum (FWHM) of 1.5 times the beam's major axis for the spatial axes, and 4 channels (proven to be optimal from previous experience) for the velocity axis. Using this smoothed copy as a mask, the data cubes were then "clipped" to the $x\sigma$ level, which means that all spaxels below this value are set to zero, where x is chosen to give the best visual result, and equals 3 or 4.

In Figure 2.3 and Figure 2.4 moment maps of NGC1387 and MCG-06-08-024 are shown, serving as examples of the regular and disturbed galaxies, respectively

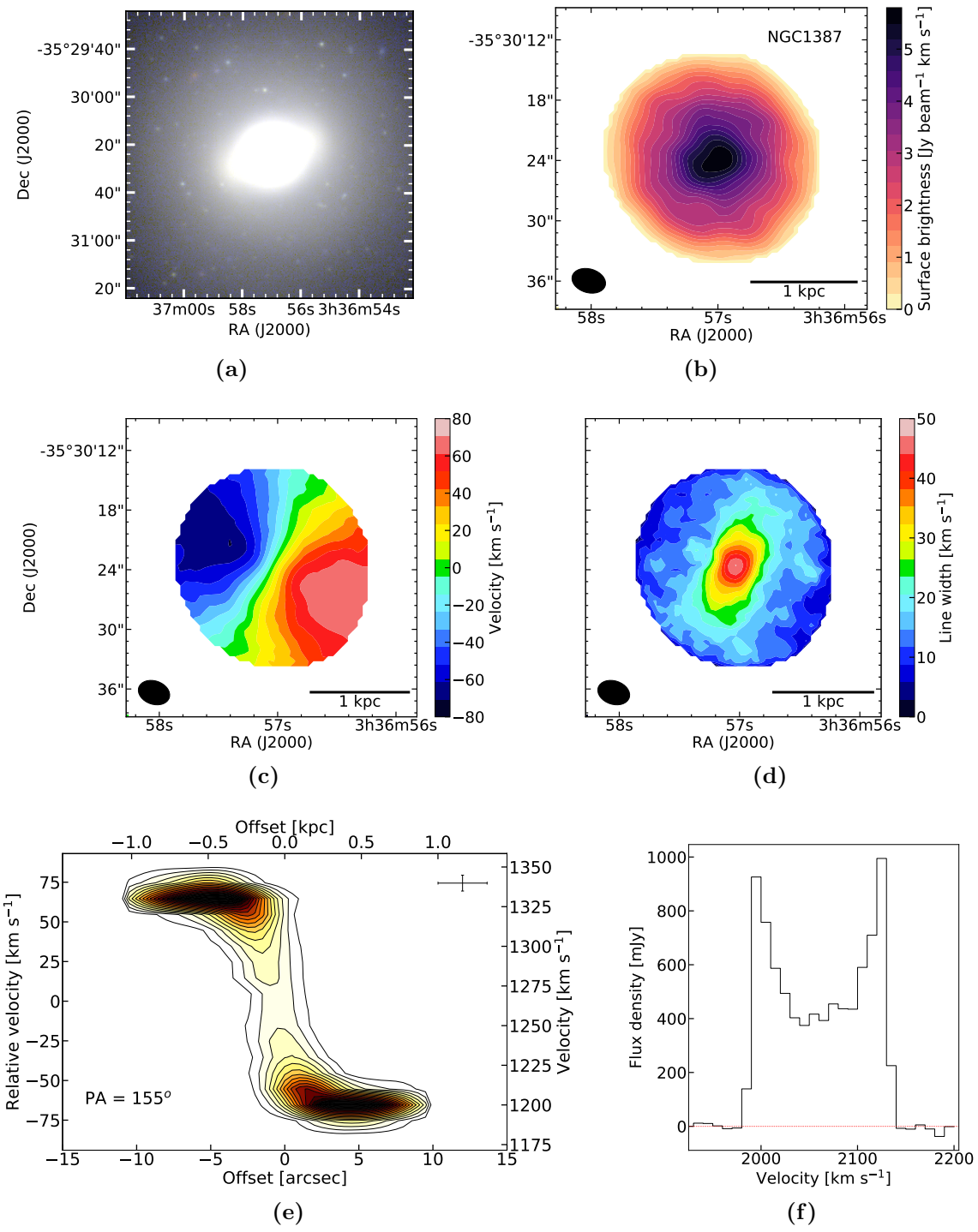

Figure 2.3: a: Three-colour (*r*-*g*-*u*) image of NGC1387. b: Moment zero map: distribution of the cold molecular gas as traced by the ALMA CO data. c: Moment 1 map: velocity map of the cold molecular gas. Each colour represents a 10 km s^{-1}velocity channel. d: Moment 2 map: linewidth of the CO integrated spectrum. e: Position-velocity diagram or of the cold molecular gas. The uncertainties in the spatial and velocity directions are indicated in the upper right corner. f: the CO(1-0) line. The beam of the observations is shown in the lower left corners of the moment maps, as well as a 1 kpc scale bar in the lower right corners. NGC1387 is a very regular galaxy with symmetric moment maps.

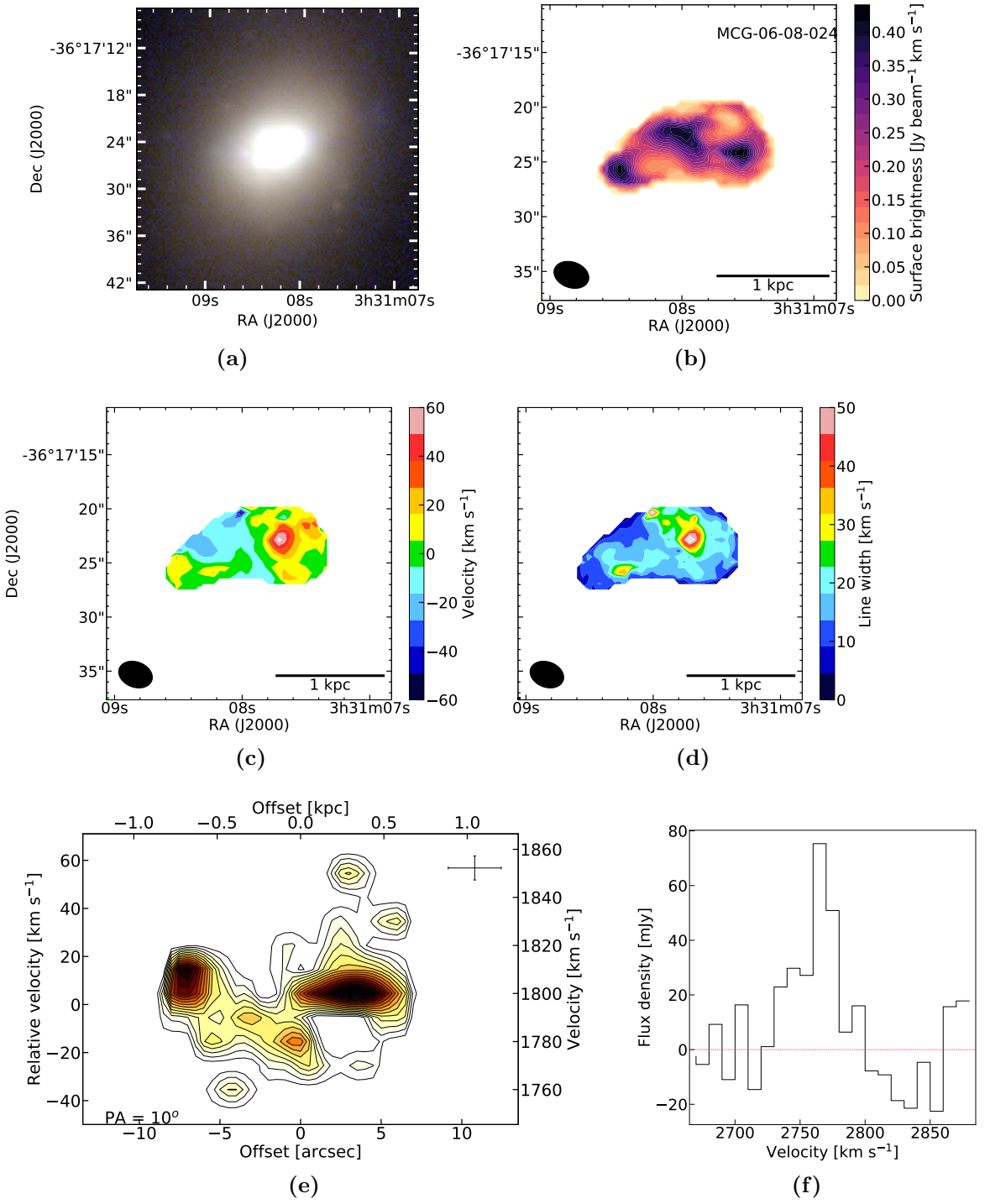

Figure 2.4: MGC-06-08-024 (FCC90), similar to Figure 2.3. MGC-06-08-024 is galaxy with irregular CO emission, and therefore has irregular moment maps and an irregular position-velocity diagram.

(see §2.5.1 for more details). The top left panel of each of these figures is a three-colour image, constructed using the r-, g-, and u- band images from the Fornax Deep Survey (Peletier et al. 2020, see §2.3.3). The top right panels are intensity or moment zero maps of the cold molecular gas as traced by the ALMA CO data, showing its spatial distribution. The black ellipse in the lower left corner shows the beam of the observations, and a 1 kpc scalebar is shown in the lower right corner. This is the same in the other two moment maps. The middle left panels are velocity or moment one maps of the galaxies. Each of the colours represents a 10 km s^{-1}(2 km $s^{-1}$for FCC207 and FCC261, see §2.3.1) velocity channel. The warm colours represent the positive, redshifted velocities, and the cold colours represent the negative, blueshifted velocities. Middle right figures are moment two maps, representing the linewidth.

The bottom left figures are position-velocity diagrams (PVDs), which reveal the motion of gas along the major axes of the galaxies. They are obtained by defining a slit the size of the beam along the major axis of the galaxy in the data cube, and collapsing it along the minor axis. The errorbars in the upper right corner indicate the PSF FWHM (horizontal) and channel width (vertical). The bottom right figures show the part of the galaxy's spectrum containing the CO(1-0) line. The spectrum was obtained by defining a rectangular aperture around the detected emission in the spatial directions, large enough to contain all its CO emission, and then collapsing the data cube along both spatial axes.

In NGC1387 (Figure 2.3b) the gas is distributed as an almost face-on disk, with the projected intensity decreasing radially. Its velocities vary between -80 and +80 km s^{-1}relative to the systemic velocity, which is determined by taking the mean of the moment one map shown here. The line is widest in a band along the kinematic minor axis, due to beam smeared rotation. The PVD of NGC1387 (Figure 2.3e) is very regular, showing a smooth and symmetric "rotation curve", which reaches its maximum very quickly. The double-peaked line profile, typical for a disk, is clearly visible in its spectrum (Figure 2.3f).

In MCG-06-08-024 the molecular gas is distributed irregularly, around three different maxima. The velocities of the gas are between -60 and +60 km s^{-1}relative to the systemic velocity. The PVD of MCG-06-08-024 has a very irregular shape.

Similar images of the remaining 14 detected galaxies were created in the same way, and can be found in Appendix A.1.

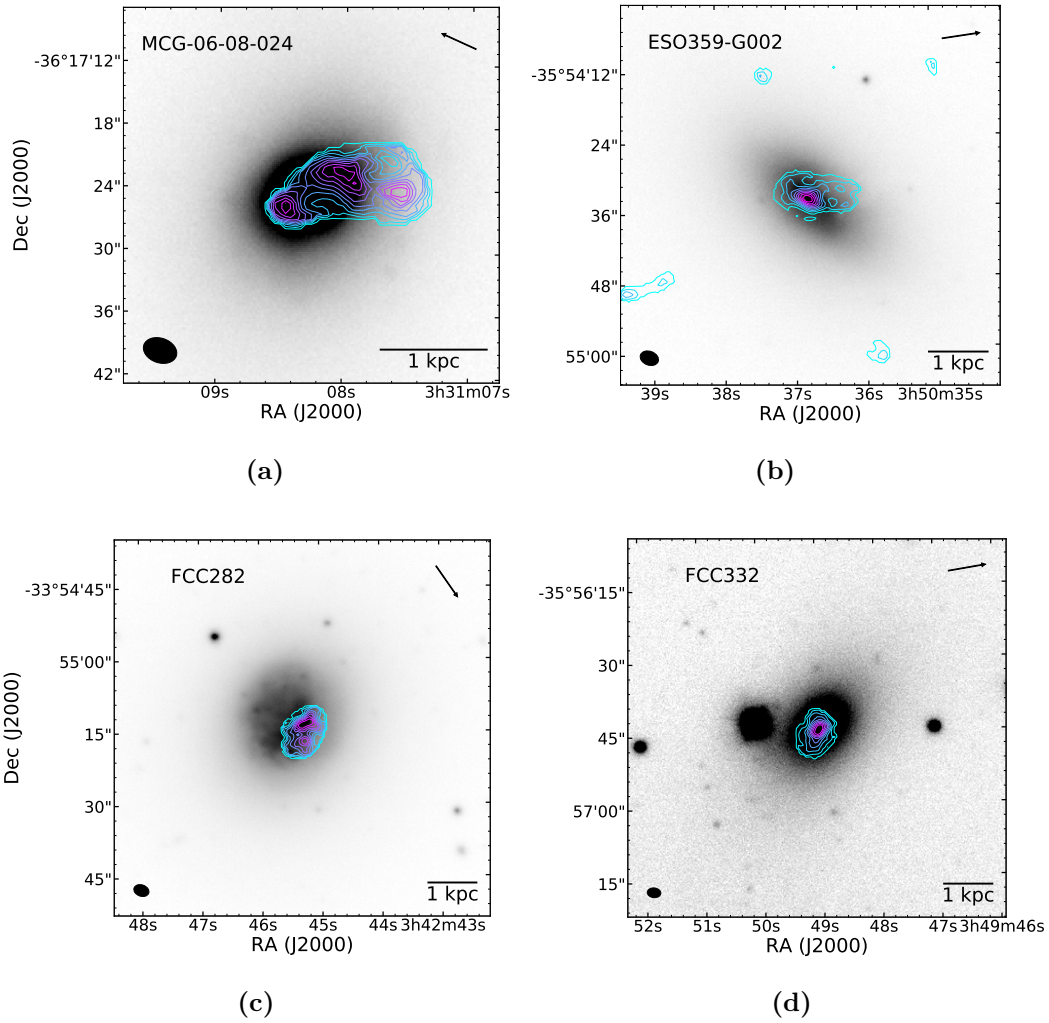

Figure 2.5: [CO(1-0) emission overplotted on optical (g-band) images from the FDS (Peletier et al. 2020)]CO(1-0) emission overplotted on optical (g-band) images from the FDS. The CO emission is shown as 10 coloured contours, the outer contour is set equal to 3 or 4 σ, while the level of the innermost contour depends on the highest signal measured in the galaxy. The beam is shown in the lower left corners, and a 1 kpc scalebar in the lower right corners. The arrow in the upper right corners indicates the direction towards the cluster centre. The molecular gas in these galaxies is asymmetric with respect to their stellar bodies. In 2.5a and 2.5b it extends beyond the stellar body and forms a tail aligned with the direction of the cluster centre.

2.3.6 COMPARISON TO OPTICAL MORPHOLOGY

Figure 2.5 overplots the CO integrated intensity contours on top of optical images of the galaxies (g-band images of the FDS were used, see §2.3.3). The CO emission is shown as 10 coloured contours, the outer contour being equal to 3-4σ, while the innermost contour depends on the highest signal measured in the galaxy in question. The arrows in the upper right corners point towards the cluster centre (here defined as the location of the BCG NGC1399). Similar plots for the remaining galaxies can be found in Appendix A.2.

The galaxies in Figure 2.5 are all examples of galaxies with irregular CO emission, asymmetric compared to the galaxy's stellar body. In MCG-06-08-024 (Figure 2.5a) and ESO359-G002 (Figure 2.5b) the molecular gas forms a tail that extends beyond the stellar body. These galaxies are discussed further in §2.5.3. Other examples of galaxies with asymmetric CO emission are FCC207 (Figure A.15g) and FCC261 (Figure A.15h). In the cases of the regular galaxies, such as ESO358-G063 (Figure A.14m), NGC1386 (Figure A.16e), NGC1387 (Figure A.16f), and NGC1351A (Figure A.16a), the CO emission follows the optical shape of the galaxy. The CO emission in NGC1380 (Figure A.16d) is very compact compared to its stellar body in our images, but has been shown to be distributed in a regular disk by Boizelle et al. (2017).

It would be interesting to compare the CO morphologies to HI morphologies, especially for the galaxies that exhibit asymmetric CO emission or gas tails. This would show us whether these galaxies also have HI tails, which is expected if ram pressure stripping is at play. The current HI observations available are not of sufficient resolution to do this. However, in the future I will be able to use data from the MeerKAT Fornax Survey (Serra et al., 2016) for this purpose.

2.4 RESULTS

CO was detected (at $> 3\sigma$) in 15 of the 30 galaxies observed. In Figure 2.6 the (projected) locations of the detections and non-detections within the cluster are shown, and morphologically and kinematically regular and disturbed galaxies are highlighted. All FDS (see §2.3.3) galaxies are shown as black dots, the AlFoCS galaxies are shown in colour. Non-detections are shown as blue plus signs, the pink squares are galaxies in which CO is detected and morphologically and kinematically regular or undisturbed, and the red triangles represent galaxies in which CO is detected and morphologically and kinematically disturbed (see §2.5.1 for more details). Both detections and non-detections are distributed evenly over the cluster. At first glance it

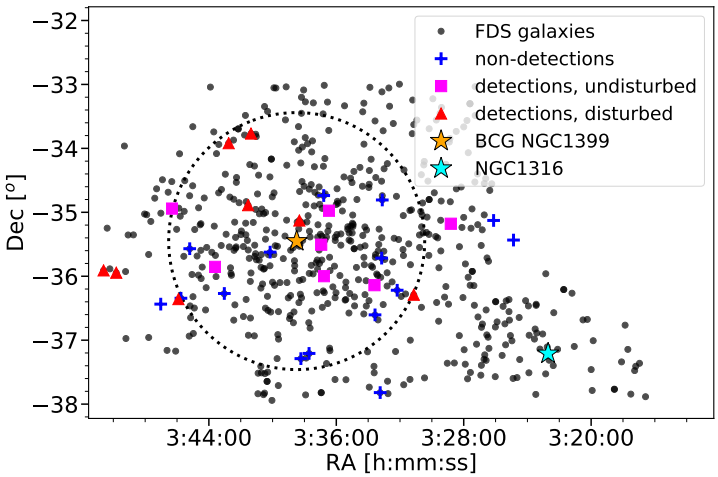

Figure 2.6: Map of the Fornax cluster, similar to Figure 2.1. The coloured symbols represent the AlFoCS targets, their shape and colour indicate whether CO was detected and if so, whether it is morphologically and kinematically disturbed or regular, as indicated in the legend. The central galaxy, NGC1399, is indicated with a yellow star, and the virial radius with a dotted line. The central galaxy of the infalling group in the lower right corner of the figure, NGC1316, is indicated with a cyan star. Non-detections, disturbed galaxies, and regular galaxies are distributed evenly over the cluster.

looks like there are slightly more non-detections south of the cluster centre, however this is not statistically significant. Galaxies with disturbed molecular gas reservoirs seem to be mainly located close to or outside the virial radius.

2.4.1 Marginal detections

In ESO358-G015, FCC32, and NGC1437A CO is detected, but only marginally. In ESO358-G015 and NGC1437A these are 4 - 5 σ detections, but the emission comes from small features away from the galactic centre, and it is not clear whether this emission is related to the galaxy observed. For FCC32 I find a tentative 2 σ peak at the centre of the galaxy. These features are likely noise, and for these reasons I do not consider these observations further in this work.

2.4.2 Continuum detections

Continuum (3 mm) was detected in NGC1380, NGC1386, NGC1387, and NGC1427A. In Figure 2.7 the continuum maps of NGC1380, NGC1386, and NGC1387 are shown as coloured contours overplotted on the g-band images from the FDS, similar to Figure 2.5. In all three cases the continuum emission originates from the

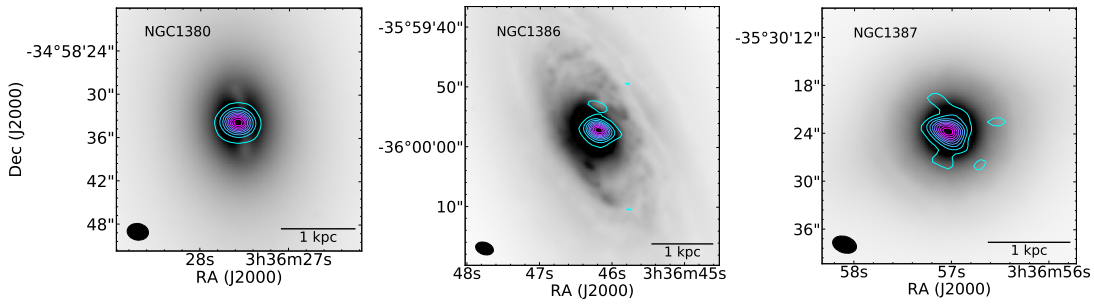

(a) NGC1380 **(b)** NGC1386 **(c)** NGC1387

Figure 2.7: 3 mm continuum emission overplotted on optical (g-band) images from the FDS (see §2.3.3), similar to Figure 2.5. The emission is shown as 10 coloured contours; the lower (outer) contour level equals 5σ. The emission originates from the galaxies' centres, and is likely due to a combination of AGN activity and thermal emission from dust.

galactic centre. Two galaxies, NGC1380 and NGC1386, are known to harbour active galactic nuclei (AGN, e.g. Boizelle et al. 2017; Lena et al. 2015; Rodríguez-Ardila et al. 2017). The emission I detect is an unresolved point source at the galactic centre, but has a positive spectral index (see Table 2.3). It is possible that both thermal and non-thermal emission is contributing the observed emission in these sources.

The 3 mm continuum emission in NGC1387 has a point-like morphology in the lower sideband, but when imaged at the higher frequencies several additional point sources are also detected, in the region where dust and molecular gas are present. This additional emission leads to the very large spectral index measured for this source (see Table 2.3). Given this, the detected 3 mm emission is again likely due to a mix of AGN activity and thermal emission from dust.

In the case of NGC1427A the emission originates from a small source at the edge of the galaxy. This is shown and discussed separately in §2.5.5.

2.4.3 H_2 MASSES

H_2 masses for all detected galaxies were estimated using the following equation:

$$M_{H_2} = 2m_H \; D^2 \; X_{CO} \; \frac{\lambda^2}{2 \; k_B} \int S_\nu \; d\nu \; , \tag{2.1}$$

where m_H is the mass of a hydrogen atom, D is the distance to the galaxy, X_{CO} is the CO-to-H_2 mass conversion factor, λ is the rest wavelength of the line observed, k_B is the Boltzmann constant, and $\int S_\nu \; d\nu$ the total flux of the line observed. I use

Table 2.3 Properties of the detected 3mm continuum emission.

Galaxy	Frequency	Flux density	Frequency USB	Flux density USB	Frequency LSB	Flux density LSB	Spectral index
-	(GHz)	(mJy)	(GHz)	(mJy)	(GHz)	(mJy)	-
(1)	(2)	(3)	(4)	(5)	(6)	(7)	(8)
NGC1380	107.765	4.18 ± 0.04	113.763	4.65 ±0.08	101.775	4.12 ±0.04	1.1 ± 0.2
NGC1386	107.718	3.69 ± 0.05	113.750	3.99 ±0.07	101.748	3.64 ±0.07	0.8 ± 0.2
NGC1387	107.718	1.85 ± 0.06	113.750	4.3 ±0.1	101.748	1.04 ± 0.06	$12.7^{+0.6}_{-0.5}$
NGC1427A	107.765	0.16 ± 0.03	113.763	0.20 ±0.06	101.775	0.16 ±0.03	$2.0^{+3.0}_{-3.5}$

Notes: 1: Name of the galaxy; 2: Central frequency of the 3 mm continuum; 3: Flux density of the 3 mm continuum emission; 4: Central frequency of the upper sideband; 5: Flux density of the continuum in the upper sideband; 6: Central frequency of the lower sideband; 7: Flux density of the continuum in the lower sideband; 8: Spectral index of the continuum emission.

the metallicity-dependent mass conversion factor derived from Accurso et al. (2017, eqn. 25):

$$\log \alpha_{\rm CO} = 14.752 - 1.623\,[12 + \log({\rm O/H})] + 0.062\,\log \Delta\,({\rm MS})\,, \qquad (2.2)$$

where $12 + \log({\rm O/H})$ is the metallicity and $\log \Delta\,({\rm MS})$ the distance from the main sequence, discussed below. The 1σ spread in $\log \alpha_{\rm CO}$ from this relation is 0.165 dex. It is multiplied by 2.14×10^{20} to obtain $\rm X_{CO}$ (Bolatto et al., 2013). For reference, this equation gives a conversion factor of $2.08 \pm 0.02 \times 10^{20}$ for solar metallicity ($12 + \log({\rm O/H}) = 8.69$, Asplund et al. 2009). Since I do not have independent metallicity measurements for each object, metallicities were derived directly from the stellar masses of the galaxies, using the mass-metallicity relation from Sánchez et al. (2017), which uses the calibration from Pettini & Pagel (2004). Stellar masses ($M_\star$) are listed in Table 3.1. They were taken from Fuller et al. (2014) where possible (see Table 3.1). Alternatively, they were obtained from aperture photometry on archival Wide-field Infrared Survey Explorer (WISE, Wright et al. 2010) band 1 (3.6 μm) images, assuming a mass-to-light ratio of 1 (see Table 3.1). Apertures were chosen using the effective radii determined by Venhola et al. (2018, see §2.3.3) if available, and alternatively chosen by eye. Uncertainties on the stellar mass in these cases are a combination of the uncertainty in the effective radius and the rms in the image.

The $X_{\rm CO}$ calibration from Accurso et al. (2017) requires a distance from the main sequence (e.g. Brinchmann et al., 2004; Noeske et al., 2007; Elbaz et al., 2007). Here I assume a distance from the main sequence $\Delta{\rm MS} = 0$ for all galaxies. It is a second order parameter, so varying this does not strongly affect our results. Equation 2.4.3 is valid for values of $-0.8 < \Delta{\rm MS} < 1.3$. Varying ΔMS over this range results in a maximum error of 0.08 in $\alpha_{\rm CO}$, which is indeed small compared to the other errors.

To make sure I include all the CO emission, while minimising the inclusion of noise, galaxies were subdivided into two groups: a group whose line profiles are best described by a Gaussian profile (mostly dwarf galaxies with narrow CO lines), and another group whose line profiles are best described by a box profile (mostly larger galaxies). Which profile best describes a galaxy is listed in Table 2.5. The widths of the CO integrated spectra are given. For boxy line profiles an uncertainty of 20 km $\rm s^{-1}$(the equivalent of two channels) is adopted, for Gaussian profiles the formal fitting errors on the linewidth are quoted. For the first group I fit a Gaussian to the CO(1-0) line and integrate this fit to obtain the total line flux. For the second group, I integrate directly under the line observed. In this case the boundaries of the line are determined using the PVDs. Uncertainties are a combination of the error on the total

integrated line emission $\int S_\nu d\nu$ and an adopted 10% calibration error, and are often dominated by the latter. For galaxies with a boxy profile, the error in the integrated line emission is estimated according to the following equation, adapted from equation 1 from Young et al. (2011):

$$\sigma_I^2 = (\Delta v)^2 \sigma^2 N_l, \tag{2.3}$$

where N_l is the number of channels that is summed over, Δv the width of each channel, and σ the rms noise level in the line free part of the spectrum. For galaxies with an approximately Gaussian line profile, the error on the total integrated line emission is estimated by combining the formal fitting errors on the parameters of the fit. The resulting molecular gas masses are listed in Table 2.5.

Upper limits

For non-detections, 3σ upper limits were determined using the rms in the (spatial) inner area of the PB corrected data cubes. Since all non-detections can be considered dwarf galaxies, I assume Gaussian line profiles with FWHM of 50 km s^{-1}. This is slightly broader than the profiles of the dwarf galaxies detected here, and therefore a conservative assumption. The maximum of the assumed line profile was set to 3 times the rms in the corresponding data cube. I use stellar mass dependent CO-to-H_2 conversion factors, as described above in §4.3.1. I then use Equation 2.1 to obtain the upper limits for the H_2 mass listed in Table 2.5.

Mopra

Of the 28 galaxies observed with Mopra, CO was detected in one additional galaxy which was not observed with ALMA; NGC1317. After removing data affected by bad weather, I was able to obtain this one additional H_2 mass measurement and 8 additional upper limits. Due to a problem with the observations, I only have single, central pointing observations of NGC1317. Since the molecular gas is usually centrally located, however, this is expected to cover most if not all of its CO emission. Upper limits are 3σ upper limits, estimated as described above. Despite the rather prominent baseline ripple in some of the observations, a known issue with the Mopra Telescope (see §4.2), these upper limits provide reasonably good constraints. The resulting upper limits, as well as the estimated H_2 mass of NGC1317, are listed in Table 2.4.

Table 2.4 Key properties and derived quantities of the Mopra targets included in this work.

Name	RA	Dec	Stellar mass	rms	$\log_{10}(M_{H_2})$	Deficiency
-	(J2000)	(J2000)	($\log(M_\odot)$)	(mJy km s^{-1})	($M_\odot$)	(dex)
(1)	(2)	(3)	(4)	(5)	(6)	(7)
NGC1316	03h22m41.718s	-37d12m29.62s	$10.0^{\dagger}$	273	$\leq$ 8.27	$\leq$ -0.52
NGC1317	03h22m44.286s	-37d06m13.28s	$9.98^{\dagger}$	192	8.69 $\pm$ 0.04	-0.08 $\pm$ 0.01
NGC1350	03h31m08.12s	-33d37m43.1s	$10.71^{\dagger}$	602	$\leq$ 8.61	$\leq$ -0.38
ESO359 G3	03h52m00.92s	-33d28m03.5s	$10.11^{+0.01\ \ddagger}_{-0.02}$	130	$\leq$ 7.95	$\leq$ 0.05
FCCB857/858*	03h33m19.49s	-35d20m41.4s	$9.31^{+0.01\ \ddagger}_{-0.04}$	34	$\leq$ 7.36	$\leq$ -0.07
FCCB950	03h34m31.65s	-36d52m20.7s	$9.47^{+0.02\ \ddagger}_{-0.04}$	31	$\leq$ 7.32	$\leq$ -0.64
FCCB990	03h35m11.38s	-33d22m25.6s	$9.39^{+0.02\ \ddagger}_{-0.04}$	97	$\leq$ 7.82	$\leq$ 0.04
FCCB713**	03h31m20.94s	-35d29m29.9s	-	55	$\leq$ 7.57	$\leq$ -0.59
FCCB792**	03h32m25.95s	-38d05m33.8s	-	21	$\leq$ 7.16	$\leq$ -0.48
FCCB1317**	03h39m11.70s	-33d31m56.0s	-	97	$\leq$ 7.81	$\leq$ 0.10

Notes: 1: Name of the galaxy observed; 2: Right ascension; 3: Declination; 4: Stellar mass (see §4.3.1); 5: rms in the spectrum; 6: Derived molecular gas mass (see §4.3.1); 7: H_2 deficiency (see §2.4.4); *FCCB857 and FCCB858 are close to each other on the sky and were therefore contained within one beam. The stellar mass quoted here is the addition of the stellar masses of both galaxies. The coordinates of FCCB858 are quoted here. **These galaxies were observed but later found to be background objects. They are therefore omitted in Figures 2.8 and 2.9, and stellar masses were therefore not determined for them; †Stellar masses from Fuller et al. (2014); †Stellar masses derived from 3.6 μm images, (see §4.3.1).

2.4.4 Gas fractions & deficiencies

In Figure 2.8 the galaxies' molecular-to-stellar mass ratios are shown as a function of their stellar mass (see §4.3.1 for more details about the stellar masses used here), and compared with those of field control galaxies with the same stellar masses. The molecular gas fraction is given by $\left(\frac{M_{\rm H_2}}{M_{\rm total}}\right)$. Since $M_{\rm HI}$ and $M_{\rm H_2}$ are relatively small contributions to the total mass of the galaxy compared to the stellar mass, for convenience and consistency with the definition in Saintonge et al. (2017) (see below), I define the gas fraction here as $\left(\frac{M_{\rm H_2}}{M_\star}\right)$. I use the extended CO Legacy Database for *GALEX* Arecibo SDSS Survey (xCOLD GASS, Saintonge et al. 2017) as a field galaxy control sample. xCOLD GASS is a survey of molecular gas in the local universe, built upon its predecessor COLD GASS (Saintonge et al., 2011). It is a mass-selected ($M_\star > 10^9 M_\odot$) survey of galaxies in the redshift interval $0.01 < z < 0.05$ from the SDSS, and is therefore representative of the local galaxy population within this mass range. I use the relation based on the median values that they obtained by subdividing the sample in bins based on their stellar mass (see Saintonge et al., 2017, their Figure 10), and interpolate linearly (in log space) to obtain the relation represented by the dashed line. Since xCOLD GASS galaxies were selected to have stellar masses $M_\star > 10^9 M_\odot$, the first stellar mass bin is located at $M_\star = 9.388 M_\odot$. Below this stellar mass, the dashed line is obtained using linear extrapolation (in log space). Expected mass fractions for galaxies in this mass range, 5 detections and 11 upper limits, should be treated with caution. The shaded areas represent the 1, 2, and 3 sigma levels in the xCOLD GASS data, from dark to lighter. Galaxies with disturbed molecular gas are shown in red, and galaxies with regular, undisturbed molecular gas are shown in black (see §2.5.1 for the definitions). Galaxies that have clear gas tails that extend beyond their optical emission, or otherwise asymmetric CO emission, are indicated with red triangles. ALMA upper limits for the H_2 mass are shown as magenta open triangles, and Mopra upper limits as cyan open triangles. NGC1317, the only Mopra detection included here, is shown as a cyan dot. There is a systematic offset between the xCOLD GASS H_2 mass fractions for field galaxies and our values of up to about $\sim$1 dex. This offset is not very significant at an individual level for regular galaxies, whose offset is mostly within or close to the 1σ scatter in the xCOLD GASS data. With exception of NGC1437B and FCC332, all disturbed galaxies lie below 3σ (for FCC261 and FCC207 I cannot be certain because they lie below the mass range of the xCOLD GASS data, but based on this figure it seems plausible to assume they would fall below 3σ as well). In particular the galaxies with asymmetric CO emission have low gas fractions.

I define H_2 deficiencies here as $\log(M_{H_2,\text{observed}})$ - $\log(M_{H_2,\text{expected}})$. Estimates of the H_2 deficiency for each galaxy are listed in Table 2.5. Galaxies with regular CO emission have an average H_2 deficiency of -0.50 dex, and galaxies with disturbed CO emission have an average H_2 deficiency of -1.1 dex. In Figure 2.9 H_2 deficiencies are plotted as a function of the (projected) distance between the galaxy and the cluster centre. Markers and colours are the same as in Figure 2.8. It seems like galaxies within a (projected) radius of 0.4 Mpc from the cluster centre are slightly more deficient than galaxies outside this radius. However, Kolmogorov-Smirnov and Mann-Whitney U tests are unable to reject the null hypothesis that both groups of galaxies are drawn from the same distribution at more than $\sim 2\sigma$. Possible explanations for this and a further discussion of this figure can be found in §2.5.3.

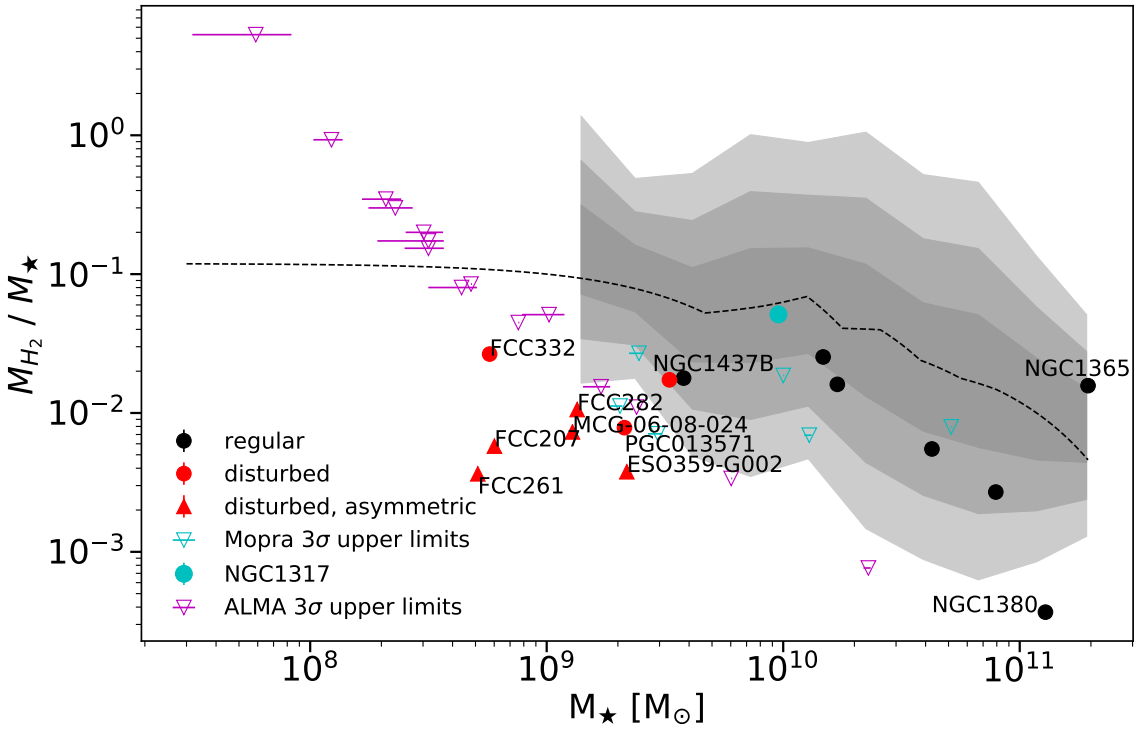

Figure 2.8: Molecular gas fraction, as a function of stellar mass. Black dots are regular galaxies, red markers are disturbed galaxies. The shape of the marker indicates whether the galaxy may be undergoing ram pressure stripping, based on visual inspection. ALMA upper limits are shown as magenta open triangles, and Mopra upper limits as cyan open triangles. The Mopra detection of NGC1317 is shown as a cyan dot. Within the shaded area, the dashed line represents the expected gas fraction based on Saintonge et al. (2017). The three shades of grey indicate the 1, 2, and 3 σ levels (from the inside out) of the xCOLD GASS data. Outside the shaded area the dashed line is based on linear extrapolation (in log space). Galaxies with high deficiencies and the galaxies that were classified as disturbed are labelled. There is a discrepancy between the expected gas fractions and the gas fractions observed, especially the disturbed galaxies are H_2 deficient compared to field galaxies.

Common name	FCC #	Reg./dist.	Gauss/box	$b_{\rm maj}; b_{\rm min}; b_{\rm PA}$	rms	Δv	$\int S_\nu d\nu$	$\log_{10}(M_{\rm H_2})$	Deficiency
-	-	-	-	(”; ”; $^{\rm o}$)	(mJy beam^{-1})	(km s^{-1})	(Jy km s^{-1})	($M_\odot$)	(dex)
(1)	(2)	(3)	(4)	(5)	(6)	(7)	(8)	(9)	(10)
FCC32	32	-	G	2.4; 1.8; 84	2.6	50	$\leq$ 2.1	$\leq$ 8.02	$\leq$ 0.01
FCC44	44	-	G	2.8; 2.0; 85	2.4	50	$\leq$ 1.9	$\leq$ 8.48	$\leq$ 1.62
NGC1351A	67	R	B	2.6; 2.0; 61	3.6	250 $\pm$ 20	19.9 $\pm$ 2.0	7.83 $\pm$ 0.07	-0.54 $\mp$ 0.01
MGC-06-08-024	90	D	G	3.3; 2.4; 71	3.0	31 $\pm$ 7	1.71 $\pm$ 0.22	6.97 $\pm$ 0.07	-1.11 $\mp$ 0.01
FCC102	102	-	G	2.8; 2.0; 85	2.4	50	$\leq$ 1.9	$\leq$ 8.00	$\leq$ 0.77
ESO358-G015	113	-	G	3.1; 2.1; 71	3.2	50	$\leq$ 2.5	$\leq$ 7.61	$\leq$ -0.36
ESO358-16	115	-	G	3.3; 2.3; 73	3.3	50	$\leq$ 2.6	$\leq$ 7.66	$\leq$ 1.36
FCC117	117	-	G	2.8; 2.0; 84	2.4	50	$\leq$ 1.9	$\leq$ 7.53	$\leq$ 1.04
FCC120	120	-	G	2.8; 2.0; 84	2.4	50	$\leq$ 1.9	$\leq$ 8.32	$\leq$ 0.44
NGC1365	121	R	B	2.4; 2.0; 12	12	940	1221 $\pm$ 20	9.49 $\pm$ 0.04	0.53 $\pm$ 0.01
NGC1380	167	R	B	2.6; 2.0; 80	3.6	660 $\pm$ 20	18.1 $\pm$ 1.8	7.67 $\pm$ 0.06	-1.39 $\mp$ 0.01
FCC177	177	-	G	3.3; 2.4; 73	3.3	50	$\leq$ 2.6	$\leq$ 8.14	$\leq$ -0.99
NGC1386	179	R	B	3.3; 2.4; 72	2.9	540 $\pm$ 20	88.9 $\pm$ 8.9	8.37 $\pm$ 0.04	-0.61 $\mp$ 0.01
NGC1387	184	R	B	3.3; 2.4; 72	3.0	200 $\pm$ 20	83.3 $\pm$ 8.3	8.33 $\pm$ 0.04	-0.74 $\mp$ 0.01
FCC198	198	-	G	2.8; 2.0; 84	2.4	50	$\leq$ 1.9	$\leq$ 7.82	$\leq$ 2.17
FCC206	206	-	G	2.8; 2.0; 83	2.5	50	$\leq$ 2.0	$\leq$ 7.34	$\leq$ 0.71
FCC207	207	D	G	2.8; 2.0; 83	2.6	11 $\pm$ 3	0.6 $\pm$ 0.3	6.54 $\pm$ 0.22	-1.33 $\mp$ 0.01
NGC1427A	235	-	G	2.9; 2.3; 80	2.2	50	$\leq$ 1.7	$\leq$ 7.42	$\leq$ -1.21
FCC261	261	D	G	2.9; 2.0; 84	2.6	9.5 $\pm$ 3.9	0.27 $\pm$ 0.55	6.27 $\pm$ 0.88	-1.47 $\mp$ 0.01
PGC013571	263	D	G	3.3; 2.4; 72	3.1	54 $\pm$ 10	7.0 $\pm$ 0.71	7.22 $\pm$ 0.05	-1.02 $\mp$ 0.01
FCC282	282	D	G	3.2; 2.4; 70	3.1	36 $\pm$ 4	3.0 $\pm$ 0.34	7.15 $\pm$ 0.05	-0.95 $\mp$ 0.01
NGC1437A	285	-	G	3.0; 2.1; 70	3.0	50	$\leq$ 2.3	$\leq$ 7.83	$\leq$ -0.85
NGC1436	290	R	B	2.6; 2.0; 79	3.2	260 $\pm$ 20	97.6 $\pm$ 9.8	8.44 $\pm$ 0.05	-0.44 $\mp$ 0.01
FCC302	302	-	G	2.8; 2.0; 83	2.5	50	$\leq$ 2.0	$\leq$ 8.82	$\leq$ 0.78
FCC306	306	-	G	2.8; 2.0; 84	2.4	50	$\leq$ 1.9	$\leq$ 8.10	$\leq$ -0.11

NGC1437B	308	D	G	3.2; 2.4; 69	3.1	91 ± 14	17 ± 1.67	7.76 ± 0.04	-0.59 ∓ 0.01
ESO358-G063	312	R	B	2.6; 2.0; 80	3.3	380 ± 20	131.5 ± 13.2	8.57 ± 0.05	-0.34 ∓ 0.01
FCC316	316	-	G	2.8; 2.0; 82	2.7	50	$\leq$ 2.1	$\leq$ 7.31	$\leq$ 0.53
FCC332	332	D	G	2.8; 2.0; 84	2.3	30 ± 5	2.0 ± 0.25	7.18 ± 0.06	-0.61 ∓ 0.01
ESO359-G002	335	D	G	3.2; 2.4; 69	3.1	37 ± 5	2.0 ± 0.24	6.92 ± 0.05	-1.33 ∓ 0.01

Table 2.5 Observed and derived properties of the AlFoCS targets.

Notes: 1: Common name of the galaxy; 2: Fornax Cluster Catalogue number of the galaxy; 3: Whether the morphology and kinematics of the molecular gas in the galaxy are regular (R) or disturbed (D) (see §2.5.1); 4: Whether the line profile of the CO(1-0) line is best described by a Gaussian (G) or a boxy (B) profile (see §4.3.1); 4/7: Upper limits were determined assuming a Gaussian line profile with a FWHM of 50 km s^{-1}(see §2.4.3); 5: Beam major axis, minor axis and position angle; 6: the typical rms in a single channel in the line-free channels of the data cube; 7: the width of the CO integrated spectrum (see §4.3.1); 8: the total CO emission; 9: total M_{H_2} mass derived from the CO emission (see §4.3.1); 10: H_2 deficiency, defined as $M_{H_2,\mathrm{observed}} - M_{H_2,\mathrm{expected}}$ (see §4.3.1).

2.5 DISCUSSION

2.5.1 GAS MORPHOLOGIES & KINEMATICS

The galaxies detected here can be divided into two categories: galaxies with disturbed molecular gas morphologies and regular systems. Whether a galaxy is morphologically disturbed or regular is determined by visual inspection of the moment 0 and 1 maps (see Figures 2.3, 2.4, Appendix A.1, and Table 2.5). Non-disturbed galaxies have molecular gas that is concentrated symmetrically around the galactic centre, whereas galaxies with disturbed morphologies contain molecular gas that is asymmetric with respect to the (optical) centre of the galaxy. It sometimes has a very irregular shape, and, in some cases, even extends beyond the galaxy's stellar body (see §A). Of the galaxies detected here, eight are classified as disturbed galaxies, and seven have regular molecular gas morphologies.

The galaxies with morphologically disturbed molecular gas reservoirs also have disturbed molecular gas kinematics. Looking at the velocity maps in Figure 2.3 and the regular galaxies in Appendix A.1, regular galaxies follow a standard "spider diagram" shape, indicative of a regular rotation. Disturbed galaxies, on the other hand, have irregular velocity maps, indicating the presence of non-circular motions. In some cases rotation is still present (in NGC1437B and PGC013571, for example, Figures A.12 and A.9, respectively), in other cases no rotation can be identified (for example, ESO359-G002 and FCC332, Figures A.15 and A.14, respectively). This is also reflected in the PVDs, which look like smooth rotation curves for the regular galaxies, but have very asymmetric and irregular shapes for the disturbed galaxies. Maps of the CO(1-0) linewidth of the regular galaxies often reveal symmetric structures such as rings or spiral arms (see, for example, Figures A.13). For disturbed galaxies this is, again, much more irregular (for example, Figure A.12). A further discussion of each galaxy in detail can be found in Appendix A.

2.5.2 STRIPPING AND GAS STIRRING IN FORNAX IN COMPARISON WITH THE FIELD

There is a clear mass split between galaxies with regular and disturbed molecular gas morphologies, where all galaxies with stellar masses below $3 \times 10^9 M_\odot$ have disturbed molecular gas (see Figure 2.8). In the absence of a comparable field sample tracing molecular gas at these stellar masses, I compare this result to the Local Irregulars That Trace Luminosity Extremes, The HI Nearby Galaxy Survey (LITTLE THINGS, Hunter et al. 2012). LITTLE THINGS is a multi-wavelength survey of 37

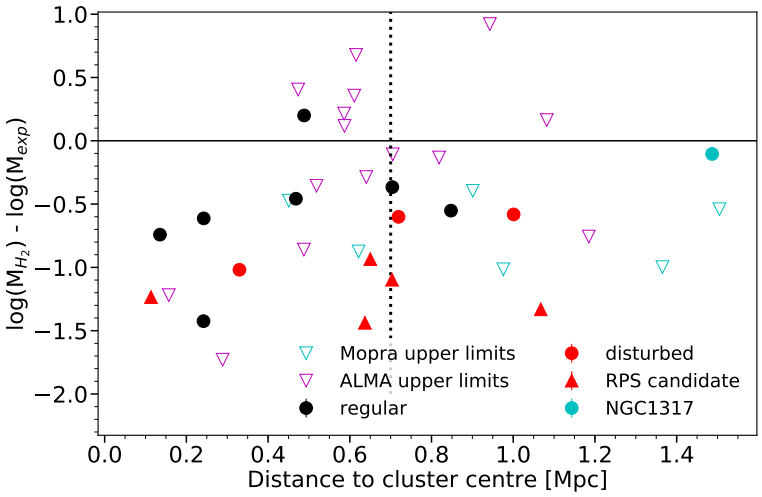

Figure 2.9: Molecular gas mass deficiencies (see §2.4.4) as a function of the (projected) distance to the cluster centre (defined as the location of NGC1399). Marker shapes and colours are the same as in Figure 2.8. There is no clear correlation between a galaxy's H_2 deficiency and its distance from the cluster centre.

dwarf irregular and 4 blue compact nearby ($\leq$ 10.3 Mpc) (field) dwarf galaxies that is centred around HI-line data, obtained with the National Radio Astronomy Observatory (NRAO) Very Large Array (VLA). It has high sensitivity ($\leq$1.1 mJy beam^{-1} per channel), high spectral resolution ($\leq$2.6 km s^{-1}), and high angular resolution ($\sim$6"), resulting in detailed intensity and velocity maps. If the molecular gas in a galaxy is disturbed, one expects their atomic gas to be disturbed as well. Therefore this comparison, although not ideal, is still meaningful. Categorising the LITTLE THINGS dwarfs in the same way as the AlFoCS galaxies (see above, §2.5.1), only about half of these dwarf galaxies show disturbed HI kinematics and morphologies. Since all AlFoCS galaxies with stellar masses lower than $3 \times 10^9 M_\odot$ have disturbed morphologies and kinematics, this indicates that these low mass galaxies are more disturbed than their counterparts in the field. This suggests that Fornax is still a very active environment, having significant effects on its members. Furthermore, it implies that less massive galaxies are more susceptible to the effects of the cluster environment, likely because of their shallower potential wells. This difference in gas deficiency between massive and less massive galaxies is also seen in simulations (e.g. van de Voort et al., 2017), and is likely driven by their shallower potential wells.

2.5.3 RAM PRESSURE STRIPPING OR GALAXY-GALAXY INTERACTIONS?

The AlFoCS galaxies with disturbed molecular gas reservoirs are H_2 deficient compared to field galaxies (see Figure 2.8 and §2.4.4). This confirms the result from Horellou et al. (1995), who find that the CO emission in Fornax cluster galaxies is relatively weak, and the H_2 masses relatively low. AlFoCS galaxies have deficiencies up to -1.1 dex (see §2.4.4). These deficiencies are higher than those found in Boselli et al. (2014b), who find H_2 deficiencies of a factor $\sim$2 for the most HI deficient galaxies in the Virgo cluster. The molecular gas in the most deficient AlFoCS galaxies is centrally located and asymmetric. Mechanisms that are possibly responsible for this include ram pressure stripping and galaxy-galaxy interactions.

Two of the irregular galaxies, MCG-06-08-024 and ESO359-G002, show molecular gas tails that extend well beyond the brightest parts of the galaxy's stellar body (see §A). Together with the dwarfs FCC207 and FCC261, they have the lowest gas fractions of the disturbed galaxies (see Figure 2.8 and Table 2.5). In both cases, this tail is aligned with the direction of the cluster centre (see §A). This, in combination with their low gas fractions, can be interpreted as a sign of ongoing ram pressure stripping. This is striking, since RPS is not thought to affect the molecular gas much, as it is bound much more tightly to the galaxy than the atomic gas. Moreover, RPS is thought to be less important in the Fornax cluster than in, for example, the Virgo cluster, given its relatively small size and large density of galaxies (see §2.1).

The fact that the gas tails align with the direction of the cluster centre is, however, not necessarily proof that ram pressure stripping is in play. There are confirmed RPS tails pointing in all directions, even nearly perpendicular to the direction of the cluster centre (e.g. Kenney et al., 2014). This is also seen in simulations (e.g. Yun et al., 2018). Moreover, the kinematics of these galaxies are more irregular than expected based on RPS alone, which suggests that a past galaxy-galaxy interaction may be (co-)responsible for this. In deep FDS images (Iodice et al. 2018, submitted to A&A), MCG-06-08-024 shows a very disturbed morphology in the outskirts, which could indicate a past galaxy-galaxy interaction. Furthermore, these RPS candidates are not necessarily close to the cluster centre, nor do they have particularly high velocities, as one might expect for galaxies that are undergoing RPS. However, Jaffé et al. (2018), recently found galaxies undergoing RPS all over the cluster, and also in a wide variety of locations in the velocity phase-space. Simulations by Yun et al. (2018) show that ram pressure stripped galaxies are more common beyond half the

virial radius, where most of the AlFoCS galaxies with disturbed molecular gas are located. Both galaxies discussed here have relatively low masses and shallow potential wells, so they are expected to be susceptible to ram pressure stripping. Yun et al. (2018) also find that galaxies with shallow potential wells can experience extended stripping due to weak ram pressure. Based on these data alone, it is difficult to say whether it is ram pressure affecting these galaxies. The combination with additional data, for example a study of the stellar kinematics of these galaxies, would allow us to distinguish between galaxy-galaxy interactions and ram pressure stripping with more certainty.

Several other galaxies, such as FCC282 and FCC332, also show asymmetric molecular gas reservoirs, and were therefore labelled as possible RPS candidates. Asymmetric molecular gas distributions and molecular gas tails can, however, also be the result of galaxy-galaxy interactions. Other galaxies, such as NGC1437B and FCC261, have relatively massive neighbours that are close to them on the sky, which could mean that they are experiencing tidal forces. NGC1437B is the least H_2 deficient of the disturbed galaxies (see Figure 2.8). Looking at its velocity map and PVD (see Figure A.12), one can see that it has maintained its rotation and still shows a coherent structure, but it appears to be influenced by a pull on its south side. Although a second tail at the north side is missing, this could be an indication of an ongoing tidal interaction. Although the extension of the molecular gas on the south side of the galaxy does not align with the direction of the cluster centre, it is also possible that this asymmetry is caused by RPS, depending on the galaxy's orbit through the cluster (see above). It is currently still relatively far out, located approximately at the virial radius on the sky.

In Figure 2.9, there appears to be no correlation between a galaxy's H_2 mass deficiency and its distance from the cluster centre. Although this result suffers from small number statistics, there are a few other possible explanations for this:

- We are looking at a 2D projection of the cluster, the positions of the galaxies along the line of sight are not taken into account.

- Lower mass galaxies end up more H_2 deficient than their higher mass counterparts, because of their shallower potential wells. The total H_2 mass per galaxy is therefore more a function of their intrinsic mass than of their location in the cluster.

- The responsible mechanism is galaxy-galaxy interactions. While RPS is much more effective in the cluster centre, depending quadratically on the density of

the hot halo, galaxy-galaxy interactions are, relatively, more common at the outskirts of the cluster. If the latter play a role, one would expect less of a trend in the gas deficiencies as one moves away from the cluster centre.

- The galaxies are moving through the cluster, so if they experienced RPS when they were near its centre, they can have moved to the outskirts of the cluster since then.

- The galaxies were selected to have FIR emission, and therefore galaxies that lost all their gas are excluded from the sample.

2.5.4 DWARFS

Among the detections are several galaxies with low stellar masses, that can be classified as early-type dwarfs. Four of these have stellar masses $M_\star \leq 1.0 \times 10^9 M_\odot$. It was long thought that early-type dwarf galaxies in cluster environments would not have a molecular ISM, due to their expected short stripping timescales and shallow potentials.

The currently accepted theory is that these galaxies are the remnants of low mass late-type galaxies that have fallen into the cluster. This hypothesis is supported by the presence of visible structures such as spiral arms, bars, disks, and nuclei and cores (Lisker et al., 2006a,b; Jerjen et al., 2000; Barazza et al., 2002; De Rijcke et al., 2003), the rotational support of their stellar kinematics (Pedraz et al., 2002; Ryś et al., 2013), and the detection of significant amounts of gas and dust in some of them (Conselice, 2002; di Serego Alighieri et al., 2007; De Looze et al., 2010, 2013; di Serego Alighieri et al., 2013).

It is also possible that they were already early-type dwarf galaxies to begin with, but re-accreted material through tidal interactions either with the intracluster medium or with another galaxy, which could also trigger new star formation. Inconsistencies in the observations supporting the infalling-spiral scenario (Miller et al., 1998; Sánchez-Janssen & Aguerri, 2012) may add to the favourability of this idea. However, the limited spatial resolution of most of these studies to date make it hard to draw strong conclusions.

De Looze et al. (2013) observed "transition-type dwarf galaxies" (TTDs) in the Virgo cluster. These galaxies are dwarfs that have an apparent early-type morphology, but still show dust emission and thus evidence of a cold ISM and star formation. They posit that TTDs are in the process of having their ISM removed by the cluster environment, transforming them from late-type dwarfs to quiescent ones (see Boselli

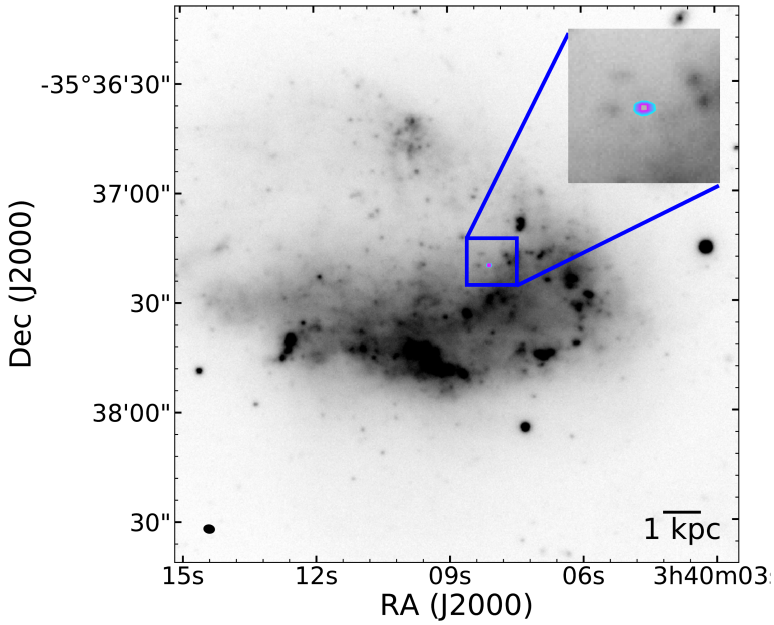

Figure 2.10: 3 mm continuum emission in the observation of NGC1427A, overplotted on an optical (g-band) image from the FDS (see §2.3.3). The emission is shown as 10 coloured contours; the lower (outer) contour level equals 4σ, the inner one 5.6σ. The emission likely originates from a background source.

et al. 2008; Koleva et al. 2013 for a more detailed description of the definition and identification of TTDs). They find that many of the dust properties of these objects lie in between what is expected for early-type galaxies and for late-type galaxies, supporting the hypothesis that they are infalling low mass spirals that are in the process of being quenched. The presence of central cores and dust concentrations are additional evidence in favour of this outside-in gas removal theory.

I suspect that the dwarf galaxies observed here are TTDs moving through the cluster and being stripped of their gas and thus in the process of being quenched. Each dwarf galaxy observed has a very disturbed and irregular molecular ISM, both morphologically and kinematically, suggesting that they are being stripped by the hot intracluster gas (for example MCG-06-08-024 and ESO359-G002, see Figures 2.4 and A.15), or being torn apart by tidal forces. This is in favour of the hypothesis that they are the remnants of infalling gas-rich galaxies. The observation that galaxies with disturbed molecular gas reservoirs seem to favour locations around the virial radius (see §4.5) supports the idea that these dwarfs are starting their first passage through the cluster, or have just crossed it for the first time.

2.5.5 NGC1427A

NGC1427A has been proposed to be undergoing ram pressure stripping (Chanamé et al., 2000; Mora et al., 2015), although recent HI observations by Lee-Waddell et al. (2018) suggest that previous tidal interactions are responsible for the galaxy's irregular shape, and for star formation triggering in the disk. It was detected in all five *Herschel* bands (Fuller et al., 2014). Based on the above observations, the expectation was to detect CO in this galaxy. However, none was detected.

NGC1427A is vigorously star forming. It is expected to have approximately solar metallicity, based on both its stellar mass and analysis of the colours of its star clusters (Mora et al., 2015). Its atomic hydrogen mass is $M_{\rm HI} = 2.1 \times 10^9 M_\odot$ (Lee-Waddell et al., 2018), I find an upper limit on its molecular hydrogen mass of $M_{\rm H_2} = 2.63 \times 10^7$ M$_\odot$, and its SFR is 0.05 ± 0.03 M$_\odot$ yr^{-1} (Mora et al., 2015). This leads to the surprisingly high atomic-to-molecular gas ratio $\frac{M_{\rm HI}}{M_{\rm H_2}} > 79$ and short depletion time $\frac{M_{\rm H_2}}{\rm SFR}$ <1.3 Gyr.

It is possible that the flux is resolved out, since the galaxy extends well beyond the largest recoverable scale of 25" (see Figure 2.10). However, as CO emission is broken between velocity channels due to its motion within the galaxy, in the mosaic one would still expect to see some emission.

If the CO emission has not been resolved out, this makes the non-detection of CO surprising. A natural explanation for this would be if the galaxy underwent a merger or other event which has diluted its gas phase metallicity. I test this by deriving the gas-phase metallicity from the measured gas-to-dust ratio. This is done using the empirical relation between the gas-to-dust ratio and metallicity from Rémy-Ruyer et al. (2014, Figure 4 and Table 1) for galaxies in the low metallicity regime, where I expect the galaxy to be. Using the relation for the higher metallicity regime instead would result in an even lower metallicity, thus only amplifying the analysis below. I use the relation for a metallicity-dependent $X_{\rm CO}$. Rewriting for the metallicity gives:

$$12 + \log({\rm O/H}) = \frac{-\left(\log\left(\frac{\rm G}{\rm D}\right) - b\right)}{\alpha_{\rm L}} + x_\odot \tag{2.4}$$

where $b = 0.96$, $\alpha_{\rm L} = 3.10 \pm 1.33$, and $x_\odot = 8.69$ the solar metallicity (Asplund et al., 2009). The gas-to-dust ratio is derived using the HI and H_2 masses stated above, and a dust mass of $4.2 \times 10^6 M_\odot$ from Fuller et al. (2014). Since our upper limit on the H_2 mass depends on $X_{\rm CO}$, I combine the relation above and that between $X_{\rm CO}$ and metallicity (Equation 2.4.3) to estimate the metallicity (and thus the resulting $X_{\rm CO}$) in this object. The resulting metallicity, assuming these relations hold, is $12 + \log({\rm O/H})$

= 8.12 (or 0.27 $Z_{\odot}$). This is significantly lower than the metallicity derived from the stellar mass ($12 + \log(\mathrm{O/H}) = 8.71$; 1.05 $Z_{\odot}$, see §4.3.1), and that found for young star clusters by Mora et al. (2015), who find values of ∼0.4-1 $Z_{\odot}$. It implies an X_{CO} of $\sim 18 \times 10^{20}$ cm^{-2} (K km s^{-1})$^{-1}$ (see §4.3.1), in which case the H_2 mass limit one can set in this object increases to $\sim 2.1 \times 10^8$ $M_{\odot}$. These revised values for the atomic-to-molecular gas ratio and the molecular gas depletion time yield >10 and <4.2 Gyr respectively, much more consistent with canonical values.

I do detect a 3 mm continuum source in our NGC1427A observations. This is shown in Figure 2.10, where the continuum is overplotted as coloured contours on a g-band image from the FDS, similar to Figure 2.7. The emission originates from a source towards the north of NGC1427A, slightly to the east side relative to its centre. There are two possible candidates for its origin: either the emission comes from a background source, or from an AGN associated with NGC1427A, that has been moved off-centre as a result of a galaxy-galaxy interaction. The latter interpretation seems quite speculative. However based on the information currently available and the galaxy's turbulent history, it is a possibility. In case the continuum originates from a background source, one would expect to see an optical counterpart in the optical FDS image. These images are quite deep, and can detect point sources down to ∼25-26 mag. However, no optical counterpart is detected. Moreover, no emission lines are detected in archival MUSE observations of this area. Thus, if it is indeed a background object, it must be heavily obscured by dust.

2.6 Conclusions / summary

I have presented the first results from the ALMA Fornax Cluster Survey (AlFoCS), a complete survey of the CO(1-0) in all Fornax cluster galaxies above $> 3 \times 10^8$ $M_{\odot}$ that contain dust (Fuller et al., 2014) and/or HI (Waugh et al. 2002, Loni et al. in prep. based on ATCA data). The goal of this survey is to study the effects of the cluster environment on the cold molecular gas inside galaxies. I present moment zero, one, and two maps, as well as position-velocity diagrams, spectra, and comparisons with optical images for all galaxies detected. Furthermore I estimate H_2 masses and derive the corresponding H_2 deficiencies compared to field galaxies. The main conclusions from this initial analysis are:

- The cold molecular gas in galaxies is indeed affected by the cluster environment. All galaxies with stellar masses below $3 \times 10^9 M_{\odot}$ (8 out of 15 detected galaxies) have morphologically and kinematically disturbed gas reservoirs. "Disturbed"

means that their molecular gas is distributed asymmetrically with respect to the optical centre of the galaxy, sometimes with irregular shapes or large tails. The moment one maps and PVDs show irregular motions, and in most cases no rotation can be identified. This suggests that Fornax is still a very active environment, having a significant impact on its members. More massive galaxies are probably experiencing the same interactions, however the molecular gas may not be affected in the same way, because of their deeper potential wells.

- Continuum was detected in four of the galaxies observed. In three of them it is likely associated with AGN activity. In one case (NGC1427A) the emission does not originate from the centre of the galaxy, but rather from the galaxy's edge. It is unclear whether the source of this emission is a background object or an AGN that was moved off-centre due to a recent galaxy-galaxy interaction.

- Galaxies with regular CO emission have an average H_2 deficiency of -0.50 dex, and galaxies with disturbed CO emission have an average H_2 deficiency of -1.1 dex. AlFoCS galaxies with disturbed molecular gas reservoirs are therefore, with few exceptions, significantly deficient in H_2 compared to their counterparts in the field (as probed by the xCOLD GASS sample).

- Whether a galaxy has a molecular gas reservoir, and whether that reservoir is disturbed or regular, appears to be independent of the galaxy's location within the cluster. However, the sample size is small.

- Two molecular gas tails were detected, that extend beyond the galaxy's stellar body and align with the direction of the cluster centre. These galaxies are possibly undergoing ram pressure stripping. Relatively high H_2 deficiencies support this explanation. Several other galaxies have molecular gas reservoirs that are asymmetric with respect to their stellar bodies as well, and are therefore possible RPS candidates, however it is difficult to draw definite conclusions from these data alone.

To be able to really distinguish between ram pressure stripping and galaxy-galaxy interactions, one would need to compare the stellar kinematics (derived from

e.g. MUSE observations: Sarzi et al. 2018) of the galaxies in question with the kinematics of their disturbed molecular gas. If both the molecular gas and stars show similar kinematics, ram pressure stripping can be ruled out. If only the molecular gas kinematics are disturbed, on the other hand, one can confirm that ram pressure stripping plays a role. This will be the aim of a future work. Similarly, I will compare my data with those of the *Herschel* Fornax Cluster Survey (Fuller et al., 2014) to compare the molecular gas and dust distributions, and derive gas-to-dust ratios for the galaxies in our sample.

In conclusion, the detection of a relatively high number of galaxies with disturbed molecular gas reservoirs and H_2 deficiencies of sometimes more than an order of magnitude reveal the importance of the cluster environment for even the tightly bound molecular gas phase, and motivate further study of environmental effects on molecular gas in nearby clusters.

Chapter 3
AlFoCS + Fornax3D: resolved star formation in the Fornax cluster with ALMA and MUSE

A dazzling symphony of cosmic strings

I feel the pulse, vibrating just out of reach
The music of space

Ayreon, *"The Theory of Everything Part 1"*

I combine data from ALMA and MUSE to study the resolved (∼300 pc scale) star formation relation (star formation rate vs. molecular gas surface density) in cluster galaxies. Our sample consists of 9 Fornax cluster galaxies, including spirals, ellipticals, and dwarfs, covering a stellar mass range of $\sim 10^{8.8} - 10^{11}$ $M_{\odot}$. CO(1-0) and extinction corrected Hα were used as tracers for the molecular gas mass and star formation rate, respectively. I compare my results with Kennicutt (1998) and Bigiel et al. (2008). Furthermore, I create depletion time maps to reveal small-scale variations in individual galaxies. I explore these further in FCC290, using the 'uncertainty principle for star formation' (Kruijssen & Longmore, 2014a) to estimate molecular cloud lifetimes, which are found to be short (<10 Myr) in this galaxy. Galaxy-averaged depletion times are compared with other parameters such as stellar mass and cluster-centric distance. I find that the star formation relation in the Fornax cluster is close to those from Kennicutt (1998) and Bigiel et al. (2008), but overlaps mostly with the shortest depletion times predicted by Bigiel et al. (2008). This slight decrease in depletion time is mostly driven by dwarf galaxies with disturbed molecular

gas reservoirs close to the virial radius. In FCC90, a dwarf galaxy with a molecular gas tail, I find that depletion times are a factor $\gtrsim 10$ higher in its tail than in its stellar body.

3.1 INTRODUCTION

The star formation relation links the observed star formation rate surface density $\Sigma_{\rm SFR}$ to the total gas surface density $\Sigma_{\rm HI+H_2}$. It was first shown by Schmidt (1959) and Kennicutt (1998), who found that, on galaxy scales, the two are related by the power law $\Sigma_{\rm SFR} \propto (\Sigma_{\rm HI+H_2})^n$ where $n = 1.4 \pm 0.15$. They used integrated measurements for entire spiral and starburst galaxies, ∼40% of which are located in the Virgo cluster, and they used Hα to trace their star formation. Since this discovery, many others have studied this relation in a variety of contexts. It has, for example, been shown that a similar, possibly even stronger correlation exists between the molecular gas surface density $\Sigma_{\rm H_2}$ and $\Sigma_{\rm SFR}$ (e.g. Wong & Blitz 2002; Leroy et al. 2008; Bigiel et al. 2008; Schruba et al. 2011; de los Reyes & Kennicutt 2019). Bigiel et al. (2008) studied a more diverse sample of galaxies on sub-kpc scales, and found a linear relation between both surface densities on these smaller scales. Other studies focused on (variations within) individual galaxies (e.g. Ford et al. 2013; Utomo et al. 2017), or compared results for individual molecular clouds to those for entire galaxies (e.g. Lada et al. 2012). The Physics at High Angular Resolution in Nearby GalaxieS survey (including PHANGS-ALMA, PI: E. Schinnerer, e.g. Leroy et al., in prep., and PHANGS-MUSE, PI: E. Schinnerer, e.g. Kreckel et al. 2019) will study the star formation relation in nearby, face-on spiral galaxies with unprecedented resolution (<100 pc). The K98 relation has recently been revisited by de los Reyes & Kennicutt (2019), who showed that this relation is still a good approximation for the star formation relation (they find a power law with $n = 1.41$, with similar dispersion). Moreover, they obtain this relation from spiral galaxies only, not including starbursting galaxies. They also find that $\Sigma_{\rm SFR}$ scales roughly linearly with H_2, while it only weakly depends on HI. This is in agreement with the resolved studies described above.

While the initial sample from which the star formation relation was derived mainly consisted of spiral galaxies and galaxies located in the field, it has been shown to hold for samples consisting of cluster spiral galaxies exclusively. For example, Vollmer et al. (2012) investigated the influence of environment on the gas surface density and depletion time in 12 spiral galaxies in the Virgo cluster on a pixel-by-pixel (of the order kpc in size) basis. The depletion time ($t_{\rm dep}$) is the ratio of the

molecular gas surface density and the star formation rate (the star formation efficiency, SFE, is the inverse of this ratio). While they find that depletion times are mostly unaffected, they do report increased depletion times in the extraplanar gas of three spiral galaxies, likely caused by the loss of gravitational confinement of stripped gas and the associated pressure of the disk. Their work was an extension of the work by Fumagalli & Gavazzi (2008), who showed that the bulk of the star formation in spiral galaxies is fuelled by a molecular interstellar medium (ISM), but that the atomic gas is important for the star formation activity in the outer parts of the disks.

The star formation relation has been studied in several Virgo cluster galaxies, e.g. NGC4501, a galaxy undergoing RPS, and NGC4567/68, an interacting pair, by Nehlig et al. (2016), and NGC4330, NGC4402, and NGC4522, all spirals undergoing RPS, by Lee et al. (2017). While no significant deviations from the K98 relations are found, some regions with modified depletion times were observed in compressed parts of RPS galaxies and the interacting pair. Furthermore, they found locally increased SFRs on the sides of the galaxies where the intracluster medium pressure acts, and the opposite on the other side.

The GAs Stripping Phenomena in galaxies (GASP) with the Multi Unit Spectroscopic Explorer (MUSE) survey targeted 114 RPS galaxies, specifically to study gas removal processes in galaxies in different environments (Poggianti et al., 2017). In this context, studies by Vulcani et al. (2018), Ramatsoku et al. (2019), and Moretti et al. (2018) have found that RPS can enhance the SFR in galaxy disks by 0.2 dex, and that depletion times in the disks of RPS galaxies are decreased, while they are increased in their tails (with a difference of a factor $\sim$10).

So far, studies of the star formation relation in cluster galaxies have been performed almost exclusively on spiral galaxies in the Virgo cluster. In this Chapter, I will study the star formation relation in 9 Fornax cluster galaxies, in the context of the ALMA Fornax Cluster Survey (AlFoCS).

Our sample is diverse, containing both spirals and ellipticals, as well as dwarf galaxies. In Chapter I, I used ALMA observations of ^{12}CO(1-0) to create maps of the molecular gas surface density at a resolution of $\sim3''$ ($\sim$0.3 kpc at the distance of the Fornax cluster). In this Chapter I combine these with Hα observations from MUSE (Bacon et al., 2010), from the Fornax3D project (F3D, Sarzi et al. 2018; Iodice et al. 2019b), binned to the same resolution as the maps from ALMA, to create maps of the star formation rate surface density. F3D targeted all galaxies from the Fornax Cluster Catalogue (Ferguson, 1989) brighter than $m_B = 15$ within or close to the virial radius ($R_{\rm vir} = 0.7$ Mpc; Drinkwater et al. 2001). Both are combined here to study the star formation relation in these galaxies on a pixel-by-pixel basis, and to

create maps of their depletion times. I compare the outcome with both the integrated K98 relation, and the one derived for kpc sized regions by B08. Since the sample, resolution, and use of molecular gas makes this study more similar to the one by B08, I expect my results to be close to this relation, should the cluster environment have no or little effect on the depletion times. I compare the galaxy-average depletion times with other parameters, i.e. stellar mass, stellar mass surface brightness, and (projected) distance from the cluster centre. Where possible, I compare the results to a field control sample.

For the purpose of consistency with F3D publications, I adopt the distance to the Fornax cluster (20 Mpc, Blakeslee et al. 2009) as a common distance to all galaxies. The cluster has a virial radius of 0.7 Mpc (Drinkwater et al., 2001).

This Chapter is structured as follows: in §4.2 the sample, observations, and data reduction are described. In §4.3 I describe how surface density maps and $\Sigma_{\rm H_2} - \Sigma_{\rm SFR}$ relations are obtained from the data. The results are shown in §4.5. These include the derived star $\Sigma_{\rm H_2} - \Sigma_{\rm SFR}$ relations and depletion time maps, as well as the relations between depletion times and various other parameters, such as stellar mass. In §3.5 the 'uncertainty principle of star formation' is applied to the face-on, flocculent spiral FCC290 to estimate its molecular cloud lifetimes and compare them to those in field galaxies. The results are discussed in §4.7, and finally summarised in §5.1.

3.2 OBSERVATIONS AND DATA REDUCTION

3.2.1 THE SAMPLE

Our sample consists of all Fornax cluster galaxies for which both CO and Hα maps are available, from AlFoCS and F3D, respectively. AlFoCS targeted all Fornax cluster galaxies that show signs of the presence of an ISM, as indicated by either far-infrared observations from the *Herschel* Space Observatory (Pilbratt et al., 2010), HI observations (from Waugh et al. 2002 and Loni et al. in prep., based on Australia Telescope Compact Array data), or both. There are 9 overlapping galaxies in these surveys. This means that 6 galaxies detected in Chapter I are not included here: the large spiral FCC121 (NGC1365), the edge-on spiral FCC67 (NGC1351A), and four dwarf galaxies with disturbed molecular gas reservoirs.

As F3D targeted only the brightest galaxies ($m_B < 15$), and AlFoCS is mostly IR selected, the sample is likely biased towards higher-mass, star forming galaxies. As we have seen in Chapter I, the lower-mass galaxies are the ones that are affected

Table 3.1 Key properties of the galaxies in the sample.

FCC	Common name	$M_\star$	Type	D	Gas distribution	M_{H_2}	H_2 def.	SFR	$\mu_{\star,e}$
-	-	($10^{10} M_\odot$)	-	(kpc)	-	(log $M_\odot$)	(dex)	($M_\odot$ yr^{-1})	(log $M_\odot$ kpc^{-2})
(1)	(2)	(3)	(4)	(5)	(6)	(7)	(8)	(9)	(10)
90	MGC-06-08-024	$0.08^\dagger$	E4 pec	595	D	6.97 ± 0.07	-1.21	0.035	$^{**}5.0 \pm 0.6 \times 10^8$
167	NGC1380	$9.85^\dagger$	S0/a	219	R	7.67 ± 0.06	-1.56	0.000	$^{\star}8.0 \times 10^8$
179	NGC1386	$1.58^\dagger$	Sa	226	R	8.37 ± 0.04	-0.70	0.155	$1.20 \pm 0.04 \times 10^9$
184	NGC1387	$4.70^\dagger$	SB0	111	R	8.33 ± 0.04	-0.85	0.008	$^{\star}2.21 \times 10^9$
207	FCC207	0.06*	-	113	D	6.54 ± 0.22	-1.43	0.004	$^{**}2.2 \pm 0.4 \times 10^8$
263	PGC013571	$0.04^\dagger$	SBcdIII	293	D	7.22 ± 0.05	-1.07	0.282	$^{**}2.0 \pm 0.3 \times 10^8$
290	NGC1436	$0.64^\dagger$	ScII	389	R	8.44 ± 0.05	-0.53	0.127	$1.82 \pm 0.02 \times 10^8$
308	NGC1437B	$0.04^\dagger$	Sd	611	D	7.76 ± 0.04	-0.64	0.167	$6.1 \pm 0.3 \times 10^7$
312	ESO358-G063	$1.48^\dagger$	Scd	584	R	8.57 ± 0.05	-0.38	0.751	$3.1 \pm 0.5 \times 10^7$

Notes: **1**: Fornax Cluster Catalogue (Ferguson, 1989) number of the galaxy; **2**: Common name of the galaxy; **3**: †Stellar mass in the MUSE FoV from Iodice et al. (2019b); *Stellar mass obtained from 3.6 μm image. The uncertainty is $^{+0.04}_{-0.05}$; **4**: Morphological type from Sarzi et al. (2018); **5**: Distance from brightest cluster galaxy NGC1399; **6**: Whether the molecular gas in the galaxy is regular (R) or disturbed (D) as classified in Chapter I; **7**: H_2 mass from Chapter I; **8**: H_2 deficiency, defined as $\log(M_{H_2,\mathrm{observed}}) - \log(M_{H_2,\mathrm{expected}})$ (where $M_{H_2,\mathrm{expected}}$ is the expected gas fraction based on field galaxies with similar stellar masses, see Chapter I). Uncertainties are 0.01 dex for each galaxy. **9**: Total star formation rate in the MUSE FoV from Iodice et al. (2019b, except FCC207, which is from this work); **10**: Stellar mass surface density: half the stellar mass divided by the area within the effective radius R_e. *Effective radii from (Iodice et al. 2019b, no uncertainties given), **effective radii from Venhola et al. (2018), remaining effective radii are from Raj et al. (2019).

most by the cluster environment, and that are most gas deficient. Including more such low mass galaxies in our analysis, or including galaxies with less molecular gas, would be required to obtain a complete census of the star formation activity in the Fornax cluster. Possible effects on our conclusions are discussed in more detail in §4.7.

The 9 galaxies in the sample are listed in Table 3.1, along with their key properties. Column 3 lists the total stellar mass in the MUSE field of view from Iodice et al. (2019b). Since FCC207 is not included in F3D, but was taken from the archive, its stellar mass was obtained from aperture photometry on its archival Wide-field Infrared Survey Explorer (WISE, Wright et al. 2010) band 1 (3.4 μm) image, assuming a mass-to-light ratio of 1. The aperture was chosen using the effective radius determined by Venhola et al. (2018). The uncertainty in this case (see Table caption) is a combination of the uncertainty in the effective radius and the rms in the image. Column 6 indicates whether the galaxy has a regular (R) or disturbed (D) molecular gas reservoir (as determined in Chapter I), and molecular gas masses and deficiencies are listed in column 8 and 9, respectively (both also from Chapter I). The latter is defined as $\log(M_{\mathrm{H_2,observed}}) - \log(M_{\mathrm{H_2,expected}})$, where $\log(M_{\mathrm{H_2,expected}})$ is the estimated molecular gas mass of a field galaxy of similar stellar mass (from interpolation of field samples). The total SFR in the MUSE field of view from Iodice et al. (2019b) is listed in column 10. These were calculated through the conversion SFR ($\mathrm{M_\odot\ y^{-1}}$) = $\mathrm{L_{H\alpha}}$ (erg $\mathrm{s^{-1}}$) / 1.82 $\times 10^{41}$ ($M_\odot$ $\mathrm{yr^{-1}\ erg^{-1}\ s^{-1}}$), provided by (Calzetti et al., 2012). Stellar mass surface densities, defined here as half the stellar mass divided by the effective radius R_e (from Venhola et al. 2018, Iodice et al. 2019b, or Raj et al. 2019, see Table caption) are listed in column 11.

3.2.2 CO DATA

The molecular gas data used are ^{12}CO(1-0) integrated intensity (moment zero) maps from AlFoCS. A detailed description of the observations and data reduction can be found in Chapter I, in which these CO data are published. Some important details are summarised below.

ALMA Band 3 observations were carried out between the 7th and 12th of January 2016 under project ID 2015.1.00497.S (PI: T. Davis), using the main (12m) array in the C36-1 configuration. The data were calibrated manually, CLEANed (interactively, using a natural weighting scheme), and continuum subtracted using the Common Astronomy Software Applications package (CASA, version 5.1.1, McMullin et al. 2007). The spaxel sizes in the final data cubes (and hence in the moment zero

maps used here) are 0.″5 (∼50 pc at the distance of the Fornax cluster), and typical beam sizes are around 3″(∼0.3 kpc at the distance of Fornax). Channel widths are 10 km s^{-1} for most galaxies, and 2 km s^{-1} for the dwarf FCC207, because of its narrow linewidth. Typical rms noise levels are ∼3 mJy/beam. The cleaned data cubes were used to produce primary beam corrected moment maps of the CO(1-0) line emission using the masked moment method (Dame, 2011).

3.2.3 Hα data

Hα maps are from F3D, with the exception of FCC207 (described below). A detailed description of the survey and data reduction can be found in Sarzi et al. (2018) and some important details are summarised here.

Integral-field spectroscopic observations were carried out with MUSE in Wide Field Mode (Bacon et al., 2010) between July 2016 and December 2017. It was mounted on the Yepun Unit Telescope 4 at the ESO Very Large Telescope (VLT). A field of 1 × 1 square arcminutes was covered, with 0.2 × 0.2 square arcsecond spatial sampling. For some of the more extended galaxies, this is smaller than their optical discs. In these cases two or three pointings were used to map the whole galaxy. An exception is FCC290, which was only observed partially (including the centre and most of the outskirts, see Figure C.7 in Appendix C). The MUSE pointings of all F3D galaxies can be found in Sarzi et al. (2018). The observations cover a wavelength range of 4650-9300 Å, with a spectral resolution of 2.5 Å (at the full width at half maximum, FWHM) at 7000 Å and spectral sampling of 1.25 Å $pixel^{-1}$.

Data reduction was performed using the MUSE pipeline (version 1.6.2, Weilbacher et al. 2012, 2016) under the ESOREFLEX environment (Freudling et al., 2013). In summary, the data reduction involved bias and overscan subtraction, flat fielding, wavelength calibration, determination of the line spread function, illumination correction with twilight flats (to account for large-scale variation of the illumination of the detectors) and similar with lamp flats (to correct for edge effects between the integral-field units).

Extinction corrected Hα maps were obtained as described in Sarzi et al. (2018) and Iodice et al. (2019b): the Gas and Absorption Line Fitting code (GandALF, Sarzi et al. 2006; Falcón-Barroso et al. 2006) was used to perform a spaxel-by-spaxel fit, simultaneously for both the stellar and ionised gas contributions. The full extent of the MILES library was used to decrease the impact of template-mismatch on the emission line measurement. As detailed also in Oh et al. (2011) and in Sarzi et al. (2018), the GandALF fit included two reddening components, a first affecting the

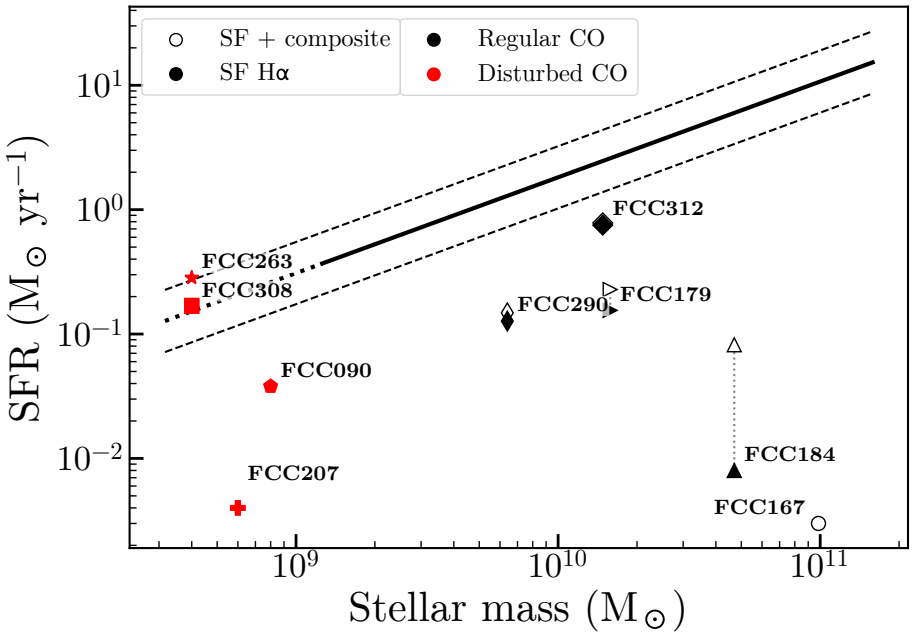

Figure 3.1: Location of the galaxies in the sample in the $M_\star$ - SFR plane (values are from Table 3.1), compared to the star formation main sequence from Elbaz et al. 2007 (solid line, the dashed lines represent the 1 σ confidence interval, and the dotted line is an extrapolation towards lower masses). Filled markers indicate data points for which only the star forming Hα was used and open markers indicate data points for which composite Hα was considered also. Both are plotted for each galaxy with the same marker shape, unless it contains only non-star forming Hα (FCC167). Galaxies' FCC numbers are indicated. Galaxies with regular molecular gas reservoirs are shown in black and galaxies with disturbed molecular gas reservoirs in red (§3.2.1, Table 3.1). With few exceptions, galaxies in the sample lie below the star formation main sequence.

entire spectrum and representing dust diffusion everywhere throughout the target galaxy, and a second which affects only the nebular emission and can account for dust more localized around the emission-line regions. Differentiating the two allows for a more accurate estimation of the effects of dust mixed with gas in star forming regions. A Calzetti (Calzetti et al., 1994) extinction law was used in both cases.

The MUSE cube of FCC207 was taken from the ESO archive, Program IDs 098.B-0239, 094.B-0576, 097.B-0761, and 096.B-0063 (PI: E. Emsellem). Observations were carried out between October 2014 and January 2017, similarly to the observations described above. A field of 1.2 arcmin^2 was covered, with 0.2 $\times$ 0.2 square arcsecond spatial sampling. The spectral range covered is 4650-9351 Å, with a spectral resolution of 2.3 Å at 7000 Å. The Hα map was obtained in the same way as the ones from F3D.

3.3 Methods

3.3.1 Obtaining surface density maps

Star formation rate surface densities

SFR maps are obtained by calculating star formation rates from the Balmer decrement corrected Hα maps as follows:

$$\mathrm{SFR}\left(M_\odot\ \mathrm{yr}^{-1}\right) = \frac{L\left(\mathrm{H}_\alpha\right)}{1.86 \times 10^{41}}, \tag{3.1}$$

where $1.86 \times 10^{41} M_\odot\ \mathrm{yr}^{-1}\mathrm{erg}^{-1}\mathrm{s}^{-1}$ was adopted from Hao et al. (2011) and Murphy et al. (2011), and $L\left(\mathrm{H}_\alpha\right)$ is the Hα luminosity in erg s^{-1}. The latter is obtained from the MUSE images via

$$L\left(\mathrm{H}_\alpha\right) = 4\pi D^2 F\left(\mathrm{H}_\alpha\right), \tag{3.2}$$

where $F\left(\mathrm{H}_\alpha\right)$ is the measured Hα flux in erg s^{-1} cm^{-2} and D the distance to the galaxy in cm. The SFR is then divided by the spaxel area in kpc^2 to obtain the SFR surface density Σ_{SFR} in $M_\odot\ \mathrm{yr}^{-1}\ \mathrm{kpc}^{-2}$. While some authors opt to correct for inclination in order to obtain a measure of the intrinsic surface density (assuming the gas is distributed in a flat disk), here I do not apply this correction, both due to the disturbed nature of some of the sources, and the fact that I am only comparing surface density maps within individual galaxies, in which case this correction cancels out. Finally, the image is convolved to match the ALMA beam and regridded to the resolution of the ALMA images.

Two sets of Σ_{SFR} images were created, one where only the Hα emission powered purely by star formation is considered, and another including also other so-called "composite" emission regions, where other sources of ionisation (such as shocks or active galactic nuclei, AGN) in addition to O-stars could contribute to the observed Hα emission. Only spaxels with Hα detections (S/N $>$ 3) are considered. Which spaxels are dominated purely by star forming Hα, and which by composite ionisation, was determined using Baldwin, Phillips & Terlevich (BPT, Baldwin et al. 1981) diagrams, using the [OIII]λ5007/Hβ and [NII]λ6583/Hα line ratios. Only spaxels with sufficient S/N (>3) in these lines to reliably determine the nature of the Hα emission were included in the maps). The boundary line from Kauffmann et al. (2003) was used as a cut-off to define which pixels contain star-forming Hα, and the one from Kewley et al. (2001) as an upper limit for composites.

The line ratios used in BPT diagrams have a certain degree of sensitivity to conditions like gas density and shocks, and relative abundances. Moreover, there

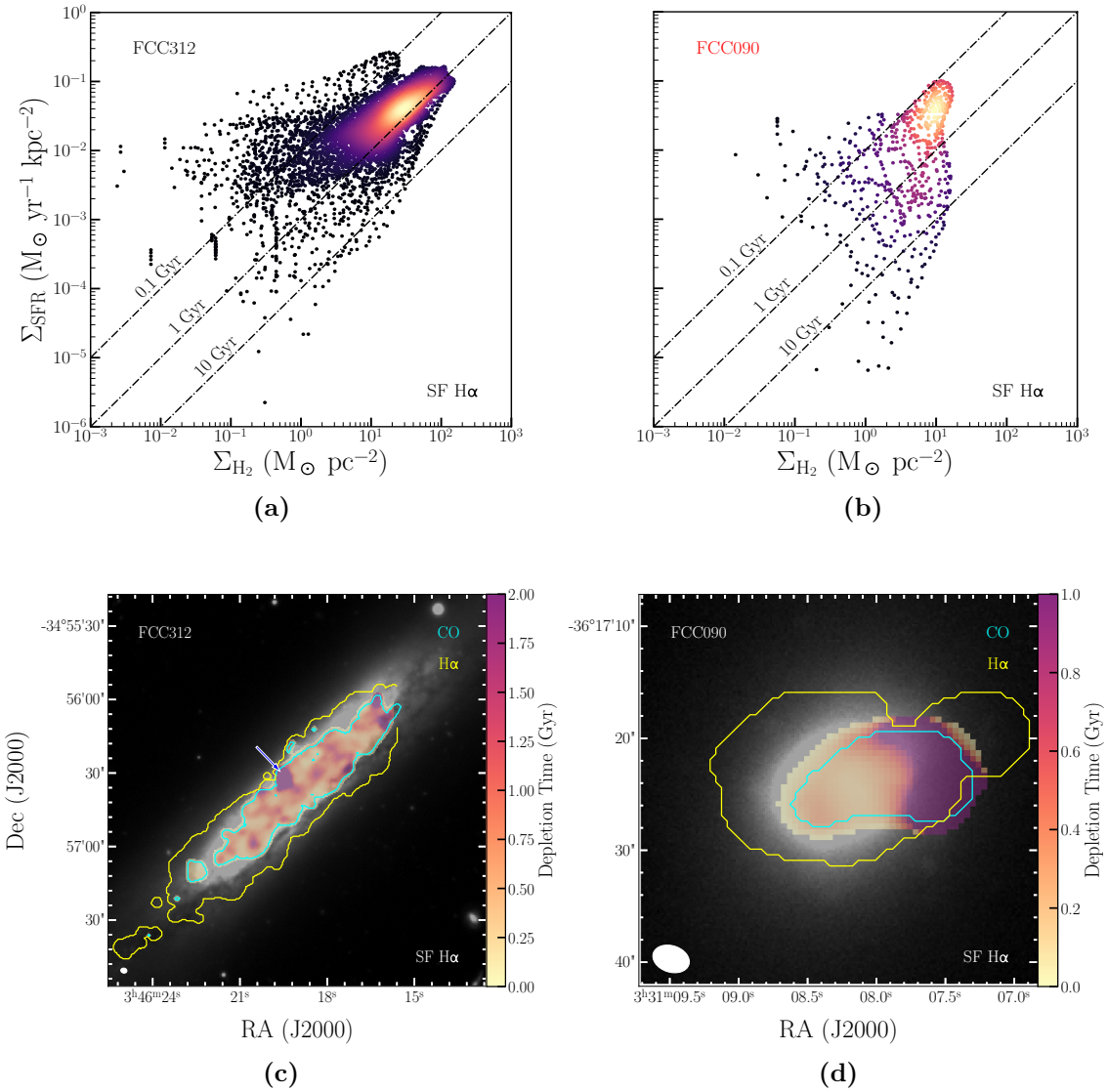

Figure 3.2: Top row: Relation between the molecular gas and star formation rate surface densities for FCC312 (left) and FCC90 (right). The colours of the markers indicate the density around the data point, determined using a Gaussian kernel density estimation. Lines of constant depletion times (0.1, 1, and 10 Gyr) are shown. The galaxy names are indicated in the upper left corners, in black if the galaxy has a regular molecular gas reservoir, and in red if it is disturbed (see §3.2.1, Table 3.1). **Bottom row**: depletion time maps of FCC312 (left) and FCC90 (right). The maps are overplotted on optical (g-band) images from the Fornax Deep Survey (FDS, Iodice et al. 2016, 2017; Venhola et al. 2017, 2018, Peletier et al., in prep.). The extent of the CO emission is indicated with a cyan contour, and that of the Hα emission with a yellow contour. The beam of the ALMA observations is shown in the lower left corner. In these examples, only the pixels dominated by star forming Hα are used (maps where composite Hα is considered can be found in Appendix C). Most regions in FCC312 have depletion times shorter than the "standard" depletion time of 1-2 Gyr, and they vary in the galaxy from region to region. The long depletion time region indicated with the blue/white arrow is due to mosaicking effects in the MUSE data: a small fraction of the galaxy was not covered by the mosaic, resulting in an overestimation of the depletion time here. FCC90 deviates from the "standard" depletion time of 1-2 Gyr by a factor 5-10. Depletion times are short in the galaxy's body (< 0.5 Gyr), but long in the gas tail ($\gg 2$ Gyr).

is a level of uncertainty in the exact dividing line between spaxels dominated by ionisation as a result of star formation, and other ionising sources (such as AGN, shocks or old stars). The Kewley et al. (2001) line is a conservative lower limit for the true number of spaxels dominated by these alternative ionising mechnisms. Kauffmann et al. (2003), on the other hand, posit that star forming galaxies tend to follow a relation on the BPT diagram with relatively little scatter, and thus all spaxels above the scatter in this relation, defined by their dividing line, can be considered as dominated by other sources. Therefore, although these are not perfect dividing lines, both are conservative in what they consider purely AGN/other sources or purely star forming spaxels, and both are widely used to disentangle between contribution from star formation and AGN/other sources to Hα emission.

Since emission from composite regions is only partly due to star formation, including these regions allows us to set an upper limit to the total star formation rate of each system. A corresponding lower limit can be set by removing these spaxels entirely. For this reason, I consider two cases throughout this Chapter: one where only the spaxels strictly dominated by star formation are taken into account, and one where spaxels classified as "composite" are included also. I remove all spaxels which are dominated purely by ionisation from other sources (such as AGN or shocks).

BPT diagrams for all galaxies in the sample (except FCC207) galaxy are presented in Iodice et al. (2019b). Which pixels are excluded from the Hα maps in the Hα-only analysis, and how this affects the resulting star formation relations, can be seen in the maps in Appendix C.

Molecular gas surface densities

$\Sigma_{\mathrm{H_2}}$ maps are obtained by first deriving $\mathrm{H_2}$ column densities from the CO maps as follows:

$$N_{\mathrm{H_2}}\left(\mathrm{mol.\ cm^{-2}}\right) = X_{\mathrm{CO}}\ \frac{\lambda^2}{2k_{\mathrm{B}}} \int S_\nu\ d\nu, \tag{3.3}$$

where X_{CO} is the CO-to-$\mathrm{H_2}$ mass conversion factor, λ the rest wavelength of the line observed, k_{B} is the Boltzmann constant, and $\int S_\nu\ d\nu$ the total flux of the line observed in Jy km $\mathrm{s^{-1}}$.

For the purpose of consistency with Chapter I, I use the metallicity-dependent mass conversion factor from eqn. 25 from Accurso et al. (2017, see §4.3 in Chapter I). Although Bigiel et al. (2008) used a fixed conversion factor, our results change only marginally when a different conversion factor is adopted, not affecting a comparison with their result. The relation used calls for a distance from the star formation main sequence (SFMS, $\log \Delta\,(\mathrm{MS})$). To calculate this, I use the SFMS from Elbaz et al.

(2007), and the star formation rates and stellar masses listed in Table 3.1. Where our targets lie in the $M_\star$ - SFR plane compared to the SFMS is shown in Figure 3.1. The SFMS is shown as a solid line, the dotted line is an extrapolation from it towards lower stellar masses. The 1 σ confidence interval is indicated with the dashed lines. Filled markers indicate data points for which only the star forming Hα was used and open markers indicate data points for which composite Hα was considered also. Both are plotted for each galaxy with the same marker shape, unless it only contains Hα that is not dominated by star formation (FCC167). Galaxies' FCC numbers are annotated. The majority of our galaxies lie well below the SFMS. This is not surprising, as they are molecular gas deficient cluster galaxies (Chapter I).

In order to obtain the gas mass surface density $\Sigma_{\mathrm{H_2}}$ in $M_\odot$ pc^{-2}, equation 3.3 is multiplied by twice the mass of a hydrogen atom (2 m_{H}, in $M_\odot$) and converted from cm^{-2} to pc^{-2}.

3.3.2 OBTAINING THE $\Sigma_{\mathrm{H_2}}-\Sigma_{\mathrm{SFR}}$ RELATION AND DEPLETION TIMES

The actual resolution of the $\Sigma_{\mathrm{H_2}}$ map is constrained by the ALMA beam size. To avoid over-interpreting the data by studying these maps on smaller scales, both images are binned to the size of the ALMA beam. When doing so, the starting point of the first bin, and therefore the location of the resulting grid, is arbitrary. As a result, the binned map is slightly different depending on the chosen starting point, which is especially noticeable in galaxies with relatively small angular sizes. To account for this, I create a separate map for each possible starting point, effectively shifting the grid up/down and sideways until each possibility is covered. I then show all resulting star formation relations in one figure. This way, the denser areas of the star formation relation will represent the more robust pixel values, whereas sparse regions and scatter are the result of small-scale variations and edge-effects. Depletion times are then calculated by dividing both surface density maps by each other. Because there is a different map for each possible grid for both the gas and SFR surface densities, I take the median of these maps in each pixel before dividing both maps by each other. This way I end up with a map at our initial resolution with the most likely depletion time in each pixel (one version where composite Hα is included, and one where only star forming Hα is considered).

3.4 RESULTS

Examples of $\Sigma_{\mathrm{H_2}}-\Sigma_{\mathrm{SFR}}$ relations and depletion time maps are shown in Figure 3.2 for FCC312 (left) and FCC090 (right) for the case where only star forming spaxels

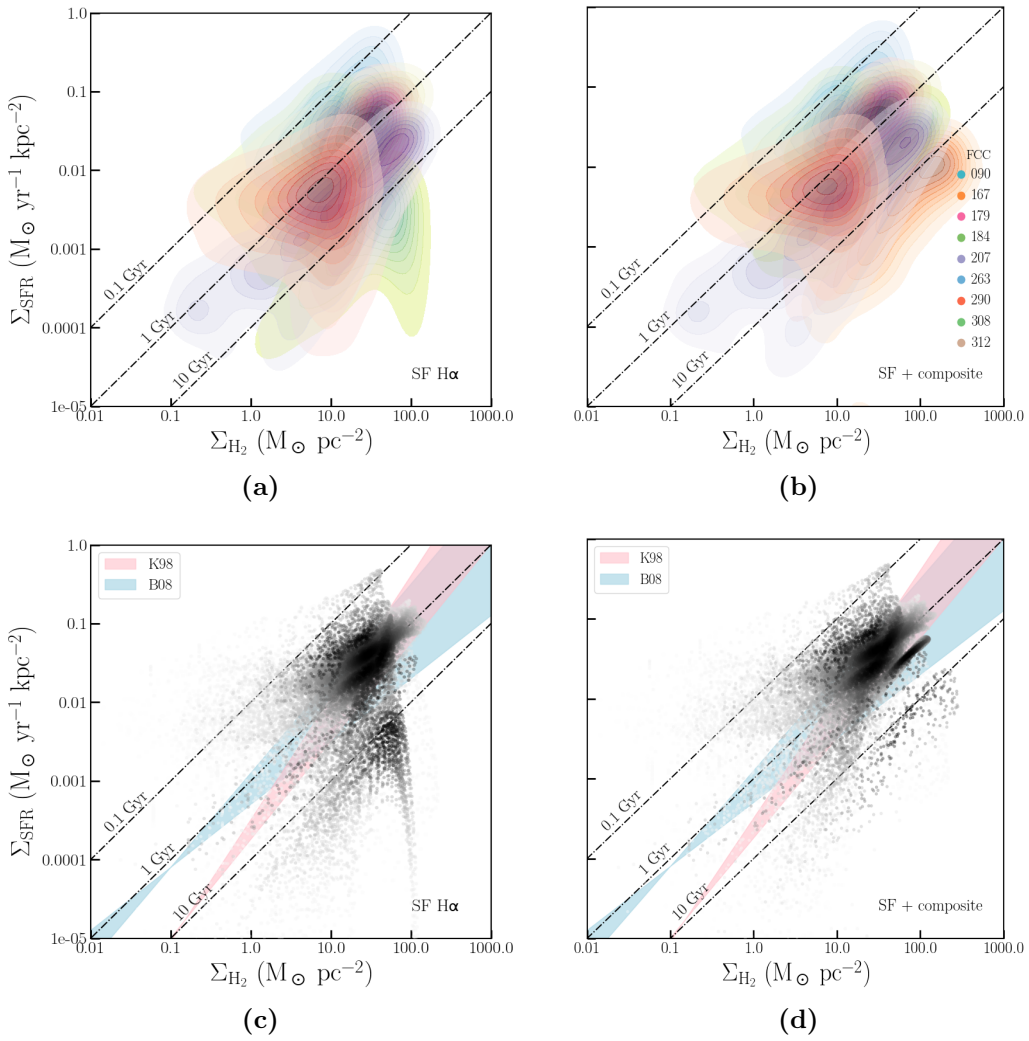

Figure 3.3: Combined $\Sigma_{H_2} - \Sigma_{SFR}$ relation for all galaxies in the sample, both considering the star forming Hα only (left column) and including composite Hα also (right column). In the top row separate contour plots (based on kernel density estimates) are shown for each galaxy, whose FCC numbers are indicated in the right-hand panel. The bottom row shows the same data, represented as points coloured by galaxies' individual KDE values, similar to the top panels (a darker shade indicates a higher KDE value), to allow for a an easier comparison between the Fornax cluster and the K98 and B08 relations, shown in pink and blue, respectively. Lines of constant depletion time (0.1, 1, and 10 Gyr) are shown in each panel. The bulk of the resolution elements in the Fornax cluster have depletion times close to what is predicted by K98 and B08. However, many have slightly decreased depletion times compared to the B08 relation, lying towards its short-depletion time side. A few galaxies have significantly longer depletion times. The $\Sigma_{H_2} - \Sigma_{SFR}$ relation is tighter and looks more physical when composite Hα is taken into account, suggesting that the contribution of AGN and other sources in ionising Hα in these galaxies is low.

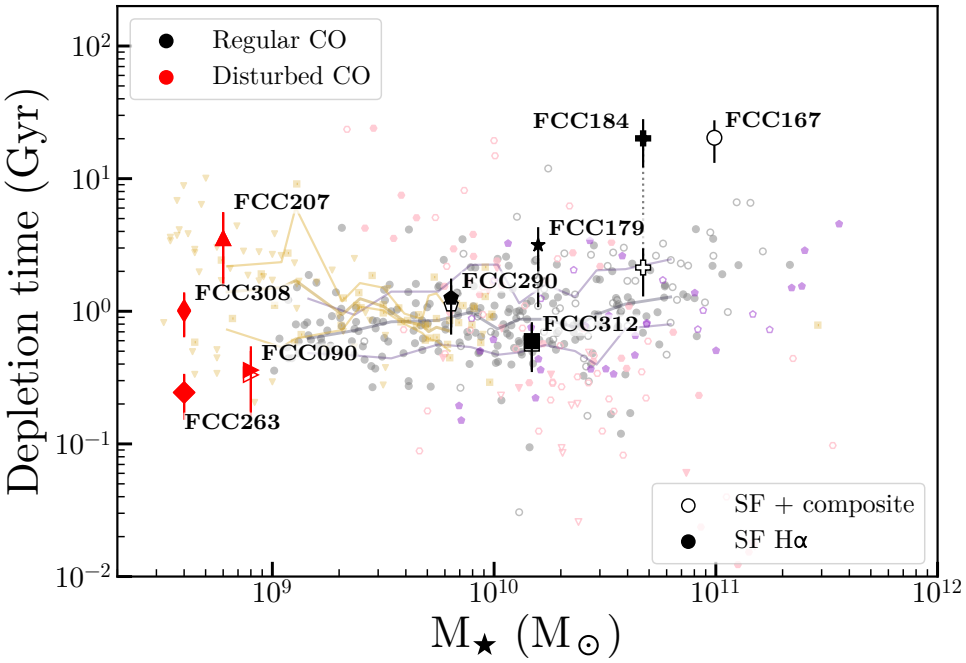

Figure 3.4: Depletion times of the galaxies in the sample as a function of their stellar mass. Markers are the same as in Figure 3.1. The underlying field sample consists of xCOLD GASS (Saintonge et al. 2017, shown as grey markers), ATLAS^{3D} (Cappellari et al. 2011; Young et al. 2011; Cappellari et al. 2013, shown as purple markers), ALLSMOG (Cicone et al. 2017, shown as yellow markers, triangles indicate upper limits), and HRS (Boselli et al. 2010, 2014a, shown as pink markers). Filled purple markers indicate field ellipticals from ATLAS^{3D}, open markers are ellipticals residing in the Virgo cluster. Similarly, pink open markers are HRS galaxies located in the Virgo cluster, and filled markers are field galaxies. Grey open markers indicate galaxies in the xCOLD GASS sample that were classified as "composite", while filled ones are classified as star forming. Upper limits are indicated with down-pointing triangles for each sample. The median of the xCOLD GASS sample, as well as the 16th and 84th percentiles, are indicated with solid lines, and similarly for ALLSMOG in yellow. Our targets mostly follow the weak relation between stellar mass and depletion time seen in the xCOLD GASS sample.

are considered. The full set of similar figures (including the versions of these examples where composite spaxels are included also, see below) for all the sample can be found in Appendix C. FCC312 was chosen because of its large angular size, which allows it to nicely demonstrate the resulting star formation relation. It is a relatively massive ($\log(M_\star/M_\odot) = 10.04$), edge-on spiral with a regular molecular gas reservoir (see Table 3.1). FCC090 was chosen because it has a stripped molecular gas tail. It is a dwarf ($\log(M_\star/M_\odot) = 8.98$) elliptical with a "disturbed" molecular gas reservoir. Only the pixels dominated by star forming Hα were used in these examples, although they would not look significantly different if composite Hα was considered (Figures C.1 and C.9).

In the $\Sigma_{H_2} - \Sigma_{SFR}$ relations (Figure 3.2, top row), the colour of the marker indicates the density of the data around the point in log space. Thus, the lighter the colour, the more resolution elements exist in the galaxy that lie on a similar location on the $\Sigma_{H_2} - \Sigma_{SFR}$ plane. Darker colours, on the other hand, correspond to locations that are only occupied by a few pixels, which usually means they lie at the edge of the detected emission. These densities were calculated using a Gaussian kernel density estimation (KDE). Furthermore, lines of constant depletion time (0.1, 1, and 10 Gyr, from top to bottom) are shown. The galaxy name is indicated in the upper left corner, in red if the galaxy has a disturbed molecular gas reservoir, and in black if it is regular (see Table 3.1).

The t_{dep} maps (Figure 3.2, bottom row) are overplotted on optical (g-band) images from the Fornax Deep Survey (FDS, Iodice et al. 2016, 2017, Peletier et al., in prep., Venhola et al. 2017, 2018). The extent of the CO emission is indicated with a cyan contour, and the extent of the Hα emission with a yellow contour (as indicated in the top right corner).

FCC312 has slightly decreased depletion times compared to the "standard" 1-2 Gyr for spiral galaxies, with the majority of the regions having depletion times lower than 1 Gyr. Both CO and Hα are present throughout the galaxy. There is some small-scale variation in depletion time, mostly towards depletion times shorter than the bulk of the resolution elements in the galaxy, shown by the scatter in the SF plot and the variations in the t_{dep} map. The relatively high-depletion time area in the middle of the disk on the north side of the galaxy (indicated with the blue/white arrow) is due to mosaicking effects in the MUSE data: a small fraction of the galaxy was not covered by the mosaic, resulting in an overestimation of the depletion time here.

FCC90 also has relatively short depletion times in its stellar body, as can be seen in the depletion time map and corresponding points in the $\Sigma_{H_2} - \Sigma_{SFR}$ relation.

In the molecular gas tail depletion times are >10 times longer, with a sharp transition between the stellar body and this tail. In the $\Sigma_{H_2} - \Sigma_{SFR}$ relation, the large "wing" towards longer depletion times corresponds to this area. This is discussed further in §4.7.

Similar figures for the remaining galaxies, along with their discussions, are provided in Appendix C. General trends in these figures are discussed in §4.7.

3.4.1 COMBINED $\Sigma_{H_2} - \Sigma_{SFR}$ RELATIONS

In order to obtain a better understanding of whether galaxies in the Fornax cluster follow the classic star formation relations, it is useful to show the $\Sigma_{H_2} - \Sigma_{SFR}$ relations for each galaxy in one figure. This is done in Figure 3.3. The top row shows the KDE plots for all the sample, similar to the top rows in Figure 3.2 and Appendix C, each in a different colour. FCC numbers are indicated in the upper right-hand panel. In the bottom panels the same data are shown, but represented with points coloured by their KDE value. This is to better visualise how the $\Sigma_{H_2} - \Sigma_{SFR}$ relation in the Fornax cluster relates to the K98 and B08 relations, which are shown in pink and blue, respectively. The left column of the figure shows the case in which only star forming Hα is included, and the right column shows the case in which composite Hα is considered also (this is indicated in the lower right corners of the panels). FCC167 is only present in the right column (where composite Hα is considered as well as star forming Hα), as its Hα image does not contain any pixels that are dominated purely by star formation according to a BPT classification.

The $\Sigma_{H_2} - \Sigma_{SFR}$ relation in the left panel, where only Hα from regions dominated purely by star formation is considered, looks unphysical for some galaxies. In particular, FCC184 shows a strong downturn in its star formation efficiency at high H_2 densities (see also Figure C.4), resulting in unrealistically long depletion times. This effect arises near the centre of this object, where other sources of ionisation begin to become important. This results in a large area consisting of "composite" spaxels in this area. Including the Hα emission from this region moves these spaxels into agreement with a normal $\Sigma_{H_2} - \Sigma_{SFR}$ relation (see the right-hand panels in Figure 3.3 and C.4). This implies that star formation contributes significantly to the "composite" spaxels in this galaxy. I therefore consider the situation where Hα originating from composite regions is taken into account, in this case, more realistic. This means that the contribution from AGN (and/or old stars/shocks) to the ionisation of the gas in composite regions is probably low in this galaxy. This Figure is discussed further in §4.7.

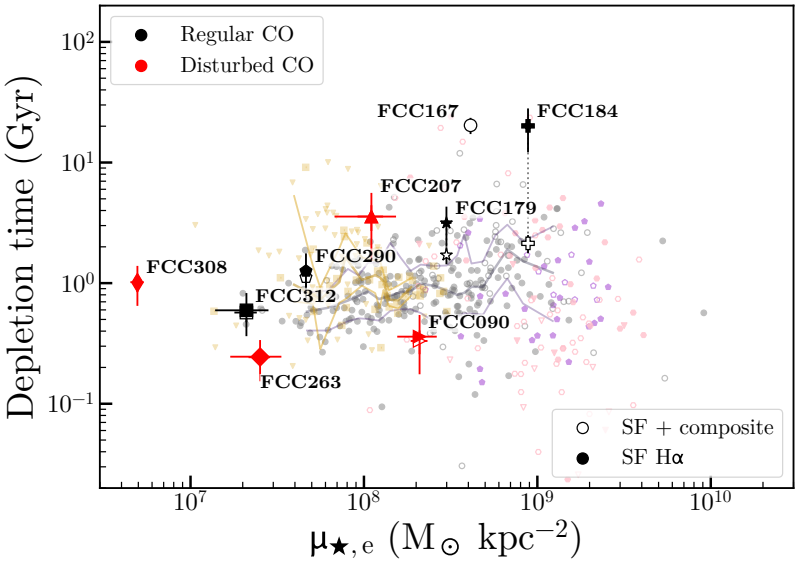

Figure 3.5: Similar to Figure 3.4, but with depletion times as a function of stellar mass surface density. A weak relation between depletion time and stellar mass surface density can be seen in the xCOLD GASS sample. The Fornax galaxies mostly follow this weak trend. Dwarf galaxies with disturbed molecular gas are widely scattered around this relation.

Together with the dwarf galaxy FCC207, which has depletion times of ∼2 - >10 Gyr, the lenticular FCC167 is the only galaxy that has depletion times significantly longer than the usual 1-2 Gyr, almost every spaxel has a depletion time significantly longer than 10 Gyr. Depletion times in the other galaxies overlap mostly with those predicted by the K98 and B08 relations, but lie towards the short-depletion time side of the B08 relation.

3.4.2 Relations with other parameters

Above we have seen that depletion times can vary significantly between galaxies in the sample. Here I test whether this variation depends on other variables, i.e. stellar mass, morphology, and (projected) location within the cluster. I compare my sample to field galaxies where possible.

Figure 3.4 shows galaxy-average depletion times as a function of stellar mass. Filled markers represent median depletion times with only the star formation dominated pixels in the Hα image taken into account, and empty markers represent the case where composite pixels in the Hα image are also taken into account. With the exception of FCC167, whose Hα image contains no pixels dominated by star formation according to our classification, there are thus two measurements for each galaxy,

represented by markers of the same shape, and connected by a dotted line. Galaxies with a disturbed molecular gas reservoir are shown with red markers, and galaxies with a regular molecular gas reservoirs in black. Uncertainties are a combination of the error on the molecular gas surface density and the error on the star formation rate surface density (in both cases the rms error and a 10% calibration error). The smaller markers in the background represent the control sample. It consists of data from the extended CO Legacy Database for *GALEX* Arecibo SDSS Survey (xCOLD GASS, Saintonge et al. 2017, grey), which is a field sample containing a broad range of galaxy types, data from the APEX low-redshift legacy survey for molecular gas (ALLSMOG, Cicone et al. 2017, yellow), which spans galaxies with stellar masses from $10^{8.5}$ to $10^{10} M_{\odot}$, data from the Herschel Reference Survey[1] (HRS, Boselli et al. 2010, 2014a, in pink), and early-type galaxies from ATLAS^{3D} (Cappellari et al. 2011; Young et al. 2011; Cappellari et al. 2013, purple). ATLAS^{3D} was added because the xCOLD GASS sample might not detect the gas in more massive ellipticals, as more sensitive observations are often required to detect CO in these galaxies. This sample was thus added to complete the higher mass end of the relation, and put the massive early-type galaxy FCC184 into more relevant context. From xCOLD GASS I only include star forming galaxies (shown as filled markers) and composite galaxies (shown as open markers), as classified by their position in the BPT diagram. Upper limits are indicated with down-pointing triangles for all samples. Error bars are omitted for visibility purposes. Uncertainties in the depletion times are typically slightly over 10% for xCOLD-GASS, 30% for ALLSMOG and 40% for the HRS.

Where necessary, I recalibrate the literature data to share the same X_{CO} prescription I use to estimate M_{H_2} in our Fornax sample (see §3.3.1 and Chapter 1). xCOLD GASS already uses this prescription. From ALLSMOG I directly use CO luminosities, allowing us to use the same recipe to derive H_2 masses. To derive X_{CO} I use their gas-phase metallicities calculated using the O3N2 calibration from Pettini & Pagel (2004), and a distance from the main sequence from Elbaz et al. (2007), as with our Fornax measurements. To recalibrate the ATLAS^{3D} values, I use stellar masses derived from r-band luminosities and M/L from Cappellari et al. (2013) to estimate metallicities. Distances from the main sequence are derived using the SFRs from Davis et al. (2014) compared to the main sequence from Elbaz et al. (2007). I then derive a correction factor from the X_{CO} I derive using my method and these parameters, compared to the X_{CO} used to derive the molecular gas masses in this sample. From the HRS I use total CO fluxes, and derive M_{H_2} following the same prescription

[1]Herschel (Pilbratt et al., 2010) is an ESA space observatory with science instruments provided by European-led Principal Investigator consortia and with important participation from NASA.

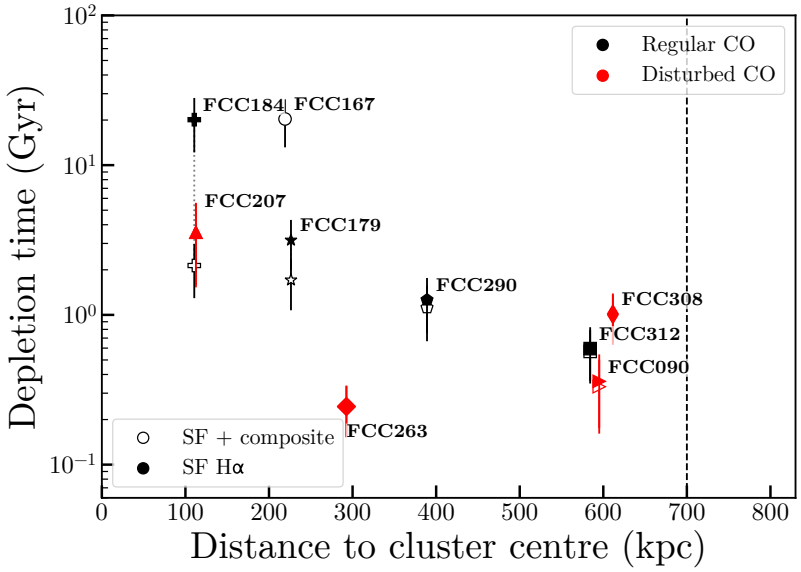

Figure 3.6: Depletion time as a function of (projected) distance to the cluster centre (i.e. BCG NGC1399). Markers are the same as in Figures 3.1, 3.4 and 3.5. The virial radius is indicated with a dashed line. A relation between depletion time and cluster-centric distance seems to exist, although it is likely partly driven by galaxy mass/morphology.

as for the Fornax, xCOLD GASS, and ALLSMOG samples. I estimate metallicities from the O3N2 line ratio, using the [NII]λ6584, [OIII]λ5007, and Hβ line fluxes (all normalised to the Hα line flux) from Boselli et al. (2013), and the calibration from Pettini & Pagel (2004).

The ATLAS^{3D} and HRS samples are split into field galaxies (filled markers) and galaxies located in the Virgo cluster (open markers). To better visualise how Fornax galaxies compare to those in Virgo, this figure is duplicated in Appendix B, but with only data from Virgo galaxies shown. The ALLSMOG sample was added to put the lower-mass galaxies into better context. To calculate depletion times for the HRS sample, I use star formation rates from Boselli et al. (2015), and molecular gas masses from Boselli et al. (2014a). The solid grey lines indicate the median and 16$^{\text{th}}$ and 84$^{\text{th}}$ quantiles of the xCOLD GASS data, indicating the 1σ spread in the data. To calculate these, running bins were used, where the data is divided into horizontal bins, each containing an equal number of (33) galaxies, where each bin is shifted by half a bin size with respect to the previous one. Similarly, the yellow lines show the median and 1σ spread in the ALLSMOG data.

Most of our cluster galaxies lie within or close to the 1σ confidence interval of the field relations.

Figure 3.5 shows the depletion times of the galaxies (obtained from the median

values of the resolution elements of their molecular gas and star formation rate surface densities) in the sample as a function of their stellar mass surface density (SMSD), here defined as half the stellar mass divided by the area enclosed by the effective radius R_e. A galaxy's SMSD is a crude measure of its radial mass profile, and can therefore be interpreted as a proxy for its morphology. Effective radii are taken from Venhola et al. (2018) for dwarf galaxies, and from Raj et al. (2019) and Iodice et al. (2019b) for more massive galaxies. Markers and lines are the same as in Figure 3.4. Most galaxies have depletion times within 1σ of what is expected from their surface densities as predicted by the field samples.

Figure 3.6 shows depletion times as a function of distance from the cluster centre, defined here as the brightest cluster galaxy (BCG) NGC1399 (FCC213). Markers are the same as in Figures 3.4 and 3.5. The virial radius (at 0.7 Mpc, Drinkwater et al. 2001) is indicated with a dashed line. There is a clear trend between cluster-centric distance and depletion time. Although this is likely partly driven by galaxy mass/morphology (massive ellipticals, which often have low SFEs (Saintonge et al., 2011; Davis et al., 2014) are in the cluster centre, whereas less massive spiral and dwarf galaxies tend to be located further out), there is possibly an additional correlation between depletion time and cluster-centric distance. The figures described above are discussed further in §4.7.

3.5 THE MOLECULAR CLOUD LIFETIME IN FCC290

FCC290 is a nearly face-on, flocculent spiral (Appendix A7, Chapter I). It is therefore an ideal candidate to study the small-scale relation between molecular gas and star formation in cluster galaxies. The molecular cloud lifetime in FCC290 was measured, by applying the statistical method (named the 'uncertainty principle for star formation') developed by Kruijssen & Longmore (2014b) and Kruijssen et al. (2018).

3.5.1 UNCERTAINTY PRINCIPLE FOR STAR FORMATION

Contrary to the tight correlation defining the K98 relation observed on galaxy scales, a spatial de-correlation between CO and Hα clumps is commonly observed in nearby galaxies (e.g. Schruba et al., 2010; Kreckel et al., 2018; Chevance et al., 2020; Hygate et al., 2019; Kruijssen et al., 2019). This spatial de-correlation, which is responsible for the observed scatter around the K98 relation below $\sim 1\,\mathrm{kpc}$ scales (Figure 2 and Appendix A; see also e.g. Bigiel et al. 2008; Blanc et al. 2009; Leroy

et al. 2013), can be explained by the fact that individual regions in galaxies follow independent evolutionary lifecycles where cloud assemble, collapse, form stars, and get disrupted by stellar feedback (e.g. Feldmann et al., 2011; Kruijssen & Longmore, 2014b). On small scales, each individual region is observed at a specific time of this cycle and it is only when averaging over many regions, sampling all phases of this cycle, that the galactic K98 relation can be retrieved.

The small-scale de-correlation between CO and Hα clumps can be directly linked to the underlying timeline of this evolutionary cycle, and represents a fundamental probe of stellar feedback physics in observations and numerical simulations (e.g. Fujimoto et al., 2019). In this Chapter, the specific implementation of this methodology presented by Kruijssen et al. (2018) and formalised in the Heisenberg code was followed to characterise the cycle of star formation and feedback in the cluster galaxy FCC290, from cloud formation (as traced by CO emission), to star formation (as traced by Hα emission), and to cloud destruction.

In practice, the CO-to-Hα flux ratio is measured in apertures of certain sizes centred on peaks of CO or Hα emission. The relative change of the CO-to-Hα flux ratio compared to the galactic CO-to-Hα ratio as a function of the aperture size (see Figure 3.7), is governed by the relative timescales of the different phases of the evolutionary cycle of cloud evolution and star formation. These observations can be fitted by the model of Kruijssen et al. (2018), which depends on three independent parameters: the duration of the cloud lifetime relative to the isolated stellar phase ($t_{\rm CO}/t_{\rm H\alpha,ref}$), the timescale during which CO and Hα coexist in a region relative to the isolated stellar phase (which is the time during which stellar feedback can affect the cloud, $t_{\rm fb}/t_{\rm H\alpha,ref}$) and the characteristic separation length λ between individual regions (i.e. molecular clouds and star forming regions). To convert these relative timescales into absolute ones, the duration of the isolated stellar phase traced by Hα only (i.e. after the complete disruption of the CO cloud, $t_{\rm H\alpha,ref}$) is used. This timescale has been calibrated by Haydon et al. (2018) and is a function of the metallicity[2] (Table 3.2).

The above measurements are potentially affected by the presence of large-scale diffuse emission, which is not associated with individual molecular clouds or star forming regions and is therefore not participating in the evolutionary cycle of the emission peaks identified. It is therefore necessary to filter the diffuse emission on scales larger than λ to ensure an unbiased measurement of the molecular cloud

[2]Note that there this Hα emission timescale can in principle be affected by extinction. However, Haydon et al. (2020) demonstrate that this only happens for kpc-scale gas surface densities $>$ 20 $\rm M_\odot$ $\rm pc^{-2}$, much larger than the typical surface density of FCC290, which is ~ 3 $\rm M_\odot$ $\rm pc^{-2}$

Table 3.2 Main input parameters of and quantities constrained (output) by the analysis of FCC290, along with their descriptions from Tables 2 and 4 in Kruijssen et al. (2018). The other input parameters use the default values as listed in Table 2 of Kruijssen et al. (2018).

Input quantity	Value	Description
D [Mpc]	17.7	Distance to galaxy
i [^{o}]	47	Inclination angle
$l_{\rm ap,min}$ [pc]	215	Minimum inclination-corrected aperture size (i.e. diameter) to convolve the input maps to
$l_{\rm ap,max}$ [pc]	6400	Maximum inclination-corrected aperture size (i.e. diameter) to convolve the input maps to
$N_{\rm ap}$	15	Number of aperture sizes used to create logarithmically-spaced aperture size array in the range ($l_{\rm ap,min}$, $l_{\rm ap,max}$)
$N_{\rm pix,min}$	10	Minimum number of pixels for a valid peak (use $N_{\rm pix,min} = 1$ to allow single points to be identified as peaks)
$\Delta \log_{10} \mathcal{F}_{\rm star}{}^a$	2.00	Logarithmic range below flux maximum covered by flux contour levels for stellar peak identification
$\delta \log_{10} \mathcal{F}_{\rm star}{}^a$	0.03	Logarithmic interval between flux contour levels for stellar peak identification
$\Delta \log_{10} \mathcal{F}_{\rm gas}{}^a$	0.6	Logarithmic range below flux maximum covered by flux contour levels for gas peak identification
$\delta \log_{10} \mathcal{F}_{\rm gas}{}^a$	0.06	Logarithmic interval between flux contour levels for stellar peak identification
$t_{\rm H\alpha,ref}$ [Myr]	4.29	Reference time-scale spanned by star formation tracer (in our case Hα)
$\sigma(t_{\rm H\alpha,ref})$ [Myr]^b	0.16	Uncertainty on reference time-scale
SFR [$\rm M_\odot\ yr^{-1}$]^c	0.127	Total star formation rate in the MUSE FoV
$\log_{10} X_{\rm gas}{}^d$	0.64	Logarithm of conversion factor from map pixel value to an absolute gas mass in $M_\odot$
$\sigma_{\rm rel}(X_{\rm gas})^b$	0.34	Relative uncertainty (i.e. σ_x/x) of $\rm X_{gas}$
$n_{\lambda,\rm iter}$	13	Characteristic width used for the Gaussian filter to filter out diffuse emission in Fourier space (see text)
Output quantity	**Value**	**Description**
$\chi^2_{\rm red}$	0.84	Goodness-of-fit statistic
$t_{\rm CO}$ [Myr]	$9.3^{+2.6}_{-2.2}$	Best-fitting gas tracer lifetime (e.g. the cloud lifetime, in our case CO)
$t_{\rm fb}$ [Myr]	$1.7^{+0.9}_{-0.7}$	Best-fitting overlap lifetime (e.g. the feedback time-scale, like in our case)
λ [pc]	327^{+133}_{-74}	Best-fitting mean separation length of independent regions (e.g. the fragmentation length)
$r_{\rm star}$ [pc]	100^{+13}_{-15}	Disc radius or Gaussian dispersion radius of star formation tracer peaks
$r_{\rm gas}$ [pc]	97^{+17}_{-13}	Disc radius or Gaussian dispersion radius of gas tracer peaks
$\zeta_{\rm star}$	$0.61^{+0.06}_{-0.11}$	Star formation tracer peak concentration parameter
$\zeta_{\rm gas}$	$0.59^{+0.07}_{-0.09}$	Gas tracer peak concentration parameter
$n_{\rm peak,star}$	49	Number of peaks in the star formation tracer map (HII regions)
$n_{\rm peak,gas}$	52	Number of peaks in the gas tracer map (giant molecular clouds)

Notes: [a]The parameters for the peak identification listed here are valid for the diffuse-emission filtered maps (§3.5.1). Different values are used for the first iteration during which emission peaks are identified in unfiltered maps, but it has been verified that the choice of these initial parameter values does not significantly affect the results.

[b]Standard error. The subscript 'rel' indicates a relative error.

[c]This is the SFR measured across the MUSE field of view considered, rather than of the entire galaxy.

[d]The gas conversion factor corresponds to $\alpha_{\rm CO(1\text{-}0)}$ in $\rm M_\odot (K\ km\ s^{-1} pc^2)^{-1}$.

lifecycle. The method of Hygate et al. (2019) was used to filter out diffuse emission in Fourier space with a Gaussian filter, using a characteristic width of 13λ. This multiplicative factor of λ has been chosen to ensure the best compromise between a selective filter to filter a maximum of the diffuse emission and a broader filter to limit the appearance of artefacts around compact structures (see Hygate et al. 2019 for details). During the analysis, a first estimation of λ is made for the original, unfiltered maps. The maps are then transformed to Fourier space and spatial wavelengths larger than 13λ are masked with the Gaussian filter, before transforming the maps back to normal space. Then, λ is estimated again using these new, filtered maps, and iterate over this process until convergence is reached (defined as obtaining the same value of λ to within 5 per cent for four successive iterations).

3.5.2 Application to FCC290

The above analysis is applied to the CO and Hα maps of FCC290, limited to the field of view of the MUSE map, in order to ensure the best possible spatial resolution (see Figure 3.7). The input parameters used for the Heisenberg code, as well as the main output quantities, are summarised in Table 3.2. Descriptions are from Table 2 and 4 from Kruijssen et al. (2018). Other input parameters not listed are set to their default values, which can be found in the same tables in Kruijssen et al. (2018) along with their descriptions.

A relatively short molecular cloud lifetime of $t_{\rm CO} = 9.3^{+2.6}_{-2.2}$ Myr was measured, and a characteristic (deprojected) separation length between regions of $\lambda = 327^{+133}_{-74}$ pc. Comparison with previous measurements of the molecular cloud lifetime using the same method (Chevance et al., 2020; Hygate et al., 2019; Kruijssen et al., 2019) reveals similarities, but also some differences with the values found in nearby spirals. They might be linked to the cluster environment of FCC290. Indeed, short molecular cloud lifetimes of $\sim 10\,$Myr are commonly measured in low mass galaxies like FCC290 (e.g. NGC300, NGC5068, and M33, which have stellar masses of $\log(M_\star/{\rm M}_\odot) \leq 9.8$, FCC290 has a stellar mass of $\log(M_\star/{\rm M}_\odot) = 9.8$), with low molecular gas surface densities (~ 3 M$_\odot$ pc^{-2} for NGC300 and NGC5068, between 1 and 10 M$_\odot$ pc^{-2} for M33). Despite a somewhat larger total gas mass, the average molecular gas surface density in FCC290 is $\Sigma_{\rm H_2} \sim 3$ M$_\odot$ pc^{-2}, very similar to NGC300 and NGC5068. The short molecular cloud lifetime of ~ 10 Myr in FCC290 is consistent with the conclusions of Chevance et al. (2020), who show that large-scale surface density is an important factor in driving the cloud lifecycle. At kpc-scale molecular gas surface densities of $\Sigma_{\rm H_2} \leq 8$ M$_\odot$ pc^{-2}, the cloud lifetime is regulated by internal

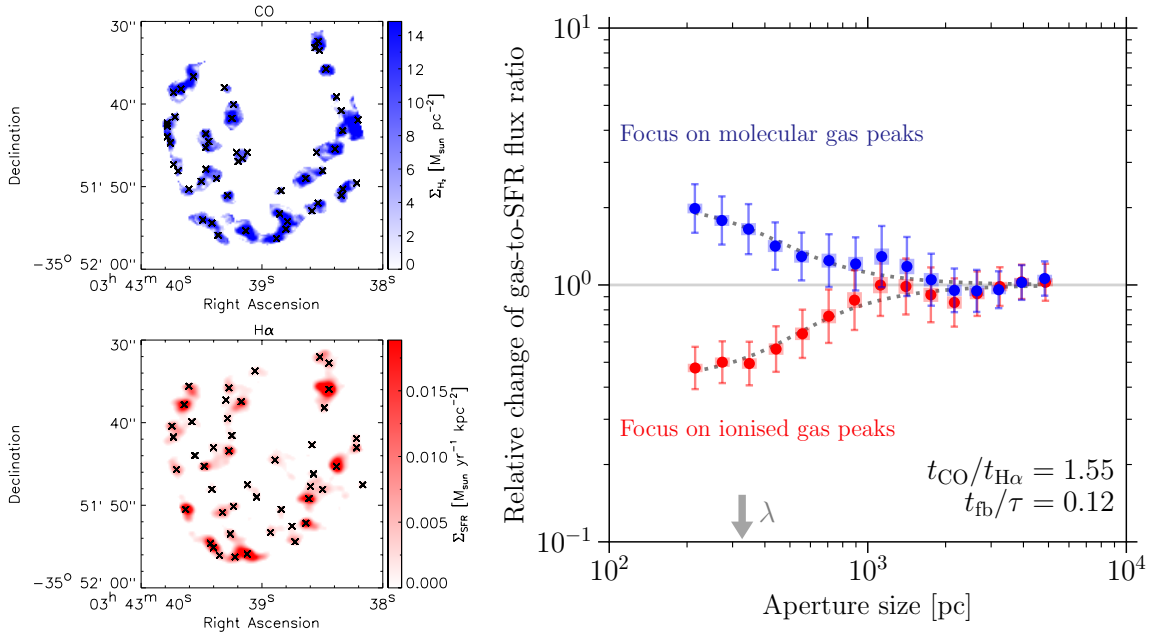

Figure 3.7: Left panels: CO (top) and Hα (bottom) maps of FCC290 after removing the diffuse emission (§3.5.1). The identified emission peaks in each map are indicated with black crosses. Right panel: Relative change of the CO-to-Hα flux ratio compared to the galactic average as a function of the aperture size, for apertures placed on CO emission peaks (blue) and Hα emission peaks (red). The error bars indicate the 1σ uncertainty on each individual data point, whereas the shaded areas indicate the effective 1σ uncertainty range that accounts for the covariance between the data points and should be used when visually assessing the quality of the fit. The horizontal solid line indicates the galactic average and the dotted line is the best-fitting model (Kruijssen et al., 2018), which allows us to constrain the molecular cloud lifecycle. The arrow indicates the best-fitting value of the region separation length λ. The ratios $t_{CO}/t_{H\alpha}$ (controlling the asymmetry between the two branches) and t_{fb}/τ (controlling the flattening of the branches) are indicated in the bottom-right corner. Also compare to Kruijssen et al. (2019, Fig. 1), Chevance et al. (2020, Fig. 2), and Hygate et al. (2019, Fig. 2).

dynamical processes and clouds live for a short time, comparable to one cloud free-fall time or cloud crossing time, with typical values of ~ 10 Myr. At larger molecular gas surface densities, the cloud lifetime is instead regulated by galactic dynamics, often resulting in cloud lifetimes of 20−30 Myr.

A notable difference between FCC290 and nearby star-forming galaxies in the field is the large characteristic distance ($\lambda \sim 300$ pc) between individual regions. By contrast, typical values measured by Chevance et al. (2020) are in the range 100–250 pc, where galaxies with low molecular gas surface densities are typically located on the lower end of this range. This could be a result of the different environment.

Despite the relatively low number of identified regions ($n_{\rm peak,star} = 49$ in the Hα map and $n_{\rm peak,gas} = 52$ in the CO map), the main output quantities ($t_{\rm CO}$, $t_{\rm fb}$ and λ) are well-constrained. As tested in Kruijssen et al. (2018), a minimum of 35 peaks in each map ensures a precision better than 50%. In addition, the region separation length λ should be well resolved to guarantee a good accuracy of the feedback time-scale $t_{\rm fb}$, i.e. the time-scale over which the CO and Hα emission co-exist. This time-scale represents the time it takes feedback from massive stars to disperse the parent molecular cloud. A ratio of λ to the minimum aperture size ($l_{\rm ap,min}$) of 1.52 was measured. This is sufficient to bring a strong constraint on $t_{\rm CO}$, but marginal for $t_{\rm fb}$ and λ, which therefore might be slightly biased because of the insufficient spatial resolution (Kruijssen et al., 2019). Indeed, the relative filling factor of the emission peaks ($\zeta_{\rm star} = 2r_{\rm star}/\lambda$ and $\zeta_{\rm gas} = 2r_{\rm gas}/\lambda$, where $r_{\rm star}$ and $r_{\rm gas}$ are the average radii of the emission peaks in the Hα and the CO maps respectively) is high (~ 0.6).

The above indications of region blending imply that our measurement of $t_{\rm fb}$ may be overestimated (see sect. 4.4 of Kruijssen et al. 2018). Given that $t_{\rm fb} = 1.7^{+0.9}_{-0.7}$ Myr is already considerably shorter than the minimum timescale for supernova feedback (~ 4 Myr, e.g. Leitherer et al., 2014), the fact that it is an upper limit implies that cloud destruction is likely driven by early feedback mechanisms in FCC290, such as photoionisation or stellar winds. This is consistent with the results found in other galaxies with similarly low molecular gas surface densities, such as NGC300 ($t_{\rm fb} = 1.5^{+0.2}_{-0.2}$ Myr, Kruijssen et al., 2019) and NGC5068 ($t_{\rm fb} = 1.0^{+0.4}_{-0.3}$ Myr, Chevance et al., 2020).

3.6 DISCUSSION

3.6.1 THE STAR FORMATION RELATION IN THE FORNAX CLUSTER

From Figure 3.2, Figure 3.3, and the figures in Appendix C, it can be concluded that depletion times of most galaxies in the sample lie close to the K98 and B08 relations. The star formation relation found in the Fornax cluster mostly overlaps with those found by K98 and B08, but is, with few exceptions, shifted towards the short-depletion time end of the B08 relation. This is noteworthy, as the study by B08 is more similar to ours than that by K98 in terms of sample, resolution, and use of molecular gas (see §4.1). There are some observational differences that can contribute to this difference. First, I use CO(1-0) as a tracer for the molecular gas rather than CO(2-1), used for most of the B08 sample. This can affect the molecular gas measurements, for example through the assumption of a line ratio (e.g. Rahman et al. 2010). Second, the CO-to-H_2 conversion factor can make a difference in the star formation relation. Here I use a conversion factor that varies with stellar mass/metallicity (§3.3.1). However, this mostly results in an increase of the conversion factor for the low-metallicity dwarf galaxies. Therefore, using a constant X_{CO} would give a lower Σ_{H_2} for these dwarfs, only moving them further away from the K98 and B08 relations. Third, I use Hα as a star formation tracer rather than UV + IR, used by B08. This traces the SFR on shorter timescales ($\sim$10 Myr rather than $\sim$100 Myr), which can also affect the star formation relation. Another factor is the increased number of early-type galaxies in our sample compared to the field samples used by B08 (and K98), whose star formation is often dynamically suppressed (e.g. Davis et al. 2014). Last, it has been shown by various authors (e.g. Schruba et al. 2010; Liu et al. 2011; Calzetti et al. 2012; Williams et al. 2018) that the index of the star formation relation can vary significantly depending on the resolution of the observations. While both B08 and this work examine the relation on sub-kpc scales, the resolution used by B08 is still a factor $\sim$2 worse than the resolution used here, which could play a role (K98 used integrated measurements for entire galaxies only). However, the integrated depletion times in Figures 3.4, 3.5, and 3.6 correspond very well with the densest areas in the star formation relations of the individual galaxies (see Appendix C), suggesting this does probably not play a significant role.

Galaxies that have depletion times significantly shorter than predicted by the K98 and B08 relations are the dwarf galaxies FCC090 and FCC263, and the more massive, edge-on spiral FCC312. Galaxies with significantly longer depletion times are the dwarf FCC207 and the lenticular FCC167. FCC184 has slightly increased depletion times of several Gyrs. Figure 3.4 shows that most of these galaxies still

have depletion times within 1 σ of what is expected based on their stellar mass. However, this figure is somewhat misleading at the low-mass end due to the low number statistics, and in reality there are probably more dwarf galaxies with increased than decreased depletion times. Indeed, de los Reyes & Kennicutt (2019) have shown that dwarf galaxies in the field have longer depletion times than spirals, and therefore lie below the K98 relation. They also note that second-order correlations with gas fraction, SMSD, and dynamical timescales can be important in dwarfs. In Chapter I we have seen that dwarf galaxies in Fornax have molecular gas fractions around an order of magnitude smaller than expected based on observations of field galaxies due to environmental processes, which could play a role here. All three dwarf galaxies have disturbed molecular gas reservoirs, so their star formation rates are likely enhanced by the tidal interactions or ram pressure that cause these disturbances and compress the molecular gas. Ram pressure is very effective at stripping the gas from dwarf galaxies (e.g. Venhola et al. 2019). The depletion times of these dwarfs are longer than the time it will take them to cross the cluster core (and therefore reach the peak of their gas stripping; e.g. Boselli et al. 2014b). They are therefore likely to be influenced by RPS before depleting their gas reservoirs. Tidal disruptions, on the other hand, should be less important (if they are as dark matter dominated as similar galaxies in the field), therefore favouring the latter as an explanation. It could be that these galaxies have unusual chemical features as a result of their bursty star formation histories, as seen for example in Pinna et al. (2019a,b). This will be explored further in future work.

With the exception of FCC263, which is closer (in projection) to the cluster centre than the other two, galaxies with very short depletion times are located around the virial radius of the cluster (Figure 3.6). This suggests that they are on their first infall into the cluster, their gas being compressed and stripped as they fall in. This explanation is supported by the observation that the galaxies with the shortest depletion times are less H_2 deficient than the ones with longer depletion times (Table 3.1), suggesting that they have not yet spent much time in the cluster. There is, however, one other galaxy in the sample with a disturbed molecular gas reservoir, FCC207, that has increased rather than decreased depletion times (§C.0.5). In projection (and redshift), FCC207 is the galaxy closest to the BCG in the AlFoCS sample. It is possible that it has passed the slight starburst phase during its first infall. However, although it is more H_2 deficient than the other dwarfs, the amount of gas present that has had to have survived the infall in this case (Table 3.1, Table 3 in Chapter I), makes this explanation unlikely. The other possibility is that it is at the edge of the cluster along the line of sight, in which case I underestimate its distance from

the BCG. In this case, it is possible that the starburst has not yet started. In Figure C.5 we can see a strong gradient in depletion times across the galaxy, suggesting that the gas is compressed on one side due to ram pressure stripping or tidal effects. This supports the idea that the galaxy is on its first infall. A future study of the stellar population content from the MUSE data could help distinguish between both scenarios.

The result that infalling objects in Fornax have relatively short depletion times is somewhat different from what has previously been found in several studies of the Virgo cluster, which concluded that RPS and interacting galaxies here do not have significantly different depletion times (Vollmer et al., 2012; Nehlig et al., 2016). Other studies of the Virgo cluster did find, on the other hand, locally increased SFRs in RPS galaxies (Lee et al., 2017). Perhaps the differences with studies of the Virgo cluster originate from a difference in sample, as most studies of the Virgo cluster were performed using observations of higher-mass spiral galaxies, whereas the shorter depletion times in the Fornax cluster are largely driven by dwarf galaxies, which are more susceptible to environmental effects (see also Chapter I).

3.6.2 THE STAR FORMATION RELATION IN INDIVIDUAL GALAXIES

There is significant scatter in the star formation relation of most individual galaxies (Figure 3.2, the figures in Appendix C). This is partly due to the statistical nature of these figures (§4.3), especially in case of the more extreme scatter and galaxies with small angular sizes. In some cases (e.g. FCC090, §C.0.1 and FCC207, §C.0.5) it is due to larger scale variations within the galaxy, as a result of the stripping and compression of the gas. Other, small scale variations (as can be seen nicely in FCC290, §C.0.7, see also §3.5, and FCC312, §C.0.9) are also seen in other studies (e.g. Bigiel et al. 2008; Blanc et al. 2009; Onodera et al. 2010; Leroy et al. 2013), and are generally contributed to individual regions in galaxies undergoing independent evolutionary lifecycles of cloud assembly, collapse, star formation, and disruption by feedback (e.g. Schruba et al. 2010; Feldmann et al. 2011; Kruijssen & Longmore 2014b). This small scale scatter can therefore be directly related to the underlying evolutionary timeline of the above processes see also §3.5.

3.6.3 Depletion time as a function of galaxy parameters

Relation with stellar mass

In the xCOLD GASS sample, there is a shallow trend between galaxies' depletion times and stellar masses (the Kendall's tau value is ∼0.21 with a corresponding p-value of $\sim 4.7 \times 10^{-7}$, Figure 3.4). Fornax galaxies follow a similar trend that is possibly slightly steeper, with dwarf galaxies having decreased and more massive galaxies having increased depletion times. However, this partly depends on the true values of the depletion times of FCC179 and FCC184, depending on whether composite Hα or only Hα classified as star forming is taken into account. Moreover, the numbers are small. If FCC184 does indeed have increased depletion times compared to the field, this can be explained by the fact that early-type galaxies in clusters tend to be very regular and relaxed, likely because they have not recently experienced any mergers. Regular and relaxed gas reservoirs are more susceptible to dynamical effects caused by the deep potential, which some studies have suggested suppress star formation (Martig et al., 2009, 2013; Davis et al., 2014; Gensior et al., 2019). A version of this Figure with Fornax and Virgo galaxies shown only is provided in Appendix B.

Relation with stellar mass surface density

If we look at depletion times as a function of SMSD rather than stellar mass (Figure 3.5), we can see there is a similar weak trend in the xCOLD GASS data (the Kendall's tau value is ∼0.23 with a corresponding p-value of $\sim 8.5 \times 10^{-8}$) between these parameters in the field. Most Fornax galaxies are close or within 1 σ of this field relation. FCC090, which follows the trend with stellar mass in Figure 3.4, is below 1 σ in this relation. This is likely because its elliptical morphology predicts longer depletion times. However, due to its low mass and shallow potential well, it is still more easily affected by the cluster environment. Its depletion time is therefore shorter than predicted by its SMSD. For this reason, galaxy stellar mass appears to be a better predictor of depletion times in the cluster than galaxy morphology as probed by their SMSD.

Relation with cluster-centric distance

Figure 3.6 shows a clear trend between galaxy depletion times and their distance from the cluster centre. Since massive ellipticals tend to be located closer to the cluster centre than less massive spirals, this trend is likely at least partly driven by galaxy mass/morphology rather than distance from the cluster centre per se. In fact, if we

compare this figure with Figure 3.4, the weak correlation between depletion time and stellar mass indeed seems mostly anti-correlated with the trend with radial distance. Galaxies that do not follow this anti-correlation are FCC207, FCC263, and FCC312. The distance to FCC207 is likely underestimated as a result of the projection, as it would not expected to have any gas left if it was actually only ∼100 kpc away from the cluster centre. The same is possibly true for FCC263. FCC263 does show evidence of either a merger or a strong bar, both of which drive gas to the centre and increase the gas (surface) density, thus decreasing depletion times. FCC312 is located close to the virial radius (in projection). Like the dwarf galaxies with short depletion times, it is likely on its first infall into the cluster, undergoing a slight starburst. Based on the location of FCC312, and that of FCC207 if it is accurate, the location of a galaxy within the cluster possibly affects its depletion times in addition to its mass (and morphology), with galaxies close to the virial radius, on their first infall, having relatively short depletion times. However, it is difficult to draw conclusions with the poor statistics and lower limits on the distance from the BCG. Improved statistics and/or simulations are needed in order to break the degeneracy between galaxy morphology and location in the cluster, and see whether this relation holds independent of galaxy morphology.

3.6.4 STAR FORMATION IN STRIPPED MATERIAL

FCC90 is a dwarf elliptical galaxy with a tail of molecular gas extending beyond its stellar body (Figure 3.2 and §C.0.1). There is a clear difference between depletion times in the galaxy's stellar body and in the tail, with a sharp transition. Depletion times in the galaxy body are low, around 0.5 Gyr. Depletion times in the tail are much higher, >10 times that in the stellar body. This is in agreement with what is observed in RPS galaxies, for example by Ramatsoku et al. (2019), who find that depletion times in the tail of the JO206 RPS galaxy are ∼10 times smaller than those in its disk. While this work studies HI rather than H_2, and overall HI depletion times are shorter than the H_2 depletion times found here, the clear split in $t_{\rm dep}$ between the stellar body and the gas tail, differing by a factor ∼10 in both works, is in good agreement. This clear split in depletion times was also observed by Moretti et al. (2018, 2019) in several GASP galaxies. Jachym et al. (2019) find that molecular gas directly stripped from the Norma jellyfish galaxy (ESO 137-001) does not form stars.

3.6.5 Sample bias

As described in §3.2.1, not all galaxies from Chapter I are represented in this work. With the exception of the massive spiral galaxy FCC121 (NGC1365), galaxies that were detected in Chapter I, but not studied here, are dwarf galaxies with disturbed molecular gas reservoirs, and a spiral galaxy close to the virial radius. As discussed above, the slightly decreased depletion times observed in the Fornax cluster are driven by disturbed dwarf galaxies and the spiral galaxy FCC312, which is also close to the virial radius and likely experiencing a slight starburst on its infall. If MUSE data were obtained such that all these additional objects from Chapter I could be included in this study, this would double the number of disturbed dwarf galaxies and add another spiral galaxy close to the virial radius. If these galaxies are similar to the ones studied here, this would move the star formation relation in the Fornax cluster further away from the K98 and B08 relations. This would strengthen the conclusion that the effects of the cluster environment on the molecular gas content of galaxies result in decreased depletion times compared to field galaxies, likely due to the compression of molecular gas as a result of environmental effects.

3.6.6 The inclusion of composite Hα

Comparing the cases using Hα from regions dominated by star formation ionisation, and also including Hα from regions with composite ionisation, only significantly changes the star formation relation for a few galaxies. These are FCC179, FCC184 (and FCC167, which has no Hα that is dominated by star formation only, according to a BPT classification). Both FCC179 and FCC184 harbour AGN, which contributes to the ionised gas emission around the galactic centre. In our star forming Hα versus star forming + composite Hα comparison, the star formation relations of these objects both change visibly (Figures C.3 and C.4), though more significantly in the case of FCC184. Its relation between molecular gas surface density and star formation surface density becomes tighter in if I include composite spaxels, and its average depletion time decreases significantly (Figures 3.4, 3.5, and 3.6). This suggests that while the AGN (and/or shocks/old stars) dominates the production of higher ionisation state lines such as [OIII]λ5007, it does not contribute significant Hα emission in the composite emission-line regions of this galaxy.

3.6.7 Spiral arm vs. interarm regions

FCC179 is a large spiral galaxy (§C.0.3, Figure C.3). From Figure C.3d it appears that it is undergoing ram pressure stripping, with both molecular gas and

ionised gas being removed from its east side. Furthermore, depletion times trace the spiral arms in this figure, which have more efficient star formation ($t_{\rm dep}$<2 Gyr) than the interarm regions (∼3 - 4 Gyr). This implies that star formation in spiral arms is more efficient than in interarm regions, which is in line with our current understanding of spiral galaxies (e.g. Elmegreen 2011).

3.7 SUMMARY

I study the resolved star formation relation in the Fornax cluster. CO is used as a tracer for molecular gas, and Balmer decrement corrected Hα as a tracer for the star formation rates. Resolved maps are obtained from ALMA and MUSE observations, respectively. The resulting surface density maps are binned to the ALMA beam size using a flexible binning method, for which I use a grid that I repeatedly move by one pixel until all possible positions are covered. The result is a set of different possible (star formation and molecular gas) surface density maps for each galaxy, depending on the position of the grid. I combine the resulting maps into one star formation relation for each galaxy. Depletion time maps of the individual galaxies are obtained using the median gas and SFR surface densities of the possible maps in each pixel. I create two versions of each map and and $\Sigma_{\rm H_2} - \Sigma_{\rm SFR}$ relation: one where only the star forming Hα is taken into account according to a BPT classification, and one where composite Hα is also considered. Besides star formation plots for each individual galaxy, I combine the possible values for each resolution element in the sample into one $\Sigma_{\rm H_2} - \Sigma_{\rm SFR}$ relation. Results are compared with the relations found by Kennicutt (1998) and Bigiel et al. (2008). I also show galaxy-average depletion times as a function of stellar mass, stellar mass surface brightness, and distance to the cluster centre, and compare the results with similar relations for field galaxies from xCOLD GASS (Saintonge et al., 2017), ALLSMOG (Cicone et al., 2017), the HRS (Boselli et al., 2010, 2014a), and ATLAS$^{\rm 3D}$ (Cappellari et al., 2011; Young et al., 2011). Our main conclusions are as follows:

- The overall star formation relation in the Fornax cluster is close to those found by K98 and B08, but lies towards the short-depletion time end of the B08 relation. This is mostly driven by dwarf galaxies with disturbed molecular gas reservoirs, although there are some observational differences between the studies that possibly contribute to this difference.

- Individual Fornax cluster galaxies lie in different locations on the star formation relation plane, their combined depletion times covering more than two orders

of magnitude. Most dwarf galaxies (with exception of FCC207, which has significantly longer depletion times than expected) and other galaxies close to the virial radius have depletion times shorter than the typical value of 1-2 Gyr for spiral field galaxies.

- Most galaxies exhibit significant scatter in their $\Sigma_{H_2} - \Sigma_{SFR}$ relations. Although some of this is due to edge-effects and the statistical nature of the relations shown, it also indicates a variety of depletion times on sub-galactic scales. Depending on the galaxy, this scatter can be mostly towards either lower or higher depletion times, or both equally. For some galaxies this is mostly the results of larger scale variations or gradients in depletion time (e.g. FCC090 and FCC207), in others it reflects small scale variations as a result of independent evolutionary lifecycles of clouds (e.g. Schruba et al. 2010; Feldmann et al. 2011; Kruijssen & Longmore 2014b). FCC290, for example, an almost face-on flocculent spiral, shows the largest and most symmetric scatter. This reveals the spatial offsets between HII regions and giant molecular clouds, and indicates the time evolution of independent regions. The 'uncertainty principle for star formation' was applied to it, and it was found that it has relatively short molecular cloud lifetimes of $t_{CO} = 9.3^{+2.6}_{-2.2}$ Myr. Such short cloud lifetimes are typically found for low-mass galaxies with low molecular gas surface densities (Chevance et al., 2020), similar to that measured in FCC290, despite a relatively high total gas mass. At such low surface densities the cloud lifetime is regulated by internal dynamical processes rather than galactic dynamics, resulting in relatively short cloud lifetimes. The characteristic distance $\lambda \sim 300$ pc between individual regions is quite large in FCC290 compared to $\lambda \sim 100 - 250$ pc in similar galaxies in Chevance et al. 2020. This could be a result of the cluster environment.

- Fornax galaxies appear to follow the shallow trend in depletion time with stellar mass seen in the field, possibly with somewhat more extreme values at the low and high mass ends, although statistics are poor. At the lower mass end of the distribution this could be explained by the dwarf galaxies in the cluster being more susceptible to effects from the cluster environment, due to their shallow potentials. The increased depletion times observed at the higher mass end are likely due to the sample being limited to massive early-types here. The HRS, which consists of spiral galaxies, and includes galaxies in the Virgo cluster, shows a spread in depletion times at the higher-mass end (see Appendix B for a version of this Figure showing cluster galaxies exclusively).

- The same low-mass galaxies are outliers if we look at depletion times as a function of stellar mass surface density (defined here as 0.5 $M_{\odot}/(\pi R_e^2)$), which can be interpreted as a proxy for galaxy morphology. However, since some low-mass galaxies are dwarf ellipticals, and some higher-mass galaxies are spirals, these outliers are no longer at the extremes of the distribution, and therefore there is a weaker trend with SMSD than with stellar mass. Therefore, stellar mass appears to be a better predictor of galaxy depletion times, especially in clusters, where lower-mass galaxies are more susceptible to environmental effects decreasing their depletion times.

- There is a relatively clear correlation between median depletion time and the (projected) distance between a galaxy and the cluster centre. It is, however, likely that this trend is (partly) caused by mass/morphological type rather than the distance itself. Massive ellipticals tend to be located in the cluster centre, and lower mass galaxies, such as spirals and dwarfs, are typically located further out. In order to break the degeneracy between these two variables, improved statistics and/or simulations are needed.

- The dwarf galaxy FCC090 has a large molecular gas tail, caused by either RPS or a tidal interaction. A similar though slightly offset tail is seen in the ionised gas. A starburst is likely taking place in its stellar body as it is falling into the cluster: depletion times there lie around $\sim$0.5 Gyr rather than the usual 1-2 Gyr. Depletion times in its gas tail, however, are much larger, typically around 10 times those in the galaxy body, or longer. This is in line with results from Moretti et al. (2018, 2019); Ramatsoku et al. (2019); Jachym et al. (2019).

In conclusion, the star formation relation in the Fornax cluster is close to the "traditional" ones (e.g. from K98 and B08), but with slightly decreased depletion times. This is mainly driven by dwarf galaxies with disturbed molecular gas reservoirs and galaxies possibly undergoing starbursts on their first infall into the cluster.

Chapter 4
AlFoCS + Fornax3D II: unexpectedly low gas-to-dust ratios in the Fornax galaxy cluster

Everything is dust in the wind

Kansas, *"Dust in the Wind"*

I combine observations from ALMA, ATCA, MUSE, and *Herschel* to study gas-to-dust ratios in 15 Fornax cluster galaxies detected in the FIR/sub-mm by *Herschel* and observed by ALMA as part of the ALMA Fornax Cluster Survey (AlFoCS). The sample spans a stellar mass range of $8.3 \leq \log(M_\star/M_\odot) \leq 11.16$, and a variety of morphological types. I use gas-phase metallicities derived from MUSE observations (from the Fornax3D survey) to study these ratios as a function of metallicity, and to study dust-to-metal ratios, in a sub-sample of nine galaxies. I find that gas-to-dust ratios in Fornax galaxies are systematically lower than those in field galaxies at fixed stellar mass/metallicity. This implies that a relatively large fraction of the metals in these Fornax systems is locked up in dust, which is possibly due to altered chemical evolution as a result of the dense environment. The low ratios are not only driven by HI deficiencies, but H_2-to-dust ratios are also significantly decreased. This is different in the Virgo cluster, where low gas-to-dust ratios inside the virial radius are driven by low HI-to-dust ratios, while H_2-to-dust ratios are increased. Resolved observations of NGC1436 show a radial increase in H_2-to-dust ratio, and show that low ratios are present throughout the disc. I propose various explanations for the low H_2-to-dust ratios in the Fornax cluster, including the more efficient stripping of H_2 compared to

dust, more efficient enrichment of dust in the star formation process, and altered ISM physics in the cluster environment.

4.1 INTRODUCTION

As explained in Chapter I, dust plays a vital role in star formation and galaxy evolution besides gas. If dust is environmentally stripped along with gas, this could have a significant impact on the evolution of galaxies in clusters, the most (galaxy)dense environments in the Universe. Dust acts as a catalyst for the formation of H_2 (e.g. van Dishoeck et al. 1993; Scoville 2013; Wakelam et al. 2017 and references therein), and helps shield it from the interstellar radiation field (e.g. van Dishoeck et al. 1993; Ciolek & Mouschovias 1995). Therefore, dust and molecular gas are typically linked, and might be expected to be stripped simultaneously. However, if the process of star formation is (indirectly) affected by dense environments, this may result in more subtle effects on the chemical evolution of a galaxy, and the relative gas and dust contents.

The gas-to-dust ratio provides a useful probe for studying the effects of environmental stripping on galaxies' gas and dust contents in more detail. Especially if it is compared with metallicity, it can teach us a lot about the chemical evolution of galaxies. The gas-to-dust ratio (G/D) as a function of metallicity has been studied extensively in field galaxies (e.g. Issa et al. 1990; Lisenfeld & Ferrara 1998; Draine et al. 2007; Sandstrom et al. 2013; Rémy-Ruyer et al. 2014; De Vis et al. 2017; De Looze et al. 2020). Rémy-Ruyer et al. (2014) compiled and homogenised a range of recent samples. They found that (total) G/D correlates strongly with metallicity, following a broken (around $12 + \log(O/H) = 7.96$) power law, with large scatter ($\sim$0.37 dex for metallicity bins of $\sim$0.1 dex). Their results are consistent with chemical evolution models from Asano et al. (2013) and Zhukovska et al. (2016). Resolved studies have shown that the gas-to-dust ratio also varies within individual galaxies, e.g. the local galaxy M33. Gas-to-dust ratios in M33 differ from that in the Milky Way, and also vary radially (Tabatabaei & Berkhuijsen, 2010; Gratier et al., 2017; Williams et al., 2019).

Studies of the Virgo cluster have shown that dust can be stripped by environmental effects as well as gas, even from the very inner parts of galaxies (Cortese et al., 2010; Corbelli et al., 2012; Pappalardo et al., 2012). Corbelli et al. (2012) find dust deficiencies of up to 75% in HI deficient Virgo galaxies. Pappalardo et al. (2012) find a strong spatial correlation between molecular gas and cold dust in non-HI-deficient galaxies, which is weakened in HI-deficient galaxies. This suggests that

both molecular gas and dust are affected by environment, though not necessarily in the same way. They find no significant radial gradient in total (i.e. HI + H_2) G/D within cluster galaxies. Cortese et al. (2016) found that (total) gas-to-dust ratios in cluster galaxies are decreased compared to those in isolated galaxies at fixed mass and metallicity. They found that this decrease is driven by the HI-to-dust ratio, while the H_2-to-dust ratio, on the other hand, is increased. They attribute this difference to differential stripping of the ISM as a result of the different spatial distribution of HI (most extended), H_2 (centrally concentrated) and dust (in between the two gas phases).

Thus far, studies of gas-to-dust ratios in cluster galaxies have mostly focused on spiral galaxies in the Virgo cluster. To obtain a broader understanding of the role of dust stripping in the baryon cycle of cluster galaxies, in a wider variety of environments, we need to expand our studies to different clusters and galaxy types. Therefore, this Chapter focuses on gas-to-dust ratios in the Fornax cluster. In Chapter II I presented resolved molecular gas maps and H_2 masses and deficiencies. In Chapter III, where I use both Atacama Large Millimiter/submillimeter Array (ALMA) and Multi Unit Spectroscopic Explorer (MUSE) observations, I studied the resolved star formation relation in the Fornax cluster. In this work, I study molecular gas-to-dust ratios in relation to their metallicities.

Recently, a 15×15 degree blind survey, covering the Fornax cluster out to its virial radius, was performed with the Australia Telescope Compact Array (ATCA, Loni et al. 2021). This survey resulted in the detection of 16 Fornax galaxies in HI. 15 of these have CO observations or useful upper limits (i.e. upper limits that provide informative constraints on the H_2-to-dust ratio) from AlFoCS, allowing us to study their total gas-to-dust ratios.

This Chapter is organised as follows. In §4.2 I describe the sample and observations. In §4.3 I describe the methods used, in particular how any masses and metallicities were estimated. In §4.4 I describe the DustPedia literature sample, to which I compare my results, and any underlying assumptions used to derive the quantities I utilise. In §4.5 I describe the main results. In §4.6 I look into the resolved H_2-to-dust ratio in NGC1436, to highlight any radial or other spatial variation, if present. The main results are discussed in §4.7. Finally, I summarise my findings in §4.8.

Throughout this work, I assume a common distance of 19.95 Mpc (Tonry et al., 2001) to galaxies in the Fornax cluster.

4.2 SAMPLE SELECTION, OBSERVATIONS AND DATA REDUCTION

4.2.1 THE SAMPLE

The Fornax sample consists of all AlFoCS galaxies that have far-infrared/sub-millimetre measurements from which dust masses can be estimated reliably (i.e. are detected in $\geq$3 *Herschel* bands, implying at least one detection with the Spectral and Photometric Imaging REceiver (SPIRE, Griffin et al. 2010, see §4.2.3). It consists of 15 galaxies, spanning a mass range of $8.3 \leq \log(M_\star/M_\odot) \leq 11.16$. Both late-type and early-type galaxies are included in the sample, as well as (irregular) dwarfs. Some of the H_2 measurements are upper limits, though these are only included if they provide a useful constraint on the H_2-to-dust ratio. Of these galaxies, 9 (of which one having a CO upper limit) have MUSE observations from F3D, and can therefore be used to study H_2-to-dust ratios as a function of metallicity. This sub-sample spans a stellar mass range of $8.3 \leq \log(M_\star/M_\odot) \leq 11.0$. Key parameters of the sample are listed in Table 4.1. Fornax Cluster Catalogue (FCC, Ferguson 1989) numbers are listed in column one. Corresponding common galaxy names are listed in column 2. Column 3 lists stellar masses, from z0mgs (Leroy et al., 2019), or from Fuller et al. (2014) if not available there, indicated with a ‡. Morphological types are given in column 4, from Sarzi et al. (2018) where available, otherwise from older references provided in the Table caption. Column 5 lists the projected cluster-centric distance in kpc. Column 6 describes whether the molecular gas reservoir is regular (R) or disturbed (D), as classified in Chapter II. Column 7 lists X_{CO}, estimated as described in §4.3.1. Molecular gas, atomic gas, and dust masses are listed in columns 8, 9, and 10, respectively. Finally, column 11 lists whether the galaxy is included in F3D (Y) or not (N).

4.2.2 CO DATA

ALMA data for the Fornax cluster targets were analysed in Chapter II, which describes the data and methods used in detail. I summarise some important details here. ALMA Band 3 observations were carried out between the 7th and 12th of January 2016 under project ID 2015.1.00497.S (PI: T. Davis), using the main (12m) array in the C36-1 configuration. The data were calibrated manually, CLEAN-ed interactively, using a natural weighting scheme, and continuum subtracted using the Common Astronomy Software Applications package (CASA, version 5.1.1, McMullin

Table 4.1 Key properties of the galaxies in the sample.

FCC	Common name	$M_\star$	Type	D	Gas dist.	X_{CO}	M_{H_2}	M_{HI}	M_{dust}	in F3D?
						10^{20} cm^{-2}				
-	-	(log $M_\odot$)	-	(kpc)	-	(K km s^{-1})$^{-1}$	(log $M_\odot$)	(log $M_\odot$)	(log $M_\odot$)	(Y/N)
(1)	(2)	(3)	(4)	(5)	(6)	(7)	(8)	(9)	(10)	(11)
67	NGC1351A	9.56 ± 0.1	SB(rs)bc[a]	694	R	2.2 ± 0.7	7.03 ± 0.07	8.67 ± 0.11	$6.637^{+0.051}_{-0.052}$	N
90	MGC-06-08-024	8.98‡	E4 pec	595	D	6.6 ± 0.7	7.33 ± 0.07	7.76 ± 0.16	$5.234^{+0.117}_{-0.114}$	Y
121	NGC1365	10.75 ± 0.1	SB(s)b[b]	420	R	1.6 ± 0.7	9.49 ± 0.04	10.18 ± 0.09	$8.093^{+0.029}_{-0.029}$	N
167	NGC1380	8.75 ± 0.11	S0/a	220	R	0.9 ± 0.7	7.43 ± 0.06	≤7.7	$5.873^{+0.039}_{-0.039}$	Y
179	NGC1386	10.92 ±0.09	Sa	226	R	1.3 ± 0.7	8.25 ± 0.04	≤7.7	$6.569^{+0.031}_{-0.032}$	Y
184	NGC1387	9.51 ± 0.18	SB0	111	R	1.1 ± 0.7	8.14 ± 0.04	≤7.5	$6.359^{+0.032}_{-0.031}$	Y
235	NGC1427A	9.1 ± 0.17	IB(s)m[b]	132	-	2.6 ± 0.7	≤7.42	9.32 ± 0.09	$6.446^{+0.113}_{-0.120}$	N
263	PGC013571	8.75 ± 0.1	SBcdIII	292	D	11.1 ± 0.7	7.88 ± 0.05	8.01 ± 0.13	$5.938^{+0.062}_{-0.062}$	Y
282	FCC282	8.86 ± 0.1	S0[c]	615	D	2.8 ± 0.7	7.15 ± 0.05	≤7.3	$5.362^{+0.085}_{-0.084}$	N
285	NGC1437A	8.71 ± 0.1	SAB(s)dm[b]	428	-	3.7 ± 0.7	≤7.83	8.75 ± 0.10	$6.508^{+0.212}_{-0.199}$	Y
290	NGC1436	10.12 ± 0.1	ScII	389	R	1.2 ± 0.7	8.28 ± 0.05	8.21 ± 0.19	$6.817^{+0.037}_{-0.036}$	Y
306	FCC306	8.68‡	S[c]	600	-	3.9 ± 0.7	≤8.10	8.03 ± 0.13	$4.478^{+0.322}_{-0.319}$	N
308	NGC1437B	9.25 ± 0.11	Sd	611	D	5.8 ± 0.7	8.17 ± 0.04	8.39 ± 0.11	$6.597^{+0.064}_{-0.068}$	Y
312	ESO358-G063	10.08 ± 0.11	Scd	584	R	4.7 ± 0.7	8.99 ± 0.05	9.23 ± 0.10	$7.057^{+0.029}_{-0.030}$	Y
335	ESO359-G002	9.17 ± 0.1	SB0^?[b]	872	D	2.4 ± 0.7	6.92 ± 0.05	≤7.0	$4.787^{+0.101}_{-0.100}$	N

Notes: **1**: Fornax Cluster Catalogue (Ferguson, 1989) number of the galaxy; **2**: Common name of the galaxy; **3**: Stellar mass from z0mgs (Leroy et al., 2019), or from Fuller et al. (2014) if not available there, indicated with a ‡; **4**: Morphological type from Sarzi et al. (2018) if available, otherwise references are listed below; **5**: Projected distance from brightest cluster galaxy NGC1399; **6**: Whether the molecular gas in the galaxy is regular (R) or disturbed (D) as classified in Chapter II; **7**: X_{CO}, estimated as described in §4.3.1; **8**: H_2 mass from Chapter II; **9**: HI mass from Loni et al. (2021); **10**: Dust mass calculated from the FIR fluxes published in Fuller et al. (2016); **11**: Whether the galaxy was observed with MUSE as part of F3D (Y) or not (N).

[a] (Lauberts & Valentijn, 1989); [b] (de Vaucouleurs et al., 1991); [c] (Loveday, 1996)

et al. 2007). The FWHM of the restoring beam is typically between $\sim$2″ and 3″ (equivalent to $\sim$200 - 300 pc at the distance of the Fornax cluster). Channel widths are 10 km s^{-1}. Typical rms noise levels are $\sim$3 mJy/beam. The cleaned data cubes were used to produce moment maps of the ^{12}CO(1-0) line emission using the masked moment method from Dame (2011). These maps were corrected for the primary beam response. Spectra, from which the H_2 masses were estimated, were calculated by summing over both spatial directions of the spectral cube, using a square spatial field around the emission. At the distance of the Fornax cluster, the largest scales recoverable with the 12m array are significantly larger than the expected sizes of the largest CO structures the galaxies observed. Therefore, I expect to have recovered the total CO(1-0) flux of each galaxy, and I expect the masses derived in Chapter II to be accurate. For one object, NGC1365, ALMA data was added from the archive (project ID: 2015.1.01135.S, PI: Fumi Egusa, see Chapter II for more details). For a more detailed, resolved study of H_2-to-dust ratios in NGC1436, described in §4.6, I use additional, deeper ALMA data from the archive to complement the observations from Chapter II (project ID: 2017.1.00129.S, PI: Kana Morokuma, see §4.6 for more details).

4.2.3 FAR-INFRARED DATA

The far-infrared (FIR) maps used to estimate dust masses are from the Photoconductor Array Camera and Spectrometer (PACS, Poglitsch et al. 2010, 100 and 160 micron) and the Spectral and Photometric Imaging REceiver (SPIRE, Griffin et al. 2010, 250, 350, and 500 micron), both mounted on the *Herschel* Space Observatory (Pilbratt et al., 2010). The SPIRE maps used here are identical to the ones used by DustPedia (Davies et al. 2017, see §4.4), and the PACS maps were reprocessed using the same techniques as DustPedia. The FWHM of the beams of the *Herschel* maps are $\sim$ 6.8, $\sim$ 10.7, $\sim$ 17.6, $\sim$ 23.9, $\sim$ 35.2″ at 100, 160, 250, 350, and 500 micron, respectively, corresponding to $\sim 660, \sim 1000, \sim 1700, \sim 2300$, and $\sim$ 3400 pc at the distance of the Fornax cluster (see the SPIRE handbook[1] and the PACS Observer's Manual[2]).

Note that FIR measurements and derived dust masses for the Fornax cluster are already available in Fuller et al. (2014), on which the AlFoCS sample is based. However, since this work was published, several improvements have been made both to the *Herschel* data reduction and the SED fitting methods. In order to obtain dust

[1] http://herschel.esac.esa.int/Docs/SPIRE/spire_handbook.pdf
[2] https://www.cosmos.esa.int/documents/12133/996891/PACS+Observers%27+Manual

masses that are as accurate as possible, I have opted to re-estimate dust masses from improved FIR maps, using updated SED fitting techniques (see §4.3.3). Dust masses calculated here are slightly lower than those published in Fuller et al. (2014), with a median difference of 0.28 dex and a 1σ spread in differences of 0.28 dex.

4.2.4 HI data

HI data[3] are from ATCA, which was used to conduct a blind survey of the Fornax cluster, covering an area of 15 deg^2 out to $R_{\rm vir}$. The observations and data reduction are presented and described in detail in Loni et al. (2021), and are summarised here. Observations were carried out from December 2013 to January 2014 in the 750B configuration (project code: C2894, PI: P. Serra). The data were reduced manually using the `MIRIAD` software (Sault et al., 1995). The dirty cube was obtained using the `INVERT` task (using natural weighting), after which the tasks `MOSMEM` and `RESTOR` were used to clean and restore the HI emission. The synthesised beam has a FWHM of $95'' \times 67''$ (corresponding to $\sim 9 \times 6.5$ kpc at the distance of the Fornax cluster). Channel widths are 6.6 km s^{-1}. Typical noise levels are 2.8 mJy beam^{-1} and go down to 2.0 mJy beam^{-1} in the most sensitive region. HI sources were identified using the SoFiA source-finding package (Serra et al., 2015). Whether detections are considered reliable is based on the algorithm from Serra et al. (2012), and by visual inspection where necessary. This has resulted in the detection of HI in 16 Fornax cluster galaxies, of which 15 have CO detections (or useful upper limits) and are thus included in this work. The spatial resolution of the ATCA data is $67'' \times 95''$ ($\sim 6 \times 9$ kpc at the distance of the Fornax cluster, see Loni et al. 2021). This means that the HI discs are marginally resolved in this data set.

4.2.5 Optical spectra

Optical spectra, used to measure the line ratios from which metallicities are estimated, are from F3D Sarzi et al. (2018); Iodice et al. (2019b). A detailed description of the survey and data reduction can be found in Sarzi et al. (2018), and some important details are summarised here.

Integral-field spectroscopic observations were carried out with MUSE (Bacon et al. 2010, mounted to VLT Unit Telescope 4, "Yepun") in Wide Field Mode, between July 2016 and December 2017. A field of 1×1 square arcminutes was covered, with 0.2×0.2 square arcsecond spatial sampling. For some of the more extended galaxies,

[3]Available from `https://atoa.atnf.csiro.au/query.jsp`

this is smaller than their optical discs. In these cases two or three pointings were used to map the whole galaxy. An exception is FCC290, which was only observed partially (including the centre and the outskirts to one side, see Sarzi et al. 2018). The MUSE pointings of all F3D galaxies can be found in Sarzi et al. (2018). The observations cover a wavelength range of 4650-9300 Å, with a spectral resolution of 2.5 Å at the full width at half maximum (FWHM) at 7000 Å and spectral sampling of 1.25 Å pixel^{-1}.

Data reduction was performed using the MUSE pipeline (version 1.6.2, Weilbacher et al. 2012, 2016) under the ESOREFLEX environment (Freudling et al., 2013). In summary, the data reduction involved bias and overscan subtraction, flat fielding, wavelength calibration, determination of the line spread function, illumination correction with twilight flats (to account for large-scale variation of the illumination of the detectors) and similar with lamp flats (to correct for edge effects between the integral-field units).

4.3 METHODS

4.3.1 H_2 MASSES

H_2 masses of the Fornax galaxies are calculated as described in §4.3 of Chapter II. Upper limits are one beam, 3σ upper limits, assuming a linewidth of 50 km s^{-1}, as described in §4.3.1 of Chapter II. In summary, I use the following equation:

$$M_{\mathrm{H_2}} = 2m_{\mathrm{H}}\ D^2\ X_{\mathrm{CO}}\ \frac{\lambda^2}{2k_{\mathrm{B}}}\ \int S_\nu \mathrm{d}v, \tag{4.1}$$

where m_{H} is the mass of a hydrogen atom, D the distance to the galaxy (in this case assumed to be the distance to the Fornax cluster), X_{CO} is the CO-to-H_2 mass conversion factor, λ the rest wavelength of the line observed, k_{B} the Boltzmann constant, and $\int S_\nu \mathrm{d}v$ the total flux of the line observed. For X_{CO} I use the metallicity-dependent mass conversion factor α_{CO} from Accurso et al. (2017, eqn. 25):

$$\log \alpha_{\mathrm{CO}} = 14.752 - 1.623\,[12 + \log(\mathrm{O/H})] + 0.062\ \log\ \Delta(\mathrm{MS}), \tag{4.2}$$

where $12 + \log(\mathrm{O/H})$ is the metallicity as estimated according to §4.3.4, and Δ(MS) the distance from the main sequence (from Elbaz et al. 2007) as estimated in Chapter III. α_{CO} is then converted to X_{CO} by multiplying it by 2.14×10^{20}. Note that this prescription includes a correction for helium, however for convenience I will use $M_{\mathrm{H_2}}$ to refer to the total molecular gas mass. The results are listed in Table 4.1.

4.3.2 HI masses

HI masses are from Loni et al. (2021), who use the prescription from Meyer et al. (2017) to convert integrated fluxes to HI masses. A common distance of 20 Mpc was assumed for all galaxies, a negligable difference with the 19.95 Mpc assumed in this work. In cases where there is no detectable HI, upper limits are calculated. These are estimated as 3 × the local rms noise in the ATCA data cube, in one beam, and assuming the linewidths of the corresponding CO(1-0) lines from Chapter II. The resulting HI masses are summarised in Table 4.1.

4.3.3 Dust masses

Dust masses are estimated directly from the *Herschel* maps described in §4.2.3. To obtain FIR flux measurements for each galaxy, I perform aperture photometry, using the Python package photutils (Bradley et al., 2019). Reasonable aperture extents were determined by eye, such that they encompass the dust emission from the entire galaxy (typical semimajor axis-sizes vary from 15″ for small galaxies to 400″ for NGC1365, which is slightly smaller than the extent of the HI disc in that galaxy, and closer to the extent of its stellar disc). To ensure all flux is included even in the lowest-resolution image, I define apertures in the longest wavelength image in which the galaxy is detected. In case there is no detection in each band, upper limits from the non-detected bands are used to constrain the SED at those wavelengths, which is reflected in the uncertainties. Background noise was estimated locally, by defining annuli around the apertures chosen. The flux in these annuli is then subtracted from the measured source flux. Uncertainties were estimated by randomly placing 100 apertures of the same dimensions as the one used for the source randomly in the *Herschel* map, and calculating the standard deviation in these. This is done for each source in each of the 5 wavelengths. The maps used are parallel-mode scan maps that cover very large areas (roughly 4.6 × 4.6 degrees, corresponding to $\sim 1.6 \times 1.6$ Mpc at the distance of the Fornax cluster). This means that it is relatively easy to find 100 apertures that do not overlap with each other, and there is only a small probability of these random apertures overlapping with other sources. However, to exclude any such overlap from the noise estimate, the resulting flux distributions are clipped beyond 3 σ from the median.

For small sources, the SPIRE beam is often larger than the aperture used to measure the flux: the full width at half maximum (FWHM) is up to ∼35″, depending on the wavelength (see the SPIRE handbook[1], while the radii of the apertures are as small as 15″ for the smallest sources. To account for any missing flux as a result

of this, which might result in an underestimation of dust masses (and therefore an overestimation of gas-to-dust ratios), I apply aperture corrections. As the sources are not very extended at *Herschel* resolutions, I apply the recommended corrections for point-sources, provided as part of the SPIRE calibration (Ott, 2010; Bendo et al., 2013). These values depend on the aperture radius, which I estimate by taking the arithmetic average of the semi-major and semi-minor axes of the elliptical apertures.

Finally, dust masses are estimated from the resulting SEDs. Modified blackbody fits were performed, described by (a simplified version of) equation 1 in Hildebrand (1983):

$$F_\lambda = \kappa_\lambda \, B_\lambda \left(T\right) D^{-2} M_{\rm dust}, \tag{4.3}$$

where $M_{\rm dust}$ the dust mass in kg, D the distance to the galaxy in Mpc, B (T) Planck's law of blackbody radiation, and κ_λ is described by

$$\kappa_\lambda = \kappa_0 \left(\lambda_0/\lambda\right)^\beta, \tag{4.4}$$

where β is the dust opacity index, which is fixed at 1.790 to match the comparison sample (DustPedia, see §4.4), and κ is the dust emissivity, which is fixed at 0.192 $\rm m^2$ $\rm kg^{-1}$ at $\lambda = 350$ μm, again following the value used by DustPedia. Both constants adopted by DustPedia are drawn from The Heterogeneous dust Evolution Model for Interstellar Solids (THEMIS) model (Jones et al., 2013; Köhler et al., 2014; Ysard et al., 2015). The fits were performed using a custom SED fitter, which is based on PyMC3 (a Python package for Bayesian statistical modelling and Probabilistic Machine Learning focusing on advanced Markov chain Monte Carlo (MCMC) and variational inference (VI) algorithms, Salvatier et al. 2016). It was written to include all beam and colour corrections as part of the fitting process, and account for correlated uncertainties between bands.

For the (log) dust mass, a Gamma prior was used with a standard deviation of 1 dex. To ensure that the code can handle a wide range of dust masses (from a small region of a galaxy to a ULIRG), the mode is programmed to be the flux at the data point closest to the peak of the blackbody. For dust temperature, a Gamma distribution is used also, with a mode of 20K and a standard deviation of 6K. The Gamma distribution was chosen because it does not allow for unphysical negative dust temperatures. It is also wider than a Gaussian distribution, which more accurately reflects the wide range of dust mass and temperatures.

The assumed calibration uncertainties are 5% for PACS (Balog et al., 2014), and 1.7% for SPIRE (Bendo et al., 2013), as well as an additional correlated uncertainty of 5% between PACS bands and 4% between SPIRE bands. The correlated

and uncorrelated uncertainties were conservatively added linearly for the SPIRE data as recommended by the handbook[1], resulting in a total uncertainty of 5.5%. For an overview of the general limitations of SED fitting techniques (in particular, dust emission in the FIR appearing to be a blend of emission from dust at different temperatures), I refer the reader to Bendo et al. (2015).

4.3.4 Metallicities

Throughout this work, I use the oxygen abundance, 12 + log(O/H), as a proxy for the gas-phase metallicity. Metallicities are estimated from F3D emission-line measurements presented in Iodice et al. (2019b), and using the strong-line calibration from Dopita et al. (2016, referred to as DOP16 throughout the rest of this work). This calibration relies exclusively on the [NII]λ6484, S[II]$\lambda\lambda$6717, 31, and Hα lines, as follows:

$$12 + \log(\mathrm{O/H}) = 8.77 + \log[\mathrm{NII}]/[\mathrm{SII}] + 0.264\ \log[\mathrm{NII}]/\mathrm{H}\alpha. \tag{4.5}$$

It is independent of the ionisation parameter, flux calibration, and extinction correction, and valid for a wide range of oxygen abundances. The required emission-line fluxes were estimated by simultaneously fitting the spectral continuum and the nebular emission lines using Gas AND Absorption Line Fitting (GANDALF, Sarzi et al. 2006), which makes use of Penalized Pixel-Fitting (`PPXF`, Cappellari 2017) to derive stellar kinematic and corresponding absorption-line broadening. More details on this procedure can be found in Sarzi et al. (2018) and Iodice et al. (2019b). The resulting resolved metallicity measurements were averaged spatially to obtain global measurements.

Of course, the choice of metallicity calibrator can significantly impact the resulting metallicity estimates. As can be seen in e.g. Sánchez et al. (2019), who compare various metallicity calibrations as a function of stellar mass, and SFR, the DOP16 calibration shows a relatively steep gradient with stellar mass. It agrees reasonably well with the calibration from PP04 at the low-mass end, with an offset of $\sim$0.1 dex, while at the higher-mass end it over predicts metallicities by up to $\sim$0.4 dex compared to PP04. A similar study can be found in Appendix C of Kreckel et al. (2019). As a result, the use of a different metallicity calibrator would likely result in the higher metallicities becoming somewhat lower, and the opposite for the lowest metallicities. As we will see in §4.5, a different choice of metallicity calibrator (i.e. shifting the data along the x-axes of the figures showing gas-to-dust ratios as a function of metallicity, making the distribution more compact) would not affect

my results. More importantly, the DOP16 calibrator was applied to both the Fornax sample and the comparison sample, which means that the offset in gas-to-dust ratio as a function of metallicity between the two would not be different had I chosen another calibrator.

4.3.5 Stellar masses

Stellar masses are from the z = 0 Multiwavelength Galaxy Synthesis (z0MGS, Leroy et al. 2019) where available. These are based on data from the Wide-field Infrared Explorer (WISE, Wright et al. 2010) and the Galaxy Evolution Explorer (GALEX, Martin et al. 2005). Leroy et al. (2019) make use of data from the GALEX-SDSS-WISE Legacy Catalog (GSWLC, Salim et al. 2016, 2018), which combines WISE, GALEX, and Sloan Digital Sky Survey (SDSS) observations. In the GSWLC SED modeling with the Code Investigating GALaxy Emission (CIGALE, Burgarella et al. 2005; Noll et al. 2009; Boquien et al. 2019) was used to yield stellar mass estimates. In Leroy et al. (2019) these data are used to derive calibrations to estimate stellar masses from their sample of WISE and GALEX data. The IMF from Kroupa & Weidner (2003) was assumed.

If stellar masses are not available from z0MGS (this only applies to two dwarf galaxies, FCC090 and FCC306), they are taken from Fuller et al. (2014). Although the stellar masses in Fuller et al. (2014) are estimated differently from those in z0MGS, even a significant error in the stellar masses of these two dwarf galaxies would not affect my results. Stellar masses, along with their sources, are listed in Table 4.1. The two stellar masses that were taken from Fuller et al. (2014) are indicated with a ‡.

4.4 The DustPedia comparison sample

In order to compare the dust and gas in the cluster galaxies to those in the field, I use data from the DustPedia project. DustPedia[4] (Davies et al., 2017) covers all 875 extended galaxies within 3000 km s^{-1} observed by the *Herschel* Space Observatory. Here, I use a sub-sample of DustPedia, consisting of the 209 galaxies for which M_{H_2} measurements are available. This sample includes the *Herschel* Virgo Cluster Survey (HeViCS, Davies et al. 2010) sample from Corbelli et al. (2012). After eliminating Fornax galaxies, I split up this sample in Virgo galaxies and field galaxies. Galaxies are defined to be in the Virgo cluster if they are within twice the virial

[4] http://dustpedia.astro.noa.gr/

Table 4.2 Estimated gas-to-dust ratios and residuals of galaxies in the sample.

Object	Total gas/dust	res. ($M_\star$)	res. (Z)	M_{H_2}/dust	res. ($M_\star$)	res. (Z)	M_{HI}/dust	res. ($M_\star$)	res. (Z)
-	-	(dex)	(dex)	-	(dex)	(dex)	-	(dex)	(dex)
(1)	(2)	(3)	(4)	(5)	(6)	(7)	(8)	(9)	(10)
FCC067	110^{+20}_{-20}	-0.75	-	2^{+0}_{-0}	-1.97	-	100^{+10}_{-10}	-0.67	-
FCC090	460^{+150}_{-140}	-0.13	0.02	130^{+20}_{-20}	-0.26	-0.06	340^{+90}_{-90}	-0.18	-0.07
FCC121	150^{+20}_{-20}	-0.62	-	25^{+1}_{-1}	-0.96	-	120^{+10}_{-10}	-0.62	-
FCC167	60^{+10}_{-50}	-1	-0.65	36^{+3}_{-3}	-0.8	-0.05	≤ 25	-1.3	-0.55
FCC179	50^{+10}_{-50}	-1.06	-0.74	48^{+2}_{-2}	-0.68	-0.14	≤ 5	$\leq$-1.95	$\leq$-1.41
FCC184	70^{+10}_{-70}	-0.96	-0.62	60^{+3}_{-3}	-0.58	0.17	≤ 6	$\leq$-1.88	$\leq$-1.14
FCC235	760^{+200}_{-210}	0.09	-	$\leq 9^{+1}_{-1}$	$\leq$-1.39	-	750^{+200}_{-210}	0.17	-
FCC263	210^{+40}_{-40}	-0.48	-0.41	90^{+10}_{-10}	-0.42	-0.37	120^{+20}_{-20}	-0.63	-0.61
FCC282	140^{+30}_{-100}	-0.64	-	60^{+10}_{-10}	-0.57	-	≤ 79	-0.81	-
FCC285	200^{+100}_{-90}	-0.5	-0.57	$\leq 21^{+4}_{-4}$	$\leq$-1.04	$\leq$-1.52	170^{+90}_{-80}	-0.46	-0.53
FCC290	50^{+10}_{-10}	-1.06	-0.72	29^{+2}_{-2}	-0.9	-0.32	24^{+2}_{-2}	-1.31	-0.76
FCC306	8000^{+6000}_{-6000}	1.1	-	$\leq 4200^{+1300}_{-1300}$	$\leq$1.26	-	4000^{+3000}_{-3000}	0.85	-
FCC308	100^{+20}_{-20}	-0.79	-0.58	37^{+3}_{-3}	-0.79	-0.51	62^{+9}_{-9}	-0.91	-0.7
FCC312	240^{+30}_{-30}	-0.42	-0.21	90^{+10}_{-10}	-0.43	-0.15	150^{+10}_{-10}	-0.53	-0.32
FCC335	450^{+120}_{-270}	-0.14	-	140^{+20}_{-20}	-0.23	-	≤ 311	$\leq$-0.21	-

Notes: **1**: Object name according to the Fornax Cluster Catalogue; **2**: Total gas-to-dust ratio $((M_{HI} + M_{H_2})/D)$; **3**: Total gas-to-dust residual compared to the DustPedia median as a function of stellar mass (see Figure 4.1); **4**: Total gas-to-dust residual compared to the DustPedia median as a function of metallicity (see Figure 4.2); **5**: H_2-to-dust ratio; **6**: H_2-to-dust residual compared to the DustPedia median as a function of stellar mass (see Figure 4.3); **7**: H_2-to-dust residual compared to the DustPedia median as a function of metallicity (see Figure 4.4); **8**: HI-to-dust ratio; **9**: HI-to-dust residual compared to the DustPedia median as a function of stellar mass (see Figure 4.5); **10**: HI-to-dust residual compared to the DustPedia median as a function of metallicity (see Figure 4.6).

radius of the Virgo cluster, assumed to be 1.7 Mpc (Fukushige & Makino, 2001). This corresponds to $\sim 5.7^{o}$ at the distance to the Virgo cluster, here assumed to be 16.5 Mpc (Mei et al., 2007). Distances to individual DustPedia galaxies, adopted from the DustPedia database, are redshift-independent distance estimates from HyperLEDA where available, and redshift-independent estimates from the NASA/IPAC Extragalactic Database (NED) if not (more details on redshift-independent distance estimates by HyperLEDA and NED can be found in Makarov et al. 2014 and Steer et al. 2017, respectively). If both are unavailable, bulk flow-corrected redshift-derived values provided by NED are used, assuming a Hubble constant of $H_0 = 73.24$ km s^{-1} Mpc^{-1} (Riess et al., 2016). Finally, I create an additional sub-sample of Virgo galaxies located inside the cluster virial radius.

H_2 masses for DustPedia galaxies were compiled and homogenised from a wide variety of sources by Casasola et al. (2020). I use their M_{H_2} estimates that were derived using a fixed X_{CO}, which I recalibrate to match the metallicity-dependent prescription used in this work.

I adopt dust masses estimated using a modified blackbody model, scaled to match the emissivity of $\kappa = 0.192\frac{m^2}{kg}$ at 350 μm, used to estimate dust masses of the Fornax sample, and a β-value of 1.790 (Nersesian et al., 2019).

To maximise consistency with my Fornax sample, rather than adopting published metallicities, I apply the DOP16 calibration to the (extinction corrected) *line ratios* from De Vis et al. (2019). I average metallicities from all detected star forming regions for each galaxy, consistent with the spatially averaged metallicities used to estimate global metallicities in the Fornax sample. Details on the line flux measurements of the DustPedia sample can be found in De Vis et al. (2019) and on the DustPedia website.

DustPedia HI fluxes were compiled from the literature (Casasola et al., in prep.) and converted to M_{HI} using

$$M_{HI} = 2.36 \times 10^5 f_{HI}\ D^2, \tag{4.6}$$

where f_{HI} is the compiled HI flux in Jy km s^{-1} and D the best distance measurement from Clark et al. (2018) in Mpc. More details and references can be found in De Vis et al. (2019).

Stellar masses of the DustPedia sample were taken from z0MGS, as described in §4.3.5. This means that the stellar masses of the DustPedia sample are fully consistent with the vast majority of the Fornax sample, with the exception of only the two objects discussed in §4.3.5.

Thus, as explained above, the dust, H_2, HI, and stellar masses I use here are calculated identically for both Fornax and the DustPedia comparison sample, and so can be directly compared.

4.4.1 Other literature samples

There are several other literature samples which have molecular gas, atomic gas, and dust masses available, as well as stellar masses and/or metallicities. These include the samples compiled by Rémy-Ruyer et al. (2014), such as the Dwarf Galaxy Survey (DGS, Madden et al. 2013), and Key Insights on Nearby Galaxies: a Far-Infrared Survey with *Herschel* (KINGFISH, Kennicutt et al. 2011), the sub-sample of LITTLE THINGS from Cigan et al., in prep., and several others. Unfortunately, it has proven impossible to recalibrate these samples to rely on the same assumptions as the Fornax and DustPedia samples studied here. Therefore, they were not included in this work. Homogenising these datasets to follow the same assumptions used here (as far as is possible) suggests the conclusions above also hold in comparison to these samples.

4.5 Analysis

4.5.1 Gas-to-dust ratios

In order to examine the effect of the Fornax cluster environment on the gas and dust in galaxies, I construct gas-to-dust ratios for the sample galaxies (listed in Table 4.2). I also tabulate the offset between the gas-to-dust ratio of each Fornax galaxy and the median gas-to-dust ratio of field galaxies at the same stellar mass, and metallicity for the nine galaxies for which MUSE data from F3D is available, (calculated using the DustPedia field galaxy sample). For comparison, I also include the DustPedia Virgo galaxies in my analysis. Total gas-to-dust ratios are shown in Figures 4.1 and 4.2, as a function of stellar mass, and metallicity, respectively. Similarly, Figures 4.3 and 4.4 show the H_2-to-dust ratio, and Figures 4.5 and 4.6 the HI-to-dust ratio. Fornax galaxies are plotted as diamond-shaped markers. Galaxies with regular molecular gas reservoirs are shown in black, and those with disturbed molecular gas reservoirs in red (as classified in Chapter II). CO upper limits (for which the molecular gas morphology is unknown) are shown in purple. Virgo galaxies are shown in orange, with galaxies inside the virial radius highlighted with larger markers. The DustPedia field sample is shown with grey markers. Upper limits are shown as downward-facing

triangles for all samples. The solid, grey line represents the rolling median of the DustPedia field sample, which is calculated using bins with a fixed number of 10 galaxies, overlapping by half a bin size. The bottom panels in these figures show the residuals of Fornax and Virgo galaxies compared to this median, which is shown as a black solid line, or a black dashed line where extrapolated.

In Figures 4.1 and 4.2 I can see that total gas-to-dust ratios in the Fornax cluster are low compared to the field, both at fixed stellar mass, and metallicity. This also applies to galaxies in the Virgo cluster, especially inside its virial radius. Figures 4.3 and 4.4 show that molecular gas-to-dust ratios are also decreased in the Fornax cluster compared to the field. However, galaxies in the Virgo cluster show the opposite result: they are (marginally, but systematically) increased compared to the field. Finally, Figures 4.5 and 4.6 show that HI-to-dust ratios are decreased in both the Fornax and Virgo clusters, although the difference between the Virgo cluster and the field is smaller if galaxies located inside $2R_{\rm vir}$ are included. In the Fornax cluster there is no significant difference in gas-to-dust ratio between galaxies with regular and disturbed CO reservoirs in any of the Figures.

I quantify the results described above by applying Kolmogorov-Smirnov (KS) tests and Anderson-Darling (AD) tests to the residuals of the Fornax and Virgo data compared to DustPedia in all six Figures. Because these tests do not take into account uncertainties, I use a Monte Carlo approach to make sure these are implemented in the final result. I perturb each value by a random number drawn from a normal distribution with μ the measured value and σ the associated uncertainty. This is done 10^6 times, after which the μ and σ of the resulting distribution of the KS and AD statistics are adopted as the test results. These are are summarised in Table 4.3. The KS statistic is between 0 and 1, and the closer to 1 it is, the less likely it is that both samples are drawn from the same distribution. The AD test returns a statistic (referred to as the A2 statistic) as well as corresponding critical values at a discrete number of confidence intervals. The null-hypothesis that both samples are drawn from the same distribution can be rejected with a certain probability if the difference between the A2 statistic and the critical level is positive at the corresponding confidence level. In Table 4.3 I report the difference between the A2 statistic and the critical value at 0.1%.

Both tests return similar results in all cases. In almost all cases, the null-hypothesis that the Fornax and Virgo samples are drawn from the same distribution as the DustPedia field sample can be rejected. The exception is the Fornax HI mass as a function of stellar mass, for which the spread in both statistics is too large to draw strong conclusions.

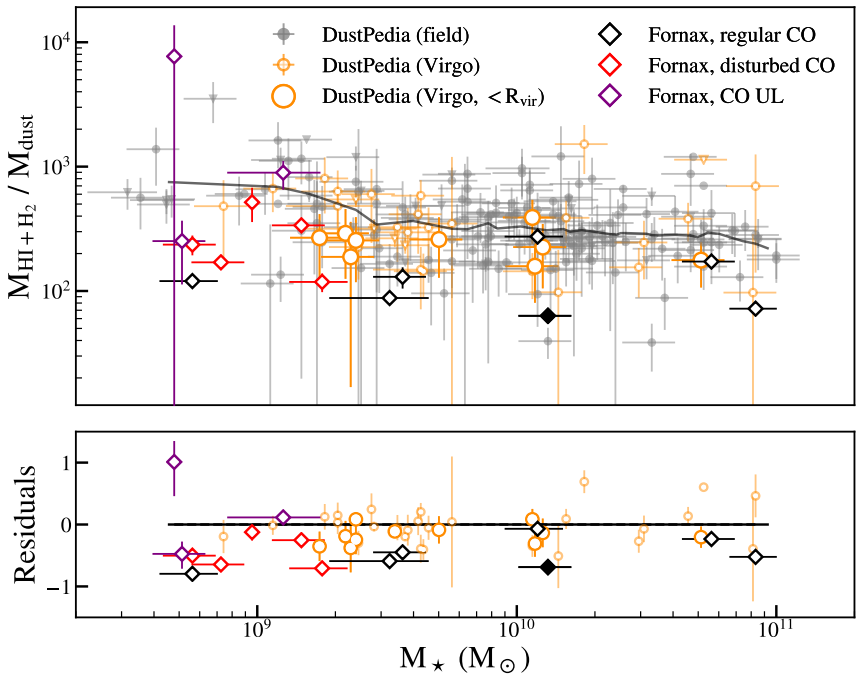

Figure 4.1: *Upper panel*: Total gas-to-dust (HI + H_2) ratios in the Fornax cluster compared to those in the DustPedia (Davies et al., 2017) field (grey) and Virgo (orange) samples. Virgo galaxies inside $R_{\rm vir}$ are highlighted with larger markers. Fornax galaxies are indicated with diamond-shaped markers, in black for galaxies with regular CO emission and in red for galaxies with disturbed CO emission as classified in Chapter II (upper limits are shown in purple). NGC1436 (see §4.6) is indicated with a filled diamond-shaped marker. Upper limits are indicated with downward-facing triangles for all samples. The solid grey line indicates the rolling median of the DustPedia field sample *Lower panel*: Residuals of gas-to-dust ratios in Fornax and Virgo cluster galaxies compared to the rolling median of DustPedia field galaxies, shown as a solid line, or a dashed line where extrapolated. Note that, for the purpose of visibility, the bottom panel is set to show values between -1.5 and 1.5, which causes the strongly discrepant galaxy FCC067 (NGC1351A) to fall off the plot in some of the following figures. According to KS tests, Fornax galaxies and Virgo galaxies inside $R_{\rm vir}$ have systematically lower gas-to-dust ratios than field galaxies at fixed stellar mass (see Table 4.3).

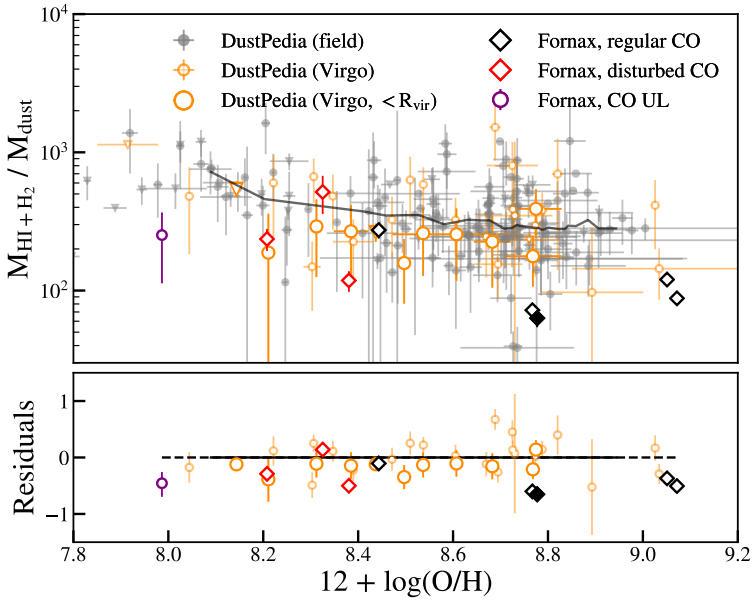

Figure 4.2: Similar to Figure 4.1, showing total gas-to-dust ratios as a function of metallicity for a sub-sample of Fornax galaxies for which MUSE data is available from F3D (see Table 4.1). Fornax cluster galaxies and Virgo galaxies inside $R_{\rm vir}$ have systematically lower gas-to-dust ratios than field samples.

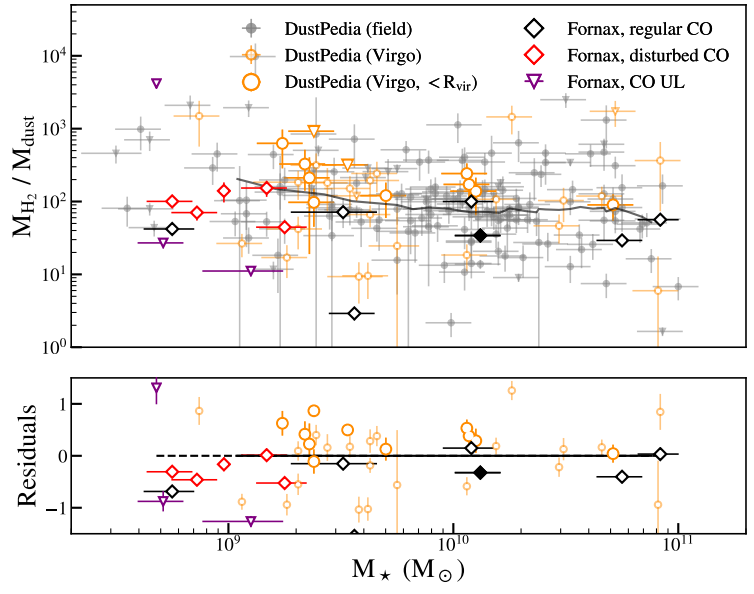

Figure 4.3: Similar to Figure 4.1, but showing molecular gas-to-dust ratios plotted as a function of stellar mass. Fornax cluster galaxies have systematically lower molecular gas-to-dust ratios than field galaxies, whereas Virgo galaxies inside $R_{\rm vir}$ show *in*creased H_2-to-dust ratios.

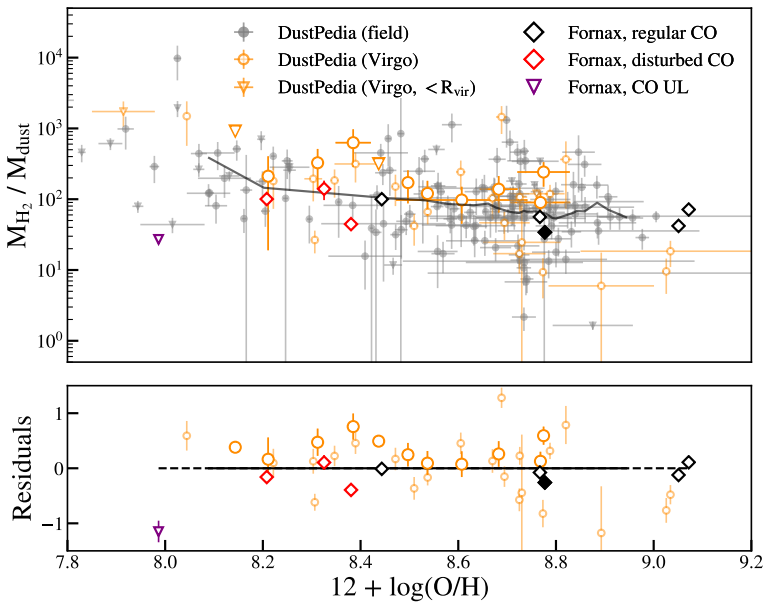

Figure 4.4: Similar to Figure 4.2, but showing molecular gas-to-dust ratios as a function of metallicity. Molecular gas-to-dust ratios of Fornax galaxies are systematically lower than those of field galaxies at fixed metallicity, while those inside the virial radius of the Virgo cluster are *in*creased.

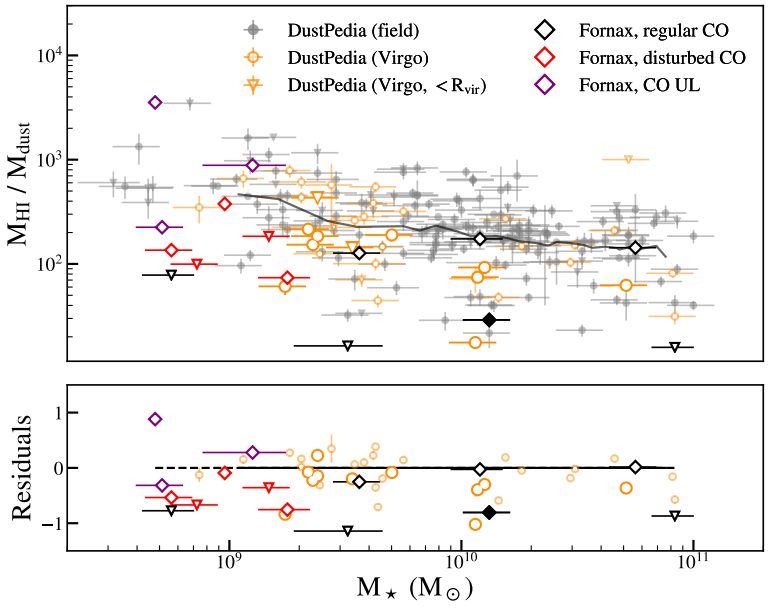

Figure 4.5: Similar to Figure 4.1, but showing HI-to-dust ratios as a function of stellar mass. Fornax galaxies and Virgo galaxies inside the virial radius have systematically lower HI-to-dust ratios than galaxies in the field at fixed stellar mass. A possible decrease is also seen in Virgo galaxies between 1 and 2 $R_{\rm vir}$.

Table 4.3 Results of a Monte Carlo analysis of KS and AD tests applied to the residuals (data of the respective clusters compared to the rolling median of the DustPedia field sample) in Figures 4.1 through 4.6.

			Fornax		Virgo (inside $R_{\rm vir}$)		Virgo (inside $2R_{\rm vir}$)	
Figure	x-axis	y-axis	D statistic	A2 - crit.	D statistic	A2 - crit.	D statistic	A2 - crit.
(1)	(2)	(3)	(4)	(5)	(6)	(7)	(8)	(9)
4.1	$M_\star$	M_{HI+H_2}	0.98 ± 0.005	28 ± 1	0.98 ± 0.05	22 ± 2	0.98 ± 0.06	59 ± 6
4.3	$M_\star$	M_{H_2}	0.89 ± 0.01	17 ± 2	0.89 ± 0.07	8 ± 3	0.87 ± 0.12	31 ± 9
4.5	$M_\star$	M_{HI}	0.79 ± 0.28	12 ± 12	0.99 ± 0.14	20 ± 6	0.99 ± 0.15	49 ± 12
4.2	12 + log(O/H)	M_{HI+H_2}	0.99 ± 0.03	17 ± 1	0.99 ± 0.04	20 ± 2	0.99 ± 0.04	46 ± 4
4.4	12 + log(O/H)	M_{H_2}	0.99 ± 0.006	17 ± 1	0.99 ± 0.04	20 ± 2	0.98 ± 0.06	46 ± 4
4.6	12 + log(O/H)	M_{HI}	0.99 ± 0.04	17 ± 2	0.99 ± 0.09	20 ± 4	0.99 ± 0.08	46 ± 6

Notes: **1**: reference to the Figure showing the data the KS test is applied to; **2**: x-axis of that Figure; **3**: y-axis of that Figure; **4, 6, 8**: D-statistic resulting from the KS test applied to the Fornax, Virgo inside $R_{\rm vir}$, and Virgo inside $2R_{\rm vir}$ data, respectively, including uncertainties from a Monte Carlo analysis; **5, 7, 9**: difference between the A2 statistic and critical value at the 0.1% confidence level resulting from an Anderson-Darling test applied to the Fornax, Virgo inside $R_{\rm vir}$, and Virgo inside $2R_{\rm vir}$ data respectively;

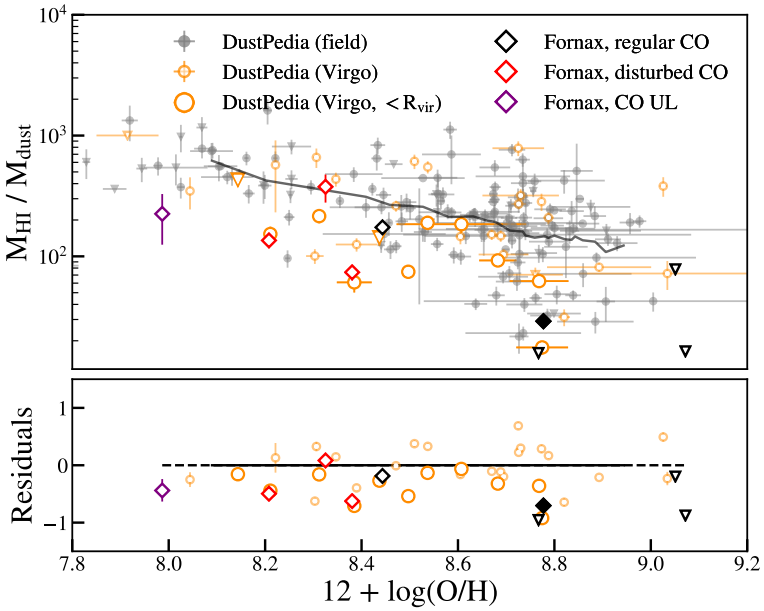

Figure 4.6: Similar to Figure 4.2, but showing HI-to-dust ratios as a function of metallicity. These are systematically lower in Fornax cluster galaxies and Virgo galaxies inside $R_{\rm vir}$ compared to field galaxies at fixed metallicity.

4.5.2 Variation with cluster-centric distance

In Figure 4.7 I show gas-to-dust ratios as a function of projected cluster-centric distance for both clusters, which are represented by the same colours as in previous Figures. These distances are normalised by each cluster's virial radius, indicated by a black dashed line. There is no clear relation between gas-to-dust ratio and cluster-centric radius for either of the clusters, although there is a possible increase in gas-to-dust ratio with cluster-centric radius in the Virgo cluster (a Kendall's Tau test returns a tau statistic of 0.23 and a p-value of 0.04). In the Virgo cluster, there is evidence that HI deficiencies decrease with cluster-centric radius (e.g. Haynes & Giovanelli 1986, Gavazzi et al. 2005), which could explain this possible trend. If HI deficiencies were the main driver of the decreased gas-to-dust ratios in the Fornax cluster, we might expect to also see such a trend in this cluster. However, no such trend is seen in Figure 4.7, although I only have a small sample of Fornax cluster objects.

4.5.3 Gas and dust fractions

To better understand whether the decreased H_2-to-dust ratios in the Fornax cluster are mostly the result of increased dust fractions, or decreased H_2 fractions, I show these as a function of stellar mass in Figure 4.8 (Figure 4.8a shows dust fractions

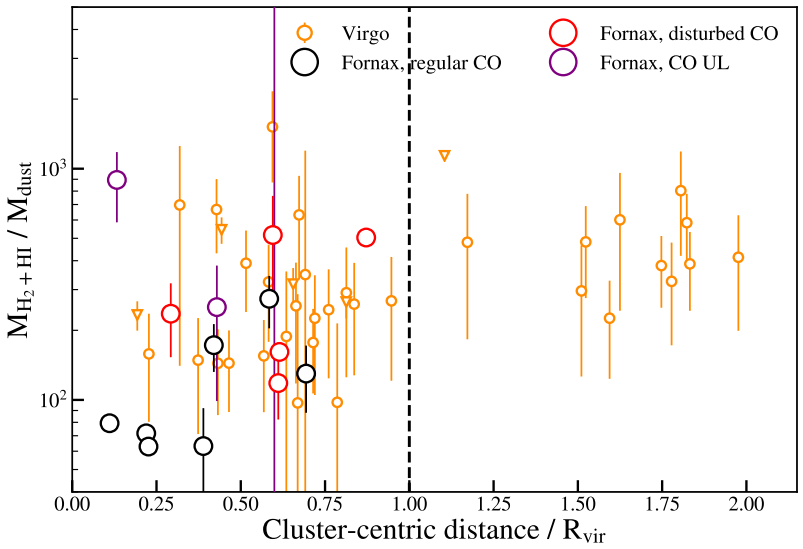

Figure 4.7: Total gas-to-dust ratios as a function of relative (projected) distance to the cluster centre are shown with colours and markers similar to those in Figure 4.3. The virial radius is indicated with a black dashed line. No significant gradient in gas-to-dust fractions is observed in any of the clusters, although there is possibly a slight increase in gas-to-dust radio with cluster-centric radius in the Virgo cluster (a Kendall's Tau test returns a tau statistic of 0.23 and a p-value of 0.04).

and Figure 4.8b H_2 fractions). Markers and symbols are the same as in previous figures. The dust content in most Fornax galaxies is normal to low compared to the DustPedia field sample, with the exception of a few dwarf galaxies, and NGC1365 at the high-mass end. The scatter in the H_2 fractions in Figure 4.8b is similar to that in Figure 4.8a, however there is a more pronounced systematic offset towards lower H_2 fractions in the Fornax cluster compared to the field. This suggests the difference seen in the Fornax cluster is driven by the lower H_2 content of these galaxies. In Virgo dust fractions are normal to slightly decreased inside the virial radius, whereas H_2 fractions are increased, especially in low-stellar mass galaxies. Outside R_{vir} no difference with the DustPedia field sample is seen.

4.5.4 DUST-TO-METAL RATIOS

A different way of visualising what fraction of metals are locked up in dust relative to gas, is to show dust-to-metal ratios: the ratio of the dust mass and the total metal-mass in the galaxy. Since dust consists exclusively of metals, the ratio of the total metal mass and the dust mass is a measure of how much of the metal content in the ISM is locked up in dust grains. To estimate these, I use the prescription by

De Vis et al. (2019):

$$M_Z \equiv f_Z \times M_g + M_d, \tag{4.7}$$

where M_g is the total gas mass, M_d the dust mass, and f_Z is the fraction of metals by mass calculated using

$$f_Z = 27.36 \times \mathrm{O/H}. \tag{4.8}$$

The factor 27.36 comes from the assumption that the Solar metallicity is 12 + log(O/H) = 8.69, and the Solar metal mass fraction Z = 0.0134 (Asplund et al., 2009). Using this method I should keep in mind that, in reality, oxygen abundance does not scale directly to the total metal mass, as the oxygen-to-total metal ratio can vary depending on star formation history and stellar metallicity. Similarly, the fraction of oxygen locked up in dust grains does not scale directly with the amount of metals locked up into them, as this depends on the dust composition. Keeping in mind these caveats, the result is shown in Figure 4.9; in Figure 4.9a as a function of stellar mass, and in Figure 4.9b as a function of metallicity. Markers and symbols are the same as in previous figures. In both panels, dust-to-metal ratios in the Fornax cluster are significantly increased compared to those in the field. This implies that a relatively large fraction of the metals in Fornax galaxies are locked up in dust. A similar, though less significant, difference is seen in Virgo galaxies inside R_{vir}. There is no significant difference between Virgo galaxies outside R_{vir} and the DustPedia field sample.

4.6 Resolved gas-to-dust ratios in NGC1436

Any (radial) trend in the gas-to-dust ratio could give us a hint as to what process might be responsible for the low gas-to-dust (total, H_2, and HI) ratios observed (e.g. the outside-in removal of dust). To investigate whether there might be any radial H_2-to-dust gradients present in these Fornax galaxies with low gas-to-dust ratios, and whether the H_2-to-dust ratio differs between star forming and more passive regions, I study the spatially resolved H_2-to-dust ratio in NGC1436. While it would be preferred to study resolved total gas-to-dust ratios, this is not feasible, as the ATCA beam is >20 times larger than the ALMA beam (and a similar size to the entire molecular disc of this object). This will be done in a future paper (Loni et al., in prep.), after completion of the MeerKAT Fornax Survey (Serra et al., 2016).

NGC1436 is an almost face-on, flocculent spiral (Figure A.11, see also Chapter II and Chapter III), making it an ideal candidate to study resolved properties of cluster galaxies in more detail, and currently the only galaxy in the sample for which this

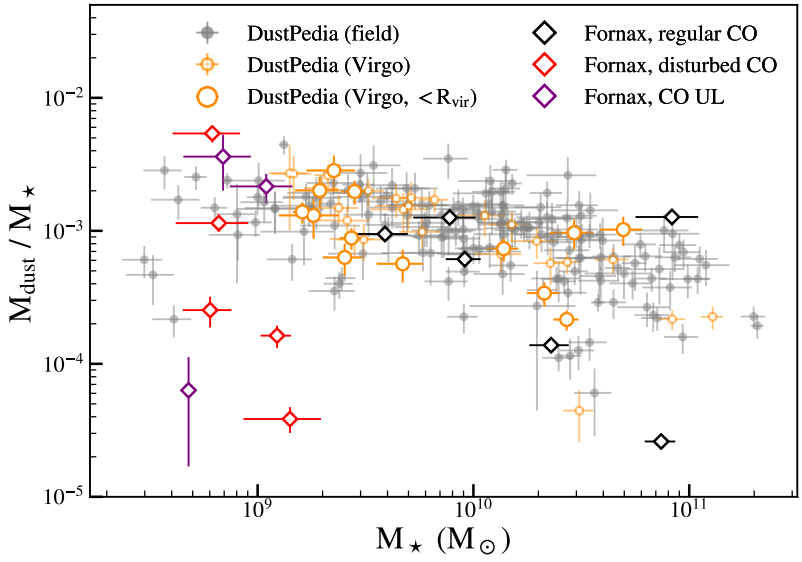

(a)

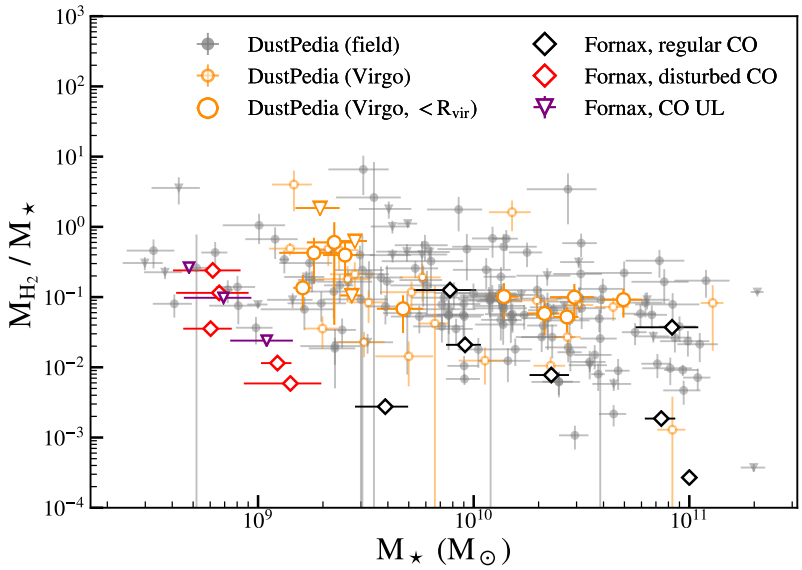

(b)

Figure 4.8: Dust- and molecular gas-to-stellar mass fractions (panel a and panel b, respectively) in the Fornax cluster compared to the field and the Virgo cluster. Samples and symbols are the same as in previous figures. While both are low, molecular gas-to-stellar mass fractions in the Fornax cluster are especially low compared to the field and the Virgo cluster. The dust content in the Virgo cluster is normal to slightly decreased, whereas molecular gas-to-stellar mass fractions are normal to slightly increased, in particular at low stellar mass.

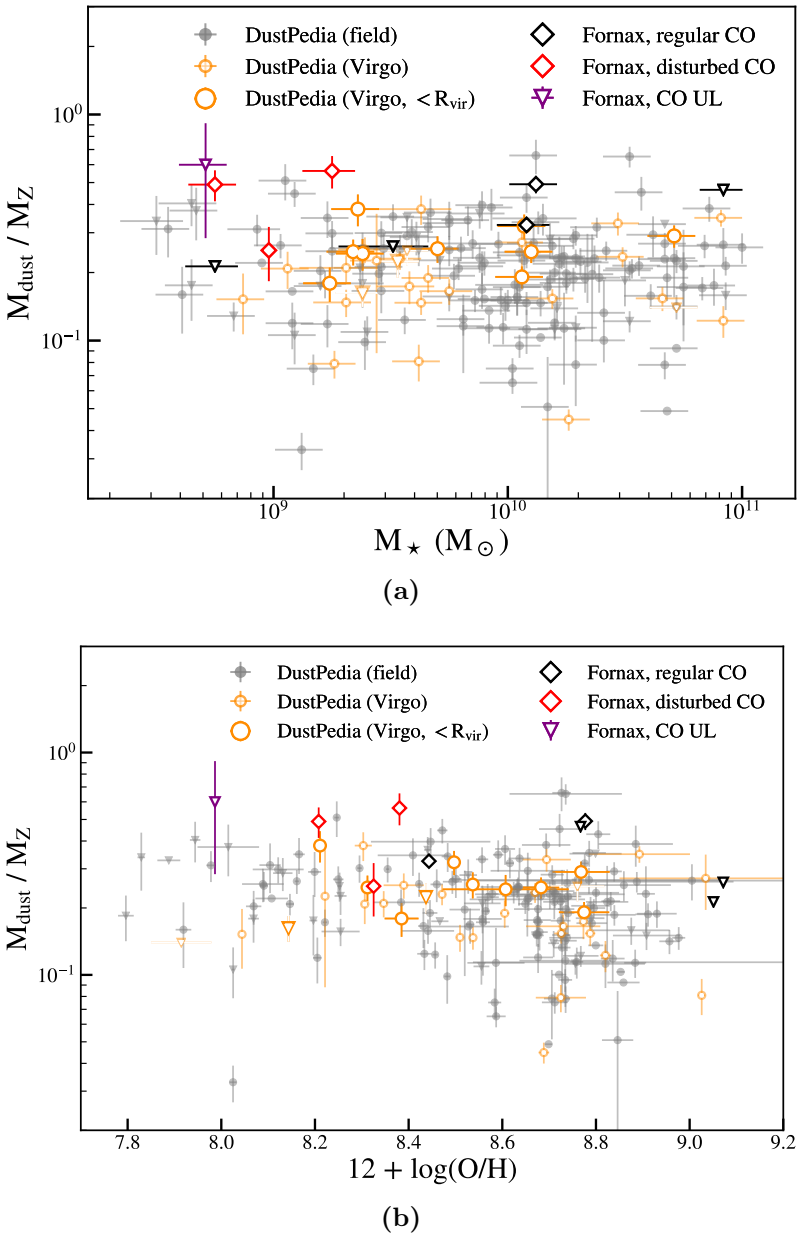

Figure 4.9: Dust-to-metal ratios as a function of stellar mass (panel a) and metallicity (panel b). Samples and symbols are the same as in previous figures. Dust-to-metal ratios in Fornax cluster galaxies are significantly higher than those in field galaxies of similar mass and metallicity, which means that a relatively large fraction of the metals in these galaxies are locked up in dust grains. Virgo galaxies inside $R_{\rm vir}$ also show a slight, but less significant, increase in dust-to-metal ratio at fixed stellar mass. This difference is less clear at fixed metallicity.

is possible. NGC1436 is highly HI-deficient, and has a high H_2-to-HI ratio (Loni et al., 2021). It has been suggested that this galaxy is undergoing a morphological transition into a lenticular, based on the absence of a clear spiral structure in its outer regions (Raj et al., 2019). From Figures 4.1 through 4.5, where NGC1436 is highlighted with a filled diamond symbol, we can see that it has a decreased gas-to-dust ratio, and that this is partly driven by a decreased H_2-to-dust ratio, in addition to a decreased HI-to-dust ratio. To ensure I have as complete as possible information on the CO emission, I combine my AlFoCS data with deep observations from the ALMA archive (project ID: 2017.1.00129.S, PI: Kana Morokuma). As part of this program NGC1436 was observed on 30 November 2017 using the Morita array (see Morokuma-Matsui et al. 2019 for a description of the data for NGC1316 from this survey). Its primary beam size is $\sim 90''$ at $\sim$115 GHz, and the total area covered is $\sim$182 square arcseconds. The spectral window covering the ^{12}CO(1-0) was centred on 114.756 GHz, with a bandwidth of 1.875 GHz, covering 3840 channels. The spectral resolution is 5.06 km s^{-1}.

I reduced this data using the CASA pipeline (version 5.4.0-68, McMullin et al. 2007) before combining it with my own data using the task CONCAT. I then imaged the resulting data set by cleaning it interactively, using the task TCLEAN (Högbom, 1974). A Briggs weighting scheme was used (Briggs, 1995) with a robust parameter of 0.5. The pixel size in the final datacube is $0\farcs5$, and the velocity resolution is 10 km s^{-1}. The synthesised beam size is $\sim 2.68 \times 2.06''$. The sensitivity reached is $\sim$2.046 mJy/beam.

Resolved dust surface-densities are estimated using PPMAP. PPMAP (Marsh et al., 2015) is a Bayesian point-process fitting algorithm that produces image cubes of differential column-density as a function of dust temperature and position. Unlike traditional SED fitting techniques which require all images to be convolved to match the angular resolution of the lowest resolution image, PPMAP uses all images in their native resolution (PSFs of each image are also taken as inputs). In my case, this means that I can estimate and plot dust column densities in NGC1436 at the PACS 100 μm resolution (FWHM $\approx 10''$), the highest resolution of the range of *Herschel* images used to estimate its dust properties.

The resulting images are shown in Figures 4.10 and 4.11. In the upper-left panel of Figure A.11 the extent of the CO (red) and dust (orange) emission is shown (both are clipped to the 3σ level), overplotted on an optical *ugb*-image from the FDS. In the upper-right panel H_2-to-dust ratios within the galaxy are shown. The bottom-left and bottom-right panels show the H_2 and dust surface densities, respectively.

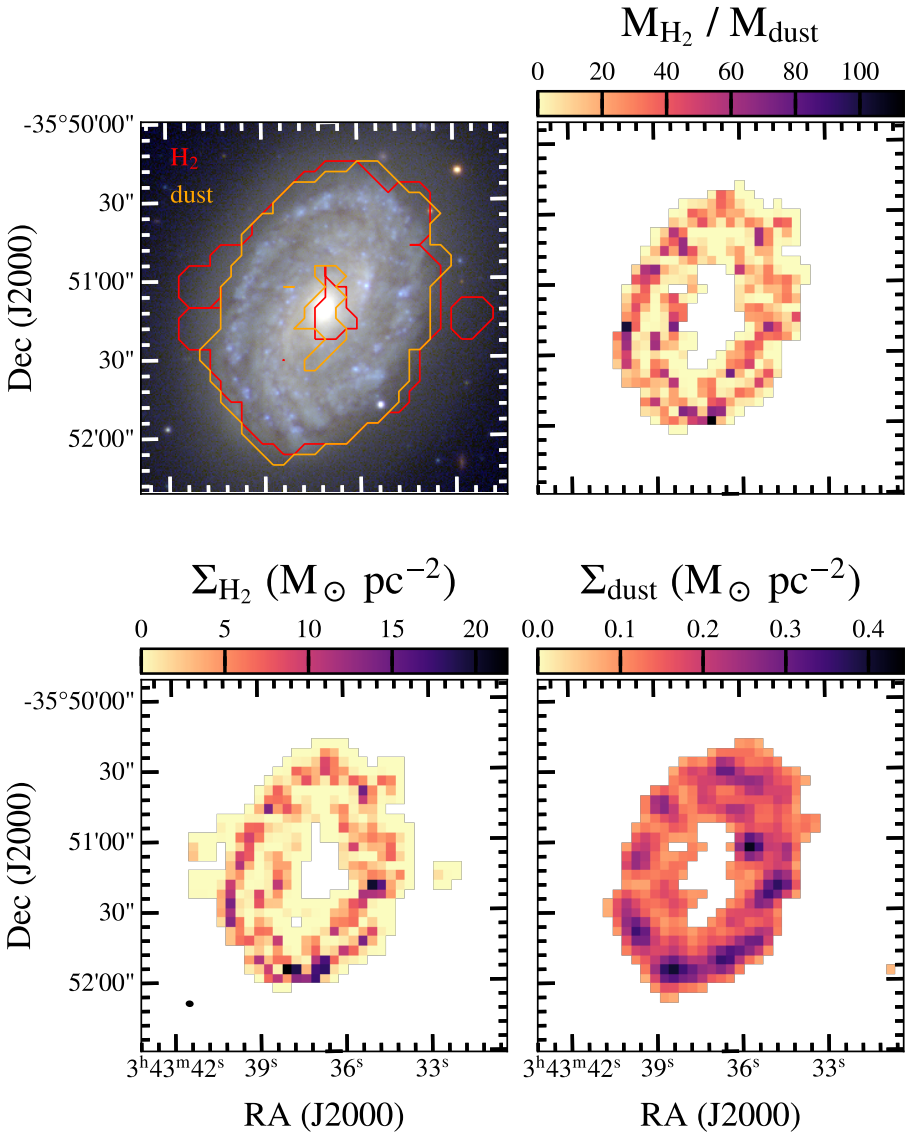

Figure 4.10: Resolved H_2 and dust properties in the flocculent spiral NGC1436. *Upper left panel:* optical *ugb*-image with the extent of the H_2 (red) and dust (orange) emission overplotted. *Upper right panel:* resolved H_2-to-dust ratios. *Lower-left panel:* H_2 surface density at the resolution of the PACS 100 μm emission. *Bottom-right panel*: dust surface density at the PACS 100 μm resolution from PPMAP. The beam of the CO observations is shown in the bottom-left corner of the bottom-left panel. There is no clear spatial trend in the H_2-to-dust ratios in this galaxy.

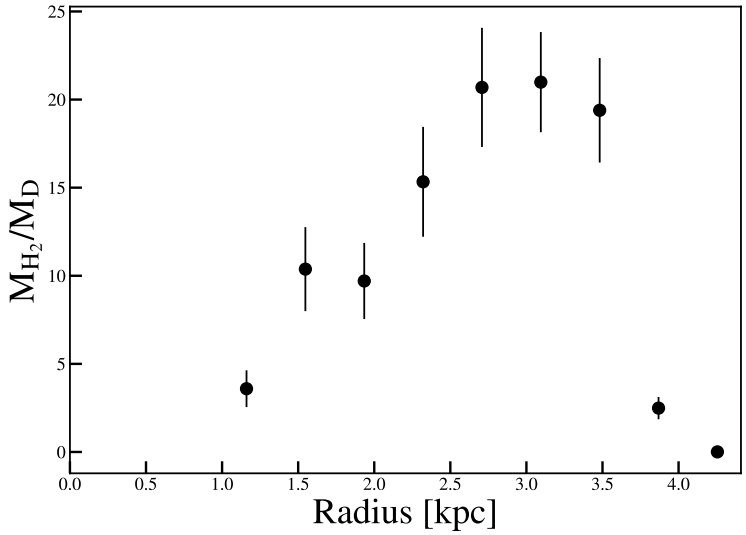

Figure 4.11: Radial profile of the H_2-to-dust ratio in NGC1436. It increases with radius, and drops off sharply at $R \approx 3.5$ kpc. The observed gradient implies that outside-in stripping of the gas/dust disc could result in lower integrated H_2-to-dust ratios. It could also imply that dust is more easily removed from the outer parts of the disc than molecular gas.

Figure 4.11 shows the radial profile of the H_2-to-dust ratio, corresponding to the top-right panel in Figure A.11. Each marker corresponds to the average H_2-to-dust ratio in an elliptical annulus (the sum of the ratio in each pixel divided by the total area of the annulus) at each radius, where the radius corresponds to the semi-major axis of the annulus.

There are small-scale variations in the H_2-to-dust ratio. Peaks in the H_2-to-dust ratio appear to mainly correlate with peaks in the H_2 surface density. There is an increase in H_2-to-dust ratio with radius, after which it drops off sharply at $R \approx 3.5$ kpc. This means that the outside-in stripping of the gas/dust disc could result in lower integrated H_2-to-dust ratios. It could also mean that dust is more easily removed from the outer parts of the disc than molecular gas, causing the gradient observed.

The average H_2-to-dust ratio does not exceed $\sim$20 at any radius. This suggests that molecular gas, and likely also dust, can be affected by environment even in the inner parts of galaxies. A comparison with the star formation dominated Hα map from MUSE (from F3D, see §4.2.5) shows no clear correlation between star forming regions and variations in the H_2-to-dust ratio.

4.7 Discussion

4.7.1 Low gas-to-dust ratios in the Fornax cluster

In §4.5.1 I have shown that gas-to-dust ratios in Fornax galaxies are suppressed compared to a field comparison sample at fixed stellar mass and metallicity. Decreased total gas-to-dust ratios might be expected in clusters as a result of stripping and truncation of HI discs, which typically have scale lengths much larger than H_2. Indeed, this is observed both in Fornax cluster galaxies and Virgo galaxies (Figures 4.1 and 4.2). The low gas-to-dust ratios in the Fornax cluster are partly driven by decreased HI-to-dust ratios compared to field galaxies at fixed mass (Figures 4.5 and 4.6). However, these low HI-to-dust ratios are not the full story. H_2-to-dust ratios are also significantly decreased in the Fornax cluster (Figures 4.3 and 4.4). In Figure 4.8 we can see that, while dust fractions are decreased in the Fornax cluster compared to field galaxies at fixed stellar mass (panel a), molecular gas fractions are even more strongly decreased (panel b). Broadly, there are three ways in which we could end up with the H_2-to-dust ratios observed:

1. H_2 is destroyed/removed more efficiently than dust,
2. both dust and H_2 are destroyed, but the dust reservoir is replenished more efficiently than the H_2 reservoir,
3. the physics of the ISM in these cluster galaxies is unusual such that "standard" observational probes fail to return accurate H_2-to-dust ratios.

Option (i): H_2 is destroyed/removed more efficiently than dust

Molecular gas could be destroyed/removed more efficiently than dust by the cluster environment if the sample galaxies had strong radial H_2-to-dust gradients, and their gas discs were truncated from the outside in (i.e. by ram pressure stripping). If this is the case, we are seeing the "relic" of a gas/dust reservoir that was larger before the galaxies fell into the cluster. This could alter the total H_2-to-dust mass ratio I would measure. For example, Bekki (2014) shows that ram pressure stripping can lead to more centrally concentrated star formation. Studies of nearby galaxies and galaxies in the Virgo cluster are inconclusive as to whether such radial molecular gas-to-dust ratios are observed. Several studies suggest that observed molecular gas-to-dust gradients are driven by a metallicity gradient (i.e. a radial change in X_{CO}, Bendo et al. 2010; Magrini et al. 2011; Pappalardo et al. 2012). Therefore, it is unclear whether an actual (non-X_{CO}-driven) gradient in gas-to-dust ratio is also present. Cortese et al.

(2010) find that the dust discs of HI-deficient galaxies are truncated as well as the HI discs. Corbelli et al. (2012) find that gas-to-dust ratios decrease as HI-deficiency increases, but only up to a certain deficiency threshold, after which they remain constant. HI-deficiency is defined as the difference between the observed HI mass and that expected in an isolated galaxy. This is because in highly disturbed galaxies both gas and dust are stripped from the inner parts of the galaxies. However, they also find stronger dust than H_2 deficiencies in these galaxies. This suggests that, although HI-deficient galaxies have lower gas-to-dust ratios, and both H_2 and dust can be stripped from their inner parts, H_2-to-dust ratios in these galaxies remain constant, or even increase slightly. This is also observed by Cortese et al. (2016) and in Virgo galaxies in this work, and is discussed further in §4.7.2. Since truncation of the gas/dust disc is concluded to result in an *in*crease in H_2-to-dust ratios in these two studies, which is also seen here in the Virgo cluster, it is unlikely to be the explanation for the H_2-to-dust ratios observed in Fornax. Observations of the molecular gas and dust in FCC167 (NGC1380, included in this sample) show a nested ISM, in which the dust extends further out than the molecular gas (Viaene et al., 2019). This could indeed mean that the molecular gas in this galaxy was stripped more severely than the dust. However, the molecular gas disc in this galaxy is extremely truncated (e.g. Chapter II, Viaene et al. 2019), and it is unclear how representative this is for the rest of the sample. The observed radial increase in H_2-to-dust ratio in NGC1436 (see Figure 4.11) suggests that the stripping of the outer parts of the disc could indeed result in lower integrated H_2-to-dust ratios.

Figure 4.12 shows a histogram of the ratio of R_{CO} and effective radius R_e (as estimated from the FDS, Peletier et al. 2020; Venhola et al. 2018; Iodice et al. 2019a; Raj et al. 2019) in the Fornax cluster (crimson) compared to this ratio in a field sample of gas-rich early-type galaxies (ETGs) from ATLAS^{3D} (Davis et al., 2013) and nearby spiral galaxies from the Berkeley-Illinois-Maryland Association Survey of Nearby Galaxies (BIMA SONG, Regan et al. 2001) in lilac. Although the numbers are small, there is no evidence that Fornax cluster galaxies have smaller R_{CO}/Re than the field sample (a KS test is not able to reject the null-hypothesis that the Fornax and ATLAS^{3D}/BIMA SONG samples are drawn from the same distribution, D=0.29, p=0.5 $\sim 0.67\sigma$).

In order to more generally test whether truncation could play a significant role in creating low H_2-to-dust ratios, I create a toy model consisting of an exponential gas/dust disc, with a molecular gas-to-dust ratio that increases linearly outward. I then explore the parameter space describing the shape of the exponential disc and the molecular gas-to-dust gradient resulting in the observed H_2 deficiencies (see table

3 in Chapter ii) and molecular gas-to-dust ratios, using a Markov chain Monte Carlo approach. I fix H_2 deficiencies and molecular gas-to-dust ratios at the more conservative observed values of 1 and 200, respectively, before truncation, and -1 and 100, respectively, after truncation (see Table 4.2 and Table 3 in Chapter ii). Truncation is simulated by removing a percentage of the disc from the outside in. This percentage is a free parameter. Although, inevitably, there is a high degree of degeneracy in the parameters describing the exponential disc, it is clear that I would need very steep H_2-to-dust gradients and severe truncation (>80% of the gas/dust disc) for this to explain the range of H_2-to-dust mass ratios and H_2-deficiencies observed. Therefore, based on this toy model, truncation in combination with a H_2-to-dust gradient is unlikely to be the sole explanation of the decreased H_2-to-dust ratios observed. In reality, the spatial extent of the dust may exceed that of the molecular gas, as, for example, observed the nearby spiral galaxy NGC2403 (Bendo et al., 2010). This implies that it would be removed by ram pressure stripping before the molecular gas, as suggested by Cortese et al. (2016). This implies that it would be even more difficult to remove significant amounts of molecular gas compared to dust in this way.

Option (ii): the dust reservoir is replenished more efficiently than the H_2 reservoir

If dust is created at a higher rate than H_2 in the star formation cycle, this could result in decreased gas-to-dust ratios. Both gas and dust are observed in supernova remnants (see Matsuura 2017 for a review). Recent, in-depth studies of supernova remnants have shown that large amounts of dust can be produced in supernovae (Dunne et al., 2003; De Looze et al., 2017, 2019; Cigan et al., 2019; Priestley et al., 2019). Gas, on the other hand, is produced in relatively small quantities, resulting in gas-to-dust ratios in supernova remnants that are much smaller (5 - 10 times) than typical ISM values (Owen & Barlow, 2015; Matsuura et al., 2017; Arias et al., 2018; Priestley et al., 2019). Therefore, ongoing star formation in combination with starvation could be (co-)responsible for the decrease in H_2-to-dust ratios observed, possibly sped up by the active removal of gas and dust. Several galaxies in the Fornax cluster have slightly increased star formation efficiencies. Furthermore, starbursts can already have occurred in the pre-processing phase, as galaxies start to interact with the intracluster medium, or in infalling groups (Pinna et al., 2019a,b), although this has mainly been observed in early-type galaxies. While this does not mean their SFRs or sSFRs are also increased (in fact, the vast majority of them lie below the star formation main sequence, see Chapter iii, so we do not expect them to produce

more dust than "average" galaxies), it is the H_2-to-dust ratio we are interested in. This can be increased as a result of this preferential dust production.

An inspection of gas-to-dust ratios in the Fornax cluster as a function of depletion time shows that they decrease with increasing depletion time: galaxies currently undergoing starbursts, often showing disturbed molecular gas reservoirs, still have relatively high gas-to-dust ratios. This could mean two things: either this is not a good explanation, or it takes a while for the dust to accumulate, and the effect is only noticeable after the star burst phase is over. The latter explanation is supported by the fact that old stellar populations are also a significant source of interstellar dust (while their gas feedback is insufficient to keep star formation going, Matsuura et al., 2009; Boyer et al., 2012; Höfner & Olofsson, 2018). Thus, as gas and dust are stripped and depleted, but star formation has not yet been quenched (the galaxy is experiencing "starvation", Larson et al. 1980) the dust produced by older stars and supernovae accumulates within the galaxy. Even without ongoing star formation, the dust mass can still continue to increase through interstellar grain growth (assuming some residual cool gas is present in the galaxy to shield the dust from sputtering in the hot intracluster medium, Hirashita 2012; Mattsson et al. 2014; Zhukovska 2014; Galliano et al., submitted). This suggests that the gas-to-dust ratio could even continue to decrease after the star formation has been quenched.

Many galaxies in the Fornax cluster are deficient in HI, or even completely devoid of it (at the survey sensitivity limit of $\sim 2 \times 10^7 M_\odot$, Loni et al. 2021). If the main formation of H_2 is through the condensation of HI, this could mean that the production of H_2 is slower than in non-HI deficient galaxies. However, there also is a significant fraction of HI-deficient galaxies in the Virgo cluster (Yoon et al., 2017), so if this was the main explanation, we might expect to see similarly low molecular gas-to-dust ratios in the Virgo cluster. Moreover, most of these galaxies have high rather than low H_2-to-HI ratios, which does not support this theory (Loni et al., 2021).

Option (iii): altered ISM physics result in inaccurate gas-to-dust ratios

It is possible that the radiation field in the cluster destroys CO (but not H_2), leading us to underestimate H_2-to-dust ratios. In the Galaxy, the radiation field only affects the outermost layers of molecular clouds (e.g. Maloney & Black 1988). However, if the radiation field is more intense, it can affect the entire cloud. In fact, besides metallicity, the strength of the FUV radiation field is the most important factor determining X_{CO} e.g. Bisbas et al. 2015 and references therein). It is possible that X-rays from the hot intracluster medium (e.g. Jones et al. 1997) have a similar

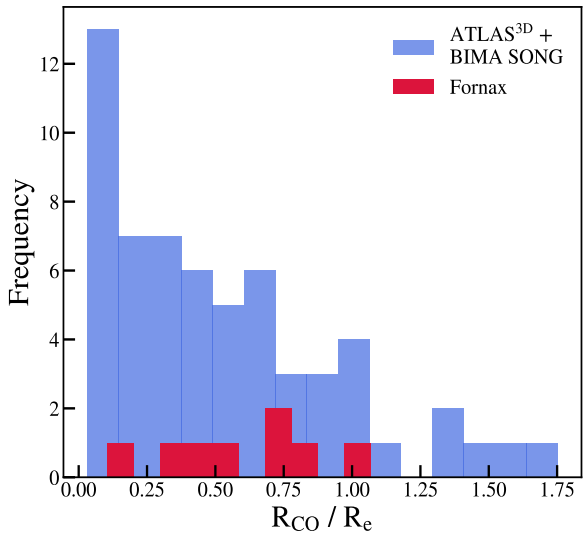

Figure 4.12: Histogram of R_{CO}/Re in the Fornax cluster (crimson) compared to a field sample consisting of gas-rich early-type galaxies from ATLAS^{3D} (Davis et al. 2013) and spiral galaxies from BIMA SONG (Regan et al., 2001), shown in lilac. Fornax cluster galaxies do not have more significantly truncated CO than the field galaxies (a KS test is not able to reject the null-hypothesis that the Fornax and ATLAS^{3D}/BIMA SONG samples are drawn from the same distribution, D=0.29, p=0.5 $\sim 0.67\sigma$).

effect. However, it would be difficult to destroy CO while leaving dust grains intact. Moreover, in that case we might expect to see a similar or stronger decrease in H_2-to-dust ratios in the more massive Virgo cluster, which is not observed.

An alternative factor that could be affecting my measurements is the dust composition. Large silicate grains are not as easily destroyed by the radiation field, which means that H_2 might be destroyed while leaving a large fraction of the dust unaffected. Indeed, in their detailed analysis of the dust content of FCC167, Viaene et al. (2019) find that almost no small grains are present in the dust reservoir of this galaxy. Only larger, self-shielding grains survive the effects of the cluster environment. Another possibility is that larger grains are broken up by the radiation field, resulting in a relatively high fraction of small dust grains. If we then assume a standard dust composition with a lower fraction of small grains to estimate the dust mass, we could be overestimating the dust mass. It seems, however, more likely that such a radiation field would continue to destroy bonds until no significant amount of dust is left. Moreover, this contradicts the observations of FCC167 described above. Furthermore, the carbon-to-silicate ratio of the dust grains can play a role. Due to

environmental conditions and typical grain sizes, silicate grains can have longer lifetimes ($\sim$ 1 Gyr) than carbon grains (of the order 100 Myr, e.g. Slavin et al. 2015). If the composition of dust grains in the Fornax cluster is relatively silicate-rich, more oxygen may be expected to be locked up in these grains.

Low gas-to-dust ratios have also been observed in field galaxies, for example in the early-type galaxy NGC5485. This object has a total G/D of <14.5, as estimated from FIR, CO, and HI observations (Baes et al. 2014, the upper limit is the result of non-detection of HI and H_2 in sensitive observations obtained as part of ATLAS^{3D}). Suggested explanations for this observation include the majority of the gas being warm or hot rather than cold, the presence of a relatively large fraction of CO-dark gas, or a recent merger with a metal-poor dwarf galaxy. There could be a larger fraction of warm/hot gas present in Fornax galaxies if the gas at larger scale-heights is affected by the surrounding hot intracluster medium. However, the molecular gas is dense and centrally located, so it would be difficult to explain the decreased H_2-to-dust ratios in this way. Furthermore, there is no obvious reason why Fornax galaxies would contain more CO-dark gas than field galaxies (at fixed stellar mass), as their metallicities are average or even high compared to the DustPedia field sample (see §4.5.1). Moreover, the latter explanation is unlikely to apply to the entire Fornax sample. Therefore, it seems more likely that the observed low gas-to-dust ratios are a result of environmental effects.

4.7.2 Comparison with the Virgo cluster

In this work, the main difference between the Fornax and Virgo clusters is that the low total gas-to-dust ratios in Fornax are partly driven by decreased H_2-to-dust ratios, while these are *in*creased inside the virial radius of the Virgo cluster. If Virgo galaxies within twice its virial radius are included, this result disappears (see Figures 4.1 - 4.6 and Table 4.3). Thus, in Virgo, decreased total-gas-to-dust ratios are purely driven by the low HI-to-dust ratios. This is in agreement with Cortese et al. (2016), who find that the decrease in total gas-to-dust ratios in HI-poor galaxies is purely driven by the decrease in HI-to-dust ratios, while H_2-to-dust ratios are increased compared to field galaxies at fixed mass and metallicity. They attribute these anomalous ratios to the different spatial distribution of the two gas phases and the dust, resulting in the differential stripping of the ISM. As described above, observations of the ISM in FCC167 indeed show a nested ISM, in which the the molecular gas disc is more compact than the dust ring present in this galaxy (Viaene

et al., 2019). However, since this galaxy is significantly deficient in molecular gas, it is unclear whether this nested ISM was already present before the galaxy entered the cluster, or if this is the result of the more efficient stripping of molecular gas compared to dust by the cluster environment.

The two main differences between the Fornax and Virgo cluster are that Virgo is more dynamically active, while Fornax is more dynamically evolved, and the Virgo cluster is much more massive than the Fornax cluster (see §4.1). The former difference could be an explanation for option ii: dust is accumulated in the star formation process while H_2 is slowly depleted. It could be that there is an initial boost in H_2 content, after which it stops being replenished, and this effect becomes more visible over time. However, since the galaxies studied here all still have a detectable ISM, which is not expected after several pericentric passages, it is unlikely that the Fornax galaxies have spent significantly more time in the cluster than the Virgo galaxies, or they would have no gas left.

It may be possible that ram pressure stripping results in the increased H_2-to-dust ratios observed in the Virgo cluster and in the galaxies studied by Cortese et al. (2016) if dust is stripped before molecular gas. This is supported by an ongoing study of the Virgo cluster (Zabel et al., in prep.), where I observe normal to high H_2 masses in the Virgo galaxies most affected by (past and ongoing) ram pressure stripping. It is possible that ram pressure compresses atomic gas, aiding its condensation into H_2, and thus contributing to the increase in H_2-to-dust ratios. This has indeed been observed in jellyfish galaxies (Moretti et al., 2020). Since the Fornax cluster is less massive than Virgo, ram pressure stripping might play less of a role there, or not be strong/violent enough to quickly remove HI or compress it into H_2. It is possible that starvation is more important in Fornax, slowly depriving its galaxies of H_2, while the dust continues to accumulate. However, this is mostly speculation, and the wildly different results between both clusters are difficult to explain. Expansion of this sort of analysis to other clusters is clearly needed to determine the true cause of this effect.

4.7.3 Gas-to-dust vs. metallicity

It is often assumed that the dust-to-metal ratio is constant with time, due to the dust formation timescale being similar to the dust destruction timescale. A constant dust-to-metal ratio implies that the gas-to-dust ratio depends on metallicity as $G/D \propto Z^{-1}$, referred to as the "reference trend" by Rémy-Ruyer et al. (2014). This trend has been shown to hold for galaxies with metallicities close to solar, but to break down at the low-metallicity regime where dwarf galaxies are found, which have

higher observed gas-to-dust ratios than predicted by this trend (Rémy-Ruyer et al. 2014 and references therein). However, a recent review by Péroux & Howk (2020) has shown that the relation between metallicity and dust-to-metal ratio indeed holds in the low-metallicity/high redshift regime, albeit with more scatter due to the more complex chemistry here. From Figures 4.2 and 4.9 we can see that gas-to-dust ratios in the galaxies in the sample are consistently lower than those in the DustPedia sample, suggesting that they do not follow such a reference trend. This implies that their chemical evolution is different from regular field galaxies, which likely has to do with the environment they reside in. Alternatively, the physics of the ISM, such as the radiation field or dust composition, in these galaxies could be different such that they contain unusually high fractions of "CO-free" molecular gas, as discussed above.

Figures 4.2 through 4.9 imply that the fraction of metals locked up in dust (versus gas) is high in the Fornax cluster. If this is the result of stripping of high-metallicity gas (and dust), these are enriching the intracluster medium. Some Fornax galaxies are quite metal-rich, while they still have significant amounts of gas left. This is in broad agreement with what is found by Hughes et al. (2013), who find that gas-poor galaxies are relatively metal-rich. This could be due to the more metal-poor outer regions of the galaxy being stripped first. However, they do not find any significant difference between metallicities in the Virgo cluster and in the field. These metal- and gas-rich galaxies could indicate that we are observing a special time in the lifespan of the galaxies (i.e. we expect many of them to be on their first infall, which is also suggested by Loni et al. 2021), or witnessing a special time for the cluster itself.

4.8 SUMMARY

I have studied gas-to-dust ratios in a sample of 15 Fornax galaxies from the ALMA Fornax Cluster Survey (AlFoCS) as a function of stellar mass. In addition, in a sub-sample of 9 galaxies that were also observed with VLT/MUSE, as part of the Fornax3D project, the gas-to-dust ratio was also studied as a function of metallicity. I have separated H_2 and HI to separately study H_2-to-dust and HI-to-dust ratios. Each gas-to-dust ratio (from HI, H_2, and HI + H_2) was compared to a field sample and galaxies in the Virgo cluster (separated into galaxies inside $R_{\rm vir}$ and inside $2R_{\rm vir}$), both from DustPedia. Dust, H_2, HI, and stellar masses were calculated using the same assumptions and methods as DustPedia where possible, to maximise homogeneity between both samples. I also studied dust-to-metal ratios as a function of stellar mass and metallicity, and H_2-to-dust ratios as a function of distance from the cluster

centre. I made use of PPMAP to study resolved H_2-to-dust ratios in NGC1436, an almost face-on, flocculent spiral galaxy, at the PACS 100 μm resolution. My main conclusions are as follows:

- Gas-to-dust ratios in the Fornax cluster are systematically decreased compared to the field. Kolmogorov-Smirnov (KS) and Anderson-Darling (AD) tests are able to reject the hypothesis that the Fornax sample and DustPedia field sample are drawn from the same distribution at $\gg 5\sigma$. According to the same tests, this difference is not only driven by HI deficiencies, but H_2-to-dust ratios are also decreased. I propose a number of explanations for this:

  - H_2 is destroyed/removed from the galaxies more efficiently than dust. This is possible if there is a radial H_2-to-dust gradient in combination with a truncated H_2/dust disc. However, Fornax galaxies do not show any evidence of having significantly truncated H_2 discs. Moreover, past studies of HI-deficient galaxies and galaxies in the Virgo cluster suggest that dust is stripped before molecular gas. Finally, from inspection of a toy model, one would need quite steep radial gradients, in combination with severe truncation of the gas disc in these objects. Thus, it seems unlikely that this is the sole explanation for the low ratios observed. However, the radial increase in H_2-to-dust ratio observed in NGC1436 suggests that this effect can contribute.

  - Both H_2 and dust are destroyed, but the dust reservoir is replenished more efficiently than the H_2 reservoir. This is possible if relatively large amounts of dust are created by the deaths of massive stars, and/or H_2 is not replenished as efficiently as a result of starvation, stripping of HI, and/or the inefficient condensation of HI into H_2. Recent observations of gas-to-dust ratios in supernova remnants, as well as the known production of dust by old stellar populations, and interstellar grain growth, suggest that this could be a possible explanation. The slightly increased star formation efficiencies observed in Chapter II possibly speed up this process. However, the H_2-to-HI ratios in Fornax galaxies are high compared to those in field galaxies at fixed stellar mass, suggesting that the conversion of HI into H_2 does take place efficiently (Loni et al., 2021).

  - The physics of the ISM is altered in such a way that "standard" assumptions I make in order to estimate H_2 and dust masses are no longer valid. For example, the strong radiation field in the cluster could disintegrate

CO, while leaving H_2 intact, leading us to underestimate H_2 masses. Alternatively, the dust composition could be altered by the radiation field, possibly resulting in a higher fraction of small grains, which leads us to overestimate the dust mass. I consider these explanations less likely, however I cannot rule them out.

- Gas-to-dust ratios as a function of metallicity are also decreased, while dust-to-metal ratios are increased. This suggests that a relatively large fraction of metals is locked up in dust in these Fornax galaxies.

- Total gas-to-dust ratios in the Virgo cluster are decreased significantly, especially inside its virial radius. However, unlike in Fornax, this decrease is purely driven by a decrease in HI-to-dust ratios, while H_2-to-dust ratios are *in*creased. The difference in dynamical state and mass between both clusters are suggested as possible explanations for this, however the differences between the two clusters remain puzzling.

- Gas-to-dust ratios do not show any obvious variation with (projected) cluster-centric distance, although this is difficult to measure because of projection effects and small-number statistics. In the Virgo cluster there is possibly a weak correlation between cluster-centric distance and gas-to-dust ratio (a Kendall's Tau test returns a tau statistic of 0.23 with a p-value of 0.04). This likely reflects the difference between galaxies inside and outside $R_{\rm vir}$, but is diluted by projection effects.

- Resolved H_2-to-dust ratios in NGC1436 show an increase with ratio, ending in a sharp drop at $R \approx 3.5$ kpc. There are very few pixels that exceed a ratio of $\sim$40, suggesting that, aside from small-scale variations, low H_2-to-dust ratios are low throughout the entire gas/dust disc. There is no clear correlation with Hα emission.

In summary, total gas-to-dust, HI-to-dust and H_2-to-dust ratios in the Fornax cluster are significantly decreased compared to those in field galaxies at fixed stellar mass and metallicity. Their significantly increased dust-to-metal ratios suggest that a relatively large fraction of metals in these galaxies is locked up in dust. There is a variety of environmental mechanisms that could explain this, and it is possible that two or all three of the suggested explanations play a role. We see an opposite effect inside the virial radius of the Virgo cluster, where decreased total gas-to-dust ratios are purely driven by decreased HI-to-dust ratios, while H_2-to-dust ratios are

*in*creased. These results disappear when galaxies inside $2R_{\rm vir}$ are included. There are several differences between both clusters that could possibly explain this, however, it remains a puzzling result.

Further study is clearly required to determine what is driving the low gas-to-dust mass ratios in cluster galaxies. To eliminate any X_{CO} related effects on the gas-to-dust ratio, one could attempt to estimate X_{CO} from the IR emission, simultaneously with dust masses. Such an approach is, for example, taken by Leroy et al. (2011) and Sandstrom et al. (2013). Their models, however, rely on resolved measurements, which are not available for my sample. If suitable data could be obtained it would interesting to investigate this further in a future work.

Furthermore, it is crucial to expand this analysis to study other galaxy clusters and groups. An ongoing, similar study of H_2-to-dust ratios in the Coma cluster (Zabel et al., in prep.) will possibly help disentangle which environmental effects and cluster properties have a significant effect on these ratios.

Chapter 5
Thesis Summary

> Now the verses I've sang don't add much weight
> to the story in my head, so I'm thinking I should
> go and write a punch line.
> But they're so hard to find in my cosmic mind.
> So I think I'll take a look out of the window...
>
> Yes, *"Going for the one"*

In this thesis I studied the effects of environment on molecular gas, and related quantities such as the star formation efficiency and gas-to-dust ratio. Molecular gas is the direct fuel for star formation, and therefore plays an important role in the baryon cycles of galaxies. Since a significant fraction of galaxies in the local Universe reside in dense environments (see §1), understanding how such environments affect molecular gas and related properties of the ISM is key to understanding galaxy evolution.

5.1 Conclusions

To learn more about the molecular gas content of cluster galaxies, I reduced and studied data from the ALMA Fornax Cluster Survey (AlFoCS): a complete HI/FIR selected survey of Fornax cluster galaxies. Of the 30 galaxies observed, 15 were detected in CO. I manually reduced the ALMA data for these 15 galaxies, and created science product such as moment maps and position-velocity diagrams. I also calculated molecular gas masses, fractions, and deficiencies. The most important conclusion from this work is that the Fornax cluster is still a very active environment,

that is having a significant effect on the galaxies it harbours. Galaxies in the Fornax cluster are systematically molecular gas deficient compared to field galaxies at fixed stellar mass. Most notably, galaxies with stellar masses below $\sim 3 \times 10^9 M_\odot$ are more significantly molecular gas deficient than galaxies with higher stellar mass. They also show morphologically and kinematically disturbed molecular gas reservoirs. This suggests not only that the Fornax cluster environment directly affects the molecular gas in the galaxies it harbours, but also that lower-mass galaxies are more susceptible to environmental effects. This is expected, as because of their shallower potential wells, they are more easily stripped of their ISM. Some dwarf galaxies show very asymmetric molecular gas discs, sometimes in the shape of tails that extend into the very faint regions of the galaxy's stellar body. This suggests either ram pressure stripping, or a past tidal or galaxy-galaxy interaction. It is difficult to distinguish between both scenarios based on observations of the molecular gas alone. In two star forming dwarf galaxies, NGC1427A and NGC1437A, we do not detect any CO. This is unexpected, and likely due to these galaxies having lower metallicities than predicted by their stellar mass and star formation rate. Last, I related molecular gas fractions and deficiencies to various galaxy- and cluster-related properties (e.g. stellar mass, cluster-centric distance). There is no clear correlation between molecular gas deficiency and cluster-centric distance or the location of a galaxy in phase-space. However, it is difficult to draw strong conclusions due to the small sample size of Fornax galaxies and projection effects.

After presenting the molecular gas data and derived quantities, I combined it with data from MUSE to study the resolved star formation relation in the Fornax cluster. I derived star formation rate surface densities Hα emission, corrected for reddening using the Balmer decrement. I made two versions of the star formation relation: one for which I included spaxels classified as dominated by star formation only, and one for which I included both star formation dominated spaxels and spaxels classified as "composite", which are dominated both by star formation and another source of ionisation. The dominant ionisation source was determined using BPT diagrams (see §1.1.6). While star formation rates in Fornax galaxies are low (almost all of them lie below the star formation main sequence), their star formation efficiencies are normal to high: the collective star formation relation in the Fornax cluster is close to those found by Kennicutt (1998) and Bigiel et al. (2008), but lies towards their shorter depletion time ends. Thus, the lack of star formation is a result of the lack of molecular gas rather than the inefficient conversion of that gas into stars. The slight

decrease in depletion times is mostly driven by low-stellar mass galaxies with disturbed molecular gas reservoirs. Most dwarf galaxies, as well as other galaxies close to the virial radius, have decreased depletion times compared to the typical value of 1-2 Gyr for isolated spiral galaxies.

There is significant scatter in the star formation relation between different Fornax galaxies. The star formation relations of some galaxies are distributed around classical star formation relations (described above), while others lie well above them, and the few well below them. Besides scatter between galaxies, there is also significant scatter within individual galaxies. This implies a variety in depletion times on sub-galactic scales. In some cases these are relatively large-scale variations (such as in FCC090, which has strongly decreased depletion times inside its stellar body, but increased depletion times in its molecular gas tail). In other cases the variations are of smaller scale, reflecting the independent evolutionary lifecycles of clouds. The application of the "uncertainty principle for star formation" to the face-on, flocculent spiral galaxy NGC1436 reveals that it has relatively short molecular cloud lifetimes. This is typical for low-mass galaxies with low molecular gas surface densities, while NGC1436 has a relatively high total gas mass. This possibly has to do with the cluster environment: the clouds may be dissipated by radiation and/or ram pressure relatively quickly, or, alternatively, transform into stars more efficiently. However, star formation efficiencies of most clouds in NGC1436 are around the expected 1-2 Gyr.

Fornax galaxies follow the shallow trend in depletion time as a function of stellar mass seen in the field. Their values are possibly more extreme at the low- and high-mass ends, though it is difficult to draw strong conclusions due to the poor statistics. Stellar mass is a better predictor of depletion time than stellar mass surface density (which can be interpreted as a proxy for morphology) in the Fornax cluster. This is mostly because dwarf elliptical galaxies have short depletion times, while their stellar mass surface densities are relatively high. There is also a correlation between median depletion time and (projected) cluster-centric distance. However, this is likely driven by stellar mass (massive ellipticals tend to be located closer to the cluster centre, and lower-mass galaxies further out). With only a small sample, and projection effects, it is difficult to say whether this is a real trend.

Finally, I studied gas-to-dust ratios in Fornax galaxies, and compared these to those in Virgo and field galaxies. In addition to H_2-to-dust ratios, I estimated HI-to-dust and total gas-to-dust ratios using HI data from ATCA. Dust masses were estimated from SED fits to FIR data from *Herschel*. I also plot gas-to-dust ratios as

a function of metallicity, and study dust-to-metal ratios. These provide information about the chemical state of the galaxies. Metallicities were estimated from emission line ratios observed with MUSE in combination with the strong-line calibration from Dopita et al. (2016). The main conclusions from this study are as follows. Gas-to-dust ratios in the Fornax cluster are systematically decreased compared to field galaxies at fixed stellar mass and metallicity. This difference is driven not only by a decrease in HI-to-dust ratios, but also in H_2-to-dust ratios. While a decrease in HI-to-dust ratios is expected in clusters, as environmental effects are first experienced by the extended HI disc (which is thus stripped first), a decrease in H_2-to-dust ratios is less straightforward to explain. Possible explanations include, in short, the more efficient removal of molecular gas compared to dust, a more efficient replenishment of the dust reservoir compared to the molecular gas reservoir, and altered ISM physics. This result is quite different from what is seen in the Virgo cluster. There, total gas-to-dust ratios are also decreased, but this is purely driven by low HI-to-dust ratios. H_2-to-dust ratios, on the other hand, are systematically *in*creased. This difference may be due to the difference in mass and dynamical state between the two clusters. However, it remains a puzzling result.

Dust-to-metal ratios are significantly increased in the Fornax cluster compared to the field at fixed stellar mass and metallicity. This suggests that a relatively large fraction of metals in Fornax galaxies are locked up in dust grains. This result is seen to a lesser extent in the Virgo cluster. There is, however, a possible trend in gas-to-dust ratio as a function of (projected) cluster-centric radius in the Virgo cluster. This trend is not seen in Fornax, however the statistics for this cluster are poor.

To investigate whether there are any radial or other spatial trends in the H_2-to-dust ratio within galaxies, I made use of a dust map created using `ppmap` to study resolved H_2-to-dust ratios in the almost face-on spiral galaxy NGC1436, at a resolution of the PACS 100 μm map ($3 \times 3''$, corresponding to $\sim 290 \times 290$ pc at the distance of the Fornax cluster). This showed no radial trend in H_2-to-dust ratios. Peaks in H_2-to-dust ratio also do not seem to correlate with HII regions identified by Hα emission from star formation.

In summary, in this thesis I have shown that molecular gas and related properties of the ISM in the Fornax cluster are affected significantly by the cluster environment. Galaxies residing in this cluster are systematically deficient in molecular gas compared to field galaxies at fixed stellar mass. While the dense environment affects all galaxies, it has a more pronounced influence on low-mass galaxies, as they are more easily stripped of their gas due to their shallow potential wells. Despite a lack of gas and low star formation rates, the conversion of this gas into stars is generally

no less efficient than suggested by classic star formation relations. If anything, more galaxies have increased star formation efficiencies compared to these relations rather than decreased efficiencies. While the dust reservoirs of galaxies in Fornax are also small compared to those of field galaxies at fixed stellar mass, molecular gas-to-dust ratios are systematically suppressed. This is surprising, as molecular gas and dust are expected to be affected similarly by the cluster environment. Moreover, the opposite result is found in the Virgo cluster. Thus, while the Fornax cluster is still a very active environment that has a significant effect on the ISM of its galaxies, the evolution of these galaxies is different from those in the more massive and dynamically active Virgo cluster.

5.2 Ongoing & Future Work

This thesis has shown significant differences in molecular gas content and related properties between the Fornax cluster and the field, and also between the Fornax and Virgo clusters. Many of these properties can be explored in more detail. Furthermore, ongoing efforts to study the molecular gas in other galaxy clusters, as well as additional observations of molecular gas and other phases of the ISM in the Fornax cluster, will help complete the picture of galaxy evolution in dense environments.

The molecular gas reservoirs of low-mass Fornax galaxies are morphologically and kinematically disturbed. From this, we can conclude that the cluster environment directly affects this gas. However, it is difficult to determine which environmental processes are responsible from this based on the data presented in this thesis alone. An approach that could help disentangle between ram pressure stripping and tidal/galaxy-galaxy interactions, would be to compare the kinematics of the molecular gas to those of the stars. Stellar kinematics are available for the vast majority of the AlFoCS sample from existing MUSE data. During my PhD, I have obtained my own MUSE data for an additional sample of dwarf galaxies, which can be included in this analysis. If the stellar kinematics are also disturbed, this would be an indication of a past galaxy-galaxy interaction. If, on the other hand, the stellar kinematics are regular, it is more likely that the disturbances are caused by ongoing ram pressure stripping.

To obtain a better understanding of the relative importance of the various environmental processes, it is crucial that we expand studies like the ones in this thesis to other galaxy clusters and groups. In an ongoing study, I am investigating the molecular gas content and molecular gas-to-dust ratios in the Coma cluster. A comparison between Coma and the clusters studied here will provide insight into which

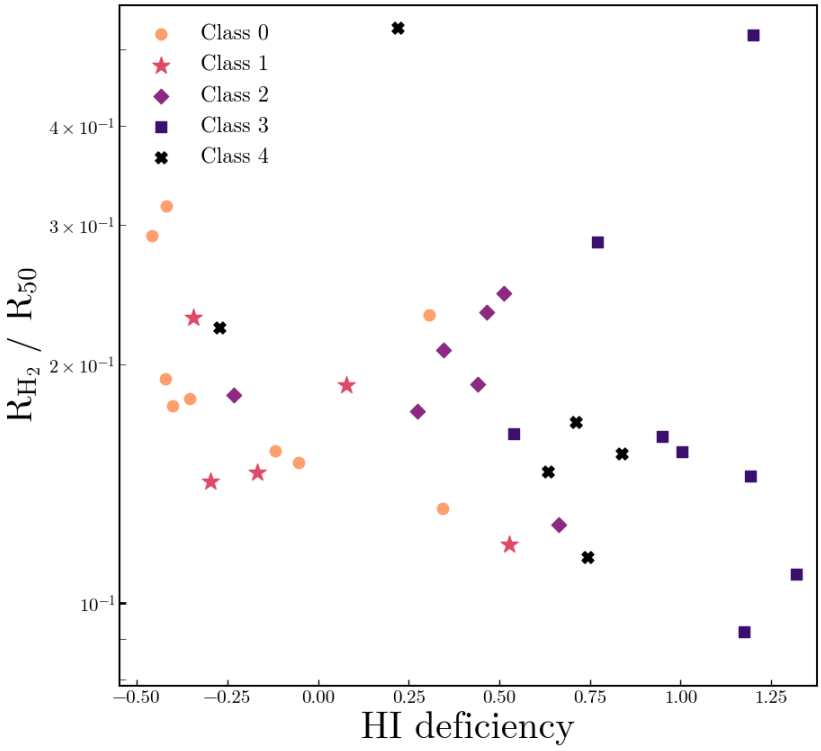

Figure 5.1: Preliminary result of my HI vs. H_2 study of galaxies in the Virgo cluster. It shows H_2 radii (normalised by R_{50}) of Virgo spiral galaxies (coloured markers) as a function of their HI deficiency. The different markers refer to different HI classes from Yoon et al. (2017), ranging from normal HI content to very asymmetric (class II) and severely truncated (class III) HI content. The radius of the H_2 disc in VERTICO galaxies decreases slightly with HI deficiency.

cluster properties (and therefore environmental processes) are responsible for the observed differences. An ongoing ALMA large program, the Virgo Environment Traced in CO (VERTICO, PI: T. Brown) survey[1], will provide a resolved and homogenised sample of 51 spiral galaxies in the Virgo cluster. These observations will also help pin down the differences between the three nearby galaxy clusters. I am a key member of this team: I am involved in several first-round science projects (of which I am leading one), and I have written the pipeline that creates science-ready data products from the reduced data cubes. The VERTICO project I am currently leading is a study of the H_2 content in Virgo galaxies in different stages of HI stripping (Yoon et al., 2017). The goal of this study is to better understand how environmental processes, as identified in HI, affect the molecular gas. For example, one might expect the H_2

[1] `https://sites.google.com/view/verticosurvey`

content of galaxies that are undergoing severe ram pressure stripping to be different from that in galaxies with more "normal" HI content. A preliminary plot from this study is shown in Figure 5.1. It shows that (surprisingly) the H_2 content in VERTICO galaxies is no different from that in the field, independent of what their HI content looks like.

Besides the ATCA data used in this thesis, the MeerKAT Fornax Survey (Serra et al., 2016) will soon be completed. It will provide resolved (1 kpc) data of HI in Fornax galaxies. This data will be very helpful for the identification of environmental mechanisms, which can be identified well through the extended HI discs. Furthermore, it will allow us to study the relative HI and H_2 contents, for example by examining their relative masses and disc sizes. This will provide more insight into the effects of the cluster environment on the ISM and star formation cycle.

Not long after AlFoCS, a deep ACA survey of the CO(1-0) in 65 Fornax cluster was carried out (program ID: 2017.1.00129.S, PI: K. Morokuma). This will provide a larger sample size of H_2 in Fornax galaxies, including the infalling group around Fornax A, that was not included in AlFoCS. This survey will be used to compare the H_2 content of the Fornax and Virgo clusters, and will be combined with data from the Widefield ASKAP L-band Legacy All-sky Blind surveY (WALLABY, Koribalski et al. 2020) to study the molecular and atomic gas simultaneously.

In this thesis, there are several hints of correlations between quantities and cluster-centric radius. However, the work in this thesis is limited by small-number statistics and projection effects. While these issues could be partly resolved by increased sample sizes, simulations (such as, for example, the Illustris TNG300 simulation) could help truly pin down these relations. They provide access to accurate, unprojected cluster-centric distances, larger sample sizes, and, moreover, much larger timescales than the snapshots we work with observationally. By varying parameters such as halo mass and dynamical state, the relative importance between physical processes can be studied. This would help pin down the differences between the Fornax and Virgo clusters.

5.3 Concluding Remarks

With the advent of ALMA we have, in recent years, been able to study the molecular gas in nearby galaxies with unprecedented detail. Moreover, with the development of other world-class facilities in the south we have expanded our multi-wavelength horizon towards targets with lower declinations, such as the Fornax cluster. Galaxy clusters are incredibly messy places, where galaxies get to experience a

variety of effects they would not encounter in isolation. How this affects the molecular gas phase, and, in turn, the baryon cycle, is still relatively unexplored territory. That we do not quite understand this yet is clearly demonstrated, for example, by differences between the two nearby clusters that we are still unable to explain. With many exceptional telescopes and instruments being commissioned and continuing to operate, I am excited to know that we will make significant progress in this area in the near future. And I am looking forward to carrying on doing my bit.

Appendix A
Discussion of individual AlFoCS detections

NGC1351A (FCC67)

NGC1351A (Figures A.1 and A.16a) is a good example of an edge-on galaxy. The CO gas shows regular rotation. The detached emission visible from both extremes probably consist of giant molecular associations (GMAs), that are separated from the galaxy's main body by lower density or atomic gas.

MCG-06-08-024 (FCC90) & ESO359-G002 (FCC335)

In MCG-06-08-024 (Figures A.2 and 2.5a) and ESO359-G002 (Figures A.15 and A.14o), the CO emission extends in a tail beyond the stellar bodies of the galaxies. The three-colour image of ESO359-G002 shows some dust in the shape of a tail that is similar to the molecular gas. If we compare the directions of these tails to the direction of the cluster centre, we can see that in the case of MCG-06-08-024 the tail points away from the cluster centre, and in the case of ESO359-G002 it points towards the cluster centre. In both cases this could indicate ram pressure stripping: either the galaxy is being stripped of its molecular gas as it falls into the cluster (MCG-06-08-024), or it has already passed through the cluster centre, and is stripped as it is moving towards the other side of the cluster (ESO359-G002). Without detailed information on the orbits of these objects, this is hard to confirm. Ram pressure as a potential candidate for the stirring and stripping of the molecular gas in the Fornax cluster galaxies is discussed in §2.5.3.

NGC1365 (FCC121)

NGC1365 (Figures A.3 and is a giant spiral galaxy, and the only galaxy in our sample that is not H_2 deficient compared to the field. The molecular gas shows regular rotation, although in the centre it is warped by the strong bar in this source.

NGC1380 (FCC167)

NGC1380 (Figures A.4 and A.16d) has very centrally located molecular gas in these images, but has been shown to be distributed in a regular disk by Boizelle et al. (2017). HST images of this galaxy have revealed that the dust in this galaxy is distributed in a ring around the galactic centre. This ring of dust appears quite evidently in the g-i colour map of the FDS (Iodice et al. 2018, submitted to A&A). Viaene et al. (in prep.) find that the molecular gas follows a distribution with a similar shape, but at smaller radii. This source will be discussed in detail in Viaene et al. in prep.

NGC1386 (FCC179)

NGC1386 (Figures A.5 and A.16e) is a good example of a spiral galaxy. The spiral arms are traced in the CO emission. It shows a regular rotation, with slightly increased velocities close to the galactic centre. The X-shape visible in the PVD probably indicates the presence of a bar. 3 mm continuum emission from the centre (see §2.4.2) is associated with a known AGN.

NGC1387

NGC1387 (Figures A.6 and A.16f) is one of the biggest and brightest early-type galaxies close to the core of the cluster. It is one of the most (if not the most) regular galaxies in the sample, showing centrally distributed CO emission, decreasing radially outward (see Figure 2.3). This gas-disk has an inclination of $\sim 18^o$ (Davis et al., in prep.). The galaxy shows a regular rotation, and a double-peaked line profile. Archival HST imaging shows that these features are likely associated with a dust disk, which is compatible with the detected CO emission. The galaxy has a strong bar, which is possibly the result of tidal forces: it is interacting with the BCG NGC1399 (e.g. Iodice et al., 2016). The molecular gas probably remains relatively unaffected by its interaction with NGC1399 because this galaxy is much more massive than the disturbed galaxies in the sample ($M_\star = 5.89 \times 10^{10} M_\odot$), and its gas is deep in its gravitational potential within the X_2 orbits of the bar. In deep FDS images (Iodice et al. 2018, submitted to A&A) it shows a nuclear disk/ring of dust (g-$i = 1.4$). A ring

of ∼6” was also found in near-infrared images in the *Ks*-band (Laurikainen et al., 2006).

FCC207

FCC207 (Figures C.5 and A.15g) is a small galaxy with disturbed molecular gas that is off-centre. Some rotation can be identified in the velocity maps, but the kinematics are clearly disturbed. Its stellar body looks relaxed (at the resolution of the data used here).

FCC261, FCC282, and FCC332

FCC261 (Figures A.8 and A.15h, FCC282 (Figures A.10 and A.15g), and FCC332 (Figures A.14 and A.14n) are small galaxies with molecular gas that is located off-centre (this is especially evident in FCC282). In FCC261 and FCC282 some rotation can be identified, although the kinematics of the molecular gas in all three galaxies are disturbed. In these galaxies the disturbance is reflected in the optical images as well. The stellar body of FCC261 is asymmetric, and there appears to be some colour gradient. The peak of the CO emission is located next to the peak of the optical emission. Something similar is seen in FCC282, where the CO emission peaks at the south-east of the galaxy, which appears bluer in the three-colour image and possibly shows the presence of dust. The stellar body of FCC332 looks slightly more regular, and its CO velocity map more disturbed.

NGC1436 (FCC290)

NGC1436 (Figures A.11 and A.15k) is a good example of a late-type galaxy. The patchy nature of the CO emission is very clear, showing the resolved GMAs in this galaxy. The gas rotates regularly. Because of the fragmentary distribution of the molecular gas, the PVD in this case was obtained using the full width of the galaxy.

NGC1437B (FCC308)

Although the morphology and kinematics of NGC1437B (Figure A.12 and A.15l) are disturbed, a rotation in the molecular gas can still be identified, and it is the least H_2 deficient of the disturbed galaxies (see Figure 2.8). This galaxy is discussed in more detail in §2.5.3.

PGC013571

The velocity map of PGC013571 (see Figure A.9) seems to consist of more than one rotation around different axes. In the intensity map there are multiple peaks. The PVD of this galaxy consists of multiple velocity structures. There are two possible explanations for these observations. First, they could be an indication that this galaxy has a strong bar/spiral arms. The pattern of the contours in the velocity map and the two components near the centre of the PVD indicate strong bar-like non-circular streaming motions, which is consistent with this interpretation. Similar kinematics are seen in the Virgo cluster spiral NGC4064 (Cortés et al., 2006), which indeed has a bar and two spiral arms, resulting in strong non-circular streaming motions (see Figure 11 in Cortés et al. 2006). The irregularity, both in the molecular gas and the stellar body, could have been caused by a tidal interaction or minor merger that caused the strong two-arm spiral disturbance.

Alternatively, it is possible that this galaxy has recently undergone a merging event and is still in the process of relaxing. The velocity map could be interpreted as two different rotating bodies: one rotating along a horizontal axis, and one around a more diagonal axis. In the three-colour image of this galaxy we can see a split in the optical emission at the south side of the galaxy, with two blue ends. Usually mergers in cluster environments are rare, however they can occur in the outskirts.

A.1 Moment maps

This appendix shows three-colour images, moment maps, position-velocity diagrams, and the CO(J = 1-0) line for all galaxies detected here.

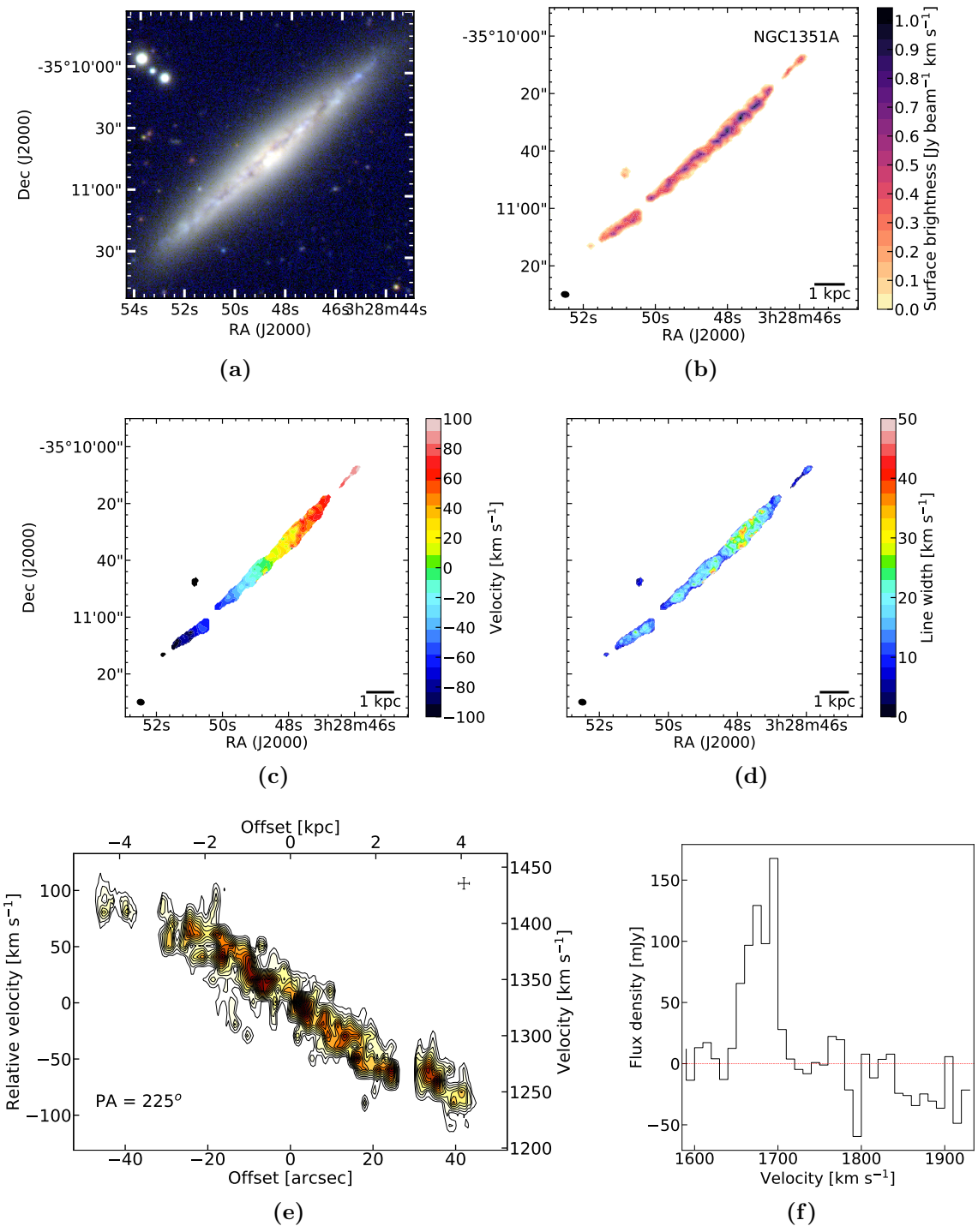

Figure A.1: a: three-colour image of ESO358-G063. b: moment zero map: distribution of the cold molecular gas as traced by the ALMA CO data. c: moment 1 map: velocity map of the cold molecular gas. Each colour represents a 10 km s^{-1} velocity channel. d: moment 2 map: line width of the CO integrated spectrum. e: Position-velocity diagram of the cold molecular gas. The uncertainties in the spatial and velocity directions are indicated in the upper right corner. f: CO(1 - 0) line. The beam of the observations is shown in the lower left corners of the moment maps, as well as a 1 kpc scale bar in the lower right corners. The beam of the observations is shown in the lower left corners of the moment maps, as well as a 1 kpc scale bar in the lower right corners.

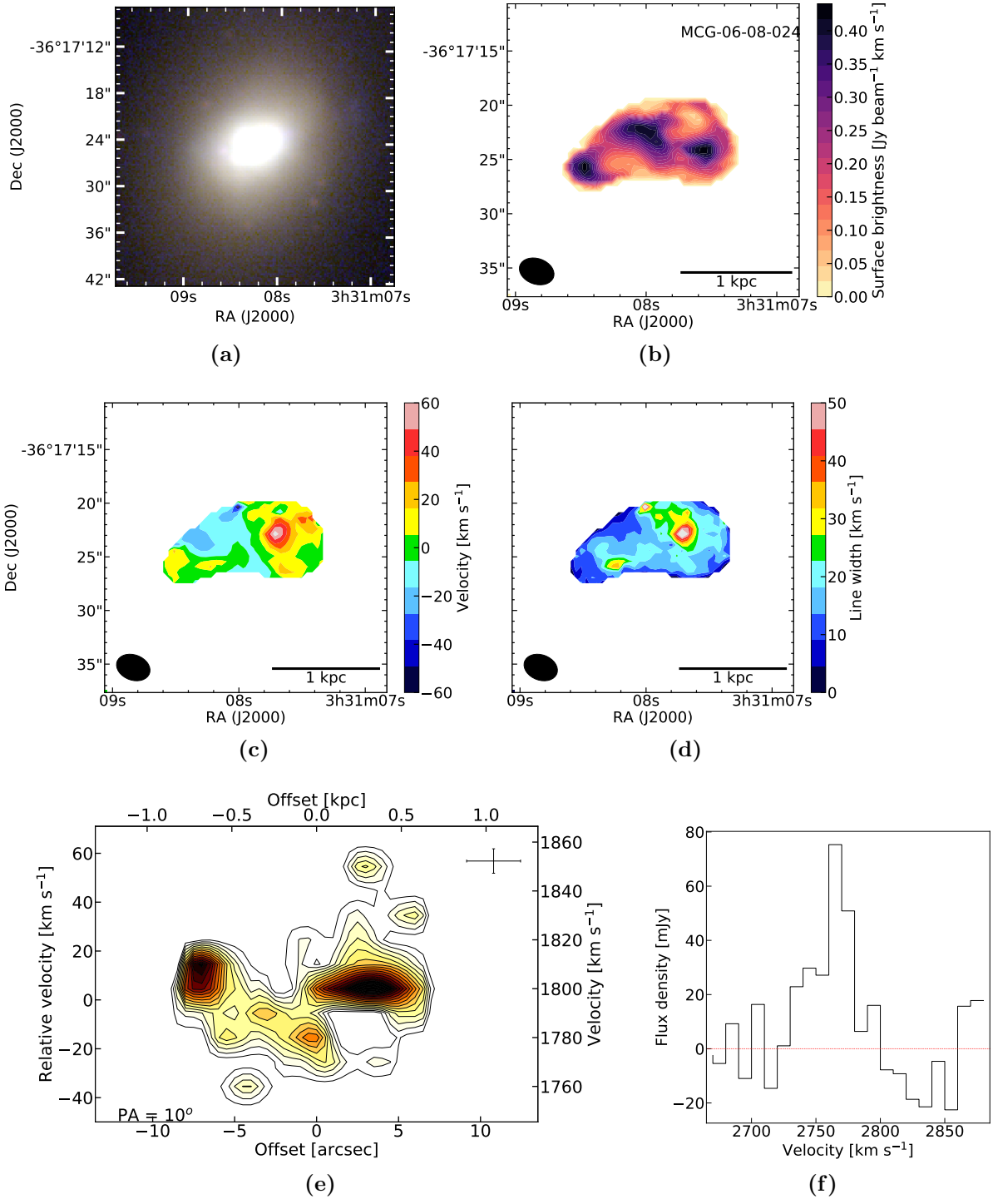

Figure A.2: MGC-06-08-024, similar to Figure A.1.

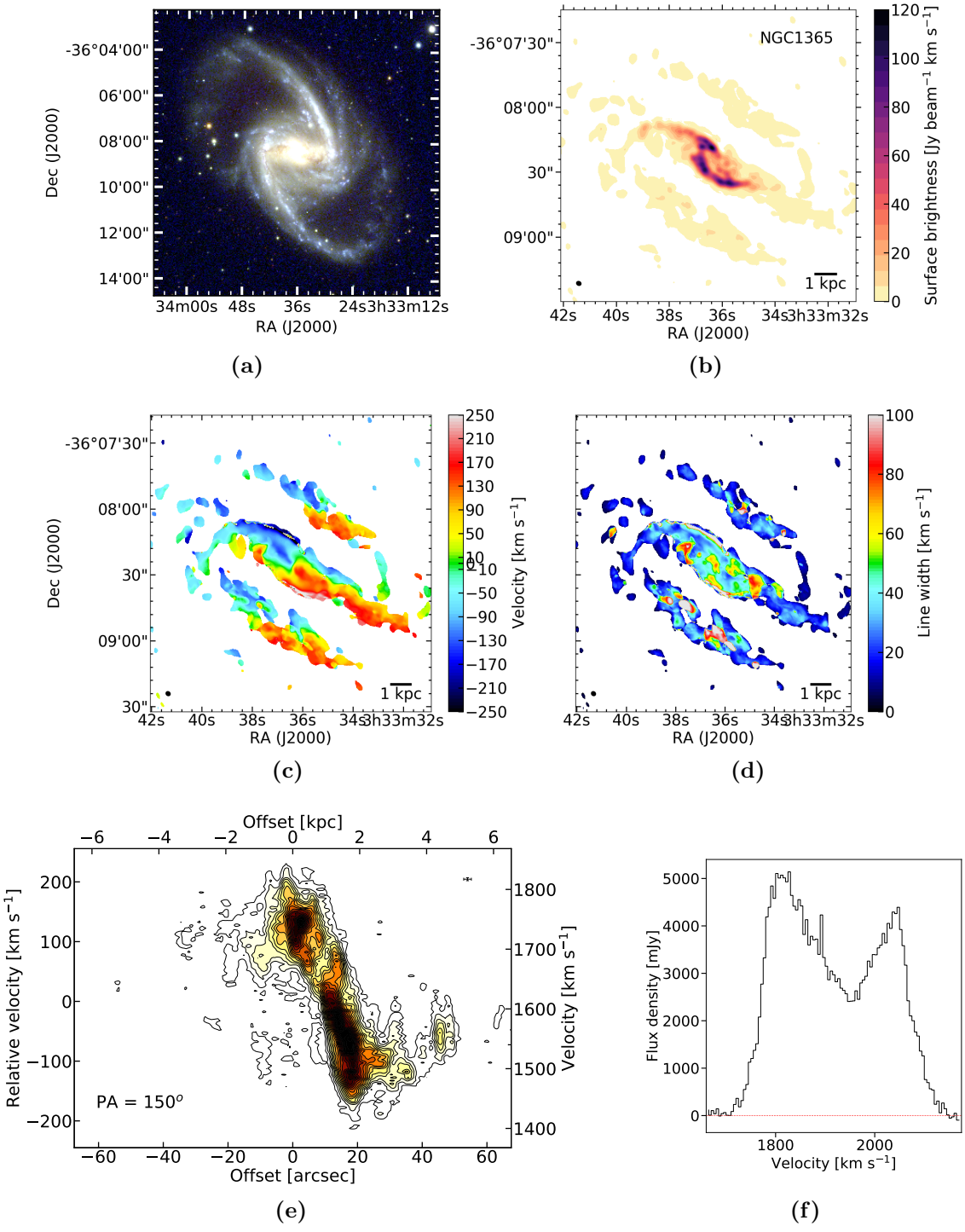

Figure A.3: NGC1365, similar to Figure A.1.

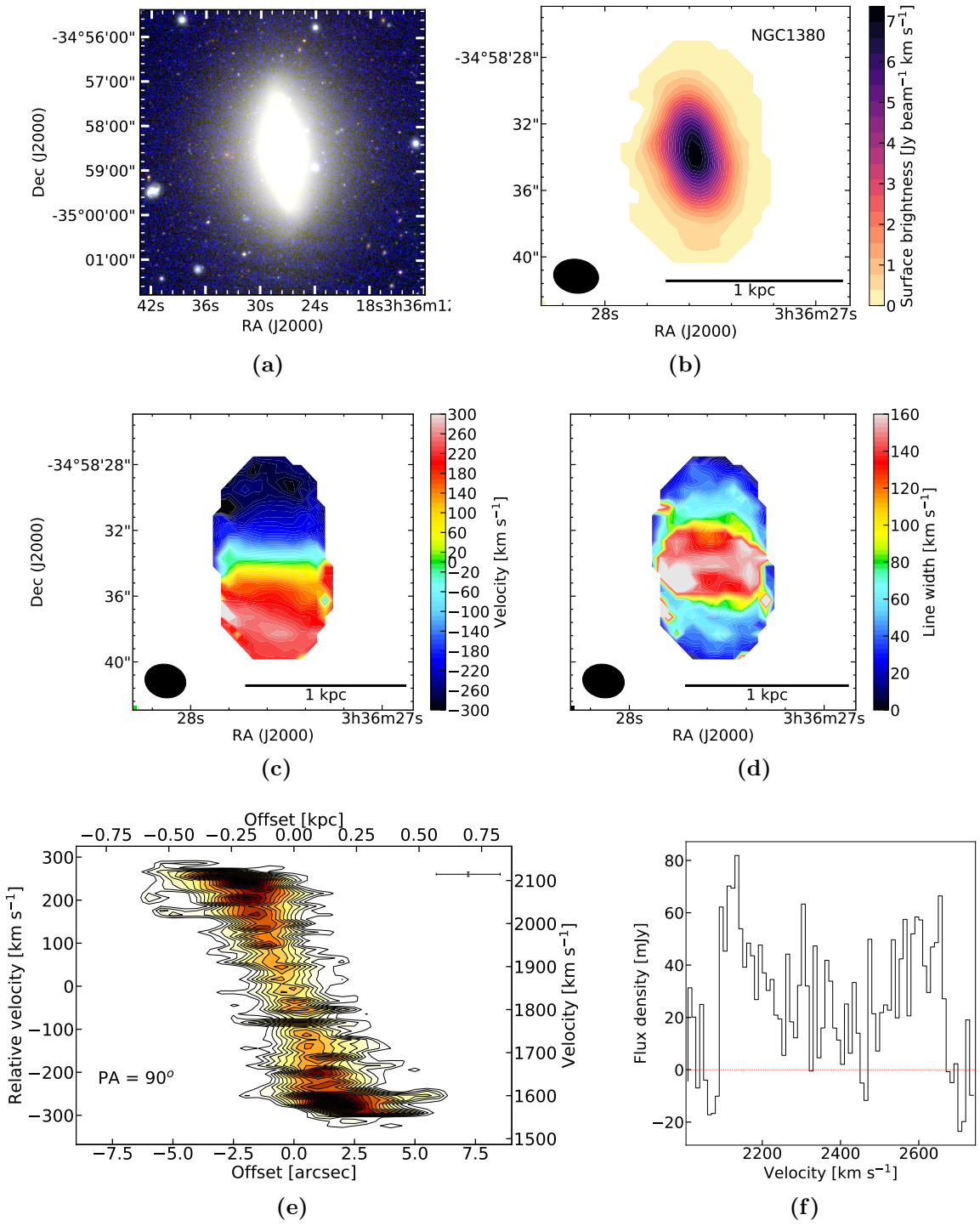

Figure A.4: NGC1380, similar to Figure A.1.

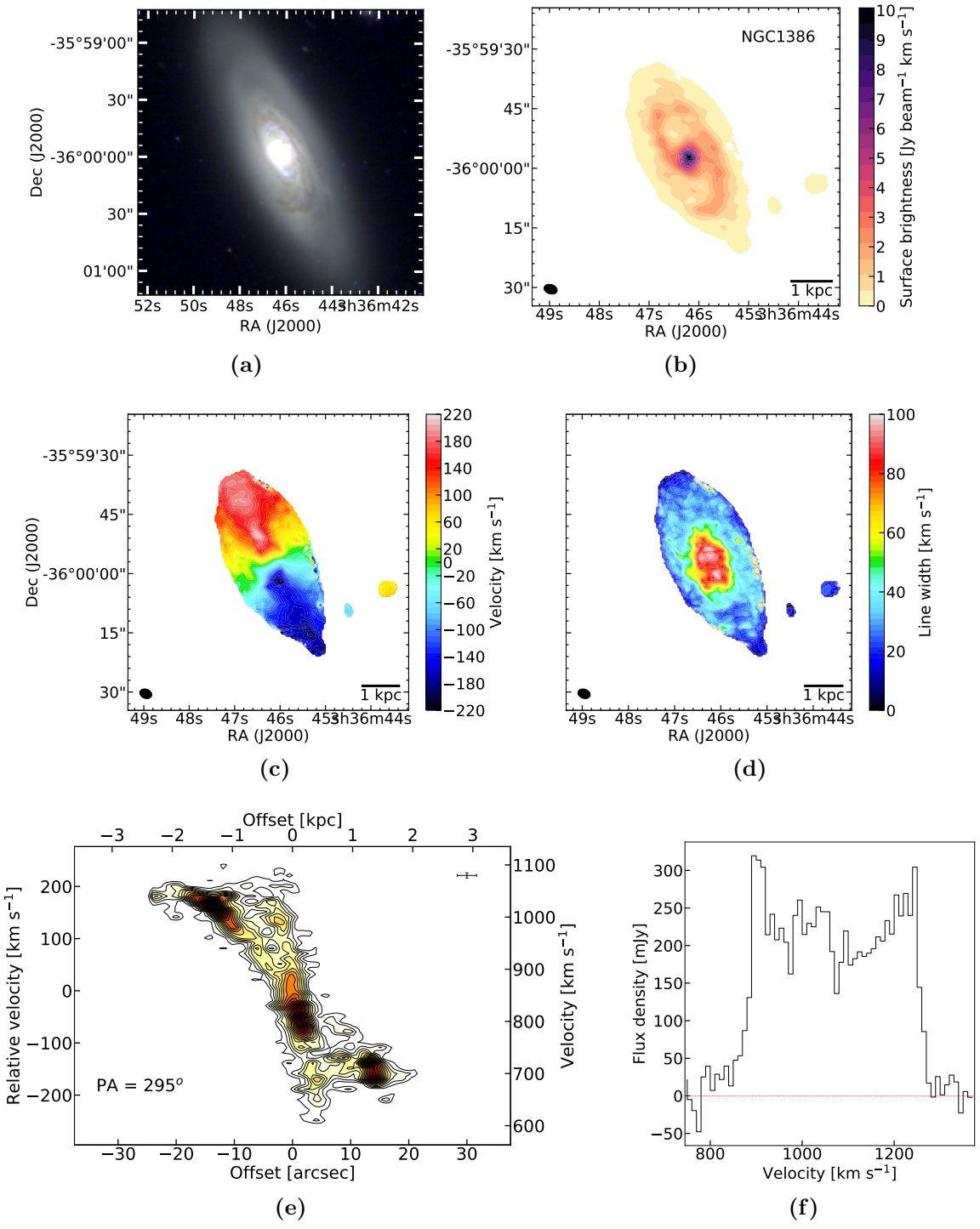

Figure A.5: NGC1386, similar to Figure A.1.

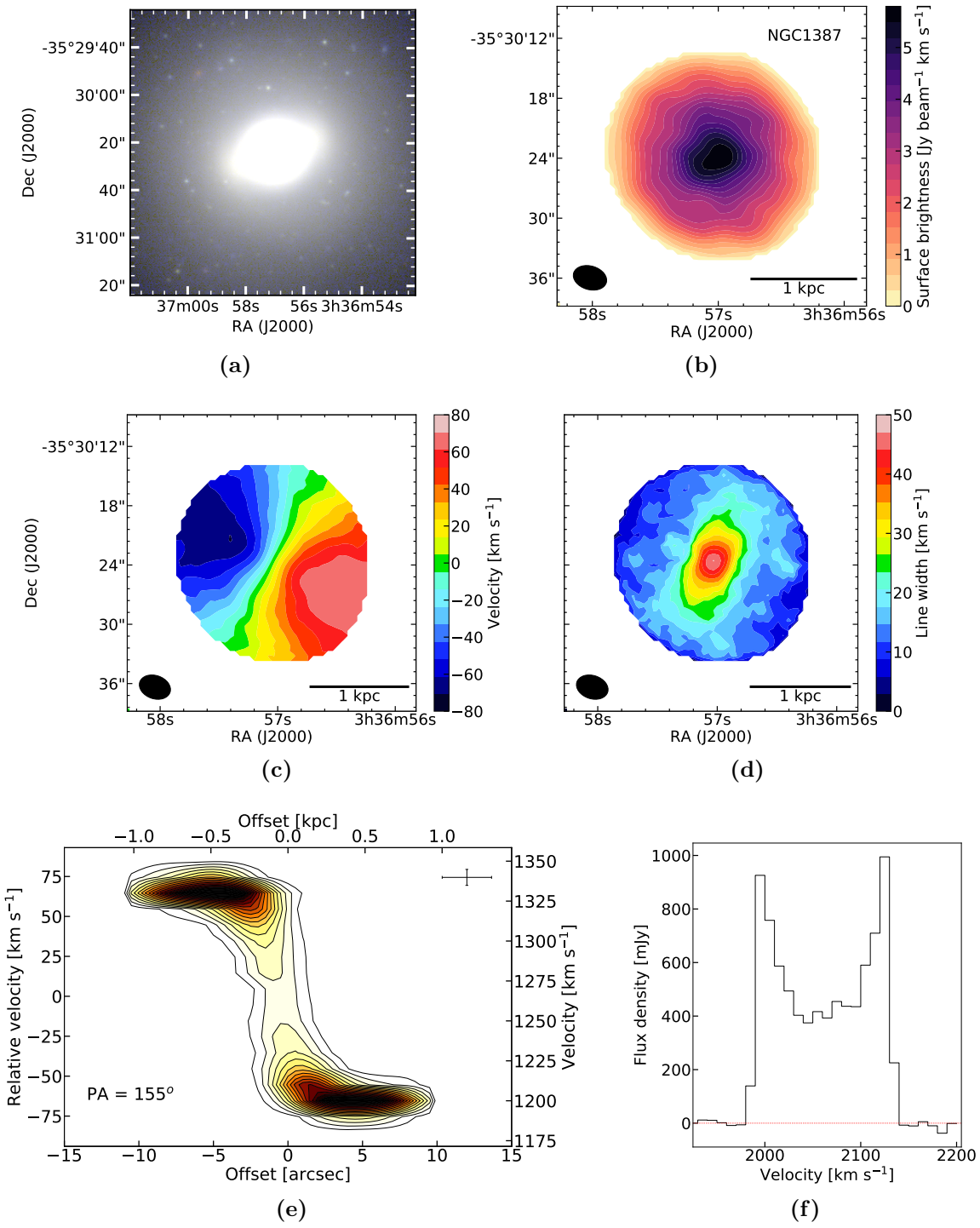

Figure A.6: NGC1387, similar to Figure A.1.

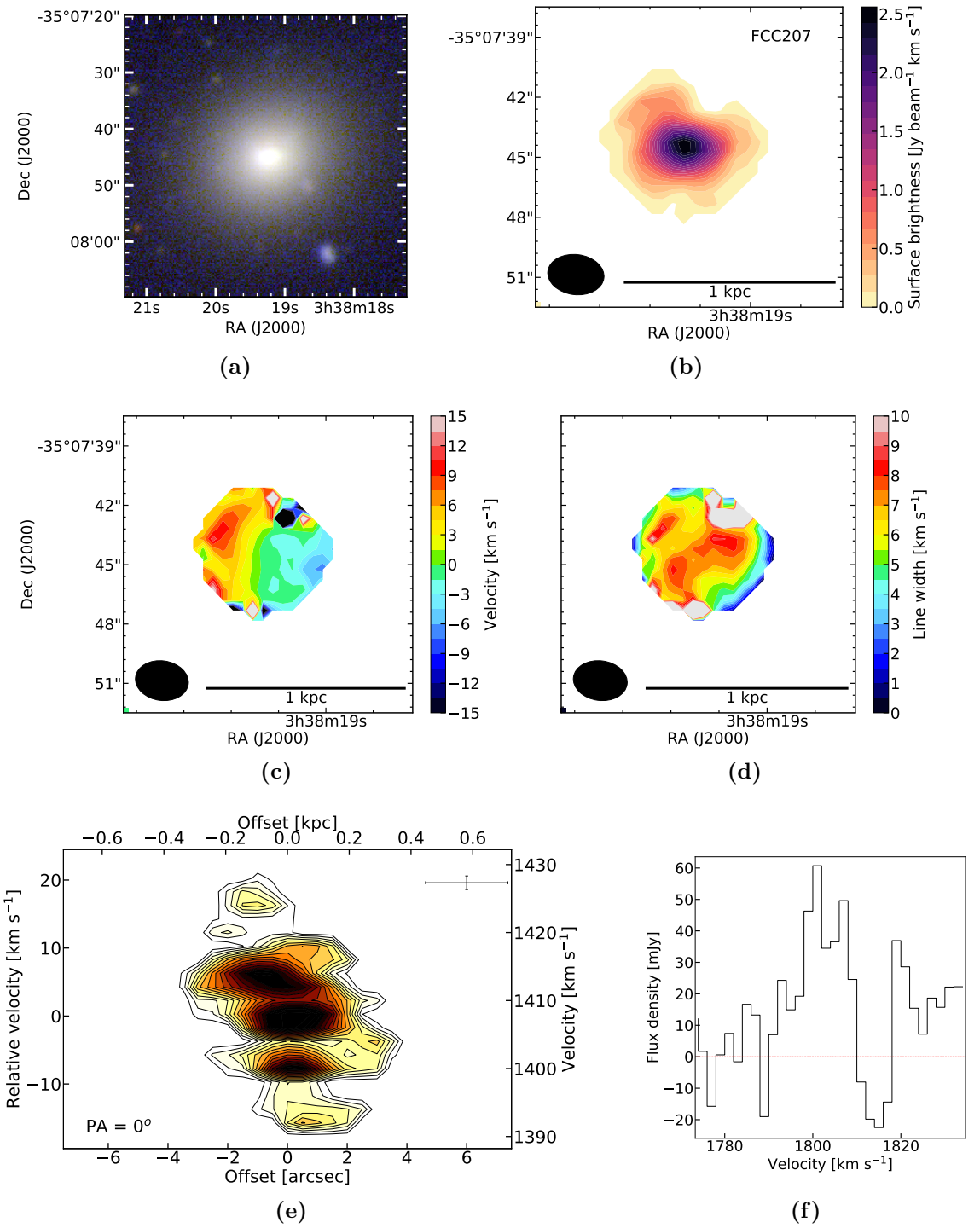

Figure A.7: FCC207, similar to Figure A.1, except that the velocity channels are 2 km s^{-1}wide.

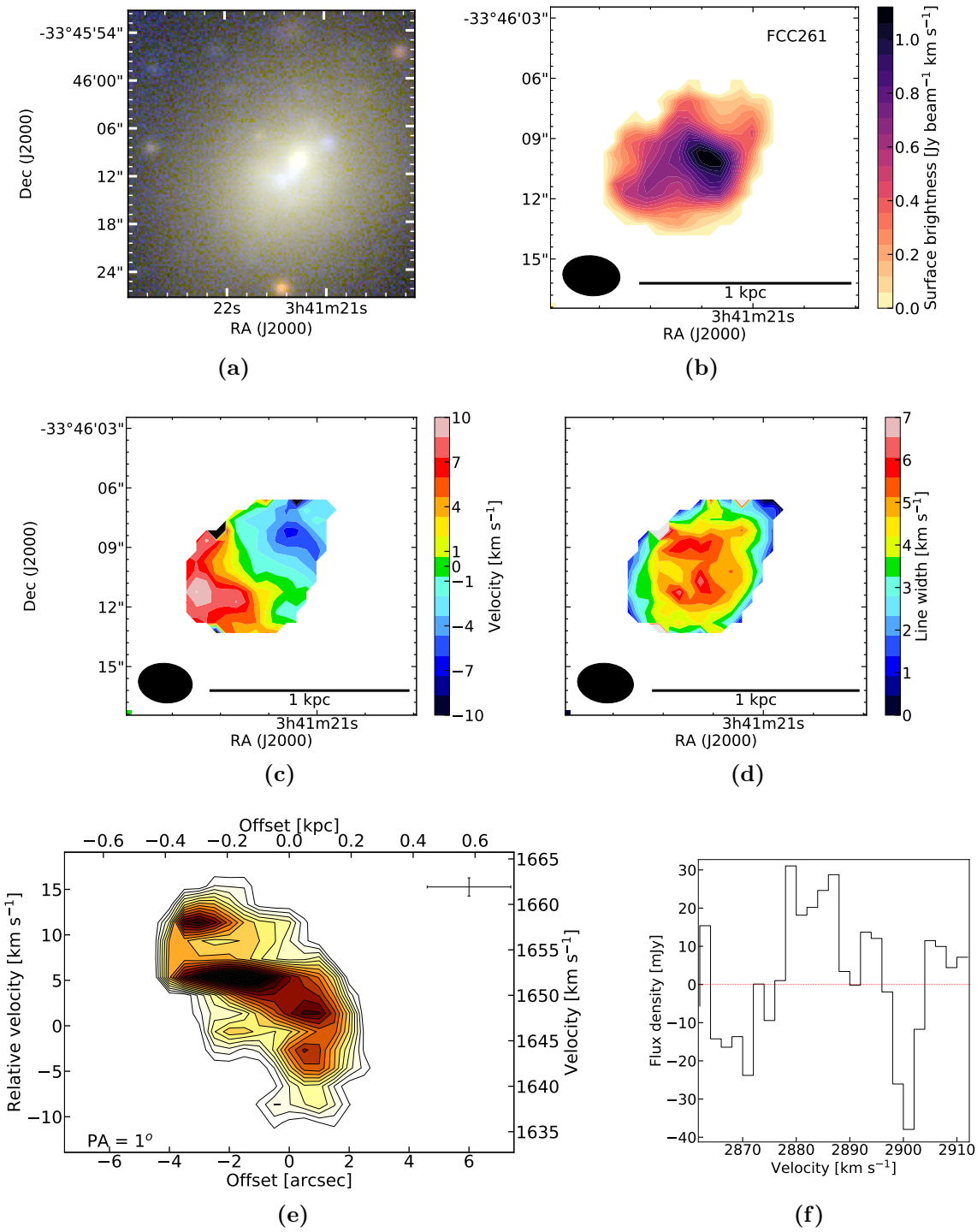

Figure A.8: FCC261, similar to Figure A.1, except that the velocity channels are 2 km s^{-1}wide.

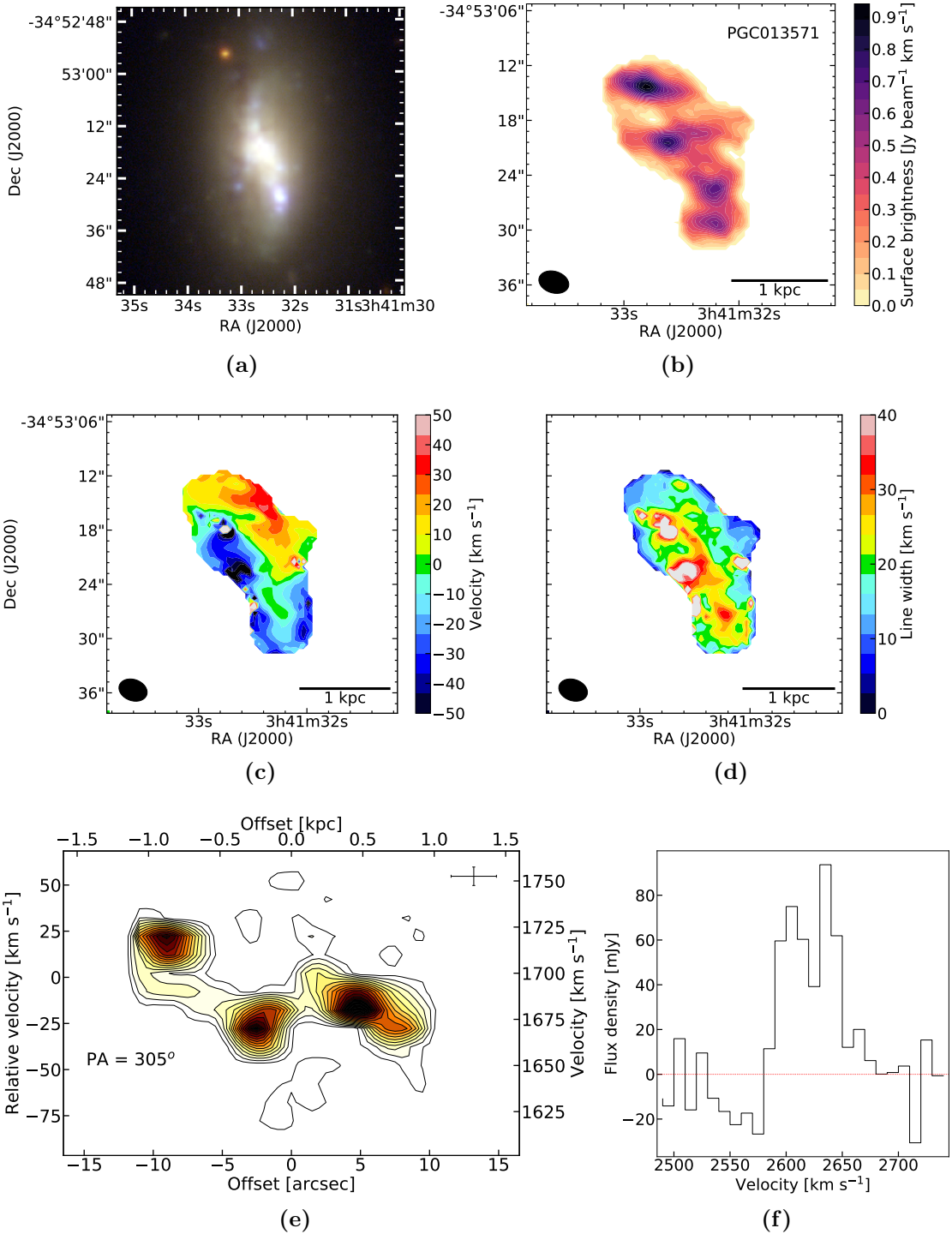

Figure A.9: PGC013571, similar to Figure A.1.

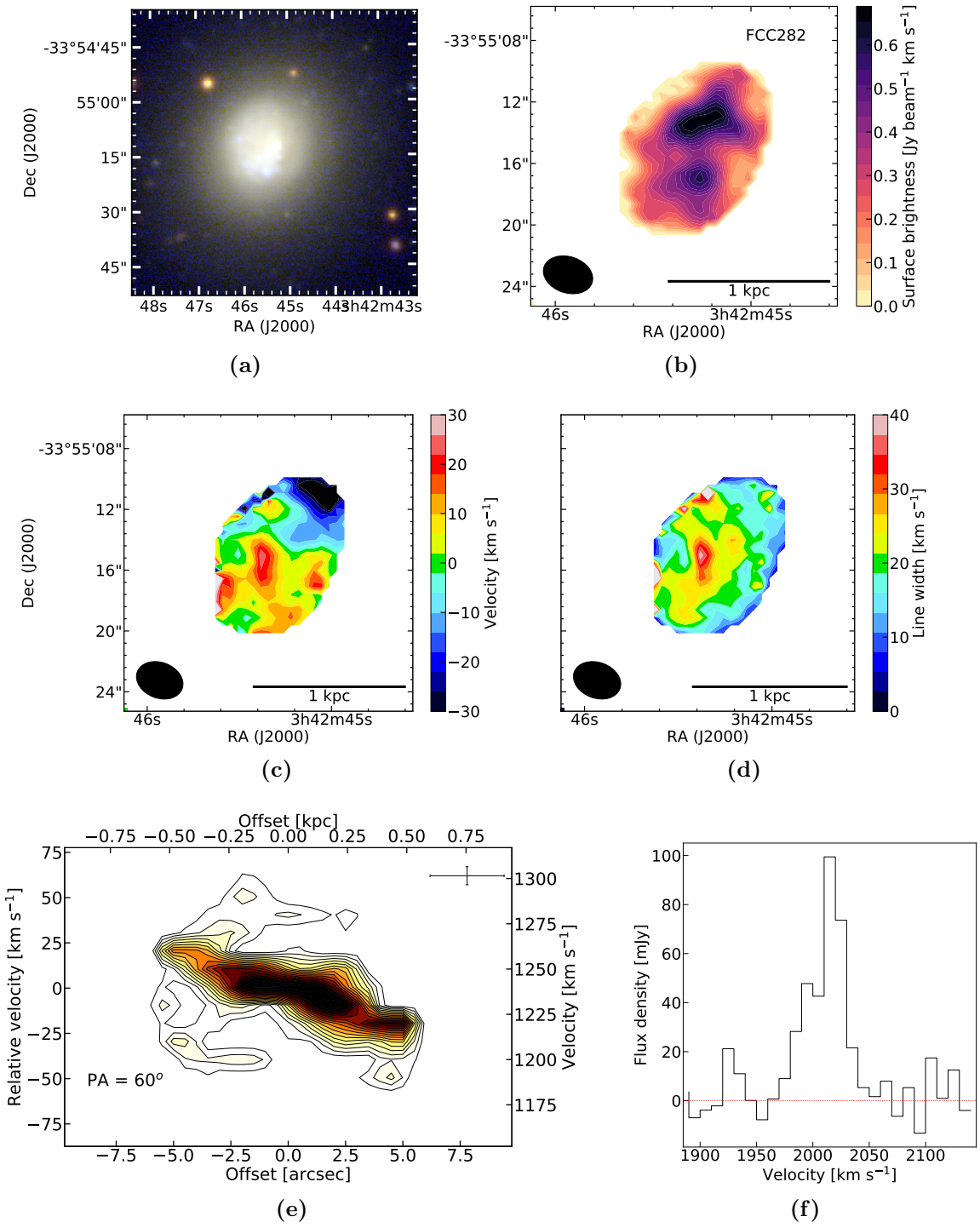

Figure A.10: FCC282, similar to Figure A.1.

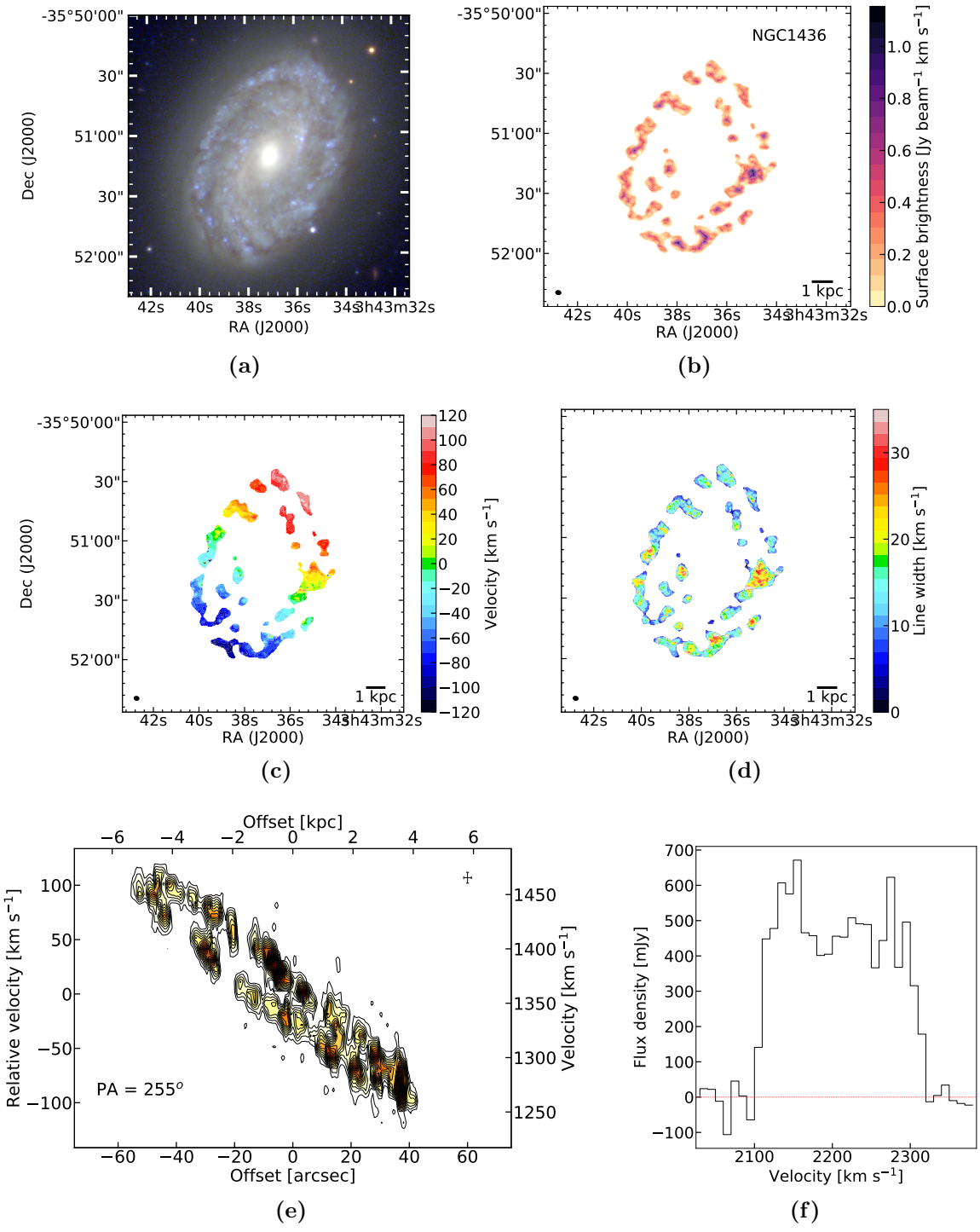

Figure A.11: NGC1436, similar to Figure A.1.

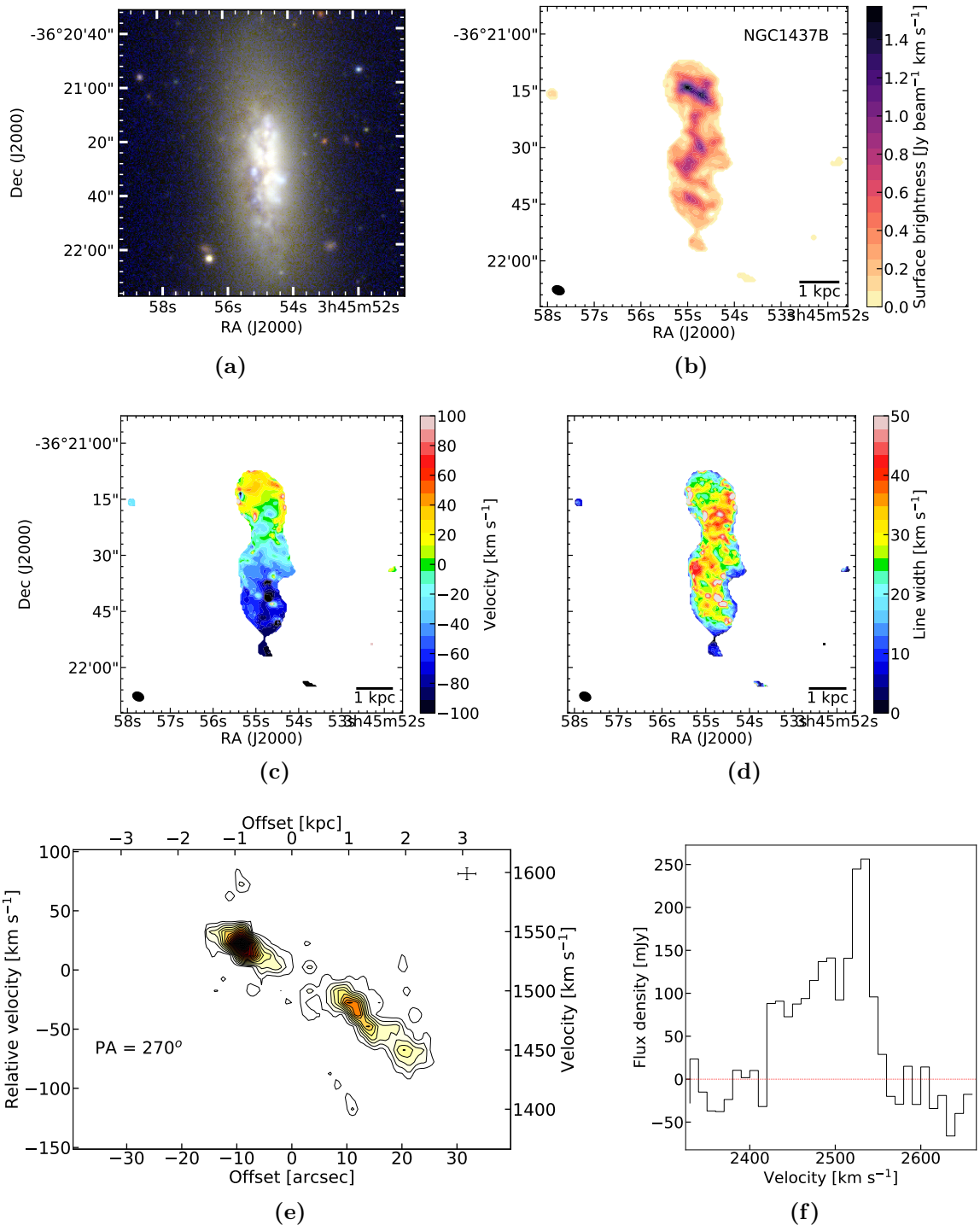

Figure A.12: NGC1437B, similar to Figure A.1.

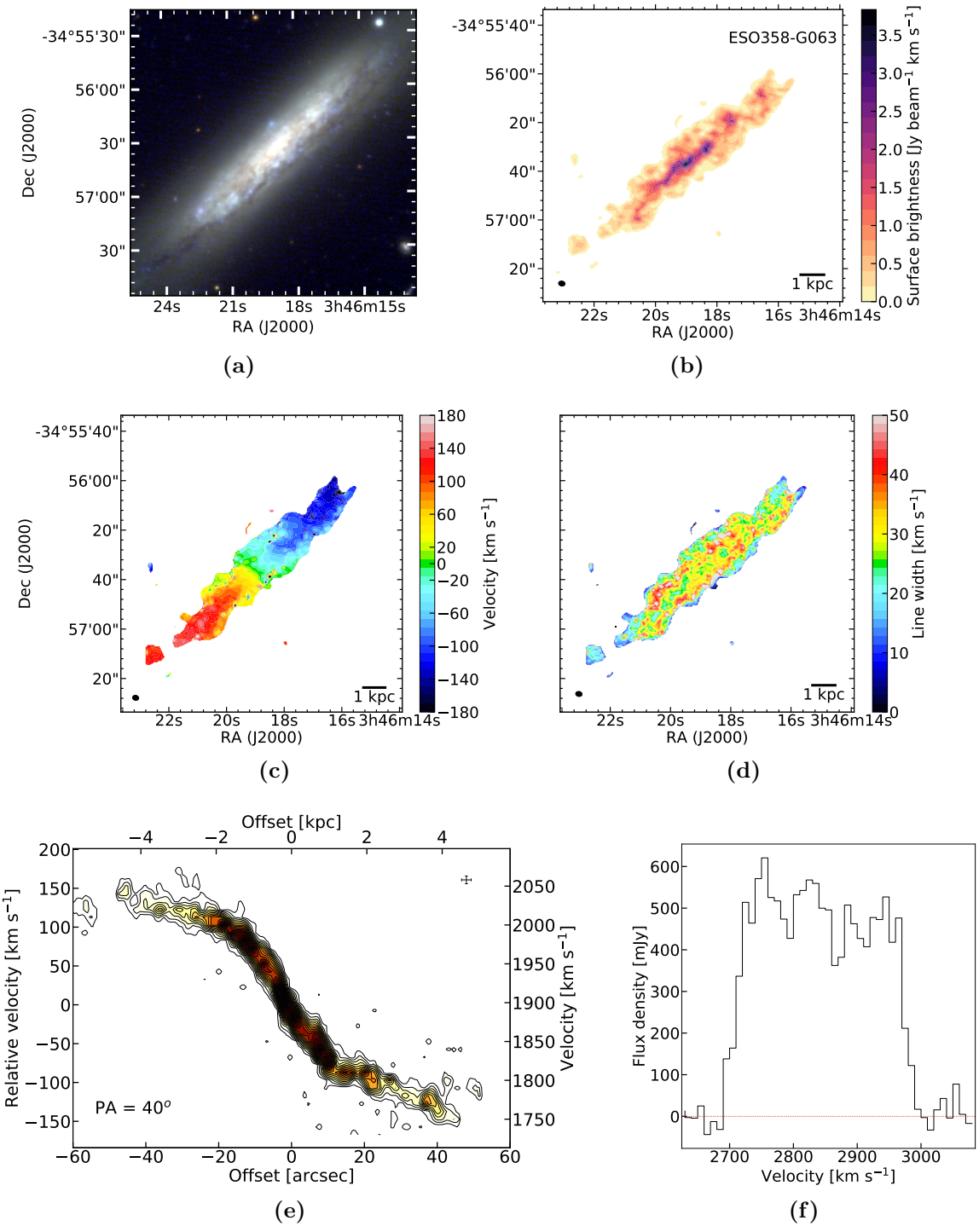

Figure A.13: ESO358-G063, similar to Figure A.1.

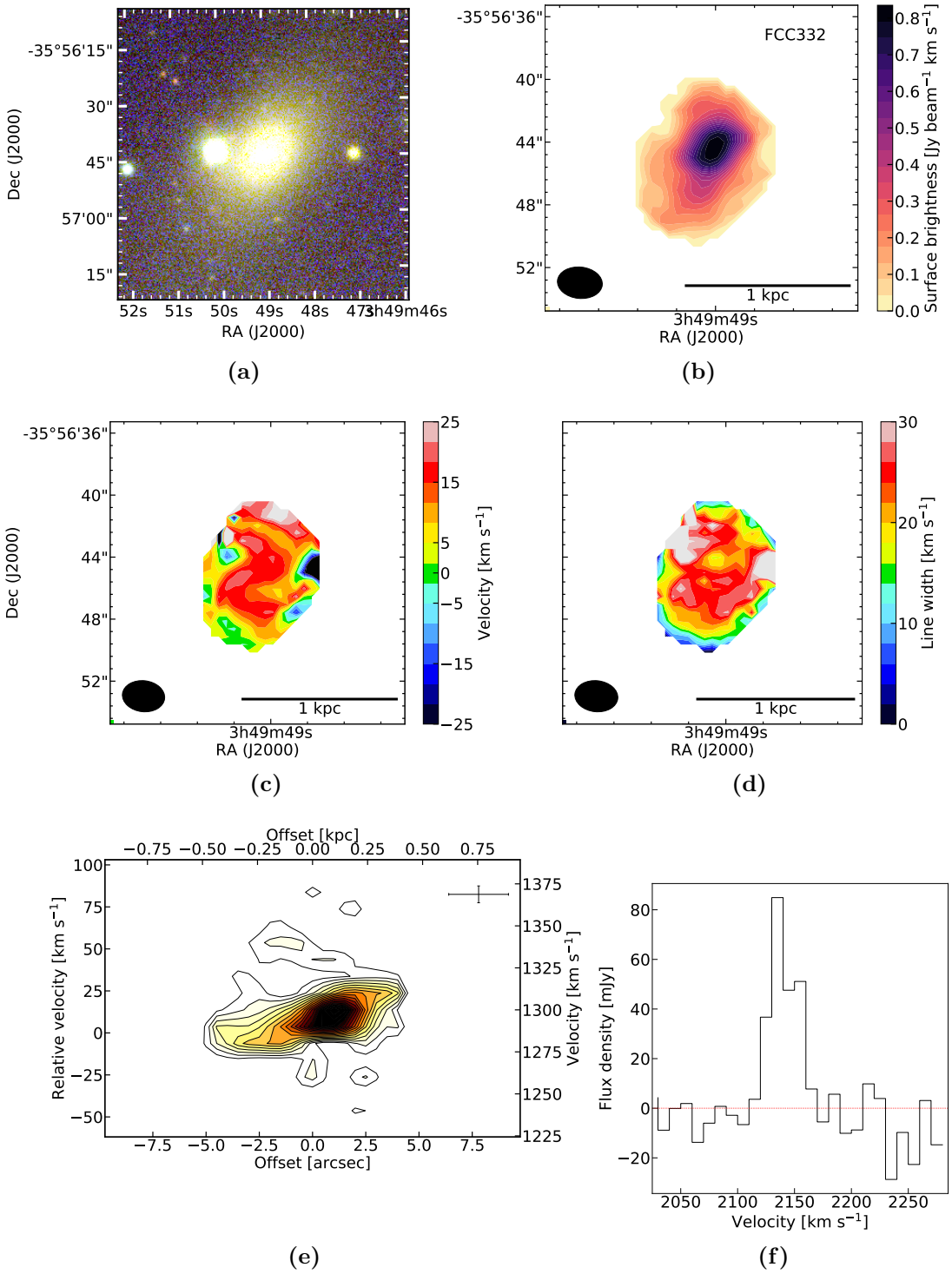

Figure A.14: FCC332, similar to Figure A.1.

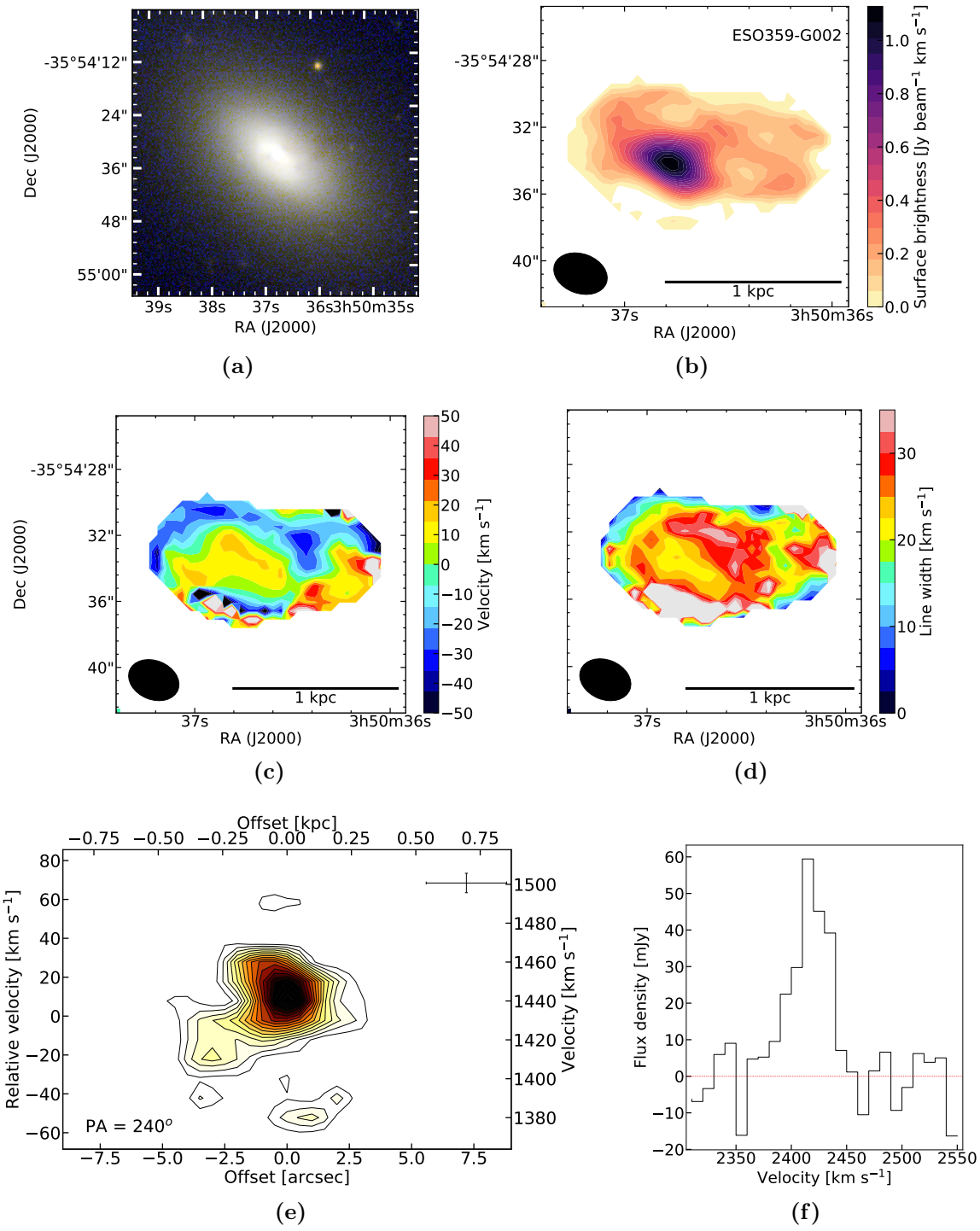

Figure A.15: ESO359-G002, similar to Figure A.1.

A.2 Comparison with optical images

Images in this appendix show the contours of the CO emission overplotted on optical (g-band) images from the Fornax Deep Survey (Peletier et al. 2020). Additional information about these figures can be found in the caption of Figure 2.5.

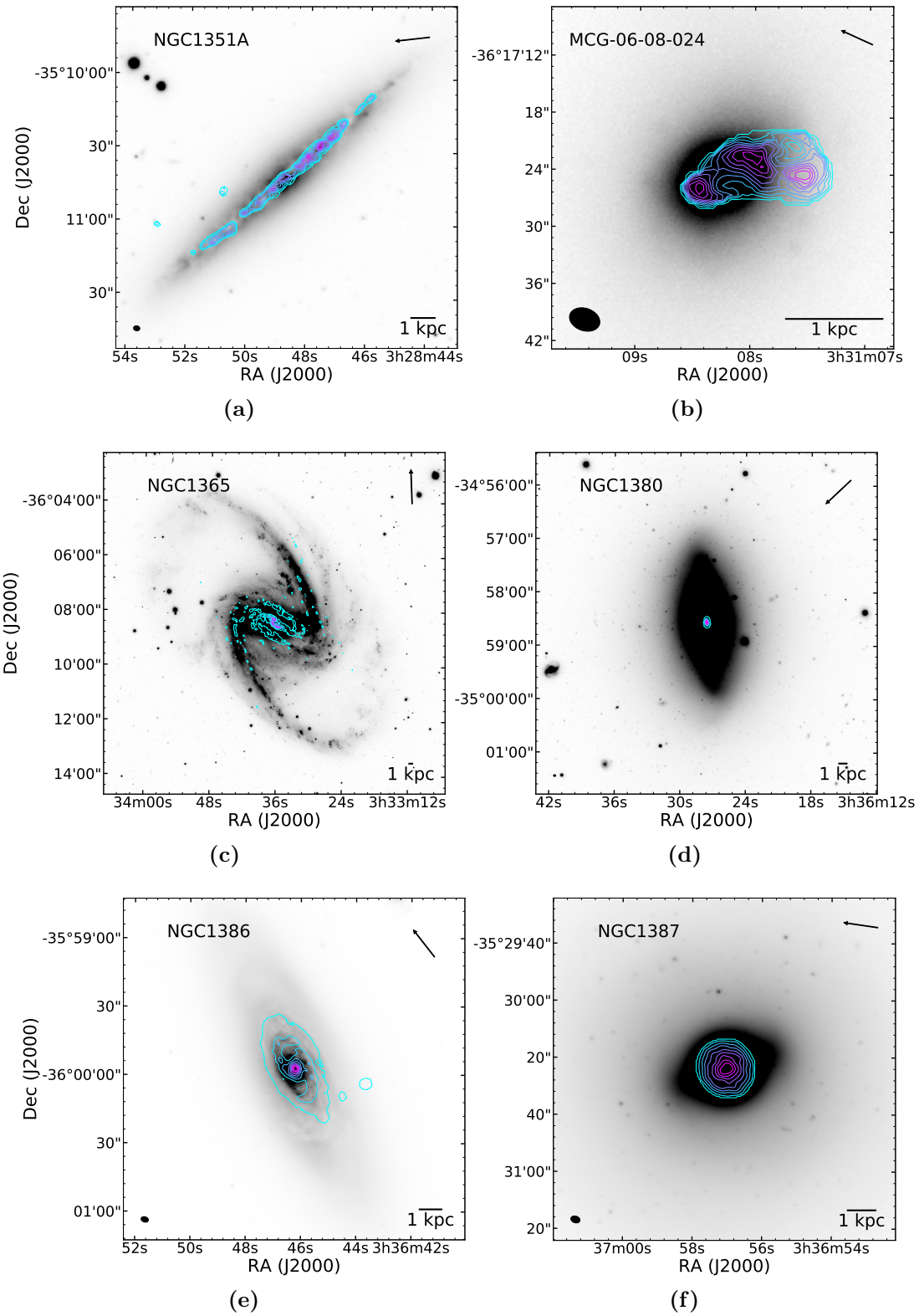
NGC1351A
-35°10'00"
30"
11'00"
30"
Dec (J2000)
1 kpc
54s 52s 50s 48s 46s 3h28m44s
RA (J2000)
(a)
MCG-06-08-024
-36°17'12"
18"
24"
30"
36"
42"
1 kpc
09s 08s 3h31m07s
RA (J2000)
(b)
NGC1365
-36°04'00"
06'00"
08'00"
10'00"
12'00"
14'00"
Dec (J2000)
1 kpc
34m00s 48s 36s 24s 3h33m12s
RA (J2000)
(c)
NGC1380
-34°56'00"
57'00"
58'00"
59'00"
-35°00'00"
01'00"
1 kpc
42s 36s 30s 24s 18s 3h36m12s
RA (J2000)
(d)
NGC1386
-35°59'00"
30"
-36°00'00"
30"
01'00"
Dec (J2000)
1 kpc
52s 50s 48s 46s 44s 3h36m42s
RA (J2000)
(e)
NGC1387
-35°29'40"
30'00"
20"
40"
31'00"
20"
1 kpc
37m00s 58s 56s 3h36m54s
RA (J2000)
(f)

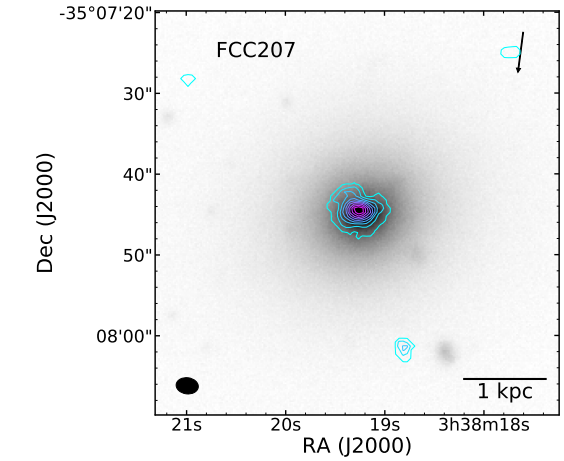
FCC207
-35°07'20"
30"
40"
50"
08'00"
Dec (J2000)
21s
20s
19s
3h38m18s
RA (J2000)
1 kpc

(g)

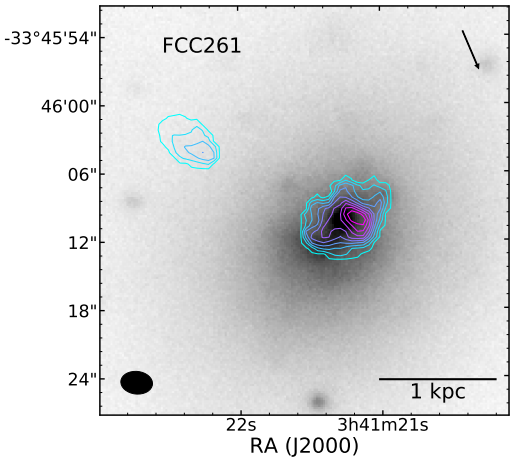
FCC261
-33°45'54"
46'00"
06"
12"
18"
24"
22s
3h41m21s
RA (J2000)
1 kpc

(h)

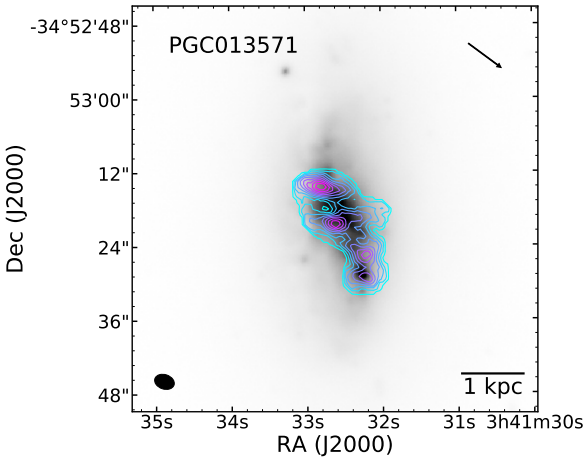
PGC013571
-34°52'48"
53'00"
12"
24"
36"
48"
Dec (J2000)
35s
34s
33s
32s
31s
3h41m30s
RA (J2000)
1 kpc

(i)

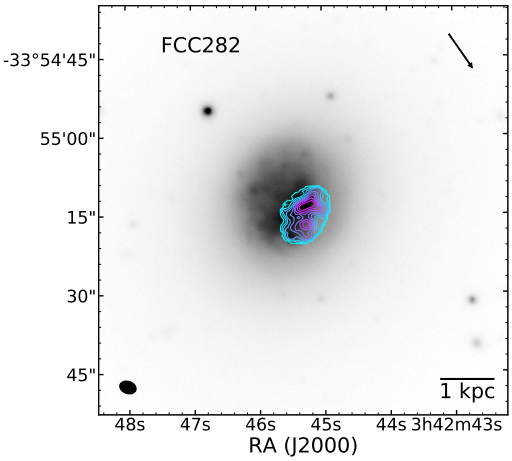
FCC282
-33°54'45"
55'00"
15"
30"
45"
48s
47s
46s
45s
44s
3h42m43s
RA (J2000)
1 kpc

(j)

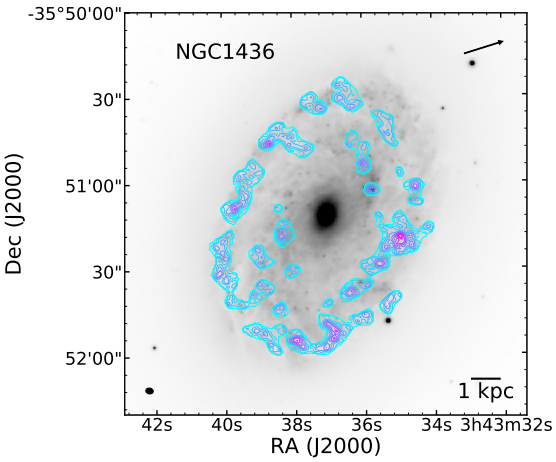
NGC1436
-35°50'00"
30"
51'00"
30"
52'00"
Dec (J2000)
42s
40s
38s
36s
34s
3h43m32s
RA (J2000)
1 kpc

(k)

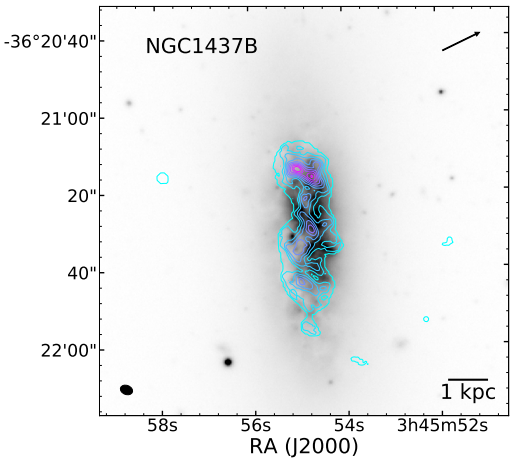
NGC1437B
-36°20'40"
21'00"
20"
40"
22'00"
58s
56s
54s
3h45m52s
RA (J2000)
1 kpc

(l)

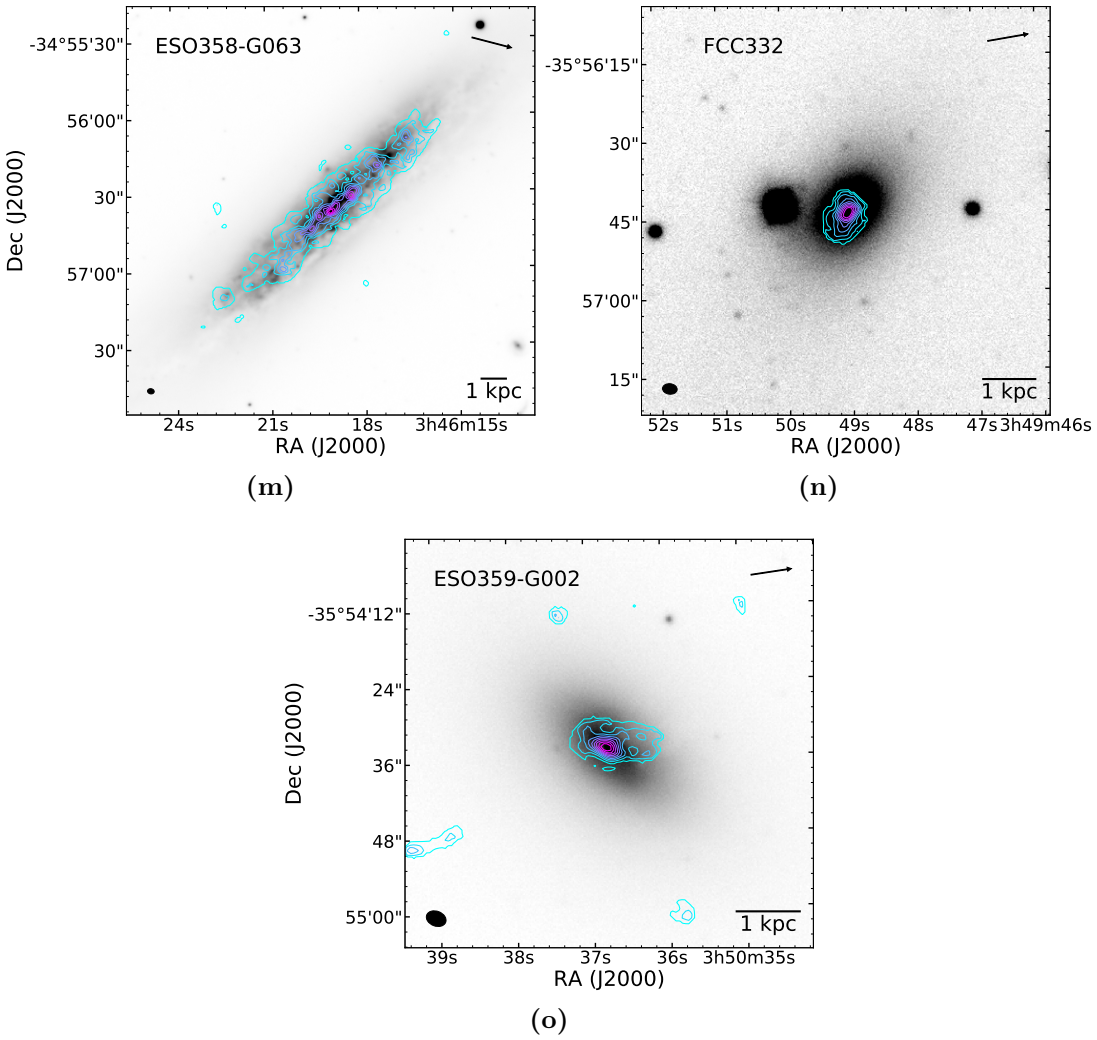

Figure A.14: CO integrated intensity contours overplotted on optical (g-band) images of the galaxies (see §2.3.6).

Appendix B
Comparison with the Virgo cluster

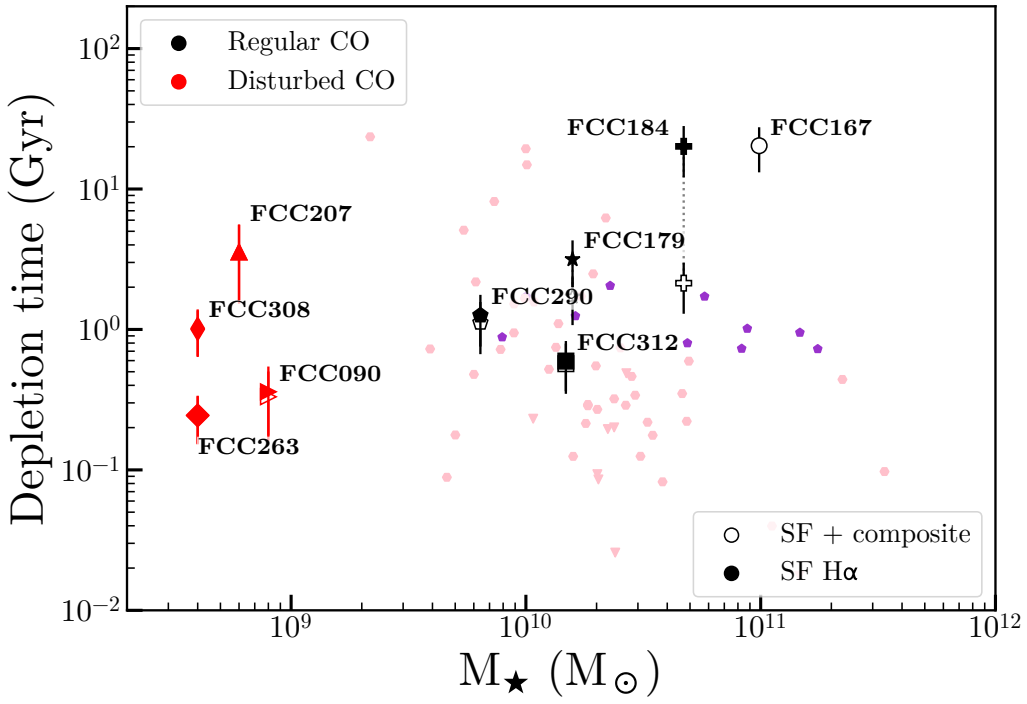

(a)

Figure B.1: Similar to Figure 3.4, but with data from the Virgo cluster only. Purple markers are ETGs from ATLAS^{3D}, and pink markers are galaxies from the HRS. High-mass Fornax galaxies have long depletion times compared to these samples (especially the HRS), probably because they are ETGs, while the HRS consists of spiral galaxies only. The low-mass end of the HRS agrees well with the Fornax data, both show a spread in depletion times here.

Appendix C
SF plots, t_{dep} maps, and discussion of individual galaxies

C.0.1 FCC90

FCC90 (MCG-06-08-024) is a dwarf elliptical galaxy located (in projection) close to the virial radius. It has a molecular gas tail extending beyond its stellar body, either caused by RPS or by a tidal interaction. The ionised gas also shows a tail in the same location, but pointed in a slightly different direction. Depletion times in the galaxy body are significantly shorter than the "normal" 1-2 Gyr for nearby spiral galaxies, and are distributed around ∼0.5 Gyr instead. In the gas tail, on the other hand, depletion times are $\gtrsim$ 10 times longer. This is in agreement with what is found in other gas tails caused by RPS (Moretti et al., 2018; Ramatsoku et al., 2019; Jachym et al., 2019).

C.0.2 FCC167

FCC167 (NGC1380) is an early-type galaxy with a nested ISM, consisting of a molecular gas ring/disk located inside a dust lane. Ionised gas is present throughout the galaxy (Viaene et al., 2019). According to our BPT classification, no star forming Hα is present in this galaxy. The majority of the pixels are in the "composite" area of the diagram. The ionised gas forms a tail at the south side of the galaxy, likely because of RPS or an ongoing tidal interaction. Depletion times are mostly around 1-2 Gyr, although there is some scatter towards shorter depletion times.

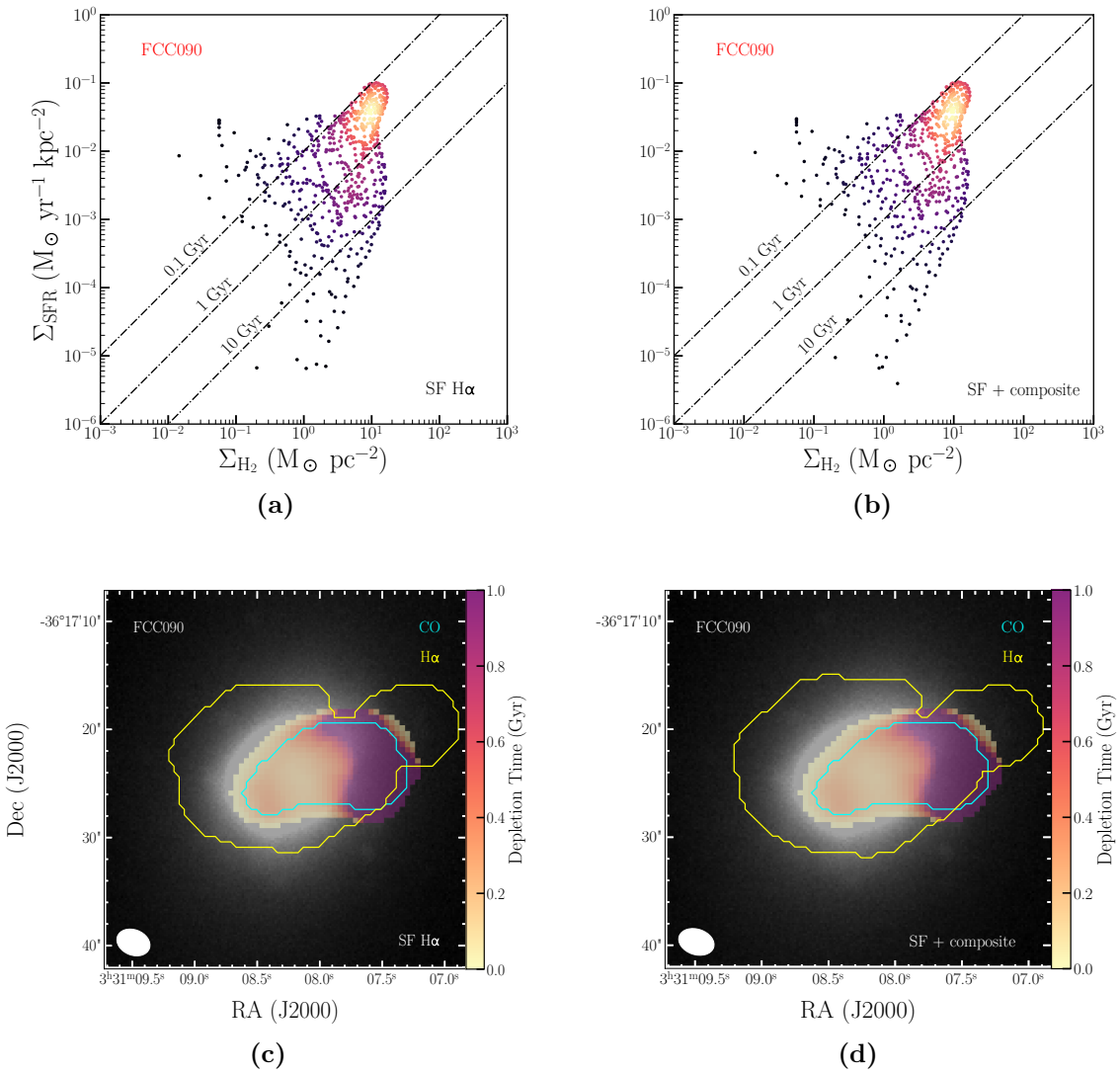

Figure C.1: Top row: Relation between the molecular gas and star formation rate surface densities for FCC90. The colours of the markers indicate the density around the data point in this plane, determined using a Gaussian kernel density estimation. Lines of constant depletion times (0.1, 1, and 10 Gyr) are shown. The galaxy name is indicated in the upper left corner, and whether composite Hα or only the star forming Hα is used is indicated in the lower right corner. FCC90 deviates from the "standard" H_2 depletion time of 1-2 Gyr often found in field galaxies (e.g. Leroy et al. 2008, Saintonge et al. 2012, Figure 3.4) by a factor 5-10. **Bottom row**: depletion time maps of FCC90. Maps were made both taking into account composite and star forming Hα (right column) and considering only purely star forming Hα (left column). Whether composite Hα or only the star forming Hα is considered is indicated in the lower right corner. The maps are overplotted on optical (g-band) images from the Fornax Deep Survey (FDS, Iodice et al. 2016, 2017; Venhola et al. 2017, 2018, Peletier et al., in prep.). The extent of the CO emission is indicated with a cyan contour, and that of the Hα emission with a yellow contour (both clipped at the 3σ level). The beam of the ALMA observations is shown in the lower left corner, and the FCC number of the galaxy is indicated in the upper left corners. Depletion times are short in the galaxy's body (< 0.5 Gyr), but long in the gas tail ($\gg$2 Gyr).

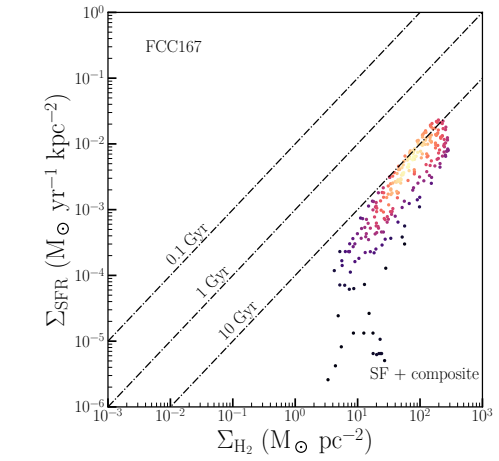

(a)

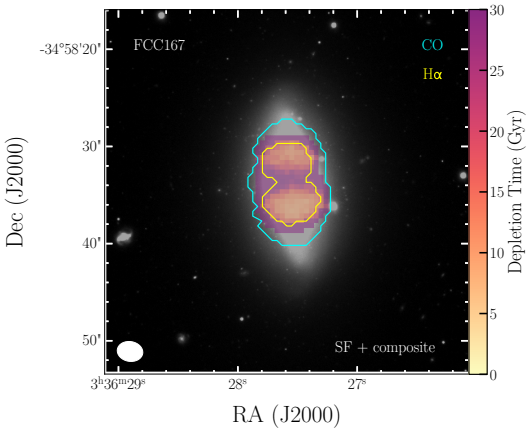

(b)

Figure C.2: Similar to Figure C.1, but for FCC167. FCC167 has no star forming Hα, so only one (equivalent to the right column in Figure C.1) column is shown. Depletion times are long, significantly longer than 10 Gyr in almost all regions.

C.0.3 FCC179

FCC179 (NGC1386) is a barred spiral galaxy, that also harbours an AGN. This results in a significant difference between the left (only Hα dominated by star formation) and right (composite Hαconsidered also) columns in Figure C.3. If only the star forming Hα is taken into account, there is significant scatter in the star formation relation. The relationship is tighter when composite Hα is considered. Depletion times are shorter in the spiral arms compared to the inter-arm regions. The shortest depletion times at high Hα surface densities originate from the region around the AGN, and are therefore potentially contaminated. The distribution of the ionised gas at the east-side of the galaxy, as well as two separate blobs of molecular gas, could be a sign of ongoing ram pressure stripping.

C.0.4 FCC184

FCC184 (NGC1387) is a lenticular galaxy. It also harbours an AGN, and again, most of the pixels in the ionised gas map were classified as "composite". Depletion times in this galaxy also vary significantly depending on whether composite Hα is included or not. If only star forming Hα is considered, depletion times are long (up to tens of Gyrs) and show large variations. If composite Hα is included, depletion times are a few Gyrs, showing an extremely tight relationship between the H_2 and SFR surface densities.

C.0.5 FCC207

FCC207 is a dwarf galaxy. It has relatively long depletion times, closer to 10 Gyr than to 1 Gyr. Molecular and ionised gas are present throughout the galaxy, but depletion times are significantly longer on the west-side compared to the east-side. FCC207 is the only dwarf galaxy with a disturbed molecular gas reservoir that has increased depletion times, rather than decreased. All Hα in this galaxy is dominated by star formation, so the left and right columns (SF Hα vs. composite + SF Hα) in Figure C.5 are identical.

C.0.6 FCC263

FCC263 (PGC013571) is another dwarf galaxy with a disturbed molecular gas reservoir. Its molecular gas morphology and kinematics suggests that it either has a strong bar or has undergone a recent merger. The molecular gas is much more

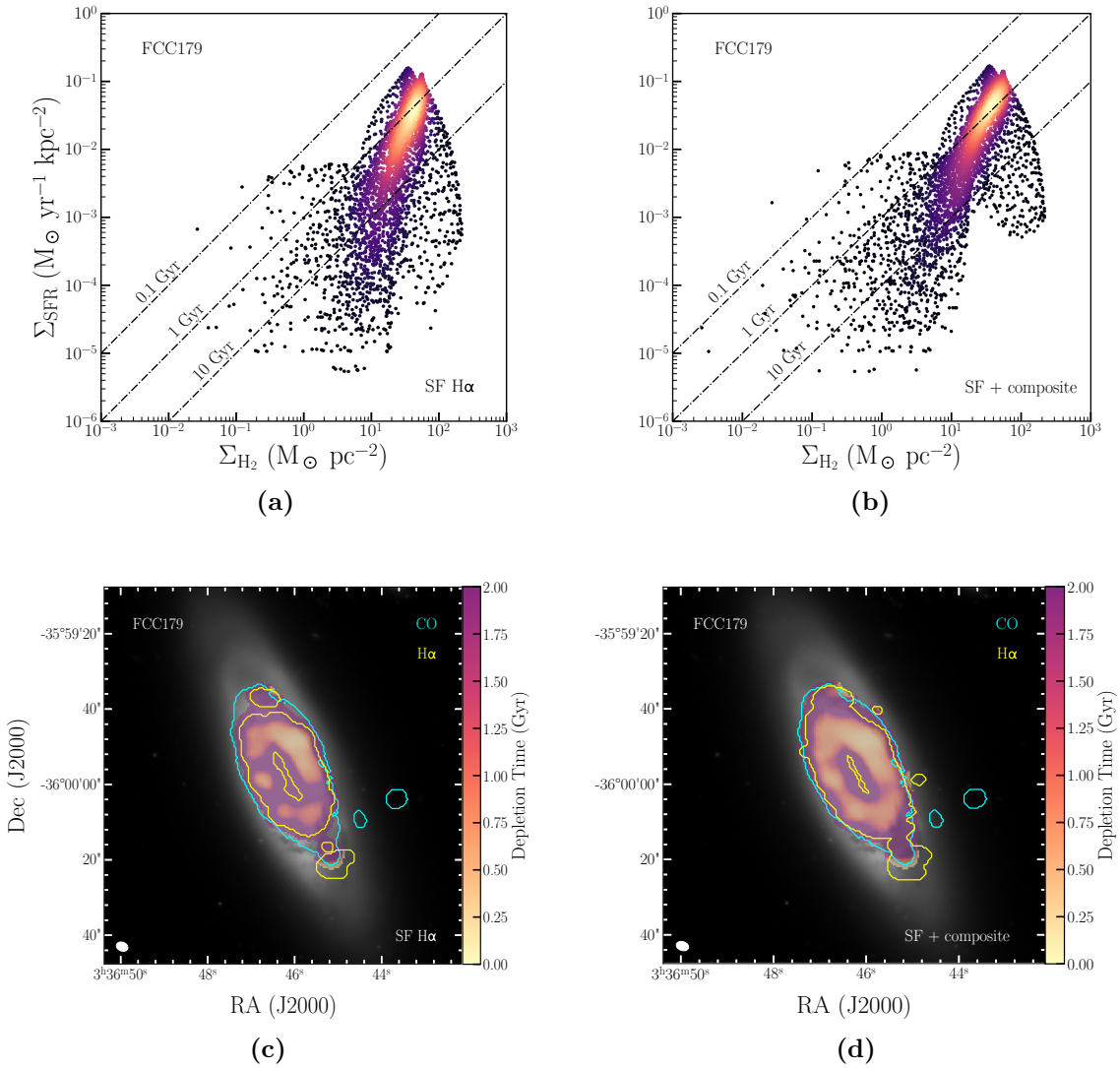

Figure C.3: Similar to Figure C.1, but for FCC179. The majority of the points are close to the 1 Gyr depletion time line, but the slope of the SF plot is quite steep, especially when only SF Hα is considered. The latter forms a ring around the galactic centre.

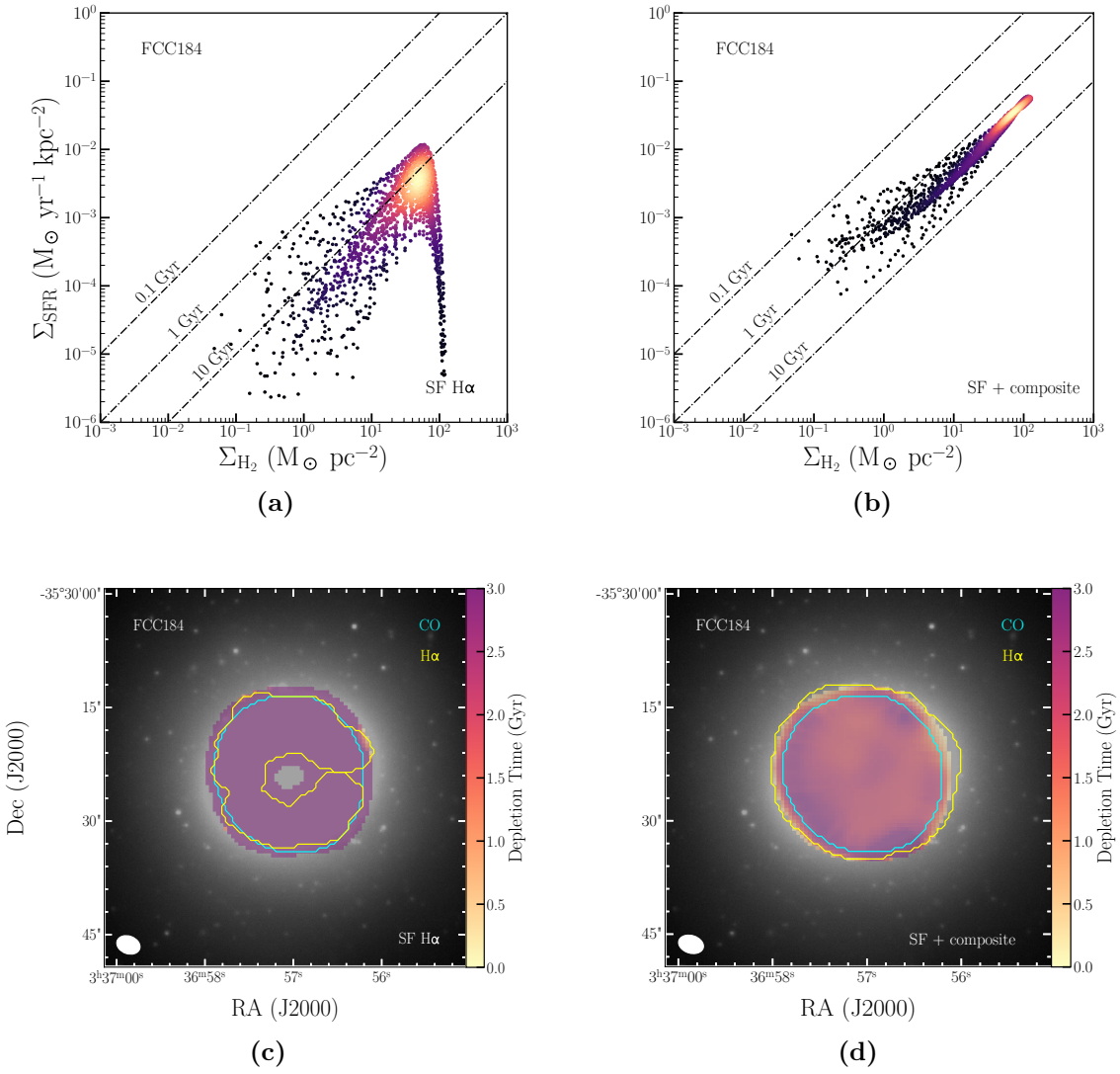

Figure C.4: Similar to Figure C.1, but for FCC184. The SF plot for composite + star forming Hα is very tight and around the expected 2 Gyr depletion time line. It is quite sparse for the star forming SF only, because that only forms a patchy ring around the galactic centre. Nearly all other Hα in this galaxy is in the transition region of the BPT diagram, so in reality there is likely some more star forming Hα, and the true SF relation plot is in between the left and right one.

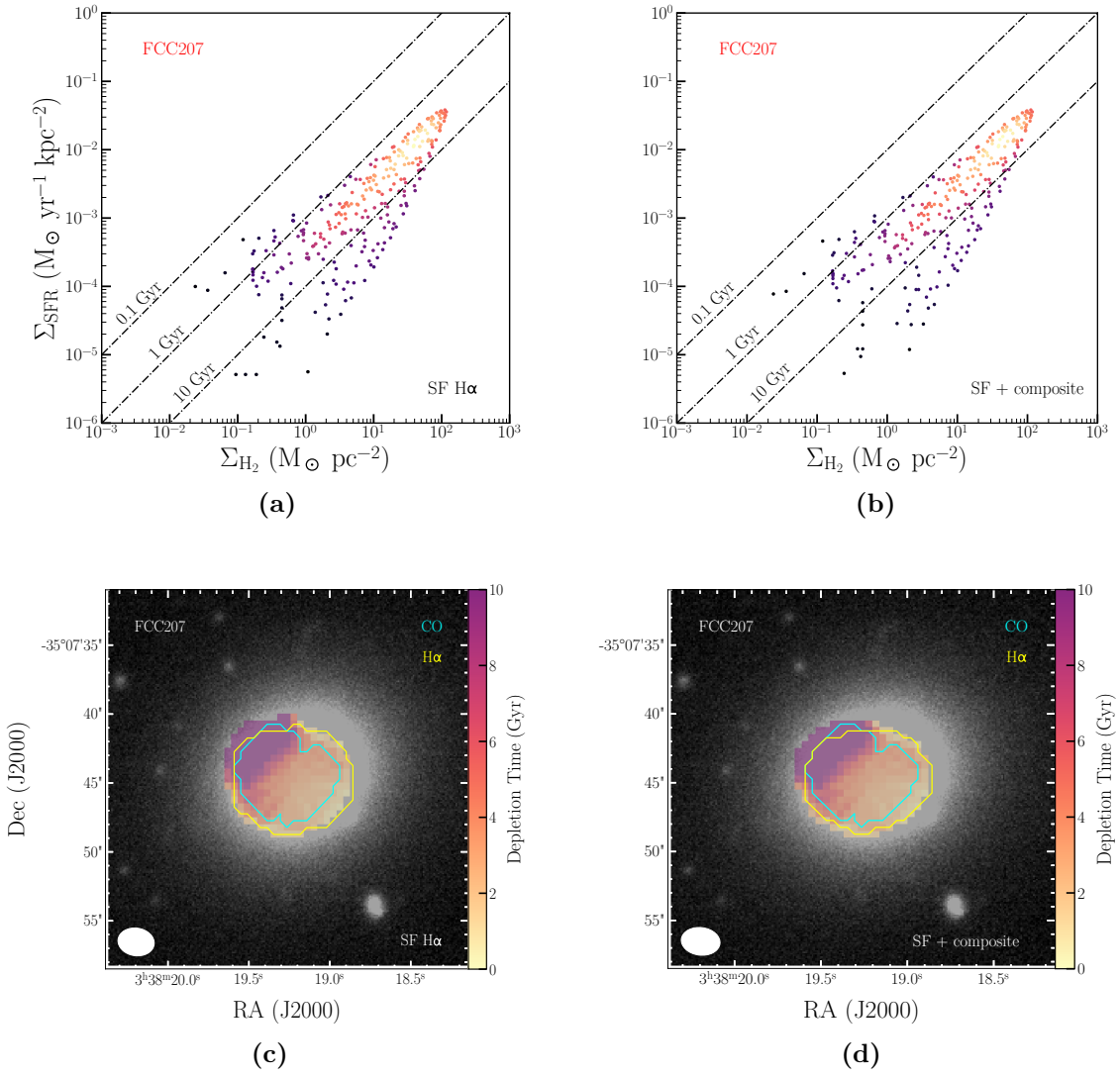

Figure C.5: Similar to Figure C.1, but for FCC207. Although there is a gradient in depletion times, suggesting compression of the molecular gas as a result of the galaxy's first infall into the cluster, depletion times in FCC207 are long, varying between several Gyrs and several tens of Gyrs. It is possible that the slight starburst seen in other dwarf galaxies on their first infall has not yet started, or has already passed.

centrally distributed than the ionised gas, resulting in identical $\Sigma_{H_2} - \Sigma_{SFR}$ relations in the left and right columns (the Hα that is added in the right column does not overlap with any molecular gas). Depletion times in this galaxy are significantly shorter than 1 Gyr, and show significant scatter. There are various patches of shorter and longer depletion times.

C.0.7 FCC290

FCC290 (NGC1436) is a flocculent spiral that is almost face-on. This makes it an ideal candidate for comparing the molecular and ionised gas distributions, without suffering too much from inclination effects. Although not all of the galaxy is covered by the MUSE observations, the data should be representative of the entire galaxy. Although not all Hα in this galaxy is star forming, the resulting $\Sigma_{H_2} - \Sigma_{SFR}$ relations for both cases are very similar, with slightly more scatter in the star formation rate surface densities in the case where only star forming Hα is taken into account. The spread in depletion times in this galaxy is large, with the densest area in the plot varying from less than a Gyr to up to 10 Gyr. It is strikingly symmetric in both directions, and the maps reveal both areas of increased and decreased depletion times. This suggests that the Hα and CO do not overlap perfectly, their offset possibly revealing the time passed since the OB stars were actually formed (see §3.5). The bulk of the depletion times is around the "standard" 1-2 Gyr.

C.0.8 FCC308

FCC308 (NGC1437B) is a very blue galaxy with a disturbed molecular gas reservoir. The ionised gas is distributed somewhat more widely than the molecular gas, but generally follows the same distribution. As the Hα that is not dominated by star formation does not overlap with any molecular gas, there is very little difference between the left and right columns in Figure C.8. As could be expected from its colour, depletion times are short in this galaxy, well below 1 Gyr. There is some scatter in the $\Sigma_{H_2} - \Sigma_{SFR}$ relation towards longer depletion times, mostly resulting from the north-west of the galaxy where the edges of the detected CO and Hα emission are very close together. Throughout the rest of the galaxy there also is some variation in depletion times.

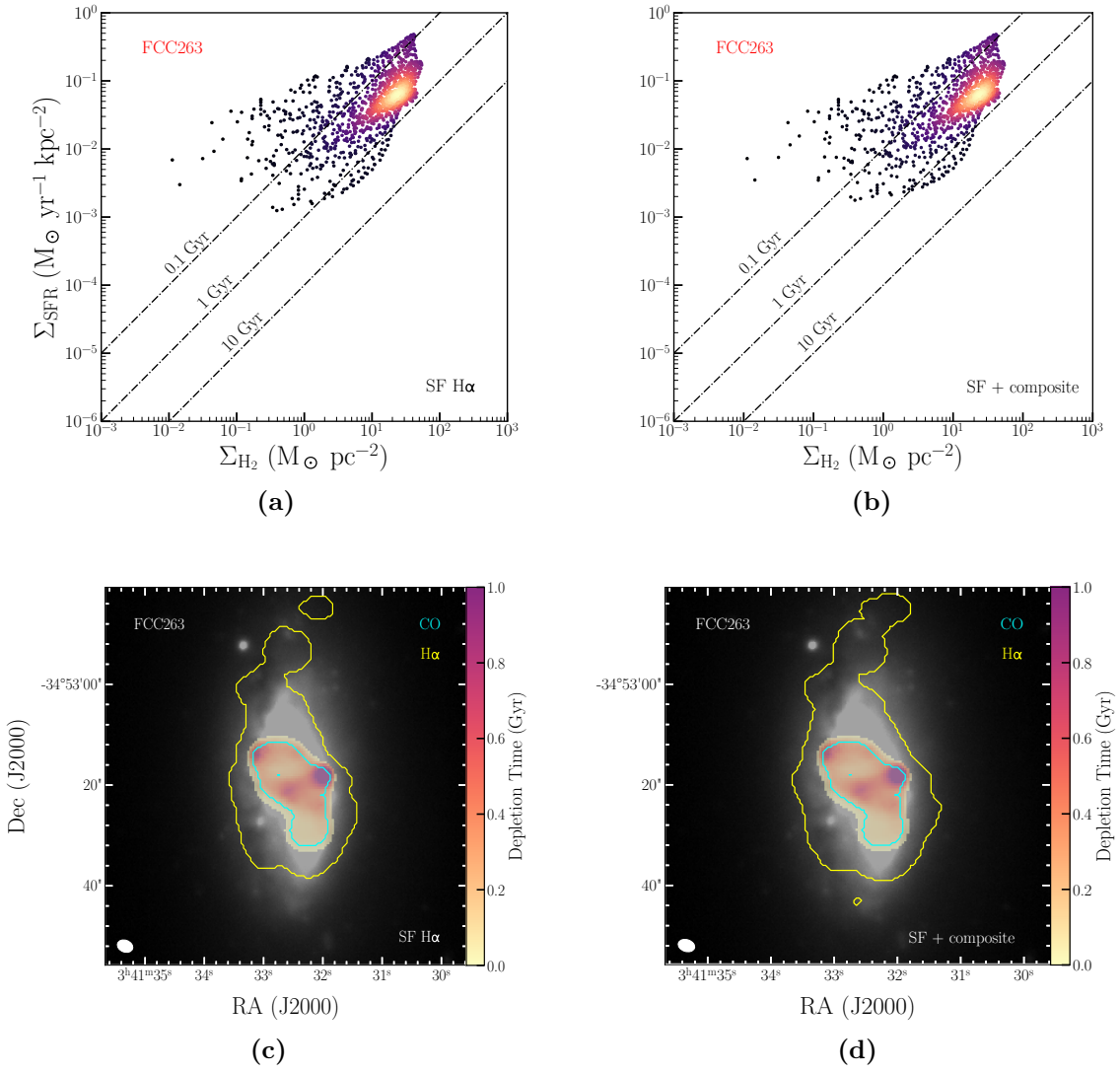

Figure C.6: Similar to Figure C.1, but for FCC263. There is some spread in the SF relation, and depletion times are around 0.5 Gyr. The CO is more concentrated than the Hα, and there are some regions where the depletion times are relatively long.

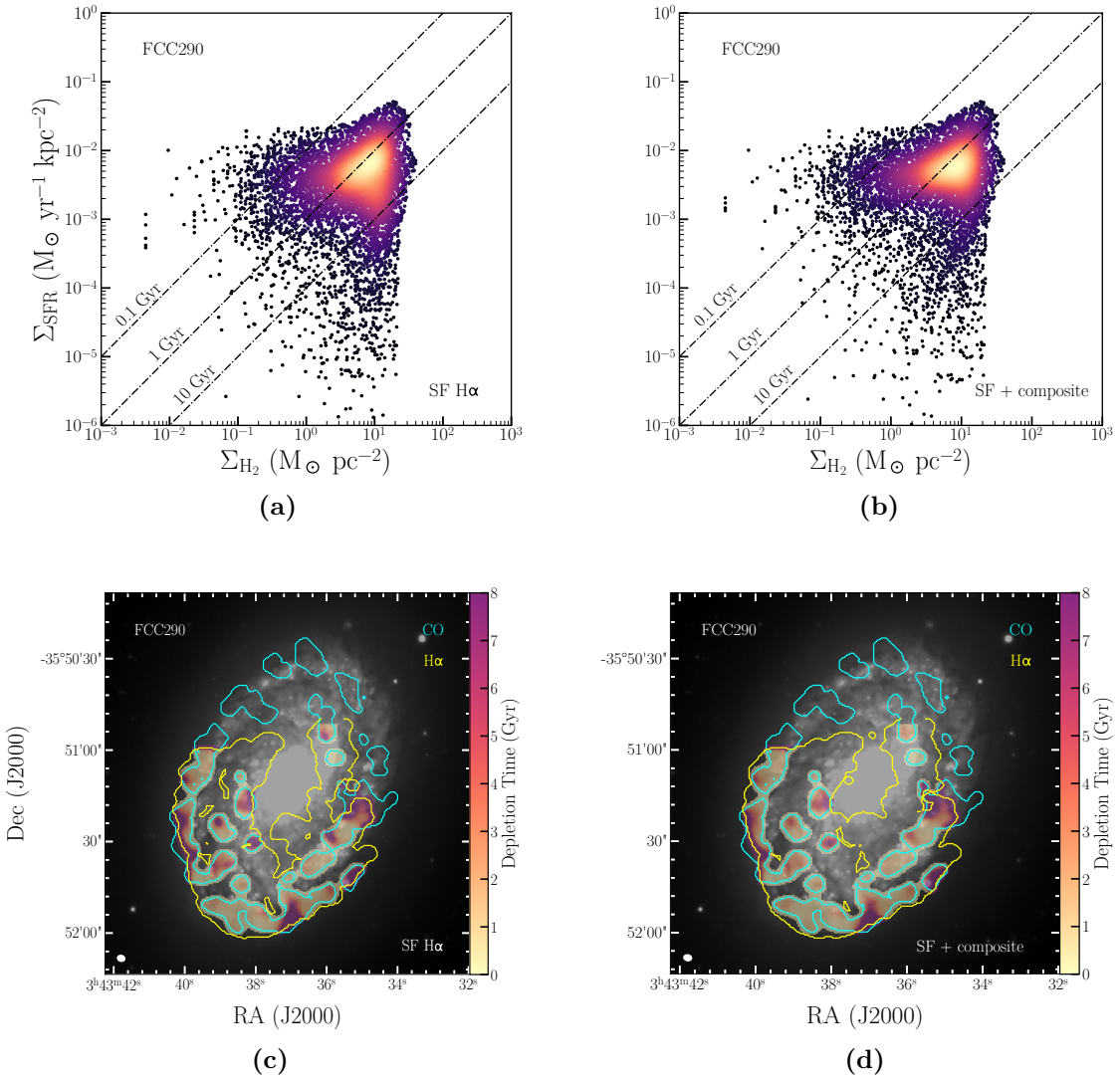

Figure C.7: Similar to Figure C.1, but for FCC290. There is some spread in the SF plot, but the majority of the points lie around the 2 Gyr line. The variation in depletion times can be seen in the maps. The MUSE field of view does not cover the entire galaxy, but the area covered should be quite representative of the entire object. There is a large spread in depletion times, that is quite symmetric around the 2 Gyr depletion time line.

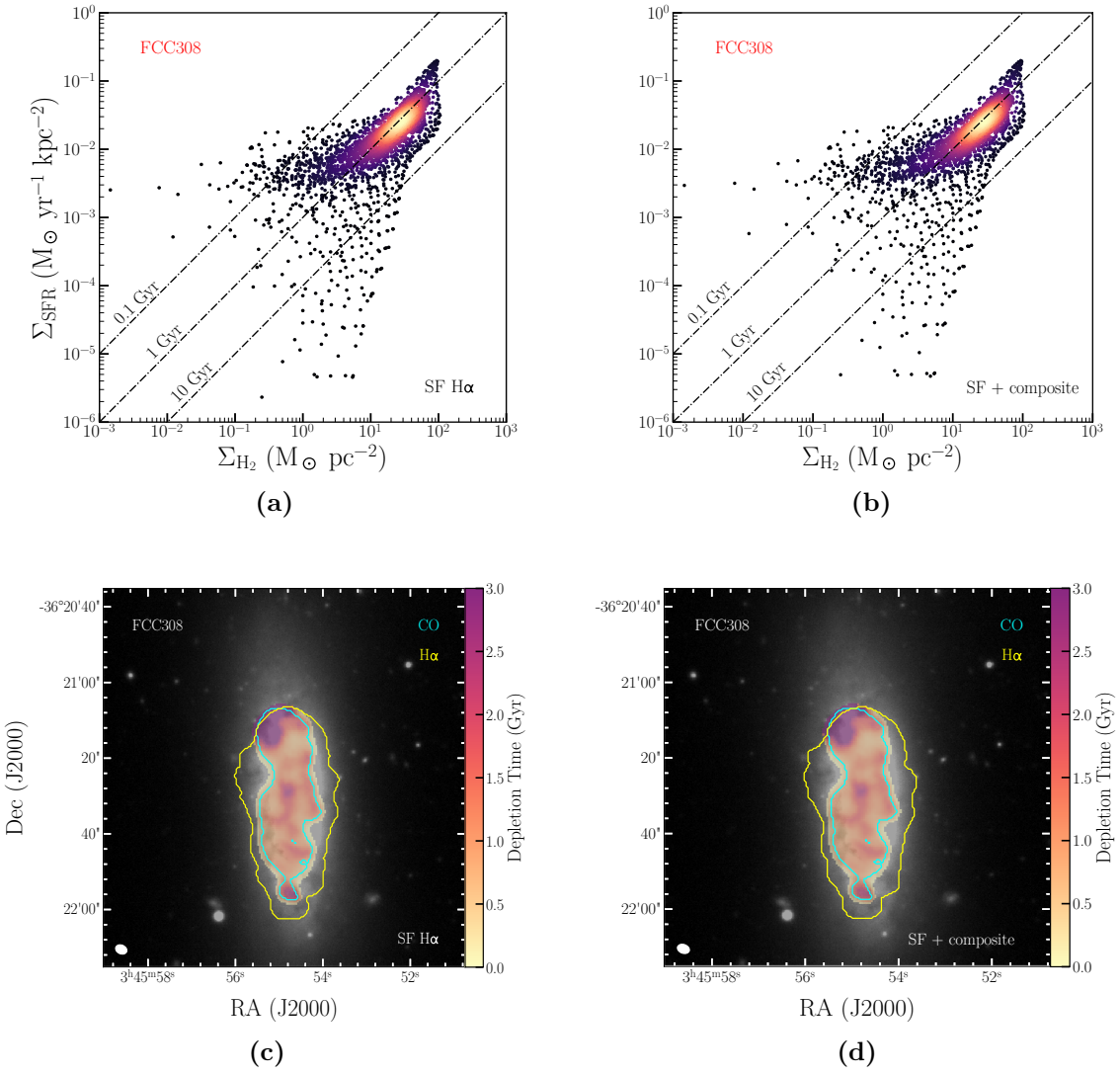

Figure C.8: Similar to Figure C.1, but for FCC308. Depletion times are relatively short, and vary slightly throughout the galaxy. There is a small patch in the north-west of the galaxy where CO is detected, but not Hα.

C.0.9 FCC312

FCC312 (ESO358-G063) is a large spiral galaxy located around the virial radius of the cluster (in projection). There is some scatter in the depletion times due to small scale variations clearly visible in the maps. Depletion times are on the short side (mostly slightly shorter than 1 Gyr, but much shorter in some locations). Most of the Hα is star forming and extends more widely than the molecular gas, resulting in very similar $\Sigma_{\rm H_2} - \Sigma_{\rm SFR}$ relations in the cases where composite Hα is taken into account versus the star formation dominated Hα only. The exception is a slight "chip" in the north-west of the galaxy (indicated with a blue/white arrow); this is likely due mosaic effects in the MUSE data. FCC312 is possibly undergoing a slight starburst as it is entering the cluster.

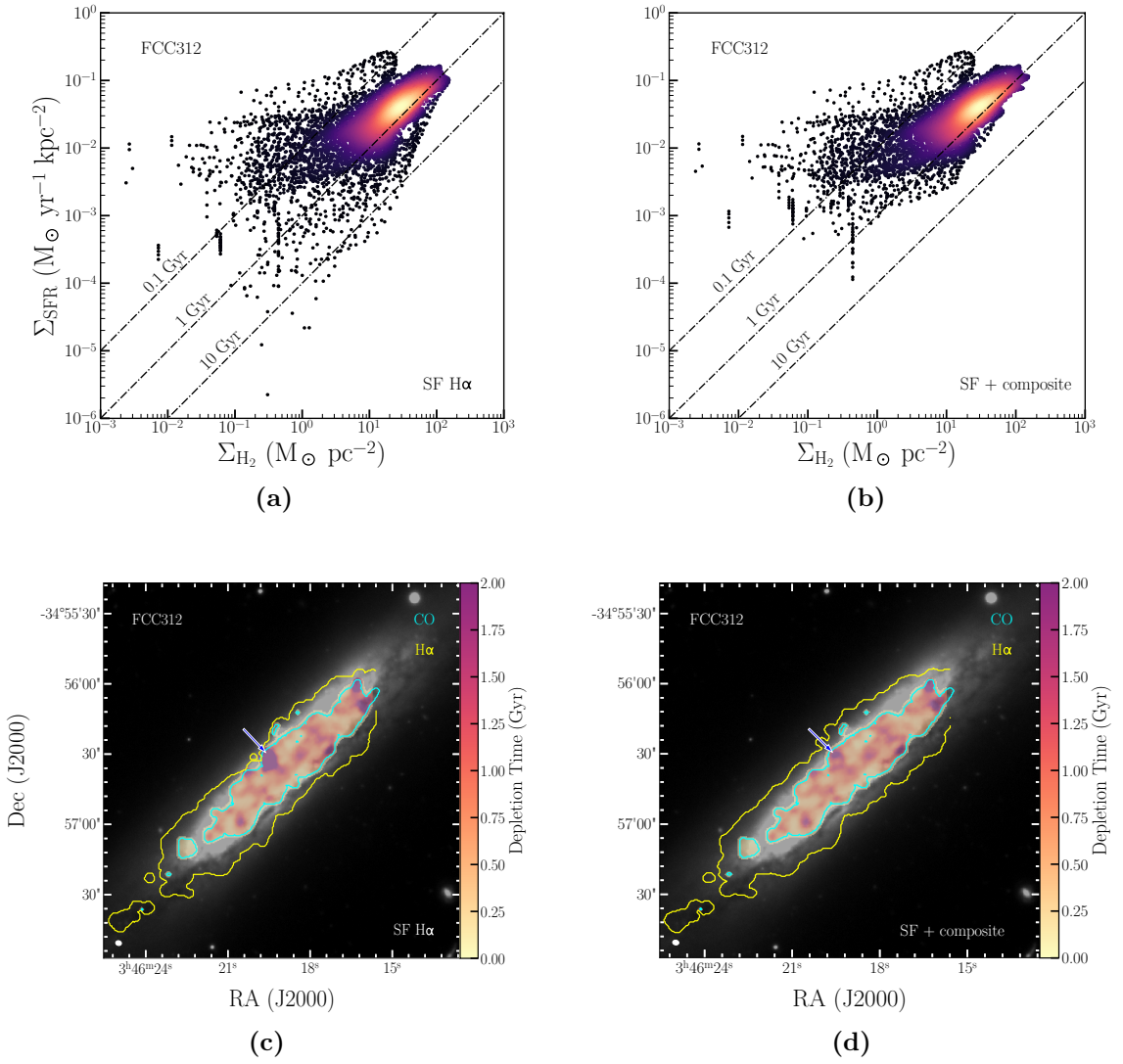

Figure C.9: Similar to Figure C.1, but for FCC312. Depletion times in this galaxy are relatively short: most resolution elements have depletion times shorter than 1 Gyr. The long depletion time area in the lower-left panel, in the centre of the top half of the galaxy (indicated with a blue/white arrow), is due to mosaicking effects in the MUSE data: a small fraction of the galaxy was not covered by the mosaic, resulting in an overestimation of the depletion time here.

Bibliography

Abadi M. G., Moore B., Bower R. G., 1999, MNRAS, 308, 947

Abell G. O., 1958, ApJS, 3, 211

Accurso G., et al., 2017, MNRAS, 470, 4750

Agertz O., Kravtsov A. V., 2015, ApJ, 804, 18

Alatalo K., et al., 2013, MNRAS, 432, 1796

Alves F. O., Caselli P., Girart J. M., Segura-Cox D., Franco G. A. P., Schmiedeke A., Zhao B., 2019, Science, 366, 90

Arias M., et al., 2018, A&A, 612, A110

Arthur J., et al., 2019, MNRAS, 484, 3968

Asano R. S., Takeuchi T. T., Hirashita H., Inoue A. K., 2013, Earth, Planets, and Space, 65, 213

Asplund M., Grevesse N., Sauval A. J., Scott P., 2009, ARAA, 47, 481

Avison A., George S. J., 2013, European Journal of Physics, 34, 7

Bacon R., et al., 2010, in Ground-based and Airborne Instrumentation for Astronomy III. p. 773508, doi:10.1117/12.856027

Bacon R., et al., 2015, A&A, 575, A75

Baes M., et al., 2014, MNRAS, 444, L90

Baldwin J. A., Phillips M. M., Terlevich R., 1981, PASP, 93, 5

Balog Z., et al., 2014, Experimental Astronomy, 37, 129

Balogh M. L., Pearce F. R., Bower R. G., Kay S. T., 2001, MNRAS, 326, 1228

Barazza F. D., Binggeli B., Jerjen H., 2002, A&A, 391, 823

Barnes J. E., 1989, Nature, 338, 123

Barnes D. G., et al., 2001, MNRAS, 322, 486

Bassett R., et al., 2013, ApJ, 770, 58

Behroozi P. S., Wechsler R. H., Conroy C., 2013, ApJ, 770, 57

Bekki K., 1998, ApJ, 502, L133

Bekki K., 2014, MNRAS, 438, 444

Benavides J. A., Sales L. V., Abadi M. G., 2020, MNRAS, 498, 3852

Bendo G. J., et al., 2010, MNRAS, 402, 1409

Bendo G. J., et al., 2013, MNRAS, 433, 3062

Bendo G. J., et al., 2015, MNRAS, 448, 135

Berentzen I., Athanassoula E., Heller C. H., Fricke K. J., 2004, MNRAS, 347, 220

Bigiel F., Leroy A., Walter F., Brinks E., de Blok W. J. G., Madore B., Thornley M. D., 2008, AJ, 136, 2846

Binggeli B., Sandage A., Tammann G. A., 1985, AJ, 90, 1681

Bisbas T. G., Papadopoulos P. P., Viti S., 2015, ApJ, 803, 37

Bitsakis T., Charmandaris V., da Cunha E., Díaz-Santos T., Le Floc'h E., Magdis G., 2011, A&A, 533, A142

Blakeslee J. P., et al., 2009, ApJ, 694, 556

Blanc G. A., Heiderman A., Gebhardt K., Evans Neal J. I., Adams J., 2009, ApJ, 704, 842

Blanchard A., Valls-Gabaud D., Mamon G. A., 1992, A&A, 264, 365

Bluck A. F. L., Mendel J. T., Ellison S. L., Moreno J., Simard L., Patton D. R., Starkenburg E., 2014, MNRAS, 441, 599

Boizelle B. D., Barth A. J., Darling J., Baker A. J., Buote D. A., Ho L. C., Walsh J. L., 2017, ApJ, 845, 170

Bolatto A. D., Wolfire M., Leroy A. K., 2013, ARAA, 51, 207

Booth R. S., et al., 1989, A&A, 216, 315

Boquien M., Burgarella D., Roehlly Y., Buat V., Ciesla L., Corre D., Inoue A. K., Salas H., 2019, A&A, 622, A103

Borisova E., et al., 2016, ApJ, 831, 39

Boselli A., Gavazzi G., 2006, PASP, 118, 517

Boselli A., Casoli F., Lequeux J., 1995, A&AS, 110, 521

Boselli A., Gavazzi G., Lequeux J., Buat V., Casoli F., Dickey J., Donas J., 1997, A&A, 327, 522

Boselli A., Boissier S., Cortese L., Gavazzi G., 2008, A&A, 489, 1015

Boselli A., et al., 2010, PASP, 122, 261

Boselli A., et al., 2011, A&A, 528, A107

Boselli A., Hughes T. M., Cortese L., Gavazzi G., Buat V., 2013, A&A, 550, A114

Boselli A., Cortese L., Boquien M., 2014a, A&A, 564, A65

Boselli A., Cortese L., Boquien M., Boissier S., Catinella B., Gavazzi G., Lagos C., Saintonge A., 2014b, A&A, 564, A67

Boselli A., et al., 2014c, A&A, 570, A69

Boselli A., Fossati M., Gavazzi G., Ciesla L., Buat V., Boissier S., Hughes T. M., 2015, A&A, 579, A102

Boselli A., et al., 2018a, A&A, 614, A56

Boselli A., et al., 2018b, A&A, 615, A114

Boyer M. L., et al., 2012, ApJ, 748, 40

Bradley L., et al., 2019, astropy/photutils: v0.7.2, doi:10.5281/zenodo.3568287, `https://doi.org/10.5281/zenodo.3568287`

Bregman J. N., Miller E. D., Irwin J. A., 2001, ApJ, 553, L125

Bremer M. N., et al., 2018, MNRAS, 476, 12

Bridges T. J., Irwin J. A., 1998, MNRAS, 300, 967

Briel U. G., Henry J. P., Boehringer H., 1992, A&A, 259, L31

Briggs D. S., 1995, in American Astronomical Society Meeting Abstracts. p. 1444

Brinchmann J., Charlot S., White S. D. M., Tremonti C., Kauffmann G., Heckman T., Brinkmann J., 2004, MNRAS, 351, 1151

Brosch N., 2015, MNRAS, 454, 3222

Burgarella D., Buat V., Iglesias-Páramo J., 2005, MNRAS, 360, 1413

Butcher H., Oemler A. J., 1978, ApJ, 219, 18

Calzetti D., Kinney A. L., Storchi-Bergmann T., 1994, ApJ, 429, 582

Calzetti D., Liu G., Koda J., 2012, ApJ, 752, 98

Caon N., Capaccioli M., D'Onofrio M., 1993, MNRAS, 265, 1013

Cappellari M., 2017, MNRAS, 466, 798

Cappellari M., et al., 2011, MNRAS, 413, 813

Cappellari M., et al., 2013, MNRAS, 432, 1709

Casasola V., et al., 2020, A&A, 633, A100

Casoli F., Boisse P., Combes F., Dupraz C., 1991, A&A, 249, 359

Casoli F., Dickey J., Kazes I., Boselli A., Gavazzi G., Jore K., 1996, A&AS, 116, 193

Chabrier G., 2003, PASP, 115, 763

Chamaraux P., Balkowski C., Gerard E., 1980, A&A, 83, 38

Chanamé J., Infante L., Reisenegger A., 2000, ApJ, 530, 96

Chevance M., et al., 2020, MNRAS, 493, 2872

Chung A., van Gorkom J. H., Kenney J. D. P., Vollmer B., 2007, ApJ, 659, L115

Chung A., van Gorkom J. H., Kenney J. D. P., Crowl H., Vollmer B., 2009, AJ, 138, 1741

Churazov E., et al., 2012, MNRAS, 421, 1123

Cicone C., et al., 2017, A&A, 604, A53

Cigan P., et al., 2019, ApJ, 886, 51

Ciolek G. E., Mouschovias T. C., 1995, ApJ, 454, 194

Clark C. J. R., et al., 2018, A&A, 609, A37

Clarke A. J., Debattista V. P., Roškar R., Quinn T., 2017, MNRAS, 465, L79

Coe D., 2010, preprint, (arXiv:1005.0411)

Colless M., Dunn A. M., 1996, ApJ, 458, 435

Colless M., et al., 2001, MNRAS, 328, 1039

Conselice C. J., 2002, ApJ, 573, L5

Conselice C. J., Gallagher John S. I., 1998, MNRAS, 297, L34

Conselice C. J., Gallagher John S. I., Wyse R. F. G., 2001, AJ, 122, 2281

Corbelli E., et al., 2012, A&A, 542, A32

Cortés J. R., Kenney J. D. P., Hardy E., 2006, AJ, 131, 747

Cortese L., et al., 2010, A&A, 518, L49

Cortese L., et al., 2012, A&A, 540, A52

Cortese L., et al., 2016, MNRAS, 459, 3574

Cowie L. L., Songaila A., 1977, Nature, 266, 501

Cox D. P., Smith B. W., 1976, ApJ, 203, 361

Coziol R., Ribeiro A. L. B., de Carvalho R. R., Capelato H. V., 1998, ApJ, 493, 563

Croom S., Saunders W., Heald R., 2004, Anglo-Australian Observatory Epping Newsletter, 106, 12

Da Rocha C., Mieske S., Georgiev I. Y., Hilker M., Ziegler B. L., Mendes de Oliveira C., 2011, A&A, 525, A86

Dame T. M., 2011, preprint, p. arXiv:1101.1499 (arXiv:1101.1499)

Davies J. I., et al., 2010, A&A, 518, L48

Davies J. I., et al., 2017, PASP, 129, 044102

Davis T. A., et al., 2013, MNRAS, 429, 534

Davis T. A., et al., 2014, MNRAS, 444, 3427

De Looze I., et al., 2010, A&A, 518, L54

De Looze I., et al., 2013, MNRAS, 436, 1057

De Looze I., Barlow M. J., Swinyard B. M., Rho J., Gomez H. L., Matsuura M., Wesson R., 2017, MNRAS, 465, 3309

De Looze I., et al., 2019, MNRAS, 488, 164

De Looze I., et al., 2020, MNRAS, 496, 3668

De Rijcke S., Dejonghe H., Zeilinger W. W., Hau G. K. T., 2003, A&A, 400, 119

De Vis P., et al., 2017, MNRAS, 471, 1743

De Vis P., et al., 2019, A&A, 623, A5

Dennis T. J., Chandran B. D. G., 2005, ApJ, 622, 205

Dib S., Piau L., Mohanty S., Braine J., 2011, MNRAS, 415, 3439

Dickey J. M., Gavazzi G., 1991, ApJ, 373, 347

Donahue M., Mack J., Voit G. M., Sparks W., Elston R., Maloney P. R., 2000, ApJ, 545, 670

Dopita M. A., Kewley L. J., Sutherland R. S., Nicholls D. C., 2016, Astrophys. Space Science, 361, 61

Draine B. T., et al., 2007, ApJ, 663, 866

Dressler A., 1980, ApJ, 236, 351

Drinkwater M. J., Sadler E. M., Davies J. I., Dickens R. J., Gregg M. D., Parker Q. A., Phillipps S., Smith R. M., 1999, in Morganti R., Couch W. J., eds, Looking Deep in the Southern Sky. p. 21 (`arXiv:astro-ph/9802095`)

Drinkwater M. J., Gregg M. D., Colless M., 2001, ApJ, 548, L139

Dunne L., Eales S., Ivison R., Morgan H., Edmunds M., 2003, Nature, 424, 285

Dwek E., Scalo J. M., 1980, ApJ, 239, 193

Edge A. C., 2001, MNRAS, 328, 762

Edge A. C., et al., 2010a, A&A, 518, L46

Edge A. C., et al., 2010b, A&A, 518, L47

Eigenthaler P., Ploeckinger S., Verdugo M., Ziegler B., 2015, MNRAS, 451, 2793

Elbaz D., et al., 2007, A&A, 468, 33

Elmegreen B. G., 2011, in Charbonnel C., Montmerle T., eds, EAS Publications Series Vol. 51, EAS Publications Series. pp 19–30 (arXiv:1101.3109), doi:10.1051/eas/1151002

Elmegreen D. M., Elmegreen B. G., 1987, ApJ, 314, 3

Fabian A. C., 1994, ARAA, 32, 277

Fabian A. C., 2012, ARAA, 50, 455

Fabian A. C., Sanders J. S., Ettori S., Taylor G. B., Allen S. W., Crawford C. S., Iwasawa K., Johnstone R. M., 2001, MNRAS, 321, L33

Fabian A. C., Sanders J. S., Taylor G. B., Allen S. W., Crawford C. S., Johnstone R. M., Iwasawa K., 2006, MNRAS, 366, 417

Falcón-Barroso J., et al., 2006, MNRAS, 369, 529

Fang J. J., Faber S. M., Koo D. C., Dekel A., 2013, ApJ, 776, 63

Farouki R., Shapiro S. L., 1980, ApJ, 241, 928

Feldmann R., Gnedin N. Y., Kravtsov A. V., 2011, ApJ, 732, 115

Ferguson H. C., 1989, AJ, 98, 367

Ferrarese L., et al., 2012, ApJS, 200, 4

Fitchett M., Webster R., 1987, ApJ, 317, 653

Ford G. P., et al., 2013, ApJ, 769, 55

Fouqué P., Solanes J. M., Sanchis T., Balkowski C., 2001, A&A, 375, 770

Fraternali F., Karim A., Magnelli B., Gómez-Guijarro C., Jiménez-Andrade E. F., Posses A. C., 2020, arXiv e-prints, p. arXiv:2011.05340

Freudling W., Romaniello M., Bramich D. M., Ballester P., Forchi V., García-Dabló C. E., Moehler S., Neeser M. J., 2013, A&A, 559, A96

Fu H., et al., 2013, Nature, 498, 338

Fujimoto Y., Chevance M., Haydon D. T., Krumholz M. R., Kruijssen J. M. D., 2019, MNRAS, 487, 1717

Fukushige T., Makino J., 2001, ApJ, 557, 533

Fuller C., et al., 2014, MNRAS, 440, 1571

Fuller C., et al., 2016, MNRAS, 458, 582

Fumagalli M., Gavazzi G., 2008, A&A, 490, 571

Fumagalli M., Krumholz M. R., Prochaska J. X., Gavazzi G., Boselli A., 2009, ApJ, 697, 1811

Gajda G., Łokas E. L., Athanassoula E., 2017, ApJ, 842, 56

Gaspari M., Ruszkowski M., Oh S. P., 2013, MNRAS, 432, 3401

Gaspari M., Brighenti F., Temi P., 2015, A&A, 579, A62

Gavazzi G., Boselli A., Scodeggio M., Pierini D., Belsole E., 1999, MNRAS, 304, 595

Gavazzi G., Boselli A., van Driel W., O'Neil K., 2005, A&A, 429, 439

Gavazzi G., O'Neil K., Boselli A., van Driel W., 2006, A&A, 449, 929

Gavazzi G., Fumagalli M., Cucciati O., Boselli A., 2010, A&A, 517, A73

Ge X., Gu Q.-S., García-Benito R., Xiao M.-Y., Li Z.-N., 2020, ApJ, 889, 132

Geller M. J., Huchra J. P., 1989, Science, 246, 897

Gensior J., Kruijssen J. M. D., Keller B. W., 2019, MNRAS submitted

Gerhard O., Arnaboldi M., Freeman K. C., Okamura S., Kashikawa N., Yasuda N., 2007, A&A, 468, 815

Gerin M., Combes F., Athanassoula E., 1990, A&A, 230, 37

Giesers B., et al., 2018, MNRAS, 475, L15

Giovanelli R., Haynes M. P., 1985, ApJ, 292, 404

Giovanelli R., et al., 2005, AJ, 130, 2598

Godwin J. G., Peach J. V., 1977, MNRAS, 181, 323

Goldsmith P. F., et al., 2011, ApJ, 737, 96

Gratier P., et al., 2017, A&A, 600, A27

Grenier I. A., Casandjian J.-M., Terrier R., 2005, Science, 307, 1292

Griffin M. J., et al., 2010, A&A, 518, L3

Grimes J. P., Heckman T., Strickland D., Ptak A., 2005, ApJ, 628, 187

Gunn J. E., Gott III J. R., 1972, ApJ, 176, 1

Guo F., Oh S. P., Ruszkowski M., 2008, ApJ, 688, 859

Hao C.-N., Kennicutt R. C., Johnson B. D., Calzetti D., Dale D. A., Moustakas J., 2011, ApJ, 741, 124

Hartogh P., et al., 2011, Nature, 478, 218

Hatch N. A., Crawford C. S., Fabian A. C., Johnstone R. M., 2005, MNRAS, 358, 765

Hayashi M., et al., 2018, ApJ, 856, 118

Haydon D. T., Kruijssen J. M. D., Hygate A. P. S., Schruba A., Krumholz M. R., Chevance M., Longmore S. N., 2018, MNRAS submitted, p. arXiv:1810.10897

Haydon D. T., Fujimoto Y., Chevance M., Kruijssen J. M. D., Krumholz M. R., Longmore S. N., 2020, MNRAS submitted

Haynes M. P., Giovanelli R., 1986, ApJ, 306, 466

Haynes M. P., Giovanelli R., Roberts M. S., 1979, ApJ, 229, 83

Heckman T. M., Baum S. A., van Breugel W. J. M., McCarthy P., 1989, ApJ, 338, 48

Hernández-Fernández J. D., Vílchez J. M., Iglesias-Páramo J., 2012, ApJ, 751, 54

Hess K. M., Wilcots E. M., 2013, AJ, 146, 124

Hildebrand R. H., 1983, Quarterly Journal of the Royal Astronomical Society, 24, 267

Hinton S. R., Davis T. M., Lidman C., Glazebrook K., Lewis G. F., 2016, Astronomy and Computing, 15, 61

Hirashita H., 2012, MNRAS, 422, 1263

Ho I. T., Lim J., Dinh-V-Trung 2009, ApJ, 698, 1191

Höfner S., Olofsson H., 2018, A&A Rev., 26, 1

Högbom J. A., 1974, A&AS, 15, 417

Horellou C., Casoli F., Dupraz C., 1995, A&A, 303, 361

Hubble E. P., 1926, ApJ, 63, 236

Hubble E. P., 1936, Realm of the Nebulae

Huchra J. P., et al., 2012, ApJS, 199, 26

Hughes T. M., Cortese L., Boselli A., Gavazzi G., Davies J. I., 2013, A&A, 550, A115

Hunter D. A., et al., 2012, AJ, 144, 134

Hygate A. P. S., Kruijssen J. M. D., Chevance M., Walter F., Schruba A., Kim J. J., Haydon D. T., Longmore S. N., 2019, MNRAS submitted,

Iodice E., et al., 2016, ApJ, 820, 42

Iodice E., et al., 2017, ApJ, 839, 21

Iodice E., et al., 2019a, A&A, 623, A1

Iodice E., et al., 2019b, A&A, 627, A136

Issa M. R., MacLaren I., Wolfendale A. W., 1990, A&A, 236, 237

Jachym P., et al., 2019, arXiv e-prints, p. arXiv:1905.13249

Jaffé Y. L., et al., 2018, MNRAS, 476, 4753

Janz J., et al., 2014, ApJ, 786, 105

Jerjen H., Kalnajs A., Binggeli B., 2000, A&A, 358, 845

Johnson M. A., Betz A. L., Townes C. H., 1974, Phys. Rev. Lett., 33, 1617

Jones C., Stern C., Forman W., Breen J., David L., Tucker W., Franx M., 1997, ApJ, 482, 143

Jones A. P., Fanciullo L., Köhler M., Verstraete L., Guillet V., Bocchio M., Ysard N., 2013, A&A, 558, A62

Joshi G. D., Wadsley J., Parker L. C., 2017, MNRAS, 468, 4625

Joshi G. D., Parker L. C., Wadsley J., Keller B. W., 2019, MNRAS, 483, 235

Jung S. L., Choi H., Wong O. I., Kimm T., Chung A., Yi S. K., 2018, ApJ, 865, 156

Kauffmann G., et al., 2003, MNRAS, 346, 1055

Kautsch S. J., Gonzalez A. H., Soto C. A., Tran K.-V. H., Zaritsky D., Moustakas J., 2008, ApJ, 688, L5

Kelvin L. S., et al., 2014, MNRAS, 444, 1647

Kenney J. D. P., Young J. S., 1989, ApJ, 344, 171

Kenney J. D. P., van Gorkom J. H., Vollmer B., 2004, AJ, 127, 3361

Kenney J. D. P., Geha M., Jáchym P., Crowl H. H., Dague W., Chung A., van Gorkom J., Vollmer B., 2014, ApJ, 780, 119

Kennicutt Jr. R. C., 1998, ApJ, 498, 541

Kennicutt R. C., et al., 2011, PASP, 123, 1347

Kewley L. J., Ellison S. L., 2008, ApJ, 681, 1183

Kewley L. J., Dopita M. A., Sutherland R. S., Heisler C. A., Trevena J., 2001, ApJ, 556, 121

Köhler M., Jones A., Ysard N., 2014, A&A, 565, L9

Koleva M., Bouchard A., Prugniel P., De Rijcke S., Vauglin I., 2013, MNRAS, 428, 2949

Koribalski B. S., et al., 2020, Astrophys. Space Science, 365, 118

Kormendy J., 1977, ApJ, 217, 406

Kormendy J., 1979, ApJ, 227, 714

Kreckel K., et al., 2018, ApJ, 863, L21

Kreckel K., et al., 2019, arXiv e-prints, p. arXiv:1910.07190

Kronberger T., Kapferer W., Ferrari C., Unterguggenberger S., Schindler S., 2008, A&A, 481, 337

Kroupa P., 2001, MNRAS, 322, 231

Kroupa P., Weidner C., 2003, ApJ, 598, 1076

Kruijssen J. M. D., Longmore S. N., 2014a, MNRAS, 439, 3239

Kruijssen J. M. D., Longmore S. N., 2014b, MNRAS, 439, 3239

Kruijssen J. M. D., Schruba A., Hygate A. P. S., Hu C.-Y., Haydon D. T., Longmore S. N., 2018, MNRAS, 479, 1866

Kruijssen J. M. D., et al., 2019, Nature, 569, 519

Krumholz M. R., 2014, Phys. Repts., 539, 49

Krumholz M. R., Dekel A., McKee C. F., 2012, ApJ, 745, 69

Kubo J. M., Stebbins A., Annis J., Dell'Antonio I. P., Lin H., Khiabanian H., Frieman J. A., 2007, ApJ, 671, 1466

Kuijken K., et al., 2002, The Messenger, 110, 15

Küppers M., et al., 2014, Nature, 505, 525

Kwak S., Kim W.-T., Rey S.-C., Kim S., 2017, ApJ, 839, 24

Kwak S., Kim W.-T., Rey S.-C., Quinn T. R., 2019, ApJ, 887, 139

Labeyrie A., 1975, ApJ, 196, L71

Lada C. J., Forbrich J., Lombardi M., Alves J. F., 2012, ApJ, 745, 190

Ladd N., Purcell C., Wong T., Robertson S., 2005, PASA, 22, 62

Lal D. V., 2020, ApJS, 250, 22

Langer W. D., Velusamy T., Pineda J. L., Willacy K., Goldsmith P. F., 2014, A&A, 561, A122

Larson R. B., 1972, Nature Physical Science, 236, 7

Larson R. B., Tinsley B. M., Caldwell C. N., 1980, ApJ, 237, 692

Lauberts A., Valentijn E. A., 1989, The surface photometry catalogue of the ESO-Uppsala galaxies

Laurikainen E., Salo H., Buta R., Knapen J., Speltincx T., Block D., 2006, AJ, 132, 2634

Lazareff B., Castets A., Kim D. W., Jura M., 1989, ApJ, 336, L13

Lee-Waddell K., et al., 2018, MNRAS, 474, 1108

Lee B., et al., 2017, MNRAS, 466, 1382

Leitherer C., Robert C., Drissen L., 1992, ApJ, 401, 596

Leitherer C., Ekström S., Meynet G., Schaerer D., Agienko K. B., Levesque E. M., 2014, ApJS, 212, 14

Lena D., et al., 2015, ApJ, 806, 84

Leroy A. K., Walter F., Brinks E., Bigiel F., de Blok W. J. G., Madore B., Thornley M. D., 2008, AJ, 136, 2782

Leroy A. K., et al., 2011, ApJ, 737, 12

Leroy A. K., et al., 2013, AJ, 146, 19

Leroy A. K., et al., 2019, ApJS, 244, 24

Lewis I. J., et al., 2002, MNRAS, 333, 279

Licquia T. C., Newman J. A., 2015, ApJ, 806, 96

Lim J., Ao Y., Dinh-V-Trung 2008, ApJ, 672, 252

Lisenfeld U., Ferrara A., 1998, ApJ, 496, 145

Lisker T., Grebel E. K., Binggeli B., 2006a, AJ, 132, 497

Lisker T., Glatt K., Westera P., Grebel E. K., 2006b, AJ, 132, 2432

Lisker T., Vijayaraghavan R., Janz J., Gallagher John S. I., Engler C., Urich L., 2018, ApJ, 865, 40

Liu G., Koda J., Calzetti D., Fukuhara M., Momose R., 2011, ApJ, 735, 63

Lo K. Y., Sargent W. L. W., 1979, ApJ, 227, 756

Łokas E. L., Athanassoula E., Debattista V. P., Valluri M., Pino A. d., Semczuk M., Gajda G., Kowalczyk K., 2014, MNRAS, 445, 1339

Loni A., et al., 2021, arXiv e-prints, p. arXiv:2102.01185

Loveday J., 1996, MNRAS, 278, 1025

Lynden-Bell D., 1967, MNRAS, 136, 101

Madau P., Dickinson M., 2014, ARAA, 52, 415

Madden S. C., et al., 2013, PASP, 125, 600

Magrini L., et al., 2011, A&A, 535, A13

Mahajan S., 2013, MNRAS, 431, L117

Makarov D., Prugniel P., Terekhova N., Courtois H., Vauglin I., 2014, A&A, 570, A13

Maloney P., Black J. H., 1988, ApJ, 325, 389

Marsh K. A., Whitworth A. P., Lomax O., 2015, MNRAS, 454, 4282

Martig M., Bournaud F., Teyssier R., Dekel A., 2009, ApJ, 707, 250

Martig M., et al., 2013, MNRAS, 432, 1914

Martin D. C., et al., 2005, The Astrophysical Journal, 619, L1L6

Massey R., et al., 2015, MNRAS, 449, 3393

Mathews W. G., Faltenbacher A., Brighenti F., 2006, ApJ, 638, 659

Matsuura M., 2017, Dust and Molecular Formation in Supernovae. p. 2125, doi:10.1007/978-3-319-21846-5˙130

Matsuura M., et al., 2009, MNRAS, 396, 918

Matsuura M., et al., 2017, MNRAS, 469, 3347

Mattsson L., De Cia A., Andersen A. C., Zafar T., 2014, MNRAS, 440, 1562

McCready L. L., Pawsey J. L., Payne-Scott R., 1947, Proceedings of the Royal Society of London Series A, 190, 357

McElroy R. E., et al., 2016, A&A, 593, L8

McLaughlin D. E., 1999, ApJ, 512, L9

McMullin J. P., Waters B., Schiebel D., Young W., Golap K., 2007, in Shaw R. A., Hill F., Bell D. J., eds, Astronomical Society of the Pacific Conference Series Vol. 376, Astronomical Data Analysis Software and Systems XVI. p. 127

Mei S., et al., 2007, ApJ, 655, 144

Mendelin M., Binggeli B., 2017, A&A, 604, A96

Mendes de Oliveira C., Plana H., Amram P., Bolte M., Boulesteix J., 1998, ApJ, 507, 691

Merritt D., 1983, ApJ, 264, 24

Meyer M., Robotham A., Obreschkow D., Westmeier T., Duffy A. R., Staveley-Smith L., 2017, PASA, 34, 52

Mihos J. C., Harding P., Feldmeier J. J., Rudick C., Janowiecki S., Morrison H., Slater C., Watkins A., 2017, ApJ, 834, 16

Miller G. E., Scalo J. M., 1979, ApJS, 41, 513

Miller M. C., Lamb F. K., Cook G. B., 1998, ApJ, 509, 793

Moore B., Katz N., Lake G., Dressler A., Oemler A., 1996, Nature, 379, 613

Mora M. D., Chanamé J., Puzia T. H., 2015, AJ, 150, 93

Moretti A., et al., 2018, MNRAS, 480, 2508

Moretti A., et al., 2019, arXiv e-prints, p. arXiv:1912.06565

Moretti A., et al., 2020, ApJ, 897, L30

Morokuma-Matsui K., et al., 2019, Pub. Astron. Soc. Japan, 71, 85

Moustakas J., et al., 2013, ApJ, 767, 50

Murphy E. J., et al., 2011, ApJ, 737, 67

Narayanan D., Krumholz M. R., Ostriker E. C., Hernquist L., 2012, MNRAS, 421, 3127

Navarro J. F., Frenk C. S., White S. D. M., 1997, ApJ, 490, 493

Nehlig F., Vollmer B., Braine J., 2016, A&A, 587, A108

Nersesian A., et al., 2019, A&A, 624, A80

Nishiura S., Shimada M., Ohyama Y., Murayama T., Taniguchi Y., 2000, AJ, 120, 1691

Noble A. G., et al., 2018, preprint, (arXiv:1809.03514)

Noeske K. G., et al., 2007, ApJ, 660, L43

Noguchi M., 1996, ApJ, 469, 605

Noll S., Burgarella D., Giovannoli E., Buat V., Marcillac D., Muñoz-Mateos J. C., 2009, A&A, 507, 1793

Nulsen P. E. J., 1982, MNRAS, 198, 1007

Odekon M. C., et al., 2016, ApJ, 824, 110

Oemler Jr. A., 1974, ApJ, 194, 1

Oh S. H., Kim W.-T., Lee H. M., Kim J., 2008, ApJ, 683, 94

Oh K., Sarzi M., Schawinski K., Yi S. K., 2011, ApJS, 195, 13

Olivares V., et al., 2019, A&A, 631, A22

Onodera S., et al., 2010, ApJ, 722, L127

Oort J. H., 1970, A&A, 7, 381

Oteo I., et al., 2016, ApJ, 827, 34

Ott S., 2010, in Mizumoto Y., Morita K. I., Ohishi M., eds, Astronomical Society of the Pacific Conference Series Vol. 434, Astronomical Data Analysis Software and Systems XIX. p. 139 (arXiv:1011.1209)

Owen P. J., Barlow M. J., 2015, ApJ, 801, 141

Owen R. A., Warwick R. S., 2009, MNRAS, 394, 1741

Paolillo M., Fabbiano G., Peres G., Kim D.-W., 2002, ApJ, 565, 883

Pappalardo C., et al., 2012, A&A, 545, A75

Paradis D., Dobashi K., Shimoikura T., Kawamura A., Onishi T., Fukui Y., Bernard J. P., 2012, A&A, 543, A103

Paudel S., et al., 2017, ApJ, 834, 66

Paudel S., Smith R., Yoon S. J., Calderón-Castillo P., Duc P.-A., 2018, ApJS, 237, 36

Pedraz S., Gorgas J., Cardiel N., Sánchez-Blázquez P., Guzmán R., 2002, MNRAS, 332, L59

Peletier R. F., Balcells M., 1996, AJ, 111, 2238

Peletier R., et al., 2020, arXiv e-prints, p. arXiv:2008.12633

Peng C. Y., Ho L. C., Impey C. D., Rix H.-W., 2002, AJ, 124, 266

Peng C. Y., Ho L. C., Impey C. D., Rix H.-W., 2010, AJ, 139, 2097

Peng Y.-j., Lilly S. J., Renzini A., Carollo M., 2012, ApJ, 757, 4

Penny S. J., et al., 2016, MNRAS, 462, 3955

Péroux C., Howk J. C., 2020, ARAA, 58, annurev

Pettini M., Pagel B. E. J., 2004, MNRAS, 348, L59

Phillipps S., 2005, The Structure and Evolution of Galaxies

Pilbratt G. L., et al., 2010, A&A, 518, L1

Pinna F., et al., 2019a, A&A, 623, A19

Pinna F., et al., 2019b, A&A, 625, A95

Poggianti B. M., et al., 2017, ApJ, 844, 48

Poglitsch A., et al., 2010, A&A, 518, L2

Pranger F., Trujillo I., Kelvin L. S., Cebrián M., 2017, MNRAS, 467, 2127

Priestley F. D., Barlow M. J., De Looze I., 2019, MNRAS, 485, 440

Pulido F. A., et al., 2018, ApJ, 853, 177

Rafferty D. A., Bîrzan L., Nulsen P. E. J., McNamara B. R., Brandt W. N., Wise M. W., Röttgering H. J. A., 2013, MNRAS, 428, 58

Rahman N., Bolatto A., Collaborators S., 2010, in American Astronomical Society Meeting Abstracts #215. p. 382.04

Raj M. A., et al., 2019, A&A, 628, A4

Raj M. A., et al., 2020, A&A, 640, A137

Ramatsoku M., et al., 2019, MNRAS, p. 1537

Ramos-Martínez M., Gómez G. C., Pérez-Villegas Á., 2018, MNRAS, 476, 3781

Rasmussen J., Ponman T. J., Mulchaey J. S., Miles T. A., Raychaudhury S., 2006, MNRAS, 373, 653

Regan M. W., Thornley M. D., Helfer T. T., Sheth K., Wong T., Vogel S. N., Blitz L., Bock D. C. J., 2001, ApJ, 561, 218

Rémy-Ruyer A., et al., 2014, A&A, 563, A31

Reuter H. P., Pohl M., Lesch H., Sievers A. W., 1993, A&A, 277, 21

Revaz Y., Combes F., Salomé P., 2008, A&A, 477, L33

Reynolds J. H., 1916, The Observatory, 39, 174

Reynolds T. N., et al., 2019, MNRAS, 482, 3591

Reynolds T. N., Westmeier T., Staveley-Smith L., Chauhan G., Lagos C. D. P., 2020, MNRAS, 493, 5089

Richstone D. O., 1976, ApJ, 204, 642

Riess A. G., et al., 2016, ApJ, 826, 56

Roberts I. D., Parker L. C., 2017, MNRAS, 467, 3268

Robotham A. S. G., et al., 2011, MNRAS, 416, 2640

Rodrigues M., 2010, PhD thesis, -

Rodríguez-Ardila A., Prieto M. A., Mazzalay X., Fernández-Ontiveros J. A., Luque R., Müller-Sánchez F., 2017, MNRAS, 470, 2845

Rubin V. C., Hunter D. A., Ford W. Kent J., 1990, ApJ, 365, 86

Rudnick G., et al., 2017, ApJ, 849, 27

Russell H. R., et al., 2019, MNRAS, 490, 3025

Ruszkowski M., Brüggen M., Begelman M. C., 2004, ApJ, 611, 158

Ryś A., Falcón-Barroso J., van de Ven G., 2013, MNRAS, 428, 2980

Saintonge A., et al., 2011, MNRAS, 415, 32

Saintonge A., et al., 2012, ApJ, 758, 73

Saintonge A., et al., 2017, ApJS, 233, 22

Salim S., et al., 2016, ApJS, 227, 2

Salim S., Boquien M., Lee J. C., 2018, ApJ, 859, 11

Salomé P., 2013, in Wong T., Ott J., eds, Vol. 292, Molecular Gas, Dust, and Star Formation in Galaxies. pp 169–174, doi:10.1017/S1743921313000975

Salomé P., Combes F., 2003, A&A, 412, 657

Salomé P., et al., 2006, A&A, 454, 437

Salpeter E. E., 1955, ApJ, 121, 161

Salvatier J., Wieckiâ T. V., Fonnesbeck C., 2016, PyMC3: Python probabilistic programming framework (ascl:1610.016)

Sánchez-Janssen R., Aguerri J. A. L., 2012, MNRAS, 424, 2614

Sánchez S. F., et al., 2017, MNRAS, 469, 2121

Sánchez S. F., et al., 2019, MNRAS, 484, 3042

Sandstrom K. M., et al., 2013, ApJ, 777, 5

Sarzi M., et al., 2006, MNRAS, 366, 1151

Sarzi M., et al., 2018, A&A, 616, A121

Sault R. J., Teuben P. J., Wright M. C. H., 1995, in Shaw R. A., Payne H. E., Hayes J. J. E., eds, Astronomical Society of the Pacific Conference Series Vol. 77, Astronomical Data Analysis Software and Systems IV. p. 433 (arXiv:astro-ph/0612759)

Saunders W., et al., 2004, in Moorwood A. F. M., Iye M., eds, Proc. SPIEVol. 5492, Ground-based Instrumentation for Astronomy. pp 389–400, doi:10.1117/12.550871

Scharf C. A., Zurek D. R., Bureau M., 2005, ApJ, 633, 154

Schawinski K., Thomas D., Sarzi M., Maraston C., Kaviraj S., Joo S.-J., Yi S. K., Silk J., 2007, MNRAS, 382, 1415

Schawinski K., et al., 2014, MNRAS, 440, 889

Schindler S., Binggeli B., Böhringer H., 1999, A&A, 343, 420

Schipani P., et al., 2012, Memorie della Societa Astronomica Italiana Supplementi, 19, 393

Schmidt M., 1959, ApJ, 129, 243

Schruba A., Leroy A. K., Walter F., Sand strom K., Rosolowsky E., 2010, ApJ, 722, 1699

Schruba A., et al., 2011, AJ, 142, 37

Scott T. C., Brinks E., Cortese L., Boselli A., Bravo-Alfaro H., 2018, MNRAS, 475, 4648

Scoville N. Z., 2013, Evolution of star formation and gas. p. 491

Serra P., Jurek R., Flöer L., 2012, PASA, 29, 296

Serra P., et al., 2015, MNRAS, 448, 1922

Serra P., et al., 2016, in Proceedings of MeerKAT Science: On the Pathway to the SKA. 25-27 May, 2016 Stellenbosch, South Africa (MeerKAT2016). Online at "https://pos.sissa.it/cgi-bin/reader/conf.cgi?confid=277, id.8. p. 8 (arXiv:1709.01289)

Sérsic J. L., 1963, Boletin de la Asociacion Argentina de Astronomia La Plata Argentina, 6, 41

Seth R., Raychaudhury S., 2020, MNRAS, 497, 466

Shapley H., Curtis H. D., 1921, Bulletin of the National Research Council, 2, 171

Sharp R., et al., 2006, in Society of Photo-Optical Instrumentation Engineers (SPIE) Conference Series. p. 62690G (arXiv:astro-ph/0606137), doi:10.1117/12.671022

Sheth K., et al., 2008, ApJ, 675, 1141

Shull J. M., 2014, ApJ, 784, 142

Slavin J. D., Dwek E., Jones A. P., 2015, ApJ, 803, 7

Smith R. J., Glover S. C. O., Clark P. C., Klessen R. S., Springel V., 2014, MNRAS, 441, 1628

Smith R., Choi H., Lee J., Rhee J., Sanchez-Janssen R., Yi S. K., 2016, ApJ, 833, 109

Snowden S. L., Egger R., Finkbeiner D. P., Freyberg M. J., Plucinsky P. P., 1998, ApJ, 493, 715

Solanes J. M., Manrique A., García-Gómez C., González-Casado G., Giovanelli R., Haynes M. P., 2001, ApJ, 548, 97

Somerville R. S., Davé R., 2015, ARAA, 53, 51

Springel V., et al., 2005, Nature, 435, 629

Stach S. M., Swinbank A. M., Smail I., Hilton M., Simpson J. M., Cooke E. A., 2017, ApJ, 849, 154

Stanke T., et al., 2010, A&A, 518, L94

Stark A. A., Knapp G. R., Bally J., Wilson R. W., Penzias A. A., Rowe H. E., 1986, ApJ, 310, 660

Steer I., et al., 2017, AJ, 153, 37

Steinhauser D., Schindler S., Springel V., 2016, A&A, 591, A51

Strickland D. K., Stevens I. R., 2000, MNRAS, 314, 511

Sun S., Guo Q., Wang L., Lacey C. G., Wang J., Gao L., Pan J., 2018, MNRAS, 477, 3136

Tabatabaei F. S., Berkhuijsen E. M., 2010, A&A, 517, A77

Teimoorinia H., Bluck A. F. L., Ellison S. L., 2016, MNRAS, 457, 2086

Teyssier R., 2002, A&A, 385, 337

Thomsen B., Baum W. A., Hammergren M., Worthey G., 1997, ApJ, 483, L37

Tinsley B. M., Larson R. B., 1978, ApJ, 221, 554

Toloba E., Boselli A., Cenarro A. J., Peletier R. F., Gorgas J., Gil de Paz A., Muñoz-Mateos J. C., 2011, A&A, 526, A114

Tonry J. L., Dressler A., Blakeslee J. P., Ajhar E. A., Fletcher A. B., Luppino G. A., Metzger M. R., Moore C. B., 2001, ApJ, 546, 681

Tüllmann R., Pietsch W., Rossa J., Breitschwerdt D., Dettmar R. J., 2006, A&A, 448, 43

Tyler K., Quillen A. C., LaPage A., Rieke G. H., 2004, ApJ, 610, 213

Upton Sanderbeck P. R., McQuinn M., D'Aloisio A., Werk J. K., 2018, ApJ, 869, 159

Utomo D., et al., 2017, ApJ, 849, 26

Venhola A., et al., 2017, A&A, 608, A142

Venhola A., et al., 2018, A&A, 620, A165

Venhola A., et al., 2019, A&A, 625, A143

Verdes-Montenegro L., Yun M. S., Williams B. A., Huchtmeier W. K., Del Olmo A., Perea J., 2001, A&A, 377, 812

Verdes-Montenegro L., Del Olmo A., Iglesias-Páramo J. I., Perea J., Vílchez J. M., Yun M. S., Huchtmeier W. K., 2002, A&A, 396, 815

Verdugo C., Combes F., Dasyra K., Salomé P., Braine J., 2015, A&A, 582, A6

Viaene S., et al., 2019, A&A, 622, A89

Voigt L. M., Fabian A. C., 2004, MNRAS, 347, 1130

Voit G. M., Donahue M., 2015, ApJ, 799, L1

Vollmer B., Balkowski C., Cayatte V., van Driel W., Huchtmeier W., 2004, A&A, 419, 35

Vollmer B., Soida M., Otmianowska-Mazur K., Kenney J. D. P., van Gorkom J. H., Beck R., 2006, A&A, 453, 883

Vollmer B., Braine J., Pappalardo C., Hily-Blant P., 2008, A&A, 491, 455

Vollmer B., Wong O. I., Braine J., Chung A., Kenney J. D. P., 2012, A&A, 543, A33

Vulcani B., et al., 2018, ApJ, 866, L25

Wake D. A., van Dokkum P. G., Franx M., 2012, ApJ, 751, L44

Wakelam V., et al., 2017, Molecular Astrophysics, 9, 1

Wang Y., et al., 2018, ApJ, 868, 130

Wang J., Xu W., Lee B., Du M., Overzier R., Shao L., 2020, arXiv e-prints, p. arXiv:2009.08159

Watts A. B., Catinella B., Cortese L., Power C., 2020, MNRAS, 492, 3672

Waugh M., et al., 2002, MNRAS, 337, 641

Weilbacher P. M., Streicher O., Urrutia T., Jarno A., Pécontal-Rousset A., Bacon R., Böhm P., 2012, in Software and Cyberinfrastructure for Astronomy II. p. 84510B, doi:10.1117/12.925114

Weilbacher P. M., Streicher O., Palsa R., 2016, MUSE-DRP: MUSE Data Reduction Pipeline (ascl:1610.004)

White S. D. M., Frenk C. S., 1991, ApJ, 379, 52

Williams T. G., Gear W. K., Smith M. W. L., 2018, MNRAS, 479, 297

Williams T. G., Gear W. K., Smith M. W. L., 2019, MNRAS, 483, 5135

Wolfire M. G., Hollenbach D., McKee C. F., 2010, ApJ, 716, 1191

Wong T., Blitz L., 2002, ApJ, 569, 157

Woo J., et al., 2013, MNRAS, 428, 3306

Wright E. L., et al., 2010, AJ, 140, 1868

Wu X., Tremaine S., 2006, ApJ, 643, 210

Yagi M., et al., 2010, AJ, 140, 1814

Yoon H., Chung A., Smith R., Jaffé Y. L., 2017, ApJ, 838, 81

Young L. M., et al., 2011, MNRAS, 414, 940

Ysard N., Köhler M., Jones A., Miville-Deschênes M. A., Abergel A., Fanciullo L., 2015, A&A, 577, A110

Yun K., et al., 2018, MNRAS, p. 3016

Zabel N., et al., 2019, MNRAS, 483, 2251

Zabel N., et al., 2020, MNRAS, 496, 2155

Zabel N., et al., 2021, arXiv e-prints, p. arXiv:2102.02148

Zabludoff A. I., Mulchaey J. S., 1998, ApJ, 498, L5

Zajaček M., et al., 2019, A&A, 630, A83

Zakamska N. L., Narayan R., 2003, ApJ, 582, 162

Zhukovska S., 2014, A&A, 562, A76

Zhukovska S., Dobbs C., Jenkins E. B., Klessen R. S., 2016, ApJ, 831, 147

Zwicky F., 1933, Helvetica Physica Acta, 6, 110

de Graauw T., et al., 2010, A&A, 518, L6

de Jong R. S., 1996, A&A, 313, 45

de La Caille N. L., 1763, Coelum australe stelliferum, doi:10.3931/e-rara-529.

de Vaucouleurs G., 1948, Annales d'Astrophysique, 11, 247

de Vaucouleurs G., 1959, Handbuch der Physik, 53, 275

de Vaucouleurs G., de Vaucouleurs A., Corwin Herold G. J., Buta R. J., Paturel G., Fouque P., 1991, Third Reference Catalogue of Bright Galaxies

de los Reyes M. A. C., Kennicutt Robert C. J., 2019, ApJ, 872, 16

di Serego Alighieri S., et al., 2007, A&A, 474, 851

di Serego Alighieri S., et al., 2013, A&A, 552, A8

van Dishoeck E. F., Blake G. A., Draine B. T., Lunine J. I., 1993, in Levy E. H., Lunine J. I., eds, Protostars and Planets III. p. 163

van Dokkum P. G., Abraham R., Merritt A., Zhang J., Geha M., Conroy C., 2015, ApJ, 798, L45

van de Voort F., Bahé Y. M., Bower R. G., Correa C. A., Crain R. A., Schaye J., Theuns T., 2017, MNRAS, 466, 3460

van den Bergh S., 1976, ApJ, 206, 883

van der Kruit P. C., Searle L., 1982, A&A, 110, 79